School of Electrical Engineering, Computing &
Mathematical Sciences

Positron scattering from complex atoms and molecules of relevance to biological, fusion, and plasma research

Nicolas Antonio Mori
0000-0002-6167-8822

This thesis is presented for the Degree of
Doctor of Philosophy
of
Curtin University

May 2024

Declaration

To the best of my knowledge and belief this thesis contains no material previously published by any other person except where due acknowledgement has been made.

This thesis contains no material which has been accepted for the award of any other degree or diploma in any university.

Portions of this thesis contain extracts from my own published work in which the copyright is held by the publisher. In each case the publishers provide the right to use an article or a portion of an article in a thesis or dissertation without requesting permission.

Nicolas Antonio Mori
27 May 2024

Abstract

This thesis is devoted to theoretical studies of positron scattering from multi-electron atoms and molecules. To perform these studies, the single-centre convergent close-coupling (CCC) theory and code were extended beyond quasi-one and -two electron systems to atoms with any number of electrons. A complex model potential, scaled to the CCC calculations, was also utilised to address the issues associated with single-centre expansions and to allow for the calculation of positronium-formation and direct ionisation cross sections. For molecular systems, a modified version of the IAM-SCAR technique was used to calculate the required cross sections.

Major results

1. Theoretical and code development for the single-centre CCC code for positron-atom scattering from atoms with any number of available electrons.

2. Development of the CCC-pot technique, where complex model potential calculations are scaled to the single-centre CCC calculation allowing for calculation of positronium-formation, direct ionisation, and inelastic cross sections between the positronium-formation and ionisation threshold. Furthermore, the development of a code that calculates the model potential atomic cross sections required by this technique.

3. Comprehensive calculations of positron scattering from carbon [1], oxygen [2], neon [3], argon [3], boron, and fluorine atoms for energies between 10^{-5} eV and 5000 eV.

4. Use of the IAM-SCAR approach with atomic CCC results [4] to calculate positron scattering cross sections for the H_2, O_2, CO, CO_2, O_3,

H_2O, CH_4, and CF_4 molecules.

Layout of thesis

Here, a brief description of each chapter is provided.

Chapter 1 contains a description of the motivations for the current research, atomic scattering processes, contemporary theoretical approaches, and an overview of the current state of the field for each of the considered targets.

Chapter 2 contains an overview of the theory behind the current implementation of the single-centre CCC approach in calculations of the target structure and positron scattering.

Chapter 3 contains a detailed overview of how the complex model potential is utilised in the current formulation, how it is scaled with single-centre CCC results, and then how it is used to calculate positronium-formation, direct ionisation, and inelastic cross sections between the positronium-formation and direct ionisation thresholds. A demonstration of this process is provided for H and He.

Chapter 4 contains an overview of the IAM-SCAR approach and the current modifications applied to it to calculate CCC-SCAR cross sections. A demonstration of this approach for H_2 is provided in this chapter.

Chapter 5 contains a comparison of results for H, He, and Ne in the frozen-core approximation calculated with the current CCC code and the existing frozen-core CCC code.

Chapter 6 presents the calculations conducted for positron scattering on atomic carbon.

Chapter 7 presents the calculations conducted for positron scattering on atomic oxygen.

Chapter 8 presents the calculations conducted for positron scattering on neon and argon.

Chapter 9 presents the calculations conducted for positron scattering on boron.

Chapter 10 presents the calculations conducted for positron scattering on atomic fluorine.

Chapter 11 presents the CCC-SCAR calculations completed for a range of molecular targets including O_2, CO, CO_2, O_3, H_2O, CH_4, and CF_4.

Finally, *Chapter* 12 contains the conclusions of the current work and how this work can be extended in future.

Also included are Appendix. A, which describes the computational implementation of the developed CCC code, and Appendix. B, which provides the scaled Born calculations for each of the considered atoms.

Contents

List of Figures

List of Tables

Acknowledgements

Financial support was provided for the work undertaken in this thesis by the Australian Government Research Training (RTP) Scholarship.

I would like to firstly express my gratitude to my supervisor, Prof. Dmitry Fursa, who has supervised me since the first research project I undertook in third year. He has provided substantial support, advice, and motivation, which has directly led to the fruition of the research undertaken in this thesis. I would also like to thank my co-supervisors, Prof. Igor Bray and Dr. Liam Scarlett, for their tutelage and assistance during this, and previous, projects. Completing a thesis is a difficult and arduous task, but this burden was significantly lightened due to the support provided by my supervisors.

I also appreciate the staff and students of the Theoretical Physics Group at Curtin. They have made my time in Curtin substantially more enjoyable and provided great companionship during my journey. I would particularly like to shout out Adam, Kade, Nick, and Haadi for assisting me in emptying my finances at lunch and being great travel companions for the conferences I was lucky enough to attend in Adelaide and Sendai.

None of this would have been possible without my family. I am beyond appreciative of the support and encouragement provided to me by my parents for my education throughout my life. Furthermore, I'm also grateful for my three younger brothers, who have provided near-infinite amounts of silly jokes and petty annoyances. Cheers Chris, Brandon, and Lucas.

I also thank Shaun, Zoe, Elliot, Oliver, Connor, and Mitch, who have been my closest friends since high school. Without the much-needed banter, memes, board games, Civ 6 world conquests, absolute chaos of Mario Party, trips to Vic Park (and further afield), and late-night gaming sessions, I would have likely already lost my sanity.

Most importantly, I must thank my partner Hannah, who has been with me almost my entire time at University and whose love and support have always been the highlight of my days. I am eternally appreciative of both the medical team at Sir Charles Gairdner and her courage and strength, which resulted in her fight with cancer ending in a win!

This thesis was undertaken during the COVID-19 pandemic, which led to a unique set of challenges, including several lockdowns. The support provided by my family and friends during this time was much appreciated. I also appreciate the decision of the government of Western Australia to keep the WA borders closed during this period. This decision led to WA having a substantially easier time during the pandemic than almost anywhere else in the world.

Finally, I would like to express my thanks to the late Dr Oleg Zatsarinny. The work undertaken in this project would not have been possible without the codes he provided.

Acknowledgement of country

We acknowledge Aboriginal and Torres Strait Islander people as the Traditional Custodians of the land and waters of Australia. We also acknowledge the Nyoongar Whadjuk Elders, their people, and their land upon which Curtin University is built.

List of Publications

During the candidacy of this PhD project (2020–2024) and the previous Honours year (2019), 8 papers have been published in refereed journals. These are listed here in reverse chronological order. Author contribution statements for each claimed publication are provided in Appendix C.

N. A. Mori, I. Bray, and D.V. Fursa. *Calculations of positron scattering from small molecules.* European Physical Journal D 78, 58 (2024)

N. A. Mori, L. H. Scarlett, I. Bray, and D.V. Fursa. *Convergent close-coupling calculations of positron scattering from neon and argon.* European Physical Journal D 78, 19 (2024)

N. A. Mori, L. H. Scarlett, I. Bray, and D.V. Fursa. *Convergent close-coupling calculations of positron scattering from oxygen.* European Physical Journal D 77, 182 (2023).

N. A. Mori, L. H. Scarlett, I. Bray, and D.V. Fursa. *Convergent close-coupling calculations of positron scattering from atomic carbon.* Physical Review A 107 (3), 032817 (2023).

The following contain results that are presented in this thesis and are in the process of being published:

N. A. Mori, I. Bray, and D.V. Fursa. *Calculations of positron scattering from F, F_2, HF, and various fluorocarbons.* Submitted to Journal of Physics B: Atomic, Molecular and Optical Physics.

N. A. Mori, I. Bray, and D.V. Fursa. *Calculations of positron scattering from boron, BH, BF, BF_2, and BF_3.* Unpublished.

The below are not claimed towards this thesis.

L. H. Scarlett, U. S. Rehill, M. C. Zammit, **N. A. Mori**, I. Bray, and D.V. Fursa. *Elastic scattering and rotational excitation of H_2 by electron impact: Convergent close-coupling calculations.* Physical Review A 107 (6), 062804 (2023).

N. A. Mori, R. Utamuratov, D.V. Fursa, M. C. Zammit, and I. Bray. *Calculation of the single differential cross section for electron-impact ionization of atoms and molecules.* Journal of Physics B: Atomic, Molecular and Optical Physics 54 (1), 015205 (2020).

N. A. Mori, R. Utamuratov, L. H. Scarlett, D. V. Fursa, A.S. Kadyrov, and I. Bray. *Calculations of positron scattering on the hydrogen molecular ion.* Journal of Physics B: Atomic, Molecular and Optical Physics 53 (1), 015203 (2019).

R. Utamuratov, D.V. Fursa, **N. Mori**, A. S. Kadyrov, M. C. Zammit, and I. Bray. *Positron-impact electronic excitations and mass stopping power of H_2.* Physical Review A 99 (4), 042705 (2019).

Conference Presentations

N. A. Mori, L. H. Scarlett, I. Bray, and D. V. Fursa. *Extraction of Ps-formation cross-sections from single-centre positron scattering calculations.* XI International Workshop on Low-Energy Positron and Positronium Physics, (2023), Indiana, United States of America.

N. A. Mori, L. H. Scarlett, I. Bray, and D. V. Fursa. *Calculations of positron scattering from atomic oxygen.* XXXIII International Conference on Photonic, Electronic and Atomic Collisions, (2023), Ottawa, Canada.

N. A. Mori, L. H. Scarlett, I. Bray, and D. V. Fursa. *Calculations of positron scattering from atomic carbon.* XXXIII International Conference on Photonic, Electronic and Atomic Collisions, (2023), Ottawa, Canada.

N. A. Mori, I. Bray, and D. V. Fursa. *Calculations of positron scattering from atomic carbon.* 24th Australian Institute Of Physics Congress, (2022), Adelaide, Australia.

N. A. Mori, I. Bray, and D. V. Fursa. *Calculations of positron scattering from atomic carbon.* 75th Annual Gaseous Electronics Conference, (2022), Sendai, Japan.

Chapter 1

Introduction

1.1 Motivation

Positrons have become a significant part of the medical industry in the past few decades due to their use in positron emission tomography (PET) scans and positherapy. PET scans are critical in the fight against cancer as a non-invasive method of accurately imaging tumours inside the body [212]. They are also a powerful tool in biomedical research as they enable imaging of internal molecular processes occurring *in vivo* in real-time [212, 213]. PET scans can also be used to investigate the pathogenesis of neurological disorders and diseases such as Alzheimer's and Parkinson's disease and could, in the future, allow for the monitoring and even presymptomatic diagnosis of these conditions [214]. Positherapy, on the other hand, utilises positrons to destroy cancer cells [215]. This treatment has proven useful in treating cancers where conventional methods are less effective, since the preferential uptake of positron emitters by tumours as a result of their high metabolic rates leads to targeted internal radiotherapy [216–218]. Positherapy is a safer alternative to current radiotherapy approaches due to the rapid clearing of positron emitters from the body and the low range of the emitted positrons [219].

Both of these technologies function by introducing a radioactive tracer into the body, which produces high-energy positrons as it decays. These positrons release energy into the surrounding tissue, which in positherapy treatments results in cancer cell death. After losing sufficient energy, positrons can bind to an electron forming positronium (Ps) atoms which un-

dergo annihilation and release gamma rays, which can be detected by PET scans and used to resolve an image of the internal biochemical processes occurring inside the body. Currently, however, quantifiable data on the exact scattering processes that occur between the emission and annihilation of these positrons are scarce and largely unknown [173]. These processes slow down the positron and eventually lead to it annihilating either directly or by first undergoing positronium-formation, a reaction critical for PET scans as its decay emits 80% of detected gamma rays [220]. Accurate positron-scattering cross sections are therefore required to calculate quantities such as positron energy deposition and range distributions in human tissue. These quantities can be used to model a positron's journey in positherapy treatments and increase the accuracy of PET scans, where uncertainty in the positron's range leads to image blur [221].

To calculate the cross sections for positron scattering on the complex molecules relevant in these processes, methods such as independent atom model (IAM) [222, 223], IAM with screening corrected additivity rule (IAM-SCAR) [224], IAM-SCAR plus interference terms (IAM-SCAR+I) [225], and Monte-Carlo [226] rely on accurate cross sections for scattering on the atoms which compose them. The two most significant are carbon (C) and oxygen (O) which comprise 83.5% of the human body by mass. Of the remaining mass, 10% is comprised of hydrogen (H), 0.4% of potassium (K), 0.2% of sodium (Na), and 0.1% of magnesium (Mg). The convergent close-coupling (CCC) method, which is a scattering technique that has been developed over the past 30 years in our group, has been applied to positron scattering on H, K, Na, and Mg to obtain extensive cross sections in single-centre, two-centre, or both approaches [5, 227–232]. Therefore, with the calculations completed in this thesis, the atomic components of 94.2% of human body mass are now encompassed by the CCC calculations.

Outside the medical industry, fusion reactor research is another area where positron collision data is relevant, with carbon and boron being viable materials for shielding and walls within these reactors. Due to the large energies involved in fusion production, electron-positron pair production is a common event, and runaway positrons are created in large quantities [233, 234]. Only 0.1% of these produced positrons annihilate within the plasma, with the rest colliding with the reactor wall [235]. Therefore, positron scattering data is important to fully understand the transport and

energy deposition of these positrons and their impact on the degradation of the reactor materials.

Atomic oxygen is a fundamental part of the Earth's atmosphere. Due to how reactive O is, it does not exist in notable quantities close to the Earth's surface. Instead, it is predominantly found in the upper parts of the atmosphere where the abundant ultraviolet radiation continuously dissociates O_2. Accordingly, studies have found O to be the main component of the atmosphere between 200 and 650km [236, 237], with atmospheric models predicting that, by volume, 96 % of the atmosphere in low earth orbit consists of O [238, 239]. As a result, O is essential for cooling the atmosphere through collisions with other atmospheric molecules or direct radiative cooling to the ground state [237].

In the same region that O is dominant, positrons are readily produced through cosmic ray interactions with the atmosphere, terrestrial gamma-ray flashes, or via nuclear reactions [240–243]. These positrons are either destroyed within the atmosphere, escape to space, or can become trapped and accumulated by the inner magnetosphere into a positron radiation belt [241–244]. Therefore, e^+-O scattering is likely a common event within the upper atmosphere, and accurate cross sections will be essential for modelling positron transport through this region or in the atmospheres of oxygen-rich bodies such as Venus [245] and Europa [246].

Fluorine (F) is an extremely reactive element that rarely exists as a free atom. As a result of this, experimental and theoretical scattering research for this atom is sparse. Consequently, interest in positron scattering from F is largely focused on the molecules that contain it. These include several complex molecules which are commonly utilised in plasma etching [247, 248], positron cooling [249–251], and positron traps [252, 253]. Due to the differences present between hydrofluorocarbons and their corresponding hydrocarbons, these molecules have become popular for investigating and better understanding positron scattering phenomena. Therefore, there exists substantial experimental research for these systems [248]. Another important molecule containing fluorine is flurorodeoxyglucose which is a radiotracer commonly used in positron emission tomography (PET) scans [254].

To date, the theoretical formulation of the convergent close-coupling (CCC) method has been limited to quasi one- and two-electron targets i.e. those which can be described by one or two active electrons above an inert

core, and hence has only been applied to positron scattering on hydrogen [5, 228, 255], helium [256–259], the alkali metals [227, 231, 232, 260], and magnesium [230, 261]. These calculations were conducted using either single-centre, two-centre, or both, methods. In addition, positron scattering from noble gases were studied using the single-centre CCC with a model accounting for one-electron excitations only [70]. As an *ab-initio* approach that can be validated via convergence studies, the CCC method has proven useful in providing comprehensive data sets and verifying the theoretical and experimental results for these targets. Although theoretical results exist for positron scattering from the atoms considered in this thesis these results are not extensive, with several important cross sections not present within the literature or only calculated above, or below, certain energies. Consequently, these systems will greatly benefit from large-scale accurate CCC calculations to verify the existing theory and reduce the gaps present in the literature.

We have extended the single-centre CCC method to allow for complex structure models accounting for any number of active electrons with or without an inert core below them. This has been achieved using the MULT program developed by Zatsarinny [262] and the Multiconfigurational Hartree-Fock (MCHF) code developed by Fischer [263]. We have utilised this approach to generate an accurate target structure model for O, C, Ne, Ar, B, and F atoms and to perform close-coupling calculations for positron collisions with these atoms. We have produced a comprehensive cross section data set for this system with incident energies between threshold and 5000 eV. To overcome the limitations of the single-centre approach, we have developed a procedure utilising a complex model potential that allows us to obtain estimates for positronium-formation and direct ionisation cross sections.

For molecular systems, the CCC method is currently limited to molecular targets with a few electrons. This includes H_2 and H_2^+ for positron [13, 264–266] and electron scattering [267–270], and HeH^+ for electron scattering [271]. The extension of this approach to the other molecules considered in this study would be a significant undertaking and calculations would require considerable computational resources. As cross sections are now available for the atoms considered in this thesis, a simpler approach is instead to use the IAM-SCAR method [224]. Typically

the atomic values utilised for these calculations are from model potential approaches. Unlike the CCC approach, some model potential approaches are not *ab-initio* and rely upon the choice of parameters to model the scattering system. For C and O, there are no existing positron scattering experiments and a small number of calculations. For F and B, on the other hand, there exist no previous theoretical or experimental studies. Therefore, the benefit of using these CCC cross sections is that they provide highly-accurate results across the entire energy range for which the errors are well-documented.

With the cross sections calculated within this work, and previous calculations for H, we have utilised a modified IAM-SCAR approach to calculate the total, positronium-formation, direct ionisation, electron-loss, and total excitation cross sections for several of molecules. These include H_2, O_2, C_2, CO, CO_2, H_2O, CH_4, F_2, and CF_4. Like the atoms that compose them, cross sections for positron scattering from these molecules are important for biological, fusion, astronomical, atmospheric, and plasma research.

1.2 Atomic scattering processes

Positron-atom collision processes are listed in Table. 1.1, with the atomic nucleus represented by A. Elastic scattering leaves the incident positron and the target atom unchanged. Bound-state excitations remove energy from the incident positron and transfer it to the target atom's electrons, leaving the target atom in an excited state (A^*). Our current extension of the CCC structure allows for the excitation of any number of electrons, however, for the energy range considered within our calculations one-electron excitations are expected to be the most significant excitation process.

Direct ionisation, positronium-formation, and direct annihilation processes remove an electron from A leaving an ion (A^+) behind. In the case of direct ionisation, an electron absorbs enough energy to escape from the atom. In positronium-formation, an electron is captured by the positron forming positronium, and in direct annihilation, the electron and positron annihilate, producing two gamma rays. As with excitation, numerous electrons can be ionised by the positron if it has sufficient energy; however,

single-ionisation is expected to be the most significant at the energy range our calculations consider. Direct ionisation occurs for incident positron energies above the ionisation threshold. The positronium-formation threshold is 6.8 eV below the ionisation threshold, whereas annihilation can occur at any energy. The annihilation cross section is expected to be negligible for the considered incident energies and, therefore, is omitted in current calculations. Electron-loss represents the sum of these ionisation processes, total inelastic is the sum of all processes except elastic, and the total scattering process is the sum of all possible collisions.

Table 1.1: Atomic scattering processes for an incident positron

Elastic scattering	$e^+ + A \rightarrow A + e^+$
Direct ionisation	$e^+ + A \rightarrow A^+ + e^- + e^+$
Positronium-formation	$e^+ + A \rightarrow A^+ + Ps$
Bound-state excitation	$e^+ + A \rightarrow A^* + e^+$
Direct annihilation	$e^+ + A \rightarrow A^+ + 2\ \gamma$

1.3 Overview of theoretical methods

1.3.1 Born, Coulomb-Born, and distorted-wave approximations

The Born approximation assumes that the interaction potential between particles is weak and that plane waves can be used to describe the initial and final states of the projectile. This approach is only applicable at higher energies, although scaling approaches have been developed to accurately calculate ionisation for incident electrons at low energies [272].

The Coulomb-Born approximation is an extension of the Born approximation in which the long-range Coulomb potential is accommodated through the description of the projectile with waves calculated in the asymptotic target field. By including the impact of the Coulomb potential, this approach is the Born approximation for charged targets. For both the Born and Coulomb-Born approximations the projectile wave is an exact solution of

the asymptotic Hamiltonians.

The distorted-wave Born approximation calculates the projectile wave function in the short-ranged distorting potential that is obtained from the properties of the target initial (or final) state. This way a distortion of the projectile wave function by the target atom is accounted for. Although this method can give more accurate results than the Born approximation at low energies it is, however, less accurate than non-perturbative approaches.

1.3.2 *R*-matrix

The *R*-matrix method, first introduced by Wigner and Eisenbud [273], is an *ab-initio* approach in which the configuration space is split into *internal* and *external* regions. The radius that splits these two regions is chosen to be large enough that within the external region, the interactions between the target and projectile are described solely by long-range forces, disregarding correlation effects. In the internal region, correlation is described through the diagonalisation of the scattering Hamiltonian, and electron wave functions and energies are obtained. Following this, the *R*-matrix is calculated with the wave function at the boundary and the scattering matrix can be produced through matching with the solution in the external region [274]. One advancement to this method is the R-matrix with pseudostates (RMPS) approach, in which an additional set of functions are included in the internal region to represent bound, and continuum states not usually included within the *R*-matrix expansion [275, 276]. This approach is applied only in the single-centre formulation and therefore is unable to calculate positronium-formation.

To date, *R*-matrix calculations have mostly focused on electron scattering from atomic and molecular systems. Positron calculations have been conducted for H [277–279], He [279], the noble gas atoms [117, 280], alkali atoms [281–283], diatomic molecules [276, 284–286], water [179], and pyrazine [287].

The *B*-spline *R*-matrix (BSR) is an implementation of the R-matrix method developed by Zatsarinny [262] in which non-orthogonal orbitals are used to represent bound and continuum one-electron orbitals, and the *R*-matrix basis functions are composed of a set of *B*-splines. These *B*-splines are bell-shaped piecewise polynomial functions defined by a given set of points in a finite radial interval, in which they form a complete basis. Atomic

states are typically generated by combining the MCHF program with this method, in which expansions for each state are generated through separate MCHF calculations. By using non-orthogonal orbitals in this approach, the inclusion of (N+1)-electron bound configuration terms in the close-coupling expansion can be avoided, and the presence of pseudo-resonances is significantly reduced.

As with the conventional R-matrix method, the configuration space is separated into an internal and external region. Changes for the BSR approach are only in the internal region where correlation and exchange are described through the diagonalisation of the scattering Hamiltonian. These dynamics are neglected in the outer region, and the projectile-target interaction is described through only the long-range potential.

This approach has been used extensively and, to date, has calculated electron scattering from the majority of atoms on the first and second rows of the periodic table [61, 123, 127, 211, 288–290]. Although the BSR approach has only been applied to electrons, the current CCC calculations of positron scattering on multielectron atoms have been developed using the techniques developed by Zatsarinny [262] for the BSR.

1.3.3 Complex model potential

Complex model potentials model the positron-atom interaction as a complex (i.e. a real and an imaginary) function. The real part of this function contains a static and polarisation component. The static part represents the average potential experienced by an incident particle as it interacts with the nuclear Coulomb field, whereas the polarisation potential results from the positron causing polarisation of the target's charge cloud [291]. The imaginary part describes the loss of flux from the elastic channel due to inelastic scattering. To calculate the components of the inelastic cross section techniques have been developed, such as the "complex scattering potential–ionisation contribution" (CSP-ic) [166] to calculate direct ionisation and the delta-variation principle for positronium-formation [51, 292].

There are a substantial number of variations to this method which utilise different formulations of the absorption, polarisation, and static components of the potential. Some specific implementations of this approach for positron scattering include the spherical complex optical potential (SCOP) [33], polarised orbital method (POM) [293], quasifree model [292], relativistic op-

tical potential (ROP) [294], the ELSEPA program [291], and semiempirical potential [295]. For scattering from molecules, cross sections can be calculated either directly with model potentials [141] or through IAM approaches [222].

1.3.4 Convergent close-coupling method

The convergent close-coupling (CCC) method, developed by Bray and Stelbovics [16], is an *ab-initio* close-coupling method that has been applied to positron scattering from quasi one- and two-electron atomic and molecular systems in both single- and two-centre formulations [5, 13, 70, 228–230, 256, 257, 264, 265]. This method functions through the expansion of the total scattering wave function in a set of target states, which results in a set of coupled equations that can be solved to obtain required cross-sections. In this method, the structure of the target is represented by a basis of square-integrable Laguerre basis functions. This basis is then used to diagonalise the target Hamiltonian, generating a set of N target pseudostates. By increasing the size of this basis low-lying pseudostates converge to true target eigenstates, whereas the remaining pseudostates span the target continuum. If enough states are included, the infinite target spectrum can successfully be described through a finite-sized expansion. Hence, the accuracy of this approach is largely determined by the completeness of the generated target states. Convergence is demonstrated through increasing the basis size, the number of target states, and the maximum ℓ of the basis and target states.

For positron scattering this method can be performed within either single-centre or two-centre formulations. The single-centre approach performs partial wave expansions over only the states of the target atom, whereas a two-centre calculation also performs this expansion over positronium states. This allows the two-centre approach to calculate positronium-formation and direct ionisation cross sections explicitly. The single-centre approach calculates these implicitly, meaning that the positronium-formation and direct ionisation components of electron-loss are combined.

1.3.5 IAM-based approaches

The independent atom model (IAM), or additivity rule, approximates the cross sections of a molecule as the sum of the cross sections of its con-

stituent atoms [222]. This approximation is valid only at high energies where atomic cross sections are small compared to the interatomic distances within the molecule, typically over 100 eV. To extend this to lower energy Blanco and García [224] developed the screening corrected additivity rule (SCAR), which utilises screening coefficients to decrease the contribution of an atom's cross section based upon its position within the molecule. This IAM-SCAR approach extends the validity of the IAM approach to energies between 20-30 eV. A further extension to this approach was the inclusion of interference terms to account for multicentre scattering effects, known as IAM-SCAR+I, which is expected to produce valid results for energies above 1 eV [225]. Typically, the atomic cross sections used within this approach are calculated using complex model potential methods.

IAM approaches have been utilised to calculate positron scattering from a substantial number of di-, tri-, and polyatomic molecules [32, 51, 133, 155, 171, 182, 225, 296–298].

1.3.6 Schwinger multichannel method

The Schwinger multichannel method (SMC) is an *ab-initio* method developed initially for electron scattering from molecular systems and later extended to positrons [299]. In this approach, after choosing trial scattering functions, the coupled equations for the scattering system are obtained following the variational principle. The target in these calculations is described with Hartree-Fock wavefunctions, and the initial trial functions are typically a set of Cartesian Gaussian functions. To better describe correlation-polarisation interactions polarised orbitals [130] or model potentials [300] can be implemented.

This approach has been utilised for numerous calculations of positron scattering from molecules [131, 180, 299–304]. In the atomic case, calculations have been conducted only for He [184, 300, 303, 305, 306], noble gas atoms [300, 303], and Be [307].

1.3.7 Many-body theory

To describe positron scattering from atomic targets, many-body theory solves the Dyson equation through a perturbative expansion of the correlation potential. This approach utilises quantum field theory to create

a perturbative expansion of amplitudes for various processes [89]. The finite number of perturbation-theory terms used, however, cannot describe positronium as it is a bound state. Virtual positronium-formation, however, can be accounted for through the use of approximations or the summation of a ladder diagram series [308].

For atomic systems, this method has been applied to calculate positron binding, annihilation and cross sections for positron scattering from various atoms [308, 309], including the noble gases [81, 89, 310, 311]. For molecules, calculations have mainly focused on positron binding, annihilation, and elastic scattering [193, 312, 313].

1.4 Current state of the field

1.4.1 Carbon

A variety of different theoretical studies have been conducted for electron scattering on carbon, using the B-spline R-matrix with pseudostates (BSR) [42, 290], R-matrix [43, 314], R-matrix with pseudostates (RMPS) [315], complex optical potential [316], momentum-space coupled-channels optical (CCO) [44], close-coupling (CC) [44, 317], Binary-encounter Bethe (BEB) [45, 318], time-dependent close-coupling (TDCC) [315, 319], and time-independent distorted-wave (TIDW) methods [315]. The only experimental data available for this system are the total ionisation cross sections (TICS) measured by Brook *et al.* [35] and Wang and Crawford [36].

Studies for positron scattering have been less thorough, with fewer calculations previously attempted and no available measurements. Elastic and total cross sections (TCS) have been calculated between 100 and 5000 eV using a model-potential approach by Reid and Wadehra [32]. Low energy elastic scattering cross sections from 0 to 40 eV were calculated using variational methods by Malik [320] for the s wave. Elastic integrated and differential cross sections (DCS) for this system have also been calculated by Dapor and Miotello [37], Cai *et al.* [38], and Chaoui and Bouarissa [39], mainly for use in Monte-Carlo simulations. Momentum-transfer cross sections (MTCS) were determined for this purpose by Cai [41] and Dapor and Miotello [37]. Dapor and Miotello [37] performed these calculations by numerically solving the Dirac equation, Cai *et al.* [38, 41] calculated cross sections using the ELSEPA code to also solve the Dirac equation [291], and

Chaoui and Bourissa [39] numerically solved the Schrödinger equation. Although these previous calculations have been completed in both relativistic and non-relativistic approaches, due to the low atomic number of carbon a non-relativistic approach will suffice for the incident energies considered in the present work.

Total cross sections have been evaluated from 1 to 5000 eV by Singh *et al.* [33] using a modified spherical complex optical potential (SCOP) method. Singh and Antony [34] followed this with calculations of positronium-formation along with total and direct ionisation cross sections using a modified SCOP and the CSP-ic method. Stopping power values for this system have been presented by Gumus *et al.* [46] between 50 eV and 10 MeV using a generalised oscillator strength (GOS) model, earlier models used by Gumus *et al.* [46], the ICRU 37 report [321], and the PENELOPE program [47]. Another stopping power calculation for this system was undertaken by Ashley [48], who used an "optical-data" model to calculate results from 40 eV to 10 keV.

1.4.2 Oxygen

For positron scattering on atomic oxygen, several theoretical methods have been used to obtain a variety of important cross sections for this system. Total cross sections have been calculated by Singh *et al.* [33] using a spherical complex optical potential (SCOP), Reid and Wadehra [32] using a parameter-free model potential, and by Pindariya *et al.* [49] using a quantum mechanical formulation based upon a complex atomic spherical potential. Singh and Antony [34] and Pindariya *et al.* [49] have also obtained results for the direct ionisation cross section through utilisation of the CSP-ic technique [24]. Pindariya *et al.* [49] obtained results for this cross section only above the ionisation threshold, but their approach could not distinguish between positronium-formation and direct ionisation. Singh *et al.* [34], on the other hand, were able to calculate results for positronium-formation and direct ionisation separately.

For the elastic cross section, calculations have been completed by Reid and Wadhera [32] and Pindariya *et al.* [49], using the same methods as before, and also by Dapor and Miotello [37] for incident positron energies between 500 and 4000 eV. Dapor and Miotello [37] have also calculated elas-

tic differential cross sections (DCS) for each of these energies. Total inelastic and the total bound excitation cross sections have been presented solely by Pindariya *et al.* [49]. Stopping power results have been presented for this system by Gumus *et al.* [46] from calculations by a generalised oscillator strength (GOS) model and the PENELOPE program [47]. No experimental studies have been conducted for positron scattering from atomic oxygen.

As cross sections for incident positron and electrons are expected to become equivalent at higher energies, direct comparisons can be made for energies above approximately 500 eV. Electron scattering from atomic oxygen has a number of experimental and theoretical results; however, there has been no recent experimental research for the e^-−O system, even after numerous requests from researchers [322–325]. Measurements have been conducted for total cross sections below the ionisation threshold [326–329], ionisation from threshold to 2000 eV [35, 54, 55], and multiple excitation and optical emission cross sections which are described in several review articles [324, 325, 330]. This system is well documented theoretically, with calculations existing for excitations, optical emission, stopping power, total ionisation, and total cross sections from multiple different approaches [61, 67, 68, 288, 322, 323, 331–333].

1.4.3 Noble gases

Beyond hydrogen and helium, positron-atom scattering experiment and theory have mostly focused on the noble gas atoms. This is a direct result of the closed valence shell of these atoms, which make them easy systems to model. Furthermore, due to existing as inert gases, measurements are also able to be conducted with sufficient ease. As a result, measurements have been conducted on positron scattering from noble gas atoms since the 1970s [72, 74, 75], with a recent resurgence [71, 78, 334–337] due, partly, to advances in low energy trap-based positron beams. This has led to the consideration that the total cross sections for argon are experimentally benchmarked for energies below 60 eV [78]. However, disagreements are still present for other transitions, intermediate energies, and energies towards threshold.

Calculations for these atoms are also abundant, and both experimental and theoretical research has been well-documented in several review articles [15, 229, 311, 338, 339]. To summarise, methods such as the R-

matrix [117], optical potential [80, 84, 90, 106, 109, 110, 115, 119], Schwinger multichannel (SMC) [300], many-body theory (MBT) [81, 89], and frozen-core CCC [70] have all been utilised to calculate various important cross sections for positron scattering on these atoms over a wide range of energies. The previous CCC calculations were conducted for one electron above a p^5 frozen-core. This limitation led to inaccurate dipole polarisabilities, which were addressed through the utilisation of a two-electron polarisation potential.

1.4.4 Boron

Research for e^+-B is scarce, as only a single calculation for positron scattering is available in the literature [37]. Theoretical work for electron scattering on Boron is not as limited, with BSR [123], BEB [124], RMPS [340, 341], R-matrix [342], and time-dependent close-coupling (TDCC) calculations [343] for elastic, excitation, and ionisation cross sections. These calculations, however, are mostly constrained to incident electron energies below 150 eV.

1.4.5 Fluorine

Previous research for positron scattering from F is limited to calculations by Tenfen *et al.* [130] and Dapor and Miotello [37]. The first investigated elastic scattering of positrons from fluorine for energies between 0.01 to 1000 eV, utilising a variety of different model potential approaches. The second calculated elastic and transport cross sections for energies between 500 and 4000 eV by solving the Dirac equation, with a Hartree-Fock potential used to model F. There have been several calculations for electron scattering, with the most comprehensive by Gedeon *et al.* [127] using the BSR method. This calculation included results for ionisation, elastic, and excitation cross sections for energies up to 125 eV. Previous theoretical electron work includes calculations of the elastic cross section [344–347] and excitation cross sections [348], but all are limited to low energies. The only electron calculations completed to high energies are the total ionisation results of Joshipura and Limbachiya [128]. There has been a single experimental study for the electron total ionisation cross section between threshold and 200 eV by Hayes

et al. [129].

1.4.6 Molecules

Measurements for positron scattering from molecular systems are generally in higher abundance than for their atomic components. Here, summaries are provided for the considered molecules and the cross sections of interest. For O_2, experiments exist for the total [50–52], elastic [51, 52], total electronic excitation [135], positronium-formation [57, 58, 111, 137], direct ionisation [111, 135], and electron-loss [111, 137] cross sections. For e^+-CO, cross sections for the total [144–147], elastic [144, 146, 147], excitation to the $A^1\Pi$ state [56], positronium-formation [56], direct ionisation [56, 154], and electron-loss [56, 154] processes have all been measured. For e^+-CO_2, total [50, 145, 147, 159, 160, 195], elastic [159, 160], positronium-formation [58, 147, 161–163, 349], direct ionisation [154], and electron-loss [154, 163] measurements are available. For H_2O, there have been measurements for total [160, 173–176, 350], elastic [160, 176, 182], the sum of excitation and ionisation [182], and positronium-formation [162, 173, 349]. CH_4 has measurements for total [50, 52, 159, 174, 192, 195], elastic [159, 192], direct ionisation [351], and positronium-formation [200, 349]. For the CF_4 molecule, experimental results exist for the total cross section [202, 352] and a single point for the positronium-formation cross section [349]. For C_2 and O_3, there exists no positron scattering experiment.

Positron calculations have been undertaken with the spherical complex optical potential (SCOP) method [24, 33, 34, 141, 190] for positron scattering from O_2, C_2, CO, CO_2, H_2, and CH_4 to obtain total, inelastic, direct ionisation, electron-loss, and positronium-formation cross sections for energies up to 5000 eV. IAM-SCAR calculations have been conducted for O_2 [51], H_2O [171, 182], and CO_2 [155]. SMC calculations have been conducted on several molecules [353, 354], including F_2 [130], H_2 [299, 301], CO [151], CO_2 [355], H_2O [184, 304], and CH_4 [192, 299]. Other theoretical approaches that have been applied in a limited fashion to some of these molecules include the BEB [28, 138], body-frame vibrational close-coupling [142, 157], distorted-wave [139, 152, 153, 185, 201], model potential [181, 191, 198], close-coupling [132], many-body theory [193, 251], and R-matrix [179, 285].

Chapter 2

Theory

This chapter presents an overview of the single-centre CCC formalism for atomic targets with any number of active electrons. First, we describe the structure component of this method, followed by a description of the scattering theory. The formulae used to calculate specific cross sections and quantities of interest are also included. As our calculations are conducted in a non-relativistic framework, we utilise the L-S coupling scheme. With this theoretical framework, a computer code was developed by the candidate to conduct the required calculations. This code is summarised in Appendix A. Some sections in this chapter text are adapted from published works by the candidate [1]. The publisher of these articles (the American Physical Society) provides the right to use an article or a portion of an article in a thesis or dissertation without requesting permission. The following textbooks were consulted: Bransden [356] and Fischer [357].

2.1 Target structure

2.1.1 Configuration-interaction approach

For an atomic target with N_e electrons and nuclear charge Z, the target Hamiltonian is given by

$$H_\mathrm{T} = \sum_{i=1}^{N_\mathrm{e}} \left(-\frac{1}{2}\nabla_i^2 - \frac{Z}{r_i} \right) + \sum_{i>j=1}^{N_\mathrm{e}} \frac{1}{|\boldsymbol{r}_i - \boldsymbol{r}_j|}, \tag{2.1}$$

where $\boldsymbol{r}_i$ and $\boldsymbol{r}_j$ are the coordinates of electrons i and j, and Z is the nuclear charge of the target. We utilise a configuration-interaction (CI) representation of the atomic wave functions:

$$\Phi_n^N(x_1, \ldots, x_{N_\mathrm{e}}) = \sum_{i=1}^{N} C_i^{(n)} \phi_i(x_1, \ldots, x_{N_\mathrm{e}}), \tag{2.2}$$

where ϕ_i are antisymmetrised N_e-electron configurations, $C_i^{(n)}$ are the CI coefficients, N is the number of configurations, and $x_i = (\boldsymbol{r}_i, \sigma_i)$ represents the spatial ($\boldsymbol{r}_i$) and spin (σ_i) coordinates of electron i. The configurations can be expressed either as an antisymmetric function

$$\phi_i(x_1, ..., x_{N_e}) = \mathcal{A} \prod_{i=1}^{N_\mathrm{e}} \varphi_i(x_i), \tag{2.3}$$

where $\mathcal{A}$ is the antisymmetrisation operator, or as a Slater determinant

$$\phi_i(x_1, ..., x_{N_\mathrm{e}}) = \frac{1}{\sqrt{N_\mathrm{e}!}} \begin{vmatrix} \varphi_1(x_1) & \cdots & \varphi_1(x_{N_e}) \\ \vdots & \ddots & \vdots \\ \varphi_{N_\mathrm{e}}(x_1) & \cdots & \varphi_{N_\mathrm{e}}(x_{N_e}) \end{vmatrix}. \tag{2.4}$$

The configuration state functions are constructed from a one-electron basis that contains one-electron orbitals,

$$\varphi_i(\vec{r_i}, \sigma_i) = \frac{1}{r_i} \phi_{k_i \ell_i}(r_i) Y_{\ell_i m_i}(\vec{r_i}) \chi(\sigma_i), \tag{2.5}$$

where $\phi_{k\ell}$ is a radial function, $Y_{\ell m}$ is a spherical harmonic, and $\chi(\sigma)$ a spin function.The radial functions for the one-electron orbitals are obtained from either an HF/MCHF calculation or the Laguerre basis functions,

$$\begin{aligned} \phi_{k\ell}(r) = \sqrt{\frac{\alpha_\ell (k-1)!}{(k+\ell)(k+2\ell)!}} (2\alpha_\ell r)^{\ell+1} \\ \times e^{-\alpha_\ell r} L_{k-1}^{2\ell+1}(2\alpha_\ell r), \quad k = 1, \ldots, N_\ell. \end{aligned} \tag{2.6}$$

Here, $L_{k-1}^{2\ell+1}$ are the associated Laguerre polynomials, α_ℓ are exponential fall-off parameters, and N_ℓ is the number of functions for each ℓ. If the one-

electron functions form an orthonormal set, the configurations constructed from them are orthonormal and therefore satisfy

$$\langle \Phi_n | \Phi_m \rangle = \sum_{i=1,j=1}^{N} C_i C_j = \delta_{ij}, \tag{2.7}$$

where δ_{ij} is the Kronecker delta function

$$\delta_{ij} = \begin{cases} 1, i = j \\ 0, i \neq j. \end{cases} \tag{2.8}$$

2.1.2 One-electron basis and Hamiltonian matrix elements

For the case where the atom structure contains a frozen-core, the core orbitals are first obtained from relevant HF/MCHF calculations for the ion of the target atom. Following this, we add an electron to this core and generate the Laguerre basis functions. By using analytical properties of these functions, we can obtain the quasi one-electron Hamiltonian matrix elements of this basis through

$$\langle \phi_{k\ell} | H | \phi_{k'\ell'} \rangle = \left\langle \phi_{k\ell} \left| \frac{\alpha_\ell (k+\ell)}{r} - \frac{\alpha_\ell^2}{2} + V(r) \right| \phi_{k'\ell'} \right\rangle, \tag{2.9}$$

where $V(r)$ contains the sum of the direct ($V_{\mathrm{d}}^{\mathrm{FC}}$) and exchange ($V_{ex}^{FC}$) terms of the one electron with the frozen-core. These are equivalent to,

$$V_{\mathrm{d}}^{\mathrm{FC}} = -\frac{Z}{r} + \sum_{\varphi_c} \int d^3 r_1 \frac{|\varphi_c(\boldsymbol{r}_1)|^2}{|\boldsymbol{r}_2 - \boldsymbol{r}_1|}, \tag{2.10}$$

and

$$V_{\mathrm{ex}}^{\mathrm{FC}} = -\sum_{\varphi_c} \int d^3 r_1 \frac{\varphi_c(\boldsymbol{r}_1)\varphi_c(\boldsymbol{r}_2)}{|\boldsymbol{r_2} - \boldsymbol{r_1}|}, \tag{2.11}$$

where φ_c represents the core orbitals. The matrix elements for the V_{ex}^{FC} term are obtained via

$$\left\langle \phi_{k\ell} \left| V_{\text{ex}}^{\text{FC}} \right| \phi_{k\ell'} \right\rangle = \sum_{\varphi_c} \sum_{\lambda} \frac{-2\ell_c + 1}{2\ell + 1} \left(C_{\ell 0, \lambda 0}^{\ell_c 0} \right)^2 \times \int_0^\infty \int_0^\infty dr_2 dr_1 \varphi_c(r_2) \phi_{k\ell'}(r_2) \varphi_c(r_1) \phi_{k\ell}(r_1) \frac{r_<^\lambda}{r_<^{\lambda+1}}, \quad (2.12)$$

where $C_{\ell_1 m_1, \ell_2, m_2}^{\ell m}$ is a Clebsch-Gordan coefficient.

We then diagonalise the Hamiltonian matrix in Eq. 2.9 which produces a set of orthonormal one-electron orbitals i.e.

$$\int_0^\infty \phi_n(r) \phi_{n'}(r) dr = \delta_{nn'}, \quad (2.13)$$

and therefore a one-electron orthonormal basis. The values of the quasi one-electron Hamiltonian matrix elements for this basis are also obtained from the diagonalisation. Within this basis, some of the orbitals are then substituted with the corresponding orbitals obtained from the HF/MCHF calculations. For the relevant orbitals, the one-electron Hamiltonian matrix elements are then recalculated numerically with

$$\langle \phi_\alpha | H | \phi_\beta \rangle = \left\langle \phi_\alpha \left| \frac{-1}{2} \frac{d^2}{dr^2} + \frac{\ell_\alpha(\ell_\alpha + 1)}{2r^2} + V(r) \right| \phi_\beta \right\rangle. \quad (2.14)$$

Orthonormality is ensured for this final basis through application of the Gram-Schmidt orthogonalisation procedure. The one-electron orbitals from the final basis are then used to build the n-electron configurations (Eq. 2.4). When the calculation does not use a frozen-core, the elements of V reduce to $\frac{-Z}{r}$ and the Laguerre basis functions are produced from $1s$.

2.1.3 Target Hamiltonian matrix elements

We can separate the target Hamiltonian (Eq. 2.1) into one-electron,

$$H_{\text{T}}^1 = \sum_{i=1}^{N_e} \left(-\frac{1}{2} \nabla_i^2 - \frac{Z}{r_i} \right), \quad (2.15)$$

and two-electron,

$$H_{\mathrm{T}}^{2} = \sum_{i>j=1}^{N_{\mathrm{e}}} \frac{1}{|\boldsymbol{r}_i - \boldsymbol{r}_j|}, \tag{2.16}$$

components. To evaluate the matrix elements of H_{T} it must be integrated over all coordinates. Due to the orthonormality of the one-electron orbital functions only some orbitals are involved in the integration whereas others reduce to zero or unity. Non-zero results are obtained from the one-electron term only when configurations differ by at most one orbital. For the two-electron term, non-zero results are obtained when the configurations differ by at most two orbitals. These are commonly referred to as Slater-Condon rules, and allow us to solve the multi-electron Hamiltonian in terms of individual orbitals.

For the two-electron term, we utilise a multipole expansion of the electron-electron potential to obtain,

$$H_{\mathrm{T}}^{2} = 4\pi \sum_{\lambda} \frac{r_{<}^{\lambda}}{r_{>}^{\lambda+1}} \frac{1}{2\lambda+1} (Y_\lambda(\hat{\boldsymbol{r_1}}) \cdot Y_\lambda(\hat{\boldsymbol{r_2}})), \tag{2.17}$$

where $(Y_\lambda \cdot Y_\lambda)$ is a tensor scalar product. Considering this expansion, the general expression of the two-electron matrix element is

$$\langle \Phi_i | H_{\mathrm{T}}^{2} | \Phi_j \rangle = \sum_{\alpha,\beta,\delta,\gamma;\lambda} C^{ij}_{\alpha,\beta,\delta,\gamma;\lambda} R_\lambda(\alpha,\beta,\delta,\gamma), \tag{2.18}$$

where the radial integral (R_λ) is given by

$$R_\lambda(\alpha,\beta,\delta,\gamma) = \int\int dr_1 dr_2 \frac{r_{<}^{\lambda}}{r_{>}^{\lambda+1}} \phi_\alpha(r_1)\phi_\beta(r_2)\phi_\delta(r_1)\phi_\gamma(r_2). \tag{2.19}$$

The values of α and β are the indexes to one-electron orbitals from the configuration i, δ and γ are the indexes to one-electron orbitals from the configuration j, λ is the multipolarity, and $C^{ij}_{\alpha,\beta,\delta,\gamma;\lambda}$ is the angular coefficients of the λ terms in the matrix expansion that are dependent on the angular symmetries of the configuration state functions.

The general expression of the one-electron term is given by,

$$\langle \Phi_i | H_{\mathrm{T}}^{1} | \Phi_j \rangle = \sum_{\alpha,\delta} C^{ij}_{\alpha,\delta} \zeta^{ij}(\alpha,\delta), \tag{2.20}$$

where $C^{ij}_{\alpha,\delta}$ is the angular coefficients and $\zeta^{ij}(\alpha,\delta)$ is the one-electron Hamiltonian matrix elements which are obtained as described in the previous section.

For each ℓ, π, s combination the target Hamiltonian matrix term is therefore expressed as

$$H^{\ell,\pi,s}_{ij} = \sum_{\alpha,\delta} C^{ij}_{\alpha,\delta}\zeta^{ij}(\alpha,\delta) + \sum_{\alpha,\beta,\delta,\gamma;\lambda} C^{ij}_{\alpha,\beta,\delta,\gamma;\lambda} R_\lambda(\alpha,\beta,\delta,\gamma), \tag{2.21}$$

with the angular coefficient terms for each component calculated with the BSR subroutines [262]. The sums (α,δ and $\alpha,\beta,\delta,\gamma$) are over the orbitals occupied in either configuration state.

2.1.4 Diagonalisation of the target Hamiltonian

To obtain the CI coefficients in Eq. 2.2 we use,

$$H_{\rm T}\Phi(r) = E\Phi(r), \tag{2.22}$$

and Eq. 2.2 to obtain the eigenvalue equation,

$$\sum_{i=1}^{N} \left(\langle \phi^N_n | H_{\rm T} | \phi^N_m \rangle - \epsilon \langle \phi^N_n | \phi^N_m \rangle \right) C_i = 0. \tag{2.23}$$

By diagonalising $H_{\rm T}$ with the set of configurations in Eq. 2.23, target pseudostates Φ^N_n are then obtained and expanded in terms of single-configuration basis states, which satisfy

$$\langle \Phi^N_n | H_{\rm T} | \Phi^N_m \rangle = \epsilon^N_n \delta_{nm}, \tag{2.24}$$

where ϵ^N_n is the pseudostate energy. For sufficiently large N the low-lying states accurately represent true eigenstates, and the target pseudostates form an arbitrarily-complete basis for the target space.

2.1.5 Electron density

Electron density is a measure of the electron's probability of being at location r. The density of one electron in subshell j can be found through

$$\rho_j(r) = \varphi^2_j(r), \tag{2.25}$$

where φ are electron orbital radial wavefunctions. For a set of subshells this becomes

$$\rho(r) = \sum_{j=1}^{q} w_j \rho_j(r) = \sum_{j=1}^{q} w_j \varphi_j^2(r), \tag{2.26}$$

where q is the number of subshells, and w_j is the occupancy number of subshell j. For calculations containing a frozen-core, the frozen-core component of the density is calculated through

$$\rho_{fc}(r) = \sum_{n=1}^{N_{\text{core}}} 2(2\ell_i + 1)\varphi_i^2(r), \tag{2.27}$$

where N_{core} is the number of core orbitals, ℓ_i is the angular momentum of core orbital i, and φ_i is the electron orbital wavefunction of core orbital i. This is summed to the density of the active electrons to give the total electron density of the target atom.

2.1.6 Oscillator strengths and multipole polarisability

For a multipole (dipole, quadrupole, or octupole) transition of state i to state n the absorption oscillator strength for length is given by [358]

$$f_{in}^k = \frac{2S_{in}^{(k)}|E_n - E_i|}{(2k+1)(2L_i+1)}. \tag{2.28}$$

Here, L_i is the orbital angular momentum of the initial state i, k is the polarity of the transition, and $E_{i/n}$ is the energy of state n/i. The value of k represents the polarity of the transition, where a dipole transition has $k = 1$, quadrupole has $k = 2$, and octupole has $k = 3$. For each polarity, different selection rules are also present. The multiplet strength (S_{in}^k) is the square of the reduced matrix element:

$$S_{in}^k = |\langle \psi_i; L_i || r^k C^k(\hat{\boldsymbol{r}}) || \psi_n; L_n \rangle|^2. \tag{2.29}$$

In this equation, k is a power for r, elsewhere it is an index. Weighted oscillator strengths are defined as,

$$gf_{in}^k = (2S_i + 1)(2L_i + 1)f_{in}^k, \tag{2.30}$$

where S_i is the spin of the state i. To obtain the polarisability for a multipole transition we use

$$\alpha_k = \sum_{n=i}^{N} \frac{f_{in}^k}{|E_n - E_i|^2}. \tag{2.31}$$

For the atoms considered, dipole transitions are the most significant transitions and, therefore, there exists substantial theoretical and experimental results for the dipole oscillator strengths and polarisability. Although not as important as the dipole polarisability (α_D), we have also calculated the quadrupole (α_Q) and octupole (α_O) polarisabilities for the atoms considered in this thesis as the accuracy of these values provides further evidence of a structure model's accuracy. These are calculated through changing the value of k in Eq. 2.31.

2.2 Scattering

2.2.1 Close-coupling equations

The total scattering Hamiltonian for the positron-atom system is given by

$$H = H_{\mathrm{T}} - \frac{1}{2}\nabla_0^2 + V, \tag{2.32}$$

where index 0 represents the positron and V is the positron-atom interaction potential:

$$V = V_0 + \sum_{i=1}^{N_e} V_{0i}. \tag{2.33}$$

Here, $V_0 = \frac{Z}{r_0}$ is the positron-nucleus potential and $V_{0i} = -\frac{1}{|r_0 - r_i|}$ are the positron-electron potential terms.

The Schrödinger equation for the total scattering wave function is given by

$$(H - E)|\Psi_i^{(+)}\rangle = 0, \tag{2.34}$$

where E is the energy of the collision system. In the single-centre CCC method, Eq. (2.34) is solved by expanding $\Psi_i^{(+)}$ in the set of target pseudostates:

$$\Psi_i^{(+)} \approx \Psi_i^{N(+)} = \sum_{n=1}^{N} F_n^{N(+)}(\boldsymbol{r}_0)\Phi_n^N(\boldsymbol{r}_1, \ldots, \boldsymbol{r}_{N_e}), \tag{2.35}$$

where $F_n^{N(+)}(\boldsymbol{r}_0)$ are the positron channel functions and we rely on the completeness of the Laguerre basis to give,

$$\lim_{N\to\infty} \Psi_i^{N(+)}(r_0,\ldots,r_{N_e}) = \Psi_i^{(+)}(r_0,\ldots,r_{N_e}). \tag{2.36}$$

This expansion is substituted into Eq. (2.34) to obtain

$$\begin{aligned}(E-K_0-U_0-H_T)\Psi_i^{N(+)}(r_0,\ldots,r_{N_e}) = \\ (V-U_0+(E-H))\Psi_i^{N(+)}(r_0,\ldots,r_{N_e}).\end{aligned} \tag{2.37}$$

Here, U_0 are arbitrary short-ranged potentials which are used to reduce the required computational resources needed to solve the coupled equations [359]. The inclusion of U_0 is purely a numerical technique, and results are independent of it. The asymptotic (large r_0) Hamiltonian is hence given by,

$$H_{\text{as}} = K_0 + U_0 + H_T. \tag{2.38}$$

With H_{as}, the spectral decomposition of the Green's function

$$G_0^{(+)}(k) = \lim_{\epsilon\to 0^+} \frac{1}{E^{(+)} - \epsilon_n^N - \epsilon_k + i\epsilon}, \tag{2.39}$$

is utilised to generate a set of coupled Lippmann-Schwinger equations from Eq. 2.34,

$$|\Psi^N\rangle = |\phi_i \boldsymbol{k}_i\rangle + \sum_{n=1}^{N} \int d^3k \frac{|\Phi_n^N \boldsymbol{k}\rangle\langle \boldsymbol{k}\Phi_n^N|T|\Phi_i^N \boldsymbol{k}_i\rangle}{E^{(+)} - \epsilon_n^N - \epsilon_k + i0}, \tag{2.40}$$

where $\epsilon_k = \frac{\boldsymbol{k}^2}{2}$ is the energy of the plane wave $|\boldsymbol{k}\rangle$. Following this, we premultiply these equations with $\langle \boldsymbol{k}_f \Phi_f^N|V$ to obtain the coupled Lippmann-Schwinger equations for the T matrix:

$$\begin{aligned}\langle \boldsymbol{k}_f\Phi_f^N|T|\Phi_i^N\boldsymbol{k}_i\rangle = \langle \boldsymbol{k}_f\Phi_f^N|V|\Phi_i^N\boldsymbol{k}_i\rangle \\ + \sum_{n=1}^{N} \int d^3k \frac{\langle \boldsymbol{k}_f\Phi_f^N|V|\Phi_n^N\boldsymbol{k}\rangle\langle \boldsymbol{k}\Phi_n^N|T|\Phi_i^N\boldsymbol{k}_i\rangle}{E^{(+)} - \epsilon_n^N - \epsilon_k + i0},\end{aligned} \tag{2.41}$$

The use of plane waves assumes a neutral target; this method can be applied to charged targets by choosing a form of the asymptotic Hamiltonian that allows for scattering from ionic targets and using Coulomb waves in place of plane waves.

2.2.2 Solving the Lippmann-Schwinger equation

We can expand Eq. 2.41 in partial waves of the total orbital angular momentum J and total parity Π, where $\Pi = (-1)^{L+\ell}$, with the reduced V (or T) partial-wave matrix elements given by

$$\langle Lk\Phi_f^N|V^{J\Pi}|L'k'\Phi_i^N\rangle = \sum_{M,m,M',m'} C_{L\ell J}^{MmM_J} C_{L'\ell' J}^{M'm'M_J} \times \int d\hat{\boldsymbol{k}} \int d\hat{\boldsymbol{k}}'\, Y_{L'M'}(\hat{\boldsymbol{k}}') Y_{LM}^*(\hat{\boldsymbol{k}}) \langle \hat{\boldsymbol{k}}\Phi_f^N|V|\Phi_i^N\hat{\boldsymbol{k}}'\rangle. \tag{2.42}$$

Following from this, we can obtain the partial-wave coupled Lippmann-Schwinger equations of the reduced T matrix

$$\langle L_f k_f \Phi_f^N|T^{J\Pi}|L_i k_i \Phi_i^N\rangle = \langle L_f k_f \Phi_f^N|V^{J\Pi}|L_i k_i \Phi_i^N\rangle + \sum_{n=1}^{N}\sum_{L} \int dk \frac{\langle L_f k_f \Phi_f^N|V^{J\Pi}|Lk\Phi_n^N\rangle\langle Lk\Phi_n^N|T^{J\Pi}|L_i k_i \Phi_i^N\rangle}{E^{(+)} - \epsilon_n^N - \epsilon_k + i0}. \tag{2.43}$$

Through residue theory we can transform Eq. 2.43 into a principle-value integral

$$\langle L_f k_f \Phi_f^N|T^{J\Pi}|L_i k_i \Phi_i^N\rangle = \langle L_f k_f \Phi_f^N|V^{J\Pi}|L_i k_i \Phi_i^N\rangle + \sum_{L}\left[\sum_{n=1}^{N}\mathcal{P}\int dk \frac{\langle L_f k_f \Phi_f^N|V^{J\Pi}|Lk\Phi_n^N\boldsymbol{k}\rangle\langle Lk\Phi_n^N|T^{J\Pi}|L_i k_i \Phi_i^N\rangle}{E^{(+)} - \epsilon_n^N - \epsilon_k} - i\pi\sum_{n=1}^{N_o}\boldsymbol{k}_n\langle L_f k_f \Phi_f^N|V^{J\Pi}|Lk\Phi_n^N\rangle\langle Lk\Phi_n^N|T^{J\Pi}|L_i k_i \Phi_i^N\rangle\right] \tag{2.44}$$

Here, $\mathcal{P}$ indicates this is a principle-value integral and N_o is the number of open channels. Since the potential V is real, we can solve Eq. (2.44) using real arithmetic by first defining the K matrix [360]

$$\langle Lk\Phi_n^N|K^{J\Pi}|L_i k_i \Phi_i^N\rangle = \sum_{L}\sum_{n=1}^{N_o}\langle Lk\Phi_n^N|T^{J\Pi}|L_{n'} k_{n'} \Phi_{n'}^N\rangle \times \left(\delta_{i,n'}\delta_{L,L_i} + i\pi\boldsymbol{k}_{n'}\langle Lk\Phi_{n'}^N|K^{J\Pi}|L_i k_i \Phi_i^N\rangle\right). \tag{2.45}$$

We can then obtain the partial-wave Lippmann-Schwinger equation for the

K matrix through substitution of Eq. 2.45 into Eq. 2.44 giving

$$\langle L_f k_f \Phi_f^N | K^{J\Pi} | L_i k_i \Phi_i^N \rangle = \langle L_f k_f \Phi_f^N | V^{J\Pi} | L_i k_i \Phi_i^N \rangle + \sum_L \sum_{n=1}^{N} \mathcal{P} \int dk \, \frac{\langle L_f k_f \Phi_f^N | V^{J\Pi} | L k \Phi_n^N \rangle \langle L k \Phi_n^N | K^{J\Pi} | L_i k_i \Phi_i^N \rangle}{E^{(+)} - \epsilon_n^N - \epsilon_k}. \quad (2.46)$$

By replacing the integral with a quadrature rule, this can then be reformatted with real quantities to a set of linear equations

$$K_{fi} = V_{fi} + \sum_n w_n V_{fn} K_{ni}. \quad (2.47)$$

Here, w_n are weights that contain the integration weights and the value of Green's function at each point. To solve this, we let f run over the same range as n and solve for the half-on-shell K matrix elements,

$$\sum_n (\delta_{fn} - w_n V_{fn}) K_{ni} = V_{ni}. \quad (2.48)$$

As the integral we are solving is a principle-value integral we cannot directly solve for on-shell K matrix elements and they are instead obtained by substituting the obtained half-off-shell elements (K_{ni}) into Eq. 2.47. Following this, we solve Eq. 2.45 to obtain the on-shell T-matrix elements.

2.2.3 Direct V-matrix element calculation

Unlike for electron scattering the process of electron exchange, which arises due to the indistinguishably of the target and projectile electron, does not occur in positron scattering. Therefore, the V operator is described entirely with the direct V-matrix elements. For calculation of these direct V-matrix elements, we perform a multipole expansion of the potential (Eq. 2.33) obtaining

$$V = 4\pi \sum_{\lambda,\mu} \frac{1}{2\lambda+1} \sum_{i=1}^{N_e} v_\lambda(r_0, r_i) Y^*_{\lambda\mu}(\hat{\boldsymbol{r}}_0) Y_{\lambda\mu}(\hat{\boldsymbol{r}}_i), \quad (2.49)$$

where $Y_{\lambda\mu}$ are spherical harmonics, and

$$v_\lambda(r_0, r_i) = V_0 \delta_{\lambda 0} - \frac{[\min(r_0, r_i)]^\lambda}{[\max(r_0, r_i)]^{\lambda+1}}. \quad (2.50)$$

Following from standard angular momentum algebra we obtain the reduced matrix elements:

$$\begin{aligned}
&\langle kLM, \Phi_n^N; JM|V|k'L'M', \Phi_{n'}^N; J'M'\rangle \\
&\quad = \sum_\lambda \frac{4\pi}{2\lambda+1} \int_0^\infty u_L(kr_0) u_{L'}(kr_1) \langle L||Y_\lambda^*(\hat{\boldsymbol{r}}_0)||L'\rangle \\
&\qquad \times \delta_{J,J'}\delta_{M,M'}(-1)^{L+\ell'+2\lambda+J} \begin{Bmatrix} L' & \ell' & J \\ \ell & L & \lambda \end{Bmatrix} \\
&\qquad \times \langle \Phi_n^N || \sum_{i=1}^{N_\mathrm{e}} v_\lambda(r_0, r_i) Y_\lambda(\hat{\boldsymbol{r}}_i) || \Phi_{n'}^N\rangle, \qquad (2.51)
\end{aligned}$$

with $|kLM\rangle$ representing a partial wave with angular momentum L and angular-momentum projection M. Using the CI coefficients we have

$$\begin{aligned}
&\langle \Phi_n^N || \sum_{i=1}^{N_\mathrm{e}} v_\lambda(r_0, r_i) Y_\lambda(\hat{\boldsymbol{r}}_i) || \Phi_{n'}^N\rangle \\
&\qquad = \sum_{mm'} C_m^{(n)} C_{m'}^{(n')} \langle \phi_m || \sum_{i=1}^{N_\mathrm{e}} v_\lambda(r_0, r_i) Y_\lambda(\hat{\boldsymbol{r}}_i) || \phi_{m'}\rangle, \qquad (2.52)
\end{aligned}$$

where $C_m^{(n)}$ and $C_{m'}^{(n')}$ are the CI coefficients of the initial and final states, respectively, and the sums over m and m' cover all configurations. We then write

$$\begin{aligned}
&\langle \phi_m || \sum_{i=1}^{N_\mathrm{e}} v_\lambda(r_0, r_i) Y_\lambda(\hat{\boldsymbol{r}}_i) || \phi_{m'}\rangle \\
&\qquad = \sum_{i=1}^{N_\mathrm{e}} a_i^{mm'} \int_0^\infty dr_i\, v_\lambda(r_0, r_i) \phi_m(r_i) \phi_{m'}(r_i), \qquad (2.53)
\end{aligned}$$

where ϕ_m are the radial functions obtained either from Eq. (2.6) or the HF/MCHF calculations, and $a_i^{mm'}$ are coefficients which depend only upon the angular symmetry of the required configurations [262]. The $a_i^{mm'}$ coefficients are calculated within the code with the BSR subroutines [262]. The resulting expression for the reduced V-matrix element is hence,

$$\begin{aligned}
&\langle kLM, \Phi_n^N; JM|V|k'L'M', \Phi_{n'}^N; J'M'\rangle \\
&= \sum_\lambda \frac{4\pi}{2\lambda+1} \times \delta_{J,J'}\delta_{M,M'}(-1)^{L+\ell'+2\lambda+J} \begin{Bmatrix} L' & \ell' & J \\ \ell & L & \lambda \end{Bmatrix} \\
&\quad \times \sum_{mm'} C_m^{(n)} C_{m'}^{(n')} \sum_{i=1}^{N_e} a_i^{mm'} \int_0^\infty \int_0^\infty dr_0 dr_i \, v_\lambda(r_0, r_i)\phi_m(r_i)\phi_{m'}(r_i) \\
&\quad \times u_L(kr_0)u_{L'}(kr_1)\langle L||Y_\lambda^*(\hat{\boldsymbol{r}}_0)||L'\rangle. \qquad (2.54)
\end{aligned}$$

2.2.4 Scattering amplitude and cross section

Once the reduced T-matrix elements are obtained for a transition, the scattering amplitude in the collision frame can be calculated through,

$$\begin{aligned}
f^S_{m_f m_i}(\theta) =& \frac{1}{\sqrt{4\pi}} \frac{1}{\sqrt{2\ell_i+1}} \sqrt{\frac{k_i}{k_f}} \sum_{L_f, L_i, J\Pi} \sqrt{(2L_i+1)} C^{m_i - m_f m_f m_i}_{L_f l_f J} i^{L_i - L_f} \\
&\times C^{0 m_i m_i}_{L_i l_i J} T^{J\Pi}_{l_i l_f L_i L_f} Y^{L_f}_{m_i - m_f}(\theta), \qquad (2.55)
\end{aligned}$$

where the subscripts i and f denote the initial and final state, ℓ is the orbital angular momentum, m the angular momentum projection, k the linear angular momenta, and L the orbital angular momenta. The reduced on-shell T-matrix ($T^{J\Pi}_{l_i l_f L_i L_f}$) is dependent on the total spin S, parity Π, and the partial waves of the total orbital angular momentum J.

With the scattering amplitude, the differential cross section can be readily obtained by averaging over the magnetic sublevels of l_i, which is accounted for by the $\sqrt{2\ell_i+1}$ term in Eq. 2.55, and summing over the magnetic sublevels of l_f,

$$\frac{d\sigma_{fi}}{d\Omega} = \sum_{m_i m_f} |f^S_{m_f m_i}|^2. \qquad (2.56)$$

The integrated cross sections are obtained by integrating this over the positron scattering angles,

$$\sigma_{fi} = \int d\Omega \frac{d\sigma_{fi}}{d\Omega}. \qquad (2.57)$$

Through substitution of these equations into Eq. 2.55 we can also directly calculate the integrated cross section from the on-shell values of the T matrix,

$$\sigma_{fi} = \frac{1}{4\pi(2l_i+1)} \frac{k_f}{k_i} \sum_{L_f, L_i, J\Pi} (2J+1) |T^{J\Pi}_{l_i l_f L_i L_f}|^2. \tag{2.58}$$

The total cross section for an initial state i is obtained from summing the σ_{fi} for every state f included in the close-coupling expansion. The electron-loss is obtained by summing σ_{fi} for all positive-energy f states. Total bound-state excitation is the summation of σ_{fi} for all the negative-energy states excluding $f = i$, which is the elastic cross section.

2.2.5 Analytical Born completion

Calculations are completed to a maximum total angular momentum value of J_{max} which is generally sufficient to achieve convergence at low energies. At high incident energies, the value of J_{max} required for convergence is typically computationally expensive. At these energies, however, Born results are typically accurate and, therefore, the analytical Born completion technique can be used to accelerate convergence by lowering the required J_{max} needed for convergence. To apply the Born approximation the T matrix elements are replaced with those of the V matrix when calculating the scattering amplitude. This technique, therefore, assumes that $T_J \approx V_J$ for large enough J, and calculates Born-completed results by replacing T with

$$T = V + \sum_J (T_J - V_J) \tag{2.59}$$

in Eq. 2.55.

2.2.6 Stopping power and mean excitation energy

Mass stopping power for positron collisions has been previously calculated with the CCC method for molecular hydrogen and its ion [13, 264]. This is a useful quantity for mass transport studies which measures the positron energy loss per unit path length per unity density:

$$-\frac{1}{\rho}\frac{dE}{dx} \equiv Q_{\mathrm{SP}} = \frac{N_{\mathrm{A}}}{M}\sigma_{\mathrm{SP}}. \tag{2.60}$$

Here, N_{A} is Avogadro's number, x is the path length, ρ is the density of the target, M is the molar mass of the target, and σ_{SP} is the stopping power cross section. In the single-centre CCC method σ_{SP} is obtained using

$$\sigma_{\mathrm{SP}} = \sum_{n=2}^{N} (\epsilon_n - \epsilon_1)\sigma_n, \tag{2.61}$$

where ϵ_n and σ_n are the energy and cross section of the nth electronic state, with $n = 1$ referring to the ground state. For our calculations, energy losses from direct annihilation have been omitted, but this cross section is expected to be small for the energies considered in this work.

To calculate the positronium-formation contribution of the stopping power we assume that all of the formed positronium quickly breaks up in subsequent collisions and that the energy loss of positronium-formation can be calculated through energy conservation. In this case, after the breakup of positronium the positron has half the kinetic energy available:

$$K_f = \frac{1}{2}(K_i - I_a^{\mathrm{Ps}}). \tag{2.62}$$

Here, $K_{i/f}$ are the initial/final energies of the positron and I_a^{Ps} is the positronium-formation energy of the atom a. Therefore, the energy loss of the positron is

$$\Delta K = K_i - K_f = \frac{1}{2}(K_i + I_a^{\mathrm{Ps}}) \tag{2.63}$$

from which the stopping power can be obtained through,

$$\sigma_{\mathrm{SP}}^{\mathrm{Ps}} = \Delta K \sigma_{\mathrm{Ps}}, \tag{2.64}$$

where σ_{Ps} is the positronium-formation cross section.

A useful parameter that can be obtained directly from the stopping power is the mean excitation energy:

$$\overline{E} = \frac{\sigma_{\mathrm{SP}}}{\sigma_{\mathrm{inel}}}, \tag{2.65}$$

where σ_{inel} is the inelastic cross-section, which is the sum of excitation, ionisation, and positronium-formation cross sections. For simplicity, the dependence on the incident positron energy was removed from the above equations.

2.2.7 Scattering length, Ramsauer-Townsend minimum, and energy of virtual positron state

From the asymptotic value of the low-energy elastic cross section, we can determine the scattering length of a system via

$$\sigma_{\mathrm{el}} \approx 4\pi A^2, \tag{2.66}$$

where A is the scattering length [78]. To determine the sign of this scattering length, we can use [361]

$$\tan(\delta_0) = -Ak - \frac{\pi\alpha_{\mathrm{D}}k^2}{3a_0}, \tag{2.67}$$

where δ_0 is the s-wave phase shift. A negative value of A indicates that this system has a strongly attractive nature at low energies [109] and implies the existence of a minimum in the s-wave, which if observed in the elastic cross section is known as a Ramsauer-Townsend minimum. The incident energy of the s-wave minimum can be found with [362]

$$E_{\mathrm{min}} = \left(\frac{e^2}{2a_0}\right)\left(\frac{3Aa_0^2}{\pi\alpha_D}\right)^2. \tag{2.68}$$

This minimum in the s-wave occurs as a result of matter wave diffraction and appears in calculations when long-range polarisation of the target by the incident projectile is taken into account [363]. For elastic scattering, a Ramsauer-Townsend minimum occurs when the s-wave phase shift becomes 0 while the contributions from higher L-wave phase shifts are small. The presence of the minimum in the s-wave can also be hidden due to the contributions of higher ℓ-waves counteracting the minimum in the s-wave. Unlike the elastic cross section, a minimum is observed in the momentum transfer cross section when the s- and p-wave phase shifts are equal while the contributions from higher L-wave phase shift differences are small [82]. As a result, even when a minimum is not observed in the elastic cross section, it can be present in the momentum-transfer cross section. Here, these L-waves refer to the angular momentum of the incident positron.

If the magnitude of A is larger than the mean radius of the atomic target, and the scattering cross section is much greater than the geometric size of the atom then it indicates the existence of a virtual level of the positron

projectile [311]. The energy of this virtual level can be obtained using

$$\epsilon = \frac{1}{2A^2}. \tag{2.69}$$

2.2.8 Limitations of the single-centre approximation

As this is a single-centre approximation the expansion is only undertaken over the target states of the atomic target. In this approximation, positronium-formation is calculated implicitly through configurations that have an electron and positron in the continuum. Therefore, the electron-loss cross sections obtained with this method contain contributions from both direct ionisation and positronium-formation processes which cannot be distinguished. The implicit inclusion of positronium-formation and the strong correlations present, due to the attractive positron-electron interaction, results in convergence being slow and the inclusion of states with high orbital angular momentum being necessary to correctly model scattering. Furthermore, between the positronium-formation threshold and the direct ionisation threshold the single-centre calculation is unstable and converged cross sections cannot be obtained. The instability in this region results from mismatched boundary conditions with channels corresponding to positive-energy pseudostates being closed while positronium-formation channels are open. The obtained electron-loss cross section threshold, therefore, is equivalent to the direct ionisation threshold and underestimates two-centre calculations until approximately 10 eV above this threshold.

2.3 Chapter summary

In this chapter we present the formalism of the single-centre CCC method for positron scattering. The formulation of the target structure and the configuration-interaction approach to the wavefunctions are presented. To solve positron scattering from atomic targets, the single-centre CCC method expands the scattering wave function within the basis of the target. Following an expansion of the Schrödinger equation, this equation is transformed using the Green's function into the momentum-space coupled Lippmann-Schwinger equations for the T matrix. Through solving these equations the scattering amplitudes for the considered channels are obtained, and relevant cross sections can be extracted. The limitations of the single-centre

approach are also described. From the theory described in this chapter a computer code was developed to calculate positron scattering from atomic targets.

Chapter 3

CCC-scaled complex model potential

The single-centre positron-atom scattering CCC method suffers from two drawbacks: the difficulty obtaining accurate cross sections between the positronium-formation and direct ionisation thresholds, and the difficulty of disentangling the direct ionisation and positronium-formation processes. To address these issues, a complex model-potential technique has been developed that uses the cross sections calculated within the single-centre approach. By scaling the model potential to fit results calculated with the single-centre model, we obtain sufficiently reliable estimates for positronium-formation, direct ionisation, and excitation cross sections between the positronium-formation and direct ionisation thresholds. In this chapter a description is provided of this technique. Based upon the theory described in this chapter, computer code was developed by the candidate to calculate the required model potential cross sections. Some sections in this chapter text or figures are adapted from a published work by the candidate [1]. The publisher of this article (the American Physical Society) provides the right to use an article or a portion of an article in a thesis or dissertation without requesting permission.

3.1 Complex model potential

The complex model-potential approach requires the calculation of a complex optical potential ($V_{\rm opt}$) given by

$$V_{\rm opt}(r, E_i) = V_{\rm st}(r) + V_{\rm pol}(r) + iV_{\rm abs}(r, E_i), \tag{3.1}$$

where $V_{\rm st}$ is the static interaction potential, $V_{\rm pol}$ is the polarisation potential, $V_{\rm abs}$ is the absorption potential, and E_i is the incident positron energy. The absorption potential accounts for all inelastic processes whereas the static and polarisation potentials account for the elastic process.

The static potential $V_{\rm st}$ is calculated using [364]

$$V_{\rm st}(r) = \frac{Z}{r} - 4\pi \left(\frac{1}{r} \int_0^r dr' \rho(r') r'^2 + \int_0^\infty dr' \rho(r') r' \right), \tag{3.2}$$

where ρ is the electron density of the target obtained from the structure calculation, as described in Section. 2.1.5. For calculation of $V_{\rm pol}$ we use a Buckingham potential [291]

$$V_{\rm pol}(r) = -\frac{\alpha_{\rm D}}{2(r^2 + d^{\frac{1}{2}})^2}, \tag{3.3}$$

where $\alpha_{\rm D}$ is the static dipole polarisability of the target, and d is an adjustable parameter. The value of d is chosen for each energy so that the model potential produces the same elastic cross section as the single-centre CCC calculation for the considered atom. We fit to a smooth interpolation of the single-centre cross-section for energies between the positronium-formation threshold and direct ionisation threshold, where the CCC elastic cross section is unstable.

For the absorption potential we follow the method of Staszewska *et al.* [365], who give

$$V_{\rm abs}(r, E_i) = -\rho(r) \left[\sqrt{\frac{T_{\rm loc}}{2}} \left(\frac{8\pi}{10 k_{\rm F}^3(r) E_i} \right) \times \theta(k_i^2 - k_{\rm F}^2(r) - 2\Delta)(A_1 + A_2 + A_3) \right]. \tag{3.4}$$

Here, Δ is the absorption threshold which represents the threshold energy for inelastic processes, $k_{\rm F}(r)$ is the magnitude of the Fermi wave vector given by,

$$k_{\rm F}(r) = [3\pi^2\rho(r)]^{\frac{1}{3}}, \tag{3.5}$$

and $\theta(x)$ is the Heaviside step function. Also present is the local kinetic energy of the projectile, which for positrons is given by

$$T_{\rm loc} = E_i - V_{\rm st}. \tag{3.6}$$

Finally, A_1, A_2, and A_3 are dynamic functions that rely on several of the above parameters. The equations for these functions are provided by Staszewska *et al.* [365],

$$A_1 = \frac{5k_{\rm F}^3}{2\Delta}, \tag{3.7}$$

$$A_2 = \frac{-k_{\rm F}(5p^2 - 3k_{\rm F}^2)}{p^2 - (k_{\rm F}^2)^2}, \tag{3.8}$$

$$A_3 = 2\theta(2k_{\rm F}^2 + 2\Delta - p^2) \times \frac{(2k_{\rm F}^2 + 2\Delta - p^2)^{5/2}}{(p^2 - k_{\rm F}^2)^2}. \tag{3.9}$$

For these equations, $p = \sqrt{2E_i}$.

3.1.1 Delta variational technique

Positronium-formation cannot be explicitly included in the absorption potential formulation as this process cannot be modelled by binary collisions [33]. Therefore, to obtain the cross section for this transition, we utilise the delta variation technique, which modifies the absorption threshold Δ in Eq. (3.4). Several different versions of this modification exist in the literature [24, 32, 51]. To determine which formulation to use, we compared positronium-formation results for the H and He targets between this method and two-centre CCC calculations. Based on these studies, we found the approach of Chiari *et al.* [51] most appropriate. Here, the absorption threshold is modified according to

$$\Delta(E) = \Delta_{\rm e} - (\Delta_{\rm e} - \Delta_{\rm p})e^{-(E_i - \Delta_{\rm p})/E_m}, \tag{3.10}$$

where Δ_e and Δ_p are the electronic-excitation and positronium-formation threshold energies, respectively. For the adjustable parameter E_m, Chiari *et al.* [51] used the energy for which σ_{inel} was found to have a maximum when not using the delta variation technique. However, we have used the energy at which the single-centre CCC TCS has a maximum as this gave results for positronium-formation in better agreement with two-centre CCC results.

3.1.2 Scattering equations

To solve the scattering equations for the complex model potential, we employ a similar approach used in the CCC method by solving the Lippmann-Schwinger equations for a potential scattering system:

$$\langle \boldsymbol{k}_f|T|\boldsymbol{k}_i\rangle = \langle \boldsymbol{k}_f|V|\boldsymbol{k}_i\rangle + \int d\boldsymbol{k}\frac{\langle \boldsymbol{k}_f|V|\boldsymbol{k}\rangle\langle \boldsymbol{k}|T|\boldsymbol{k}_i\rangle}{k_i^2/2 - k^2/2 + i0}. \tag{3.11}$$

We perform a partial-wave expansion of the T- and V-matrix elements and integrate over the singularity at $k = k_i$, giving the partial-wave Lippmann-Schwinger equation

$$\begin{aligned} T_\ell(k_f, k_i) = V_\ell(k_f, k_i) + \mathcal{P}\int_0^\infty dk \frac{V_\ell(k_f, k)T_\ell(k, k_i)}{k_i^2/2 - k^2/2} \\ - \frac{i\pi}{k_i}V_\ell(k_i, k_i)T_\ell(k_i, k_i), \end{aligned} \tag{3.12}$$

where $\mathcal{P}$ indicates a principal-value integral. We discretise the k domain, and after some rearranging obtain

$$\sum_n (\delta_{f,n} - w_n V_{fn})T_{ni} = V_{fi}, \tag{3.13}$$

where $T_{fi} \equiv T_\ell(k_f, k_i)$, and w_n contain the integration weights and the denominator of the integrand for all off-shell k-grid points, while for the on-shell point it is

$$w_n = -\frac{i\pi}{k_n}. \tag{3.14}$$

By allowing f to run over the same range as n, i.e. all on- and off-shell k-grid points, we obtain a set of linear equations that can be solved to obtain the T-matrix elements. For this complex model potential calculation, the k

domain is discretised into a series of points following the standard approach detailed by Bray and Stelbovics [366], with convergence tested through calculations with increasing number of points.

3.1.3 Cross section evaluation and CCC-scaling

Once the on-shell partial-wave T-matrix elements $T_\ell \equiv T_\ell(k_i, k_i)$ are obtained, the TCS is given by

$$\sigma_{\rm tot} = 4\pi^3 \sum_{\ell=0}^{\infty} (2\ell+1)|T_\ell|^2, \tag{3.15}$$

and applying the optical theorem, the elastic cross section is

$$\sigma_{\rm el} = -\frac{4\pi^2}{\sqrt{2E_i}} \sum_{\ell=0}^{\infty} (2\ell+1)\mathrm{Im}(T_\ell). \tag{3.16}$$

The inelastic cross section, not including positronium-formation, is then given by

$$\sigma_{\rm inel} = \sigma_{\rm tot} - \sigma_{\rm el}. \tag{3.17}$$

The positronium-formation cross section ($\sigma_{\rm Ps}$) is equal to the difference between the inelastic cross sections obtained from calculations with $\Delta(E) = \Delta_{\rm e}$ and $\Delta(E)$ given by Eq. (3.10). By comparing with two-centre CCC results for positron scattering on H and He, we have found that this approach significantly underestimates the inelastic and positronium-formation cross sections. To correct this for systems where two-centre calculations are not available, we scale the cross section for inelastic scattering minus positronium-formation to reproduce the total cross section $\sigma_{\rm tot}$ obtained from the single-centre CCC calculations at high energies. Following this, we scale the $\sigma_{\rm Ps}$ to reproduce the single-centre $\sigma_{\rm tot}$ at the maximum cross-section between the direct ionisation threshold and 10 eV above this threshold. Exact details of this scaling procedure are provided for the hydrogen atom in Section. 3.2 and for the helium atom in Section. 3.3.

We can disentangle the direct ionisation by subtracting the calculated positronium-formation cross section from our ELCS. We have done this for incident energies above 20 eV. To calculate direct ionisation for energies below 20 eV, we have followed the CSP-ic method [166] and, using our

results for positronium-formation and direct ionisation, have calculated the ratio

$$R(E_i) = \frac{\sigma_{\text{ion}}}{\sigma_{\text{in}}}. \tag{3.18}$$

Where σ_{ion} is the direct ionisation cross section and σ_{in} is the direct inelastic cross section, given by $\sigma_{\text{in}} = \sigma_{\text{inel}} - \sigma_{\text{Ps}}$. The values for σ_{inel} are obtained directly from the single-centre CCC calculation for $E > 20$ eV since the single- and two-centre results for H and He were found to be in close agreement by 10 eV above the direct ionisation threshold. Using a cubic spline, we extrapolate the calculated $R(E_i)$ down to the direct ionisation threshold, where $R(E_i)$ is zero by definition. Following this we can obtain σ_{ion} for $E < 20$ eV by multiplying the σ_{in} calculated with the CCC-scaled complex model potential by $R(E_i)$. This process is illustrated in Section 3.2 for the hydrogen atom.

3.1.4 Low energy scaling of the positronium-formation

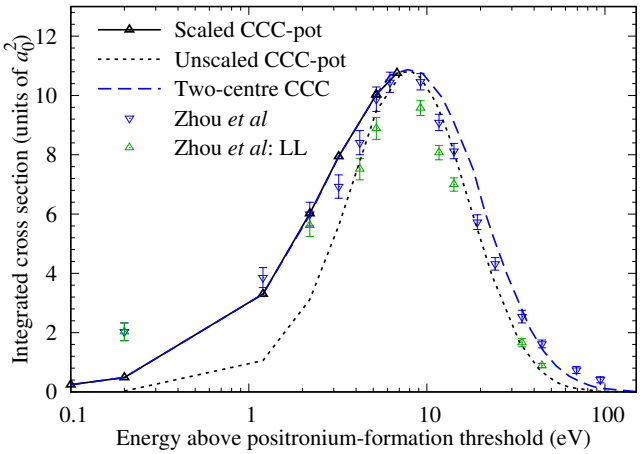

Figure 3.1: Impact of scaling factor on CCC-pot positronium-formation cross section compared against two-centre CCC results [5] for positron scattering on atomic hydrogen. Also shown are the experimental values of Zhou *et al.* [6].

Through analysis of calculations for atomic hydrogen presented in section. 3.2, we find that the CCC-pot approach significantly underestimates two-centre calculations for positronium-formation at energies below its maximum. For atoms with similar direct ionisation thresholds to hydrogen, we

Table 3.1: Fit parameters

i	p_i	q_i
1	0.7803	-6.552
2	-2.994	13.66
3	-5.337	6.343
4	37.67	0.09373
5	21.71	-3.539×10^{-5}
6	1.072	

expect this same deficit to occur. To accommodate for this, we have extended the CCC-pot calculation to include a scaling factor which increases the positronium-formation component of V_{abs} for energies between the positronium-formation threshold and the maximum positronium-formation cross section calculated in our CCC-pot method. The values for this factor were determined to produce positronium-formation equal to that of the two-centre calculation for atomic hydrogen for energies below the positronium-formation maximum. The unscaled and scaled results for atomic hydrogen are shown in Fig. 3.1 alongside the two-centre CCC calculation [5] and experimental results of Zhou *et al.* [6].

To allow for calculations at any energy below the maximum of positronium-formation this factor was then fitted with a function of the form

$$F_s(E) = \frac{p_1 E_f^5 + p_2 E_f^4 + p_3 E_f^3 + p_4 E_f^2 + p_5 E_f + p_6}{E_f^5 + q_1 E_f^4 + q_2 E_f^3 + q_3 E_f^2 + q_4 E_f + q_5}, \tag{3.19}$$

where,

$$E_f(E) = E - E_{\mathrm{Ps}}^{\mathrm{H}}. \tag{3.20}$$

Here, E is the incident energy and $E_{\mathrm{Ps}}^{\mathrm{H}}$ is the positronium-formation threshold of atomic hydrogen, with both units in eV. The parameters for Eq. 3.19 are shown in Table 3.1.

To apply this to atoms beyond atomic hydrogen, we have formulated an approach based upon the difference in energy between the positronium-

formation threshold and maximum for each atom. This replaces Eq. 3.20 with,

$$E_f(E) = \frac{E - E_{\rm Ps}^{\rm A}}{U_s} \tag{3.21}$$

where

$$U_s = \frac{E_{\rm max}^{A} - E_{\rm Ps}^{\rm A}}{E_{\rm max}^{H} - E_{\rm Ps}^{\rm H}}. \tag{3.22}$$

Here, $E_{\rm Ps}^{\rm A}$ is the positronium-formation threshold for atom A and $E_{\rm max}^{A}$ refers to the energy that the maximum positronium-formation is found for this atom, with $E_{\rm max}^{H}$ representing this for the hydrogen atom. For Eq. 3.21 units are in eV, whereas Eq. 3.22 is dimensionless.

Unlike atomic hydrogen, the CCC-pot approach accurately models the positronium-formation cross section for the helium atom at low energies, as shown in Fig. 3.14. Therefore, it is expected that the need for the scaling factor is reduced the closer the direct ionisation threshold of the atom is to helium. We have therefore used the following modified scaling parameter:

$$\tilde{F}(E) = (F_s(E) - 1)\left(1 - \frac{I_a - I_{\rm H}}{I_{\rm He} - I_{\rm H}}\right) + 1, \tag{3.23}$$

that reduces the impact of the scaling factor based on the direct ionisation threshold of the considered atom. Here, I_a represents the direct ionisation thresholds for atom a, I_H for hydrogen, and I_{He} for helium.

3.2 CCC-scaled complex model potential: Hydrogen atom calculation

To demonstrate the efficacy of the CCC-scaled complex model potential approach, we present calculations for positron scattering from the hydrogen atom for which both single- and two-centre CCC results are available. We first obtain the complex model potential results utilising the same approach as described in the previous section. To summarise, we fit the polarisation potential parameter d in our polarisation potential given in Eq. 3.3 to obtain elastic cross sections equal to the single-centre CCC for each energy. Between the positronium-formation and the direct ionisation thresholds we instead fit to a line smoothly connected between these two thresholds. This is because the single-centre approach is unstable between these two thresh-

olds, this instability can be viewed in Fig. 3.3 as a large dip occurring at 10 eV.

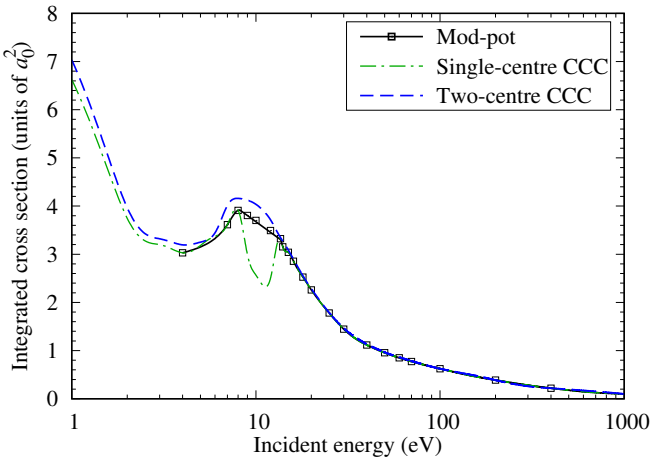

Figure 3.2: Elastic cross section for positron scattering on the hydrogen atom. Single- and two-centre CCC results are compared with the results obtained using the model potential.

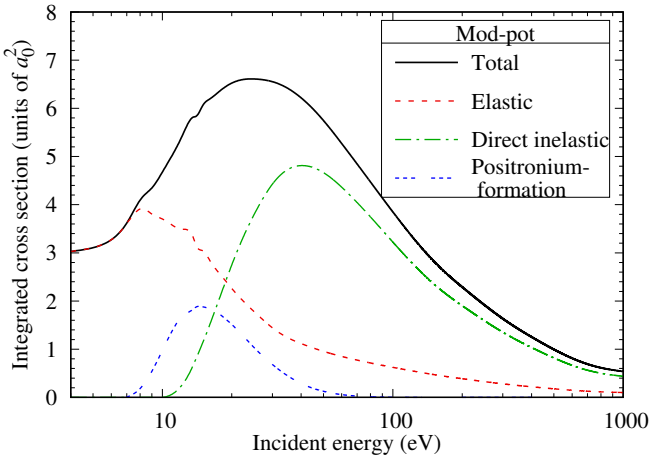

Figure 3.3: The total cross sections and its components for the unscaled model potential calculation of positron scattering from hydrogen presented from the positronium-formation threshold to 1000 eV.

Elastic cross sections from our complex model potential are presented in Fig. 3.2 alongside single- and two-centre CCC results. As expected, outside of the region between the positronium-formation and direct ionisation thresholds, elastic results from the complex model potential are exactly equal to those of the single-centre calculation. Our absorption potential is

obtained following the method of Staszewska *et al.* [365] as described in Section. 3.1, with values for the positronium-formation cross section obtained through the delta variational technique. With these positronium-formation values, we can obtain the direct inelastic cross section which is equal to the bound state excitations summed with the direct ionisation cross section. Hence, the total cross section contains three components: the direct inelastic cross section, the positronium-formation cross section, and the elastic cross section. The total cross section of this unscaled complex model potential and its components are presented in Fig. 3.3.

The first step of the CCC-scaling procedure is to scale the direct inelastic component of the total cross section to agree at large energies with the values predicted by the single-centre CCC result. This is presented in Fig. 3.4, in which this component has been scaled by a factor of 2.4. Also shown are the single-centre CCC results and the unscaled model potential.

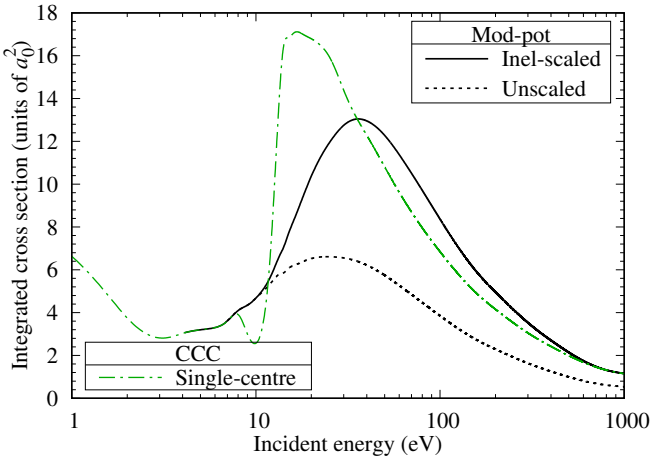

Figure 3.4: Complex model potential total cross section results for positron scattering on hydrogen in which direct inelastic cross sections have been scaled to agree with CCC results for larger energies. In these results positronium-formation cross sections are currently unscaled. These results are presented with the single-centre CCC results.

The second step is to scale the positronium-formation component of the total cross section. We uniformly increase this cross section so that the CCC-scaled model potential total cross section reproduces the maximum single-centre total cross section between the direct ionisation threshold and 10 eV above the direct ionisation threshold. For example, this occurs at

16 eV for hydrogen, so we scale the CCC-scaled model potential result to agree with the single-centre CCC at 16 eV. In this case, the positronium-formation cross section was scaled by a factor of 5.75. The final results are depicted in Fig. 3.5, in which scaled positronium-formation and inelastic results are summed with the elastic cross section to obtain the new total cross section. These results are again shown alongside corresponding single-centre CCC results. The improvement in results from this scaling procedure is clear when comparing the unscaled results in Fig. 3.4 and the final scaled results in Fig. 3.5 to single- and two-centre CCC results. The CCC-scaled model potential overestimates the single-centre cross section for energies above 25 eV, resulting in inaccuracies in the CCC-scaled complex model calculation for the excitation cross section between 25 and 600 eV. As our subsequent calculations do not require these values this is not considered an issue. By construction, the elastic cross section is equivalent to the single-centre CCC results; therefore, this component does not require any scaling.

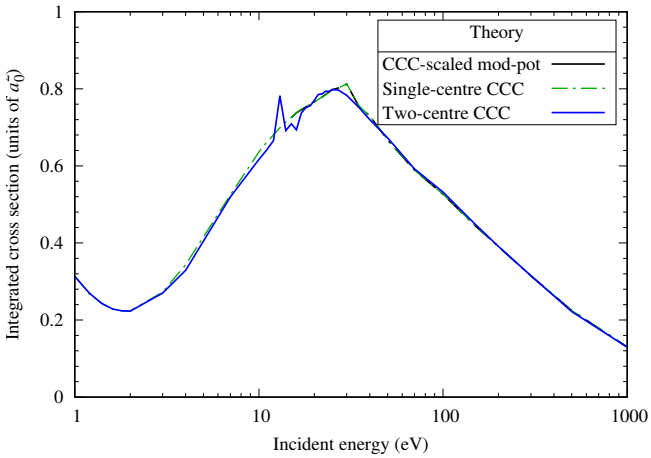

Figure 3.5: CCC-scaled complex model potential and CCC single-centre results for the positron-hydrogen total cross section. Here, the total cross section is comprised of the elastic, scaled direct inelastic, and scaled positronium-formation cross-section.

We can directly compare the scaled positronium-formation cross section with the two-centre CCC. We present this in Fig. 3.6, where it can be seen that our scaled result is both equal to and has the correct position of the peak cross-section of the positronium-formation. However, our calculation somewhat underestimates the two-centre result for energies above and below

this peak.

We can obtain direct ionisation results for energies 10 eV greater than the ionisation energy by subtracting these values from the single-centre electron-loss cross section from our positronium-formation results. For energies below this point, we rely on the CSP-ic method. First, we obtain $R(E)$ values for energies greater than 10 eV above the direct ionisation threshold, and then we fit a spline interpolant to obtain the $R(E)$ for lower energies. We can obtain the direct ionisation cross section by multiplying these fitted values by the direct inelastic cross section obtained from our CCC-scaled complex model potential. The calculated and fitted $R(E)$ results are depicted in Fig. 3.7. These results rise to a maximum of approximately 0.55 at 50 eV before dropping to an asymptote of approximately 0.4 by 1000 eV. This represents that by 1000 eV 40% of the direct inelastic cross section is composed of direct ionisation.

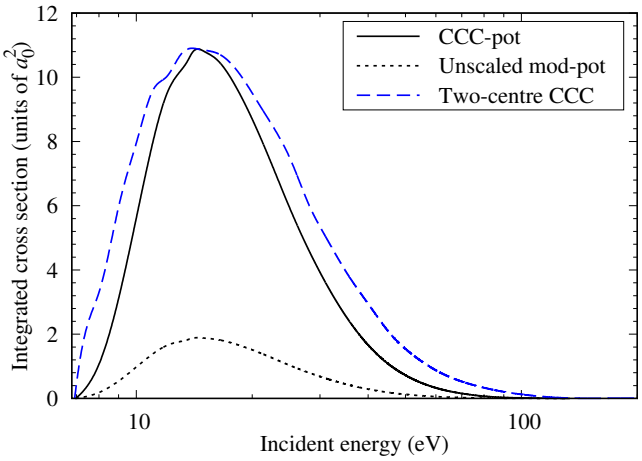

Figure 3.6: Positronium-formation cross section for positron scattering from hydrogen. Our unscaled and CCC-scaled complex model potential results are presented with the two-centre CCC results for energies ranging from the positronium-formation threshold to 200 eV.

In Fig. 3.8, we present our results for direct ionisation obtained using the CCC-scaled complex model potential approach and those obtained via the two-centre CCC. We can observe that differences between these methods mainly occur for energies less than 75 eV, which directly results from the errors in our positronium-formation calculation. The peak of this

approach overestimates the two-centre CCC, with differences within 25%. For lower energies, particularly near the direct ionisation threshold, we find larger differences; however, the magnitude of the cross section at these energies is small.

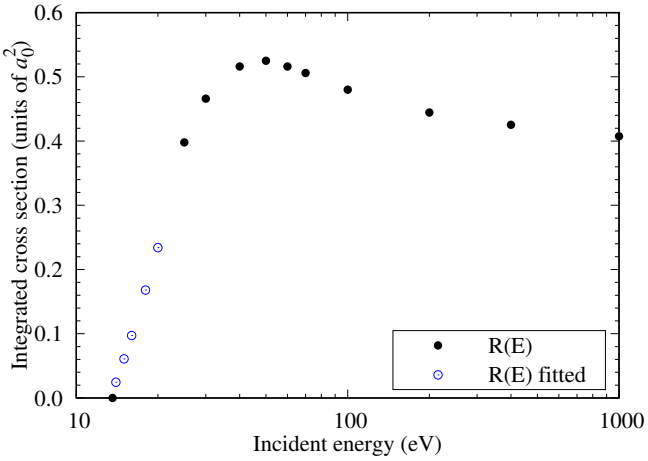

Figure 3.7: Calculated R(E) and fitted R(E) values for positron scattering from hydrogen. R(E) is equivalent to $\sigma_{\rm ion}/\sigma_{\rm in}$.

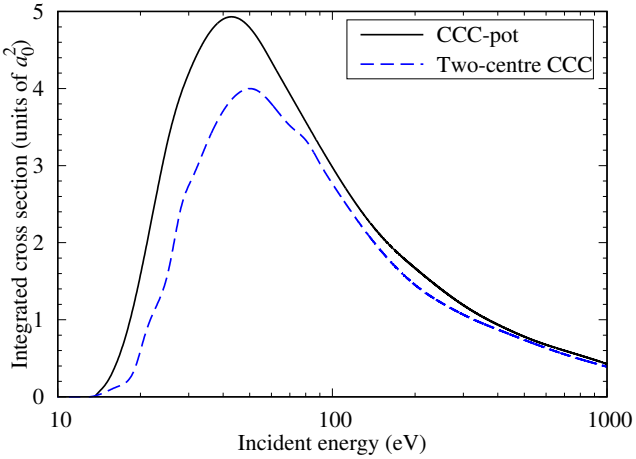

Figure 3.8: The direct ionisation cross section for positron scattering from hydrogen for our unscaled and CCC-scaled complex model potential calculations presented alongside the two-centre CCC results.

We have direct ionisation and positronium-formation results and can now calculate the electron-loss cross section. This is calculated from the

summation of our scaled positronium-formation and direct ionisation cross sections with these results presented in Fig. 3.9 alongside single- and two-centre CCC results. The benefit of our new approach compared to the single-centre CCC is clear with our new results in significantly better agreement with the two-centre calculation from positronium-formation threshold to 10 eV above the direct ionisation threshold. Below the direct ionisation threshold, the differences between CCC-pot and the two-centre calculation are the same as for the positronium-formation. Whereas, from the direct ionisation threshold to 10 eV above it, the differences are within 5%.

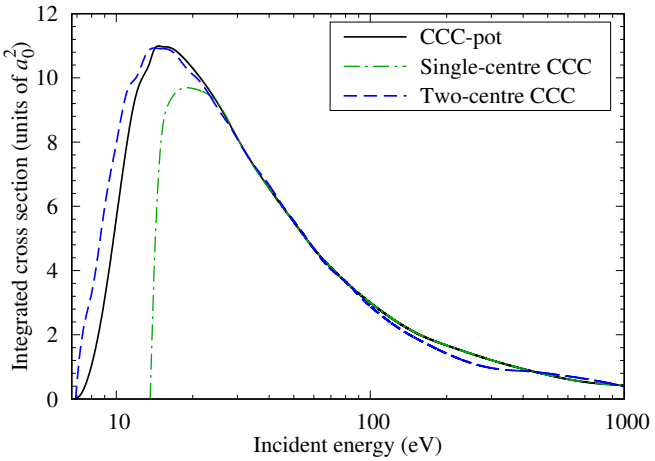

Figure 3.9: Electron-loss cross section for positron scattering from hydrogen from our new approach presented alongside the single- and two-centre CCC results. Results are presented from the positronium-formation threshold to 1000 eV.

The excitation cross section can also be calculated using the direct ionisation cross section. For energies higher than 10 eV above the direct ionisation threshold, we use $\sigma_{\text{exc}} = \sigma_{\text{tot}} - \sigma_{\text{Ps}} - \sigma_{\text{ion}} - \sigma_{\text{el}}$ where σ_{tot} is from our single-centre CCC result. For energies below this, we do the same but use σ_{tot} from our CCC-scaled complex model potential calculation. The total bound excitation cross section is shown in Fig. 3.10 alongside single- and two-centre CCC results. We can observe that this new approach is a great improvement over the single-centre for lower energies, where instabilities in the single-centre calculation for energies near the direct ionisation threshold have resulted in substantially larger results than the two-centre calculation. We find differences between this new approach and the two-centre calcula-

tion to be within 5%.

Finally, for the calculation of the total cross section, we now combine the results of the single-centre and CCC-scaled model potential. For this, we use our single-centre results for energies below the positronium-formation and higher than 10 eV above the direct ionisation threshold. For energies between the positronium-formation threshold and 10 eV above direct ionisation, we use the total cross section calculated by the CCC-scaled model potential. We have compared these results with the single- and two-centre CCC result for hydrogen in Fig. 3.11. We find that results are significantly improved from the single-centre CCC calculation for the energies between the positronium-formation and direct ionisation thresholds. Results still underestimate the two-centre CCC over this energy range, with our results within 20% of the two-centre results. From the direct ionisation threshold to 10 eV above this threshold, errors between our results and the two-centre CCC are within 10%.

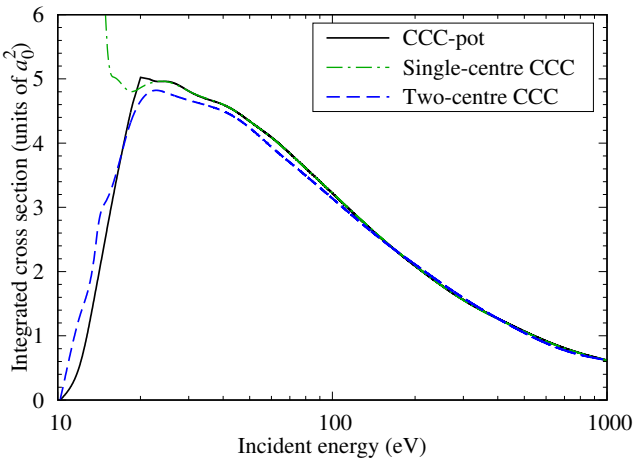

Figure 3.10: Total excitation cross section for positron scattering from hydrogen calculated from our new approach alongside single- and two-centre CCC results.

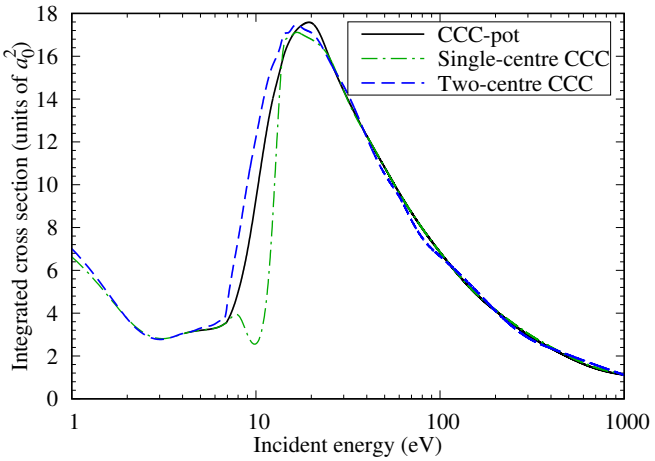

Figure 3.11: Combined results for the positron-hydrogen total cross section alongside single- and two-centre CCC results.

3.3 CCC-scaled complex model potential: Helium atom calculation

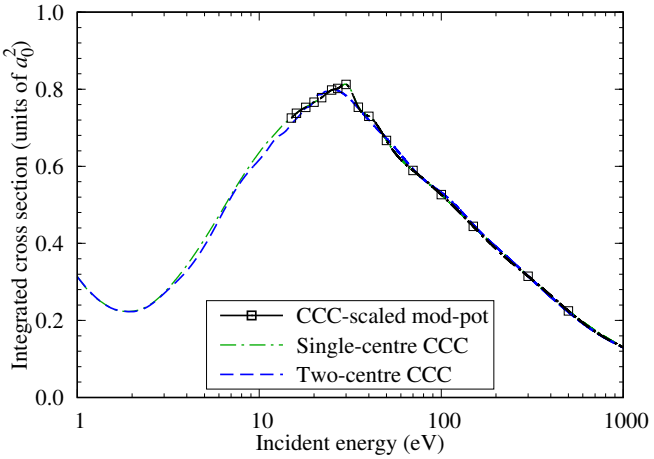

Figure 3.12: Elastic cross section for positron scattering on the helium atom. Single- and two-centre CCC results are compared with the results obtained using the model potential.

As we have already depicted the process of the CCC-scaling of the direct inelastic and positronium-formation cross sections for the hydrogen model potential calculation, we only present the final results for the helium atom. Model potential calculations are undertaken following the same process de-

scribed in section 3.1. As with hydrogen, smooth elastic cross sections were obtained using a line fit between the positronium-formation and direct ionisation thresholds. These elastic cross sections are presented in Fig. 3.12 alongside single- and two-centre CCC results. Firstly we present CCC-scaled model potential total cross section results in Fig. 3.13 alongside single-centre CCC results. For this model, the direct inelastic component was scaled by a factor of 1.51 and the positronium-formation component by a factor of 6.71. For helium, the maximum cross-section for the single-centre calculation occurs at 70 eV, a much higher energy than is observed in the hydrogen case.

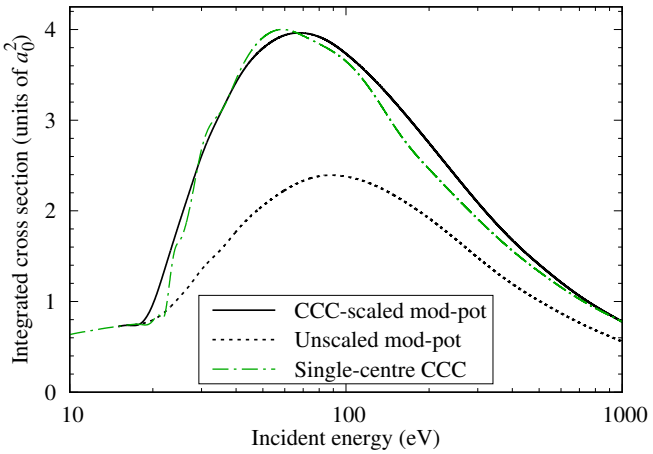

Figure 3.13: CCC-scaled complex model potential, unscaled complex model potential, and CCC single-centre results for the positron-helium total cross section.

Presented in Fig. 3.14 are positronium-formation cross sections for the CCC-scaled complex model potential, unscaled complex model potential, and two-centre CCC results. Unlike hydrogen, our new results only underestimate the two-centre results around the peak cross section and are higher for energies above 55 eV. These results are within 10% of the two-centre results for results up to 60 eV. Excellent agreement is observed with the presented experiment for both the two-centre CCC calculation and the current CCC-pot result. As expected, the unscaled CCC-pot result is significantly lower than both the two-centre calculation and the experimental results.

In Fig. 3.15, we present the direct ionisation result for this approach against the two-centre CCC results. Unlike hydrogen, our direct ionisation underestimates at lower energies and the peak cross section. However, compared to experiment excellent agreement is observed across the entire presented energy range with the CCC-pot calculation. The differences between the two methods are less here than with hydrogen, with all values within 20% of the two-centre CCC result. We also find much better agreement for energies below this peak cross section than was viewed with hydrogen, likely because the positronium-formation has a much lower magnitude for helium.

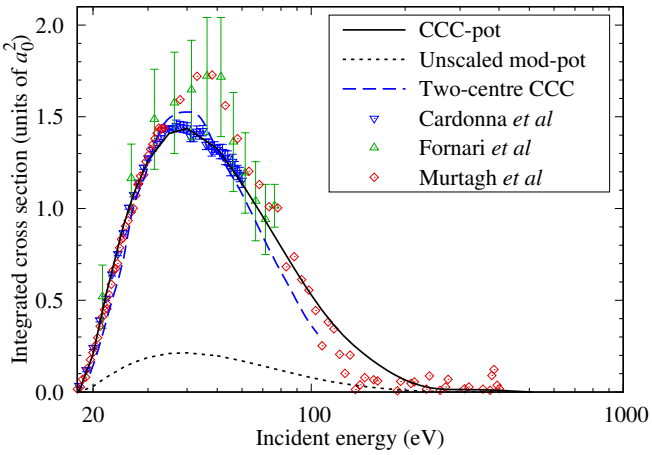

Figure 3.14: Positronium-formation cross-sections for positron scattering from helium. Results from our unscaled and CCC-scaled complex model potential are presented alongside two-centre CCC results. Experimental results are from Caradonna *et al.* [7], Fornari *et al.* [8], and Murtagh *et al.* [9]. Results are presented from the positronium-formation threshold to 1000 eV.

We have also used our new method to calculate the total excitation cross section for the helium atom. This is shown in Fig. 3.16 with single- and two-centre CCC results. We see significant improvement from the single-centre results for energies below 10 eV above the direct ionisation threshold, with the cross sections here having near perfect agreement with the two-centre calculation.

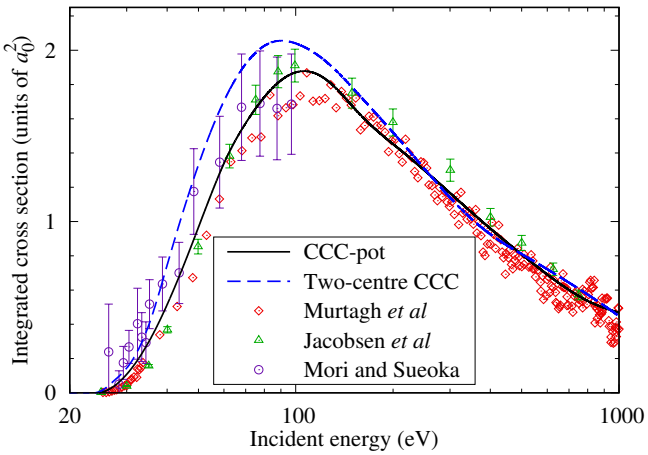

Figure 3.15: The direct ionisation cross section for positron scattering from helium. Our unscaled and CCC-scaled complex model potential results are presented alongside the two-centre CCC results. Experimental results are from [9], Jacobsen *et al.* [10], and [11]. Results are presented from the ionisation threshold to 1000 eV.

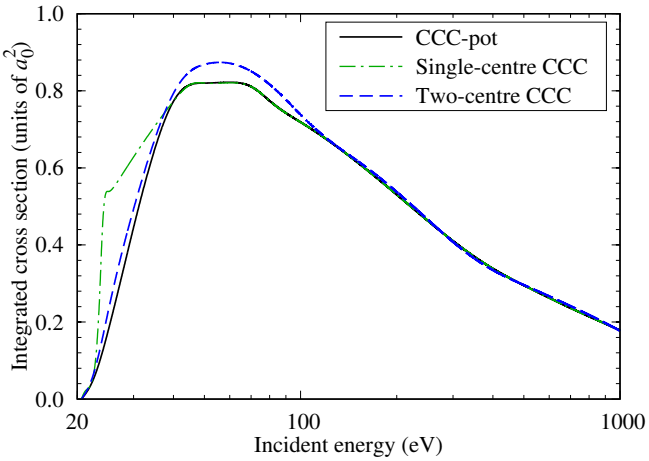

Figure 3.16: Total excitation cross section for positron scattering from helium. Results calculated from our new approach are presented alongside single- and two-centre CCC results.

Finally, in Fig. 3.17 we can find the combined results of the CCC-scaled complex model potential and single-centre CCC alongside the single- and two-centre CCC. As with hydrogen over the energy range between positronium-formation and direct ionisation, our new results are a significant improvement over the single-centre calculation. As the elastic cross

section is scaled to be equivalent to the single-centre CCC result, there is no point in calculating CCC-pot below the positronium-formation threshold, as the only process available below this threshold is elastic scattering. Here we find even better agreement than was found with hydrogen, with our total cross sections having errors of 5% or lower over this energy range. From the direct ionisation threshold to 10 eV above this threshold, we find similar errors with results within 5%, again an improvement from hydrogen.

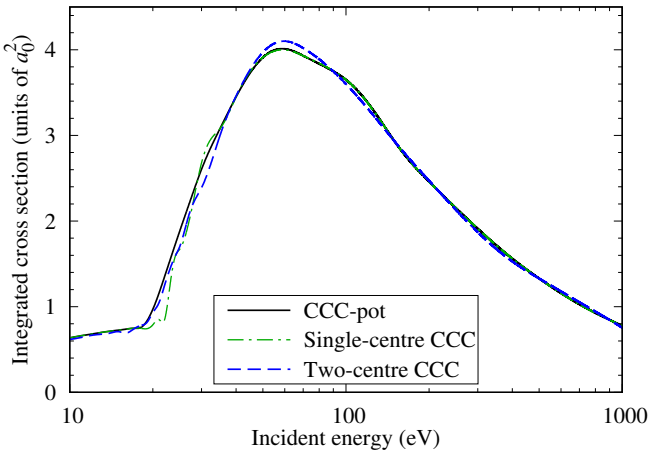

Figure 3.17: Combined results for the total cross section of positron scattering from helium alongside the single- and two-centre CCC results.

3.4 Error analysis and limitations of CCC-scaled complex model potential

The accuracy of this approach and the improvement it provides for single-centre CCC calculations for both the hydrogen and helium targets is promising. It justifies its application to other targets, as these two targets have very different scattering behaviours, polarisation potentials, and direct ionisation, excitation, and positronium-formation thresholds. Following analysis of these systems, we expect positronium-formation to have an accuracy of 20% for energies above the maximum cross section to up to 3 times the ionisation threshold from this method. With the inclusion of the scaling method based on the hydrogen results we expect that results below the maximum positronium-formation cross section will have an accuracy of about 10 %. Although the positronium-formation results are not particularly accurate

for higher energies as the magnitude of this process decreases rapidly with increasing energy, they can still be utilised to calculate sufficiently accurate direct ionisation cross sections.

For direct ionisation, we expect the peak cross section to be within 20% of the two-centre value, with energies below the peak value having higher inaccuracies if the positronium-formation cross section is significantly larger than the direct ionisation. For higher energies, where the positronium-formation cross section is small, we expect the accuracy for this cross section to be within 5%. For the total excitation cross section, we expect an error of 10% for energies where results are obtained from the model potential. Across the energy range in which the CCC-scaled complex model potential is utilised for the total cross section, we expect the errors to be within 15%.

For atoms with direct ionisation thresholds below 10 eV, the positronium-formation process is significant and the maximum of the total cross section typically occurs between the positronium-formation and direct ionisation threshold, where single-centre results cannot be accurately obtained. Therefore, due to the scaling processes utilised, for atoms with direct ionisation thresholds below 10 eV the uncertainty is expected to be larger than discussed above. Hence, in conjunction with accurate single-centre CCC results, we expect this method to be most accurate for atoms with direct ionisation energies greater than 10 eV.

3.5 Chapter Summary

This chapter provides a description of the complex model potential approach utilised in conjunction with our single-centre CCC calculations to calculate positronium-formation, direct ionisation, and inelastic cross sections between the positronium-formation and direct ionisation thresholds. The equations for the required potentials used within our complex scaled potential calculations are provided and described. A description of how we solve these equations with the complex potential Lippmann-Schwinger equations is given. The two techniques utilised, the delta variational technique and the CSP-ic technique, are also explained. To find agreement with the results of the complex model potential and the accurate single-centre CCC calculations it was necessary to apply a scaling procedure. These procedures and the current methodology are illustrated through a breakdown of the calcu-

lations conducted for positron scattering from hydrogen and helium, with figures provided for all relevant cross-sections. As two-centre CCC calculations exist for these two systems, we conduct an error analysis through comparison of the two-centre and current results.

Chapter 4

IAM-SCAR method

This chapter presents the process of the IAM-SCAR calculation as described by Blanco and García [224] and Blanco *et al.* [225]. Modifications to this approach for its use with the cross sections obtained through the CCC and the CCC-scaled complex model potential approaches are also provided. CCC-SCAR calculations for H_2 are also shown as there is existing one- and two-centre CCC calculations for positron scattering from this molecule.

4.1 IAM-SCAR

The IAM method for a molecule containing N_a atoms is given by

$$\sigma_m = \sum_{i=1}^{N_a} \sigma_i, \tag{4.1}$$

where σ_m is the cross section of the considered molecule and σ_i is the cross section of each independent atom i. This is a simple approximation and is expected to only be accurate for high incident energies, where the projectile "sees" the molecule as a sum of its independent atoms. For lower energies, the atomic cross sections are typically too large and, if they are geometrically visualised, will overlap the cross sections of the surrounding atoms within the molecule. Without accounting for these overlaps, the IAM method double-counts these interactions with the projectile and overestimates the cross section. The fundamental concept of the IAM-SCAR method [367], therefore, is the use of screening coefficients (s_i) that account for the geometry of a molecule and reduces the individual atomic contributions to the molecular

cross section. This concept leads to a reformulation of Eq. 4.1 to

$$\sigma = \sum_i s_i \sigma_i. \tag{4.2}$$

These screening coefficients are calculated through,

$$s_i = 1 - \frac{\epsilon_i^{(2)}}{2!} + \frac{\epsilon_i^{(3)}}{3!} - \frac{\epsilon_i^{(4)}}{4!} + \cdots \tag{4.3}$$

where,

$$\epsilon_i^{(k)} = \frac{N_a - k + 1}{N_a - 1} \sum_{j \neq i} \frac{\sigma_j \epsilon_j^{(k-1)}}{\alpha_{ij}} \qquad (k = 2, \cdots, N_a), \tag{4.4}$$

and $\alpha_{ij} = \max(4\pi r_{ij}^2, \sigma_i, \sigma_j)$. Here, r_{ij} is the distance between the centres of the atoms i and j and σ_j is the cross section of atom j. The first coefficient is defined as $\epsilon_i^{(1)} = 1$. For each molecule, the molecular geometries were obtained from the CCCB database of NIST [368].

This approach does not account for the vibrational or rotational motion of the target molecule and is expected to be most accurate for energies above 30 eV [225]. Furthermore, rotational cross sections, if available, can be included through their summation to the IAM-SCAR result, a process referred to as the IAM-SCAR+rot method [296].

4.2 CCC-SCAR

To obtain the cross sections for molecular systems with the CCC calculations for independent atoms the IAM-SCAR method has been modified. First, we utilise the IAM-SCAR approach for the total cross section to obtain screening coefficient values for each atom at each considered energy. Following this, these screening coefficients are applied independently to all of the cross sections that compose the total cross section for each atom at that energy. For molecules, the thresholds for each process, besides elastic, are typically different to the atoms that compose them. Therefore, we shift the cross sections for each process so that its threshold is equal to its accepted threshold value for each molecule. These shifted cross sections can then be summed to obtain the final total cross section of the molecule at each energy. Calculations conducted with this approach and utilising atomic CCC cross sections are referred to as CCC-SCAR.

4.3 H-atom scaling

For CCC-SCAR calculations of H_2, we found large discrepancies with existing MCCC calculations, with the CCC-SCAR substantially overestimating the total cross section. This is most transparent at high energies, see Fig. 4.1, where the IAM cross section is systematically larger than the MCCC cross section. To validate the current cross sections we have also included Fig. 4.2. In this figure, we present the MCCC results for incident positrons [13] and electrons [12] alongside the recommended electron results of Yoon *et al.* [14]. There is near-perfect agreement between these results to 1000 eV. Also shown in this figure are the IAM results of the CCC for both of these projectiles [5, 16]. We have also included the recommended results for positron scattering from H [15] and the measurements of Zhou *et al.* [6] for electron scattering on H, both multiplied by a factor of two in accordance with the IAM. Comparing the IAM results there is excellent agreement between the CCC and experimental cross sections across the presented energy range. Apparently, the IAM method fails to approximate H_2 cross sections with corresponding atomic cross sections for both calculated and measured results for both electron and positron impact.

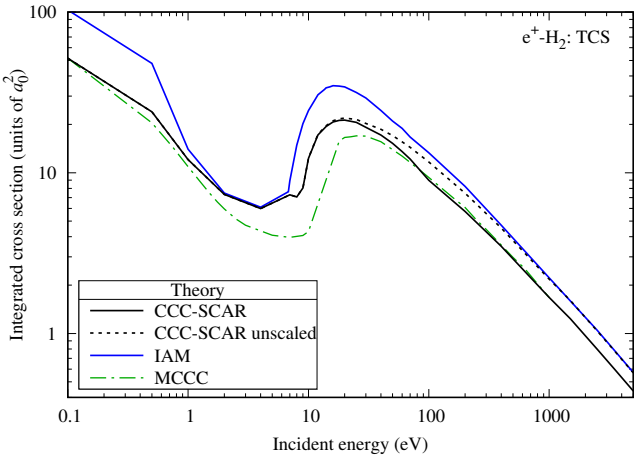

Figure 4.1: Total cross section for positron scattering on molecular hydrogen. Theoretical CCC-SCAR, CCC-SCAR without the scaling described in text and IAM results are shown alongside one- and two-centre CCC calculations.

To correct this, we have introduced a scale factor of 0.77, which the H component of the CCC-SCAR cross section is uniformly multiplied

by above 100 eV. Between the positronium-formation threshold and 100 eV this factor is linearly reduced from 1 to 0.77. The linear scale was included to 100 eV as the CCC-SCAR approach is expected to be of high accuracy above these energies and should accurately reflect the high-energy behaviour. We have chosen not to scale the CCC-SCAR results to the known MCCC values at all energies. The aim here is to rectify the obvious problem with the CCC-SCAR technique in a way that can be easily extended to other molecular scattering systems where often accurate close-coupling calculations are not available while it is often relatively easy to establish the high energy behaviour of the total cross section through either existing electron measurements or Born approximation calculations.

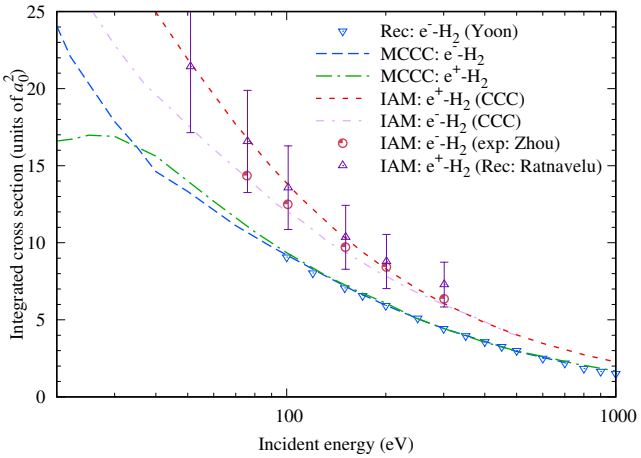

Figure 4.2: Total cross section for positron and electron scattering on molecular hydrogen. MCCC results are from [12] and [13] for electrons and positrons respectively. The recommended electron results for H_2 are from Yoon *et al.* [14]. For the IAM results we use the electron measurements of Zhou *et al.* [6], the recommended positron results of Ratnavelu *et al.* [15], and the CCC calculations for positrons [5] and electrons [16].

The impact of this scale factor is demonstrated in Fig 4.1 for H_2 where, after applying this scale factor, substantially better agreement is found between the CCC-SCAR results and the MCCC calculations. For other molecules containing H, similar disagreements were found at high energies with existing high-energy electron measurements for the total cross section. For molecules that did not contain H, no such discrepancies were found. This suggests that there is a failure in the IAM approach when including

the current cross sections for H. Therefore, for the molecules containing H, i.e. H_2O and CH_4, we have scaled the H component of these calculations. With this modification, we found a very good agreement with high energy electron measurements for the total cross section as will be demonstrated in Chapter. 11.

4.4 H_2 scattering

For H_2, CCC-SCAR calculations are conducted with existing single- and two-centre results for atomic H [5, 228]. Where two-centre results are used for energies $\leq$ 1000 eV, and single-centre for energies $>$ 1000 eV. The distance between atomic centres was obtained from the CCCDB database of NIST [59]. Through comparison of the CCC-SCAR calculations with the MCCC calculations for H_2, the error of the current approach is estimated.

4.4.1 Total cross section

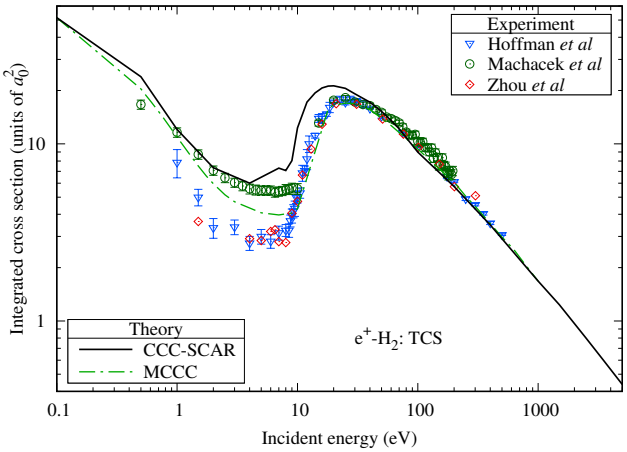

Figure 4.3: Total cross section for positron scattering on molecular hydrogen. Theoretical CCC-SCAR results are shown alongside MCCC calculations [13] and the experiments of Hoffman *et al.* [17], Zecca *et al.* [18], Machacek *et al.* [19], Karwasz *et al.* [20], Deuring *et al.* [21], and Zhou *et al.* [6].

In Fig. 4.3, we present the CCC-SCAR calculations for the total cross section of H_2 alongside previous MCCC calculations and several experiments [6, 17–21]. Close agreement is found between the MCCC and CCC-SCAR calculations for energies above 50 eV and below 3 eV. Between these two energies,

the CCC-SCAR overestimates the MCCC calculations. Above 40 eV, good agreement is found with the presented experimental results. At low energies there is little consensus between experiments, however, the MCCC and CCC-SCAR are closest to the most recent experiment of Machacek *et al.* [19].

4.4.2 Elastic cross section

The elastic cross section for positron scattering on H_2 is shown in Fig. 4.4. The CCC-SCAR elastic cross section is close to the MCCC results for energies below the positronium-formation threshold. From 15 eV to 1000 eV, however, the CCC-SCAR results are slightly lower than the MCCC calculations. The opening of the positronium-formation channel can result in resonant-like structures in the elastic cross section known as a Wigner cusp [108]. As the positronium-formation thresholds, and the magnitudes of this cross section, are different in H and H_2 this is likely the source of the discrepancy between the CCC-SCAR and MCCC results for energies between 4 eV and 15 eV.

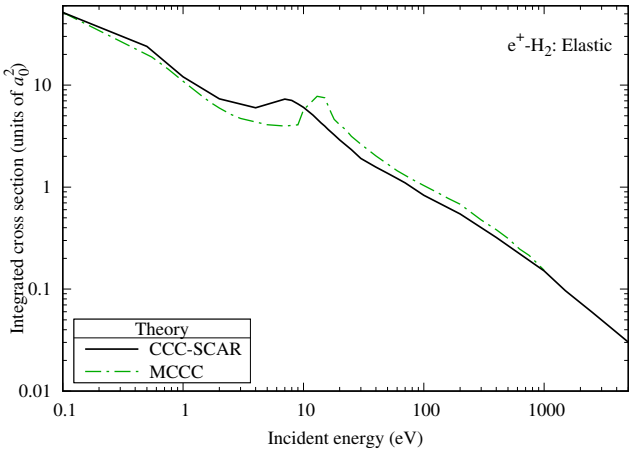

Figure 4.4: Elastic cross section for positron scattering on molecular hydrogen. Theoretical CCC-SCAR results are shown alongside single- and two-centre CCC calculations.

4.4.3 Total electronic excitation cross section

The current CCC-SCAR results for the total electronic excitation cross section for H_2 are shown in Fig. 4.5 alongside the MCCC calculations [13] and

the summed $B^1\Sigma_u^+$ and $C^1\Pi_u$ BSMC results of Arretche and Lima [22]. The measurements of Sullivan *et al.* [23] for excitation to the $B^1\Sigma_u^+$ state are also shown, there are no experimental results for the total electronic excitation. The CCC-SCAR results are close to the MCCC calculations for energies below 20 eV and both are within the error of Sullivan *et al.* [23] under 15 eV. Other excited channels open above 15 eV, therefore, this experiment will be smaller above this energy. Above 20 eV, the CCC-SCAR results are higher than the MCCC calculations to 5000 eV. However, above 100 eV, differences between these calculations decrease. Compared to the summed results of Arretche and Lima [22] for the first two excitations the MCCC and CCC-SCAR calculations are higher even towards threshold.

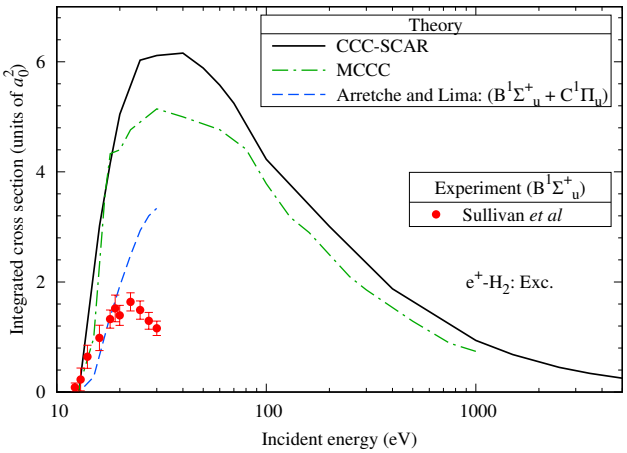

Figure 4.5: Total electronic excitation cross section for positron scattering on molecular hydrogen. CCC-SCAR results are shown alongside MCCC calculations [13] and the summed $B^1\Sigma_u^+$ and $C^1\Pi_u$ BSMC results of Arretche and Lima [22]. The experiment of Sullivan *et al.* [23] for excitation to the $B^1\Sigma_u^+$ state is also shown.

4.4.4 Electron-loss, direct ionisation, and positronium-formation cross section

The positronium-formation cross section for H_2 is shown in Fig. 4.6. The CCC-SCAR results are shown alongside the MCCC calculations [13] and those of Singh and Antony [24] and Biswas *et al.* [25]. The experiments of Machacek *et al.* [19], Zhou *et al.* [6], and Fromme *et al.* [26] are also presented. The CCC-SCAR method is in close agreement with the MCCC

calculations for energies above 30 eV, although it slightly underestimates between 50 and 100 eV. Compared to the experiments, we find the two-centre and CCC-SCAR to be lower than experimental uncertainty for energies between 40 eV and 80 eV. The two-centre calculations lies below the uncertainty of both experiments for energies below 15 eV. In contrast, the CCC-SCAR is within experimental uncertainty below 9 eV and above 30 eV but above experimental points between these energies. The MCCC results follow a similar shape to the calculations of Biswas *et al.* [25] but are slightly lower across the energy range. The results of Singh and Antony [24] are close to the MCCC result to 15 eV but predict a much lower maximum. Above 40 eV, both of these theoretical calculations are of a higher magnitude than the MCCC and CCC-SCAR results. Disagreements with experiment at high energy could be a result of errors associated with the formation of positronium in ortho- or electronically excited states.

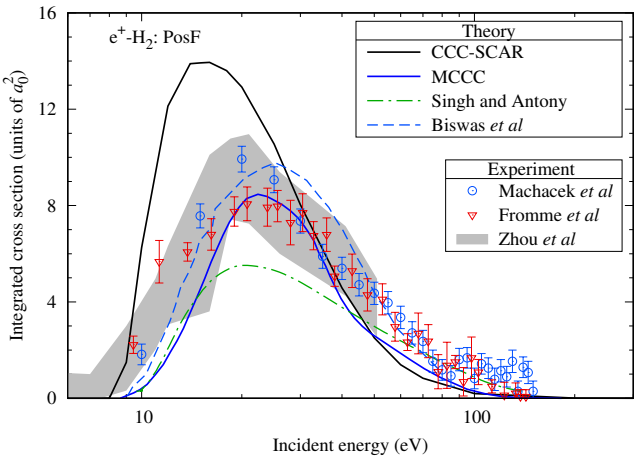

Figure 4.6: Positronium formation cross section for positron scattering on molecular hydrogen. Theoretical CCC-SCAR and MCCC [13] results are shown alongside the calculations of Singh and Antony [24] and Biswas *et al.* [25], and the measurements of Machacek *et al.* [19], Zhou *et al.* [6], and Fromme *et al.* [26].

The CCC-SCAR direct ionisation results are presented in Fig. 4.7 alongside the MCCC calculations [13], other previous theory [24, 27, 28], and previous measurements [10, 26, 29, 30]. The CCC-SCAR are in excellent agreement with experiment for energies below 40 eV, whereas the two-centre results are larger than experiment for this energy range. Between 30 eV and

90 eV, the CCC-SCAR is above the MCCC calculations, finding a sharper peak than these results. Above 80 eV, the CCC-SCAR slightly underestimates the MCCC and is in close agreement with experiment above 700 eV. For energies between 40 eV and 300 eV, there is little consensus among experiments and theory. In this region, the MCCC results are closest to the BEB calculations of Fedus and Karwasz [28] whereas the CCC-SCAR is similar to the SCOP results of Singh and Antony [24] to its peak. We expect that the two-centre MCCC results are of higher accuracy than the CCC-SCAR results and that the CCC-SCAR approach is overestimating for energies between 30 eV and 80 eV.

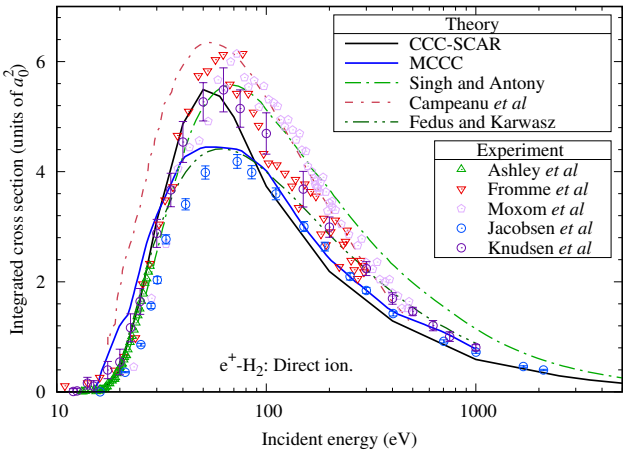

Figure 4.7: Direct ionisation cross section for positron scattering on molecular hydrogen. Theoretical CCC-SCAR and MCCC [13] results are shown alongside the calculations of Singh and Antony [24], Campeanu *et al.* [27], and Fedus and Karwasz [28]. Experimental results are those of Knudsen *et al.* [29], Fromme *et al.* [26], Ashley *et al.* [30], and Jacobsen *et al.* [10].

The electron-loss cross section of H_2, presented in Fig. 4.8, is equivalent to the sum of the positronium-formation and direct ionisation cross sections. Therefore, we find similar discrepancies as with these two components. There is agreement with the CCC-SCAR and MCCC [13] results for energies above 80 eV. For energies below 80 eV, the current approach is significantly higher than the MCCC results. Compared to the measurements of Fromme *et al.* [26] and Moxom *et al.* [31], good agreement is found below 10 eV, between 20 eV and 30 eV, and above 70 eV. With the CCC-SCAR results much higher than these experiments for energies between 10 eV and

30 eV, and lower for energies between 50 eV and 70 eV. Compared to the only other theoretical calculation of Singh and Antony [24] we find substantial differences across the energy range.

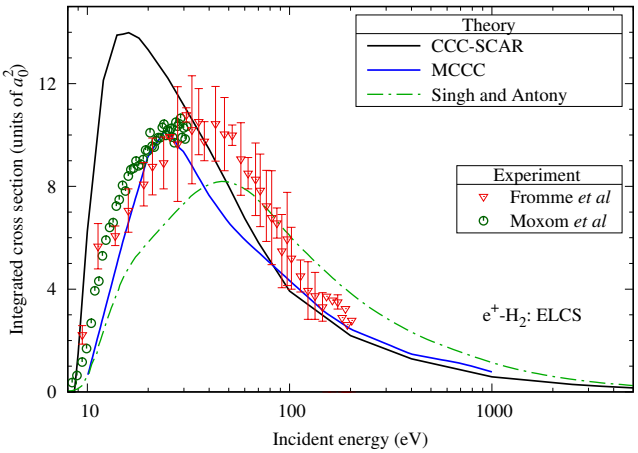

Figure 4.8: Electron-loss cross section for positron scattering on molecular hydrogen. Theoretical CCC-SCAR and MCCC [13] results are shown alongside the calculations of Singh and Antony [24] and the measurements of Fromme *et al.* [26] and Moxom *et al.* [31].

4.4.5 CCC-SCAR error analysis

For the total cross section, we find the largest disagreement between the CCC-SCAR and the MCCC for energies between the positronium-formation threshold and 50 eV. This discrepancy is directly related to the positronium-formation cross section, which the CCC-SCAR finds to be significantly larger than the MCCC calculation. Outside this region, the CCC-SCAR results are within 10% of the MCCC calculations. For energies above 30 eV, the positronium-formation cross section results for the CCC-SCAR are within 20% of the MCCC results to 100 eV, above which this cross section becomes negligible. Below 30 eV, the CCC-SCAR positronium-formation is significantly higher than the MCCC result and existing experiments. The total electronic excitation cross section is within 10-20% of the MCCC results at low and high energies, with larger discrepancies observed at intermediate energies. For the direct ionisation cross section, the CCC-SCAR results are within 20% of the MCCC calculations for high and low energies but much larger at intermediate energies. For the electron-loss cross section, the CCC-SCAR results are within 10% of the

MCCC results for energies above 50 eV.

This approach relies on simple approximations and does not account for vibrational or rotational processes or the different polarisabilities present within molecules. For diatomic non-polar molecules, we expect a similar error of approximately 20% as found here for all H_2 processes besides positronium-formation. For the positronium-formation cross section, we instead expect an error of 20% for energies above 30 eV. Below this energy, we estimate a higher error of 30%, based on the comparison with experiment. For molecules with more atoms or that are polar, we expect that the accuracy of the current approach will also decrease for low and intermediate energies. However, without accurate calculations or experiments for these molecules to compare with we are unable to estimate to what extent the accuracy will decrease.

4.5 Chapter summary

The process for calculating molecular cross sections with the IAM-SCAR approach and CCC cross sections is described. Results are presented for positron scattering from the H_2 molecule and compared against existing single- and two-centre CCC calculations. Good agreement is found for energies above 50 eV with the CCC-SCAR, past CCC results, and experiment. However, the CCC-SCAR approach is found to overestimate the past CCC calculations and experiment for energies between the positronium-formation threshold and 50 eV. Through comparisons between the CCC-SCAR and single- and two-centre calculations the uncertainties of the CCC-SCAR approach are estimated.

Chapter 5

Validation

To demonstrate and validate the accuracy of the developed code, we can directly compare calculations completed with the new code for atomic systems with the results of the frozen-core atomic CCC code (CCC_{FC}). In this chapter, we present the results of positron scattering calculations undertaken with both codes for atomic hydrogen, helium, and neon. For helium, results are provided for positron scattering from the ground state, the metastable 2^3S excited state, and the 2^3P excited state. These calculations allow us to validate scattering from target states of different angular momenta and spin. To distinguish between the two codes the frozen-code CCC code is referred to as CCC_{FC} and the newly developed code as CCC.

5.1 Hydrogen

For atomic H, we compare calculations with $N_l = 30 - \ell$, $\alpha_\ell = 1$, and with maximum target orbital angular momentum of $\ell_{max} = 9$. All 255 generated target states were included and calculations were completed to total angular momentum $J = 20$. These results were calculated for incident energies between 0.1 eV and 1000 eV.

In Table. 5.1 we present the energies of the 10 lowest states for H from the current and frozen-core CCC code. Perfect agreement is found between the two codes for these energies. In Fig. 5.1 we present the close-coupling results for positron scattering from atomic hydrogen for both the current CCC and the frozen-core CCC codes. There is near-perfect agreement between the two calculations. The electron-loss cross section for this system are presented in

Fig. 5.2, with agreement again near-perfect between the current and frozen-core CCC calculations.

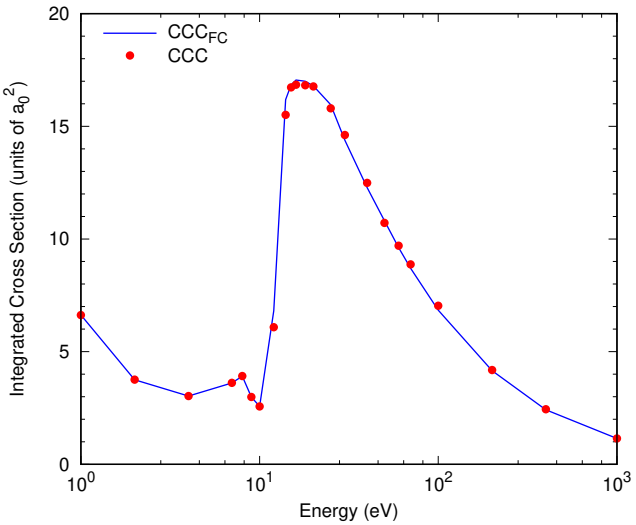

Figure 5.1: Positron-hydrogen total cross section close-coupling results from the frozen-core CCC code (CCC_{FC}) and the current CCC code.

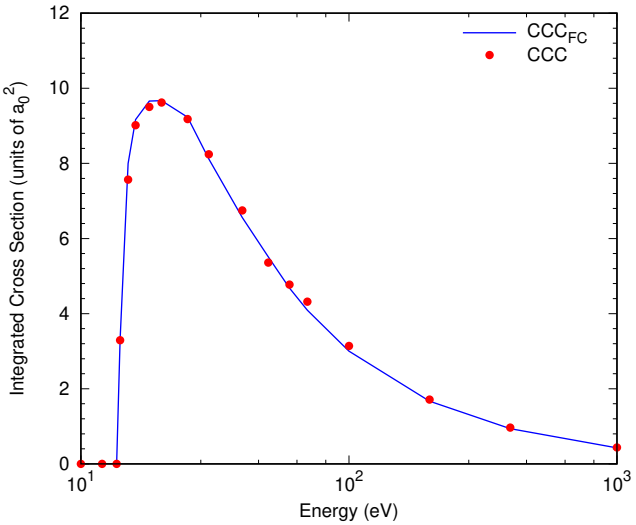

Figure 5.2: Positron-hydrogen electron-loss cross section close-coupling results from the frozen-core CCC code (CCC_{FC}) and the current CCC code.

Table 5.1: Energy of 10 lowest states for H.

State	CCC	CCC_{FC}
1^1S	-13.606	-13.606
1^1P	-3.401	-3.401
2^2S	-3.401	-3.401
1^1D	-1.512	-1.512
2^1P	-1.512	-1.512
3^1S	-1.512	-1.512
1^1F	-0.850	-0.850
2^1D	-0.850	-0.850
3^1P	-0.850	-0.850
4^1S	-0.850	-0.850

5.2 Helium ground state

This calculation was a 189 state calculation with $N_l = 25 - \ell$ and with maximum target orbital angular momentum of $\ell_{max} = 8$. The values of α_ℓ was 1.5 for each ℓ-value and results included partial waves up to $J = 10$. Configurations included the ground state $1s^2$ and the $1sn\ell$ continuum. Results were calculated over a wide energy range from 0.01 eV to 500 eV.

The structure model generated by each code can be directly compared through the energy levels produced. The 10 lowest energy levels are presented in Table. 5.2 for both codes. Results are in near-perfect agreement for all values with only minor differences of the order of 10^{-3} present.

Another comparison can be made between the length and velocity oscillator strengths for each calculation, with results for various transitions shown in Table. 5.3. Near-perfect agreement is again found between the results of both codes with only minor differences of 1×10^{-3} present.

Table 5.2: Energy of 10 lowest singlet states for He.

State	CCC	CCC_{FC}
1^1S	-23.741	-23.742
2^1S	-3.903	-3.904
2^1P	-3.332	-3.332
3^1S	-1.648	-1.648
3^1D	-1.511	-1.511
3^1P	-1.489	-1.489
4^1S	-0.862	-0.862
4^1F	-0.840	-0.840
4^1D	-0.819	-0.819
5^1P	-0.784	-0.784

Table 5.3: Oscillator strength length and velocity forms for He.

Transition	CCC len.	CCC_{FC} len.	CCC vel.	CCC_{FC} vel.
2^1P - 1^1S	0.282	0.282	0.255	0.256
3^1P - 1^1S	0.076	0.076	0.068	0.068
4^1P - 1^1S	0.044	0.044	0.039	0.039
2^1P - 2^1S	0.371	0.370	0.363	0.362
3^1P - 2^1S	0.157	0.158	0.158	0.159
4^1P - 2^1S	0.070	0.070	0.071	0.071
1^1S - 2^1P	0.094	0.094	0.085	0.085

Table 5.3: Oscillator strength length and velocity forms for He.

Transition	CCC len.	CCC_{FC} len.	CCC vel.	CCC_{FC} vel.
2^1S - 2^1P	0.124	0.123	0.121	0.121
3^1S - 2^1P	0.047	0.047	0.047	0.047
3^1D - 2^1P	0.725	0.724	0.726	0.725

The cross section results of the analytical Born approximation for both calculations are shown in Figs. 5.3 and 5.4 for the total and total ionisation cross section, respectively. The results from both codes for these cross sections are indistinguishable.

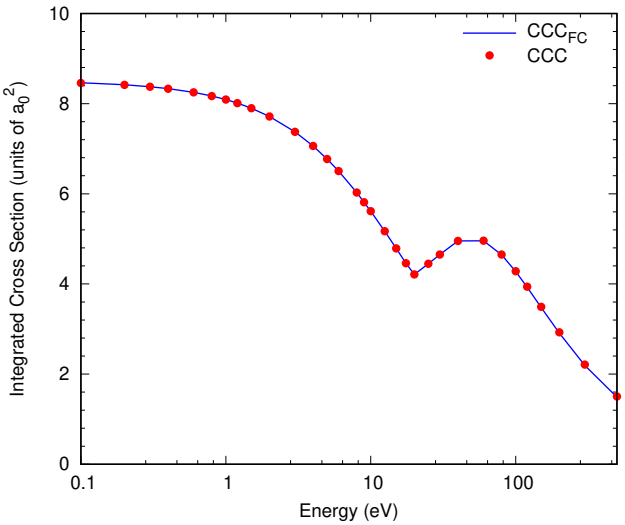

Figure 5.3: Analytical Born total cross sections for positron scattering on helium generated with the frozen-core CCC code (CCC_{FC}) and the current CCC code.

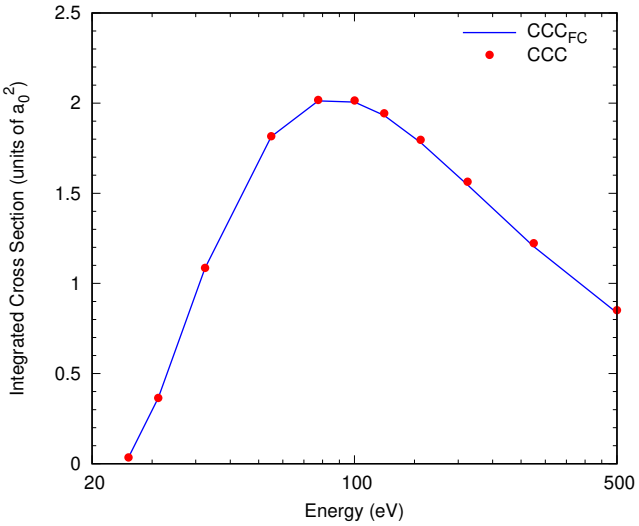

Figure 5.4: Analytical Born total ionisation cross sections for positron scattering on helium generated with the frozen-core CCC code (CCC_{FC}) and the current CCC code.

Next we can compare close-coupling results for each calculation. The total cross section for each calculation is shown in Fig. 5.5 and the electron-loss cross section in Fig. 5.6.

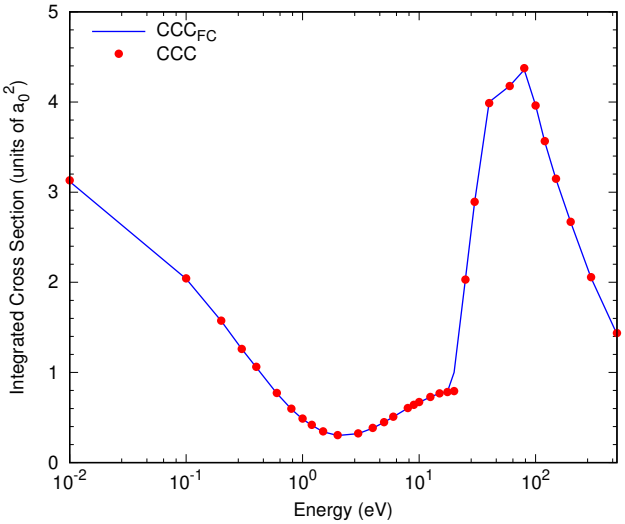

Figure 5.5: The total cross section close-coupling results for positron scattering from the singlet ground state. Results are from the frozen-core CCC code (CCC_{FC}) and the current CCC code.

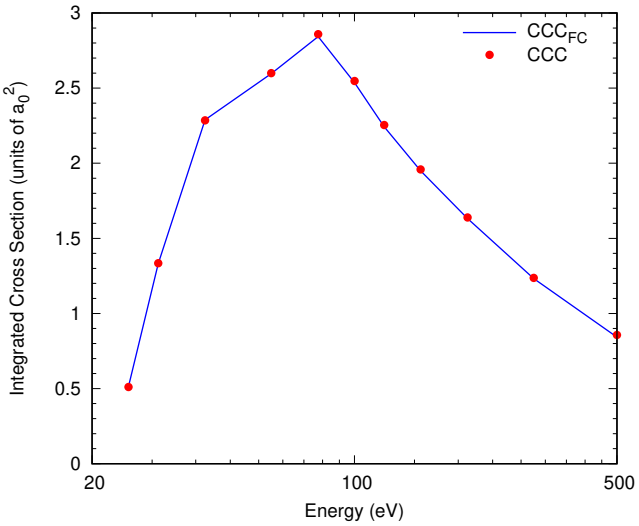

Figure 5.6: The electron-loss section close-coupling results for positron scattering from the helium ground state. Results are from the frozen-core CCC code (CCC_{FC}) and the current CCC code.

5.3 Triplet excited states of helium

For scattering of a positron from the metastable 2^3S excited state of helium the current 161-state calculation has $N_\ell = 14 - \ell$, α_ℓ=1.5, and ℓ_{max}=8.0. These calculations were conducted up to $J = 20$. In Table. 5.4 we compare the excitation energies of the current code with previous CCC calculations [257]. For the first five states perfect agreement is found between both codes. For the next three states, however, the current results are slightly higher but are in closer agreement with the experimental values.

In Fig. 5.7 the total cross section for positron scattering on the 2^3S state of helium is shown for energies between 5 eV and 50 eV. The current CCC results are indistinguishable from the frozen-core single-centre calculation. The single-centre results are in agreement with the two-centre results for energies above 15 eV. In Fig. 5.8 the elastic and $2^3S \rightarrow 2^3P$ excitation cross section are shown. As before, results from the current code are indistinguishable from that of the CCC_{FC} code.

Table 5.4: Energy of 8 lowest triplet states for He.

State	CCC	CCC_{FC}	Exp. [59]
2^3S	-4.742	-4.742	-4.767
2^3P	-3.573	-3.573	-3.622
3^3S	-1.864	-1.864	-1.868
3^3P	-1.566	-1.566	-1.580
3^3D	-1.512	-1.512	-1.513
4^3S	-0.968	-0.944	-0.993
4^3P	-0.830	-0.792	-0.879
4^3D	-0.819	-0.791	-0.851

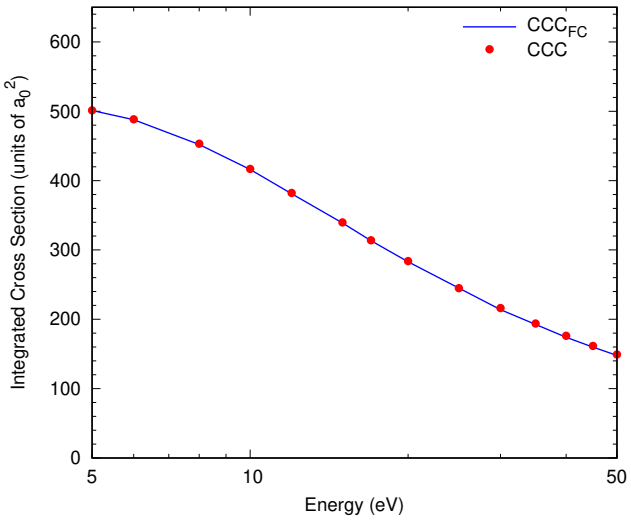

Figure 5.7: Total cross section for positron scattering from the metastable 2^3S excited state of helium. Results are shown for the frozen-core CCC code (CCC_{FC}) and the current CCC code.

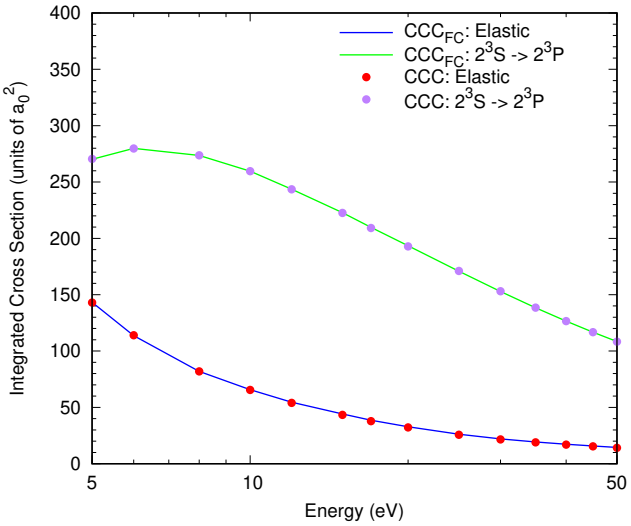

Figure 5.8: Elastic and $2^3S \rightarrow 2^3P$ excitation cross section for positron scattering from the metastable 2^3S excited state of helium. Results are shown for the frozen-core CCC code (CCC_{FC}) and the current CCC code.

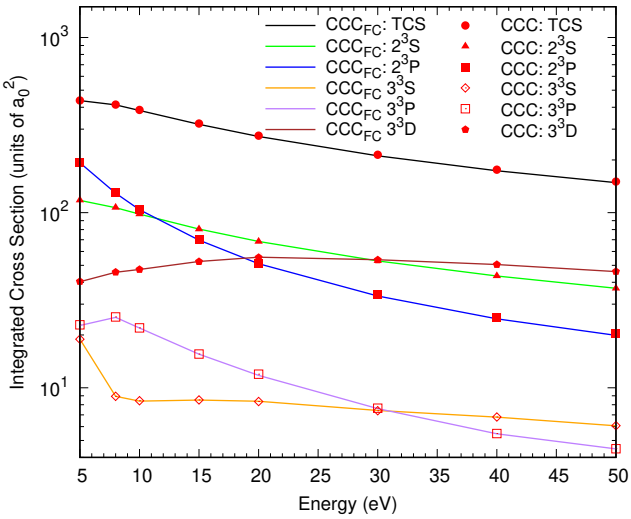

Figure 5.9: Total, elastic, and excitation cross sections for positron scattering from the 2^3P state of helium. Results are shown for the frozen-core CCC code (CCC_{FC}) and the current CCC code. The final state of each transition is shown in the key.

In Fig. 5.9 cross sections of the total, elastic, and the first five excitations for positron scattering from the 2^3P state of helium are presented. These results were calculated with the same model used for the 2^3S calculation

The results of the current code are in agreement with the frozen-core code for all presented transitions.

5.4 Neon

Neon calculations were completed in a basis of $N_\ell = 16 - l$ with $\ell_{max} = 8$ and $\alpha_\ell = 2.0$ with calculations completed with partial waves up to $J = 5$ for energies between 0.01 eV to 8 eV. This structure model contained the ground configuration $2s2p^6$ alongside the $2s2p^5n\ell$ continuum, which generated a total of 227 target states.

The ten lowest energies produced by the structure model are shown in Table. 5.5 where differences between each code are under 0.02 eV for each energy. The close-coupling total cross section calculated with the current and frozen-core CCC codes are shown in Fig. 5.10 for energies between 10^{-5} eV and 60 eV. There is excellent agreement between these two calculations for this result across the energy range.

Table 5.5: Energy of 10 lowest singlet states for Ne

State	CCC	CCC_{FC}
$1\ ^1S$	-20.573	-20.550
$1\ ^1P$	-4.579	-4.566
$1\ ^1D$	-2.892	-2.876
$1\ ^1P^o$	-2.847	-2.831
$2\ ^1S$	-2.545	-2.529
$2\ ^1P$	-1.632	-1.617
$3\ ^1P$	-1.349	-1.333
$1\ ^1F$	-1.345	-1.329
$1\ ^1D^o$	-1.320	-1.304
$2\ ^1D$	-0.844	-0.828

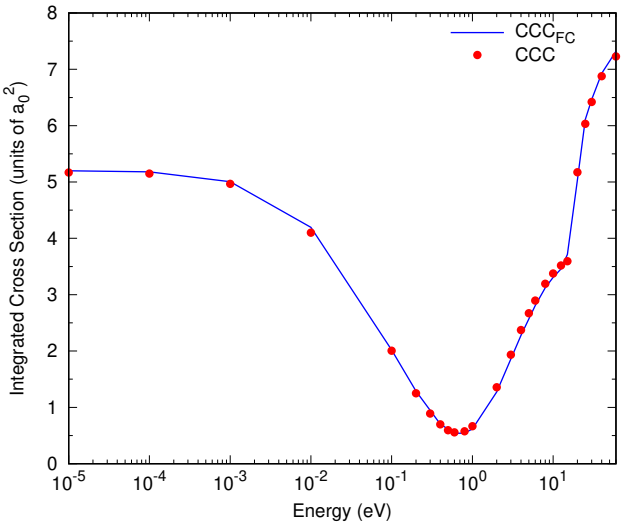

Figure 5.10: Positron-neon total cross section close-coupling results from the frozen-core CCC code (CCC_{FC}) and the current CCC code.

5.5 Chapter summary

This chapter presents calculations for positron scattering from atomic hydrogen and helium completed with the current CCC code and the established frozen-core atomic CCC code. Comparing results between both codes finds negligible differences for the presented cross sections, excited energy states, and oscillator strengths of hydrogen and the singlet states of helium. For scattering from the 2^3S and 2^3P excited states of helium, perfect agreement is found between the current and frozen-core codes. For neon, near-perfect agreement is found between the two codes for the total cross section. The agreement observed for each system with the frozen-core CCC code verifies the veracity of the results calculated throughout this thesis.

Chapter 6

Positron scattering from carbon

This chapter presents the single-centre CCC and CCC-scaled complex model potentials calculations for positron scattering from atomic carbon. First, the calculation details are provided, followed by the results for the total elastic, momentum-transfer, excitation, direct ionisation, electron-loss, total inelastic, positronium-formation, stopping power, and total cross sections from threshold to 5000 eV. We also present oscillator strengths, the scattering length, the hidden Ramsauer-Townsend minimum, the energy of the positron-carbon virtual level, and the mean excitation energy. Some sections in this chapter text or figures are adapted from a published work by the candidate [1]. The publisher of this article (the American Physical Society) provides the right to use an article or a portion of an article in a thesis or dissertation without requesting permission.

6.1 Calculation details

To begin, we utilise MCHF calculations for the carbon ion (C^+) to obtain orbitals ranging from 1s to 5s that were optimised for the $2P^o$ ground state of this ion. All other orbitals are obtained via the Laguerre basis given in Eq. 2.6 with $N_\ell = 18-\ell$, $\ell_{\max} = 8$, and $\alpha_\ell = 1.0$. The present close-coupling expansion includes the states of carbon derived from the configuration sets detailed here. The $2s^2 2pn\ell$ configurations were included for all orbitals up to $n = 18 - \ell$ with $\ell_{\max} = 8$. To account for the inner-core correlation, a

set of different configurations had to be included in the structure model. These included $2s2pn\ell n'\ell'$ and $2s2pn\ell^2$ configurations, where $n\ell$ and $n'\ell'$ were all possible combinations of the $n = 3$, $n = 4$, and $5s$ orbitals. Also included were $2p^3n\ell$ configurations for $n = 18 - \ell$ with $\ell \leq 2$. The first of these configurations has strong coupling with the states derived from $2s^22p^2$ [290]. Additionally we included $2sn\ell^3$ configurations for $n\ell \leq 3d$. The $2p^4$ configuration was also included due to its strong mixing with the $1s2s^22p^2$ configuration [290]. Furthermore, the $2s^2n\ell^2$ configurations for $n\ell$ between $3s$ and $4f$ were also included.To keep calculations at a reasonable size the $2s2p^2n\ell$ configurations were included only for $n = 18-\ell$ with $\ell \leq 4$. These configurations are important as all states derived from them are autoionising [369], so their inclusion is necessary for a complete description of ionisation.

We included the first 943 out of 1797 target states generated using this basis in the close-coupling expansion, corresponding to those with excitation energies up to 40 eV above the ionisation energy. Calculations were conducted for partial waves up to $J = 10$ for energies up to 5000 eV. A smaller close-coupling model was utilised to calculate elastic DCS for energies above 500 eV, as a large number of partial waves, even with the analytic Born completion technique, was required to obtain convergence in the DCS. This model was similar to the 943-state model but with the $2s2p^2n\ell$ configurations limited to $n\ell \leq 5s$. Excitations were included only up to 25 eV above the ionisation threshold, which generated a total of 379 states. Integrated elastic cross sections for this model and the 943-state model were converged within 2% for 500 eV and within 0.5% for energies above 1000 eV.

To obtain converged results for ionisation, a 4571-state Born model with $\ell_{\max} = 8$ and a maximum n of 25 was also used. This model had a similar configuration structure as the previous model but with $2p^3n\ell$ states for $n = 25 - \ell$ with $\ell \leq 6$ and with a $2s2p^2n\ell$ continuum with $\ell_{\max} = 8$. Furthermore, all generated states were used, which included states with excitation energies up to 2057 eV above the ionisation threshold. Using this model, we can approximate the contribution to the ionisation cross section from states which were not included in the CCC calculation. Further details are given in Sec. 6.4.4, where the extrapolation of the electron-loss cross section is presented. This extrapolation is also present within the

direct ionisation and total cross sections as they are calculated from the extrapolated electron-loss result.

6.2 Structure

Excitation energies for C target states are presented in Table 6.1 for the 943-state CCC model and compared with the theoretical results of Wang *et al.* [42], Stancalie [314], Dunseath *et al.* [43] and NIST [59]. Differences between our calculated energies and NIST results range from 0.009 eV to 0.612 eV, with the difference generally increasing with increasing energy. The ionisation limit from our structure model was within 0.04 eV of the NIST value. For the higher energy states, our results are typically in between the calculations of Dunseath *et al.* [43] and other calculations.

Absorption oscillator strengths calculated in the 943-state CCC model are presented in Table 6.2 for 3 different lower-level states alongside the theoretical results of Wang *et al.* [42], Stancalie [314], Dunseath *et al.* [43] and NIST [59]. We find generally close agreement between our results and the results of Wang *et al.* [42] and NIST [59], however some notable disagreements are present for the $2s^2 2p 3d\ ^1F^o$, $2s^2 2p 3d\ ^3D^o$ and $2s^2 2p 3d\ ^1P^o$ states where our calculations overestimate other results. The overestimation of these results is likely directly related to the limiting of the CI expansions in the current structure model due to the large angular momentum required to achieve convergence for positron scattering.

The convergence of the energy levels and oscillator strengths has been established by comparison between the 4571- and 943-state models. Differences between models were found to be under 1%. The dipole polarisability (α_{D}) of the 943-state model is 11.61 a_0^3, which is in close agreement with the 11.67 a_0^3 result of Das and Thakkar [370] and within 3% of the currently recommended value of 11.3 a_0^3 [371]. For C, it is expected that only α_D will be relevant, however, for completeness we have calculated values for higher polarisabilities. The quadrupole polarisability of our 943-state model was 54.5 a_0^5 and the octuplet polarisability was 678.00 a_0^7. This α_Q is 18 % lower than the CEPA-NO value of 64.2 a_0^5 Reinsch and Meyer [372], but is close to the coupled HF result of 55.2 a_0^5 Reinsch and Meyer [372]. There are no other octupole polarisability calculations for C within the literature.

Table 6.1: Excitation energies (eV) for C target states from the ground state, and the ionisation limit.

	State	Term	CCC	Ref. [42]	Ref. [314]	Ref. [43]	NIST [59]
1	$2s^2 2p^2$	^3P	0.000	0.000	0.000	0.000	0.000
2	$2s^2 2p^2$	^1D	1.372	1.302	1.557	1.545	1.260
3	$2s^2 2p^2$	^1S	2.748	2.629	2.602	2.545	2.680
4	$2s2p^3$	$^5S^o$	3.940	3.963	3.092	3.133	4.179
5	$2s^2 2p3s$	$^3P^o$	7.617	7.527	7.401	8.488	7.481
6	$2s^2 2p3s$	$^1P^o$	7.818	7.750	7.740	8.936	7.680
7	$2s2p^3$	$^3D^o$	7.951	8.004	8.340	8.412	7.942
8	$2s^2 2p3p$	^1P	8.897	8.534	8.451	9.456	8.534
9	$2s^2 2p3p$	^3D	9.032	8.649	8.600	9.589	8.642
10	$2s^2 2p3p$	^3S	9.188	8.775	8.772	9.785	8.767
11	$2s^2 2p3p$	^3P	9.332	8.857	9.309	10.390	8.845
12	$2s2p^3$	$^3P^o$	9.481	9.379	9.517	9.981	9.326
13	$2s^2 2p3p$	^1D	9.553	9.014	9.443	10.757	8.998
14	$2s^2 2p3p$	^1S	9.766	9.172	10.424	11.370	9.168
15	$2s^2 2p3d$	$^1D^o$	10.166	9.614	9.772	10.719	9.627
16	$2s^2 2p4s$	$^3P^o$	10.258	9.673	10.142	10.810	9.683
17	$2s^2 2p3d$	$^3F^o$	10.271	9.687	9.517	10.809	9.695
18	$2s^2 2p3d$	$^3D^o$	10.288	9.705	9.607	10.888	9.705
19	$2s^2 2p4s$	$^1P^o$	10.301	9.685	9.549	10.834	9.709
20	$2s^2 2p3d$	$^1F^o$	10.333	9.716	9.607	10.947	9.732

Table 6.1: Excitation energies (eV) for C target states from the ground state, and the ionisation limit.

	State	Term	CCC	Ref. [42]	Ref. [314]	Ref. [43]	NIST [59]
21	$2s^2 2p 3d$	$^1P^o$	10.370	9.748	9.653	10.970	9.758
22	$2s^2 2p 3d$	$^3P^o$	10.404	9.840	13.407	11.018	9.830
Ion.	Limit		11.234				11.268
23	$2s 2p^3$	$^1D^o$	13.600	12.968	14.470	14.645	
24	$2s 2p^3$	$^3S^o$	13.279	13.073	13.407	15.366	13.117
25	$2s 2p^3$	$^1P^o$	15.883	15.401	15.927	16.182	

Table 6.2: Oscillator strengths for C.

Lower level	Upper level	CCC	Ref. [42]	Ref. [314]	Ref. [43]	NIST [59]
$2s^2 2p^2\ ^3P$	$2s^2 2p 3s\ ^3P^o$	0.146	0.143	0.124	0.154	0.140
	$2s 2p^3\ ^3D^o$	0.076	0.073	0.098	0.152	0.072
	$2s 2p^3\ ^3P^o$	0.078	0.056	0.028	0.117	0.063
	$2s^2 2p 4s\ ^3P^o$	0.037	0.027	0.023	0.010	0.021
	$2s^2 2p 3d\ ^3D^o$	0.144	0.096	0.112	0.132	0.094
	$2s^2 2p 3d\ ^3P^o$	0.037	0.037	0.340	0.069	0.040
	$2s 2p^3\ ^3S^o$	0.143	0.156	0.171	0.269	0.152
$2s^2 2p^2\ ^1D$	$2s^2 2p 3s\ ^1P^o$	0.118	0.103	0.128	0.103	0.118
	$2s^2 2p 3d\ ^1D^o$	0.017	0.012	0.009	0.007	0.013
	$2s^2 2p 4s\ ^1P^o$	0.015	0.007	0.004	0.010	0.011
	$2s^2 2p 3d\ ^1F^o$	0.123	0.080	0.061	0.099	0.085

Table 6.2: Oscillator strengths for C.

Lower level	Upper level	CCC	Ref. [42]	Ref. [314]	Ref. [43]	NIST [59]
	$2s^2 2p3d\ ^1P^o$	0.011	0.011	0.018	0.014	0.009
	$2s2p^3\ ^1D^o$	0.256	0.224	0.344	0.529	
	$2s2p^3\ ^1P^o$	0.151	0.155	0.351	0.333	
$2s^2 2p^2\ ^1S$	$2s^2 2p3s\ ^1P^o$	0.088	0.090	0.021	0.0076	0.094
	$2s^2 2p4s\ ^1P^o$	0.008	0.011	0.007	0.001	0.005
	$2s^2 2p3d\ ^1P^o$	0.170	0.116	0.050	0.142	0.125
	$2s2p^3\ ^1P^o$	0.148	0.124	0.122	0.633	

6.3 Convergence study

The TCS was found to be converged for energies less than 5 eV and above 18 eV for $\ell_{\max} \geq 6$, while the ELCS is converged for energies higher than 20 eV for $\ell_{\max} \geq 6$. Convergence studies for the ELCS are presented in Fig. 6.1 for the 575-state $\ell_{\max} = 2$, 834-state $\ell_{\max} = 4$, 901-state $\ell_{\max} = 6$ and 943-state $\ell_{\max} = 8$ calculations. The large differences for energies below 20 eV are representative of positronium-formation as high $\ell_{\max}$ values are necessary to accurately model positronium-formation channels in the single-centre approach.

6.4 Scattering

6.4.1 Total cross sections

The present results for the TCS are compared with the calculations of Singh *et al.* [33] and Reid and Wadehra [32] in Fig. 6.2. Due to the mismatched boundary conditions with channels corresponding to positive-energy pseudostates being closed while positronium-formation channels are open, accurate cross-sections between the positronium-formation and ionisation thresholds cannot be calculated with the single-centre approach. To address this,

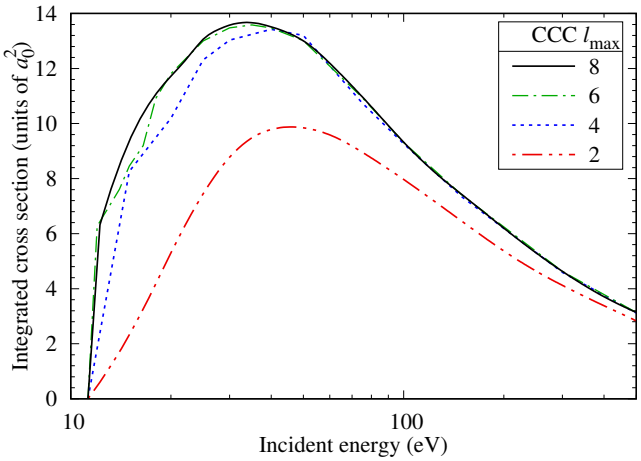

Figure 6.1: CCC convergence study for electron-loss cross section.

we have utilised our CCC-scaled complex optical potential model to calculate the total cross section between the positronium-formation threshold and 20 eV. In this model, the direct inelastic component was scaled by a factor of 1.1 and the positronium-formation by a factor of 2.91 to yield agreement with the CCC total cross section. We present this in the figure as CCC-pot, with results for all other energies in this model obtained from our single-centre calculation. Following analysis of previous single- and two-centre calculations, the single-centre approach is believed to be sufficiently accurate for energies approximately 10 eV above the ionisation threshold, which is why single-centre CCC results are used for energies greater than 20 eV. Below the positronium-formation threshold, we also use the single-centre CCC results as at these energies this approach gives practically exact results (as soon as convergence is established). We have also included in this figure the CCC results to demonstrate the difference between the ionisation threshold and 20 eV. The CCC-pot cross section is larger for this energy range as it includes positronium-formation, which cannot be adequately accounted for by the single-centre model. For energies above 55 eV, the ELCS component of the TCS is scaled according to the procedure detailed in section 6.4.4. Smooth cubic spline fitting has been applied for current results in all figures, except those presenting differential cross sections.

Comparing our TCS to those of Singh *et al.* [33], we find good agreement above 70 eV and very close agreement above 800 eV. For energies between 18 and 70 eV, our results are slightly lower than those of Singh *et al.*

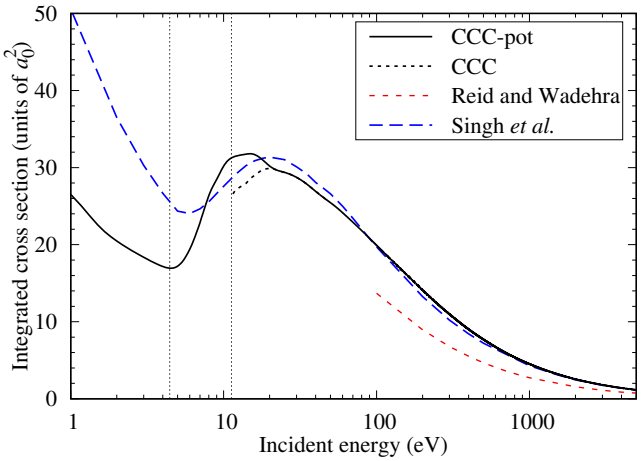

Figure 6.2: Total cross section for positron scattering on carbon. CCC results are presented alongside theoretical results of Reid and Wadehra [32] and Singh *et al.* [33]. For energies between the positronium-formation threshold and 20 eV the CCC-pot results were calculated with the CCC-scaled complex model potential calculation. Below this threshold and above 20 eV the CCC-pot results are the same as the CCC. The vertical lines represent the positronium-formation and ionisation thresholds.

[33], whereas from 7 to 18 eV, they are slightly larger. Below 7 eV, the CCC cross section is significantly lower than these results, most notably below the positronium-formation threshold of 4.46 eV. For this energy range, the only contribution to the TCS is the elastic cross section, and the CCC results are up to a factor of 2 lower than those of Singh *et al.* [33]. As current results are expected to be accurate for these energies, this discrepancy indicates that the potential is too strong in the calculations of Singh *et al.* [33], resulting in a larger absolute value of the scattering length. Another aspect that differentiates the current method and that of Singh *et al.* [33] is that they do not account for virtual positronium-formation. This is an important aspect of positron scattering at energies below the positronium-formation threshold. For example, in positron scattering from helium Gribakin and King [373] found that it accounted for 20% of the total correlation potential and that its inclusion was necessary to produce an accurate elastic cross section at low energies.

The TCS in both methods decreases from 1 eV to the positronium-formation threshold as a result of the decreasing elastic cross section. Above this threshold, as inelastic channels open, cross sections quickly rise to

a maximum. This maximum cross section is predicted by the CCC and Singh *et al.* [33] to occur at approximately 20 eV, whereas the CCC-pot approach predicts the maximum at 15 eV. The model-potential calculations of Reid and Wadehra [32] were only conducted over an energy range of 100 to 5000 eV, and their cross section is lower than both the SCOP method of Singh *et al.* [33] and the single-centre CCC approach.

6.4.2 Electron-loss cross section

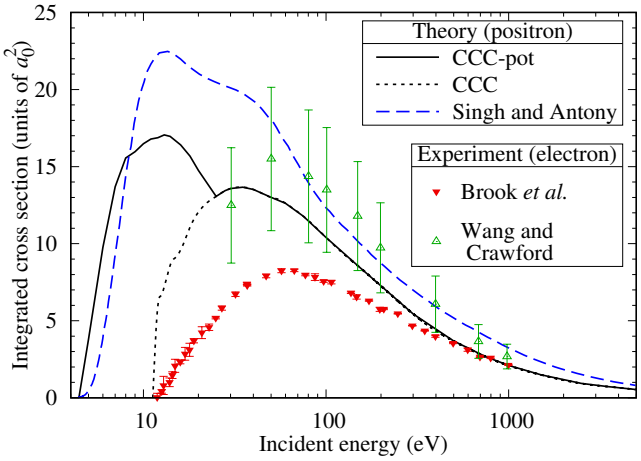

Figure 6.3: Electron-loss cross section of positron scattering on carbon from the positronium-formation threshold to 5000 eV. CCC-pot results are presented alongside CCC results, the theoretical results of Singh and Antony [34] and experimental results for electrons incident on carbon measured by Brook *et al.* [35] and Wang and Crawford [36].

For the electron-loss cross section, which is equal to the sum of direct ionisation and positronium-formation, the current CCC results are compared with the results of Singh and Antony [34] and experimental results for the incident electron case [35, 36] in Fig. 6.3. The CCC results predict a double maximum in the cross section, the first due to positronium-formation and the second due to direct ionisation. Of these, the first maximum has a larger magnitude. The results of Singh and Antony [34] predict a much larger positronium-formation cross section than the direct ionisation, leading to a less-pronounced shoulder due to direct ionisation. The first maximum due to positronium-formation occurs at 10 eV in both our CCC-pot calculation and the results of Singh and Antony [34]. Our method, however, predicts

this maximum cross section to be almost 30% lower than that of Singh and Antony [34]. At high energies, electron and positron results are expected to be equal due to the exchange, Ps-formation, and inter-channel coupling effects becoming negligible. For this scattering system, we see this occurs for ELCS above 500 eV as the CCC results are within the experimental error of both electron experiments above this energy. Although in agreement for high energies, for lower energies large discrepancies exist between the electron results of Brook *et al.* [35] and Wang and Crawford [36]. The uncertainties of these two experiments are, however, significantly different with Wang and Crawford [36] measurements having an uncertainty of 30% whereas the uncertainty of Brook *et al.* [35] decreases with increasing energy, with an uncertainty of 9% at 20 eV decreasing to less than 2% by 1000 eV. The results of Singh and Antony [34] are significantly larger than the CCC-pot results for energies above 7 eV and are in disagreement with the electron experiment results at high energies. Further analysis of the discrepancies at high energies is provided later in our discussion of direct ionisation in section 6.4.3.

As we consider incident energies up to 5000 eV, the ionisation from the inner $1s$ shell becomes possible. We have performed Born calculations to determine the impact of ionisation from this shell, which has an ionisation threshold of approximately 300 eV. This calculation included $1s^1 2s^2 2p^2 n\ell$ configurations for $n \leq 25$ and $\ell \leq 8$ into our 4571-state Born model, which raised the total number of states to 6380. Comparing the TICS between this 6380-state and the 4571-state model, we found that the difference in TICS was within 1% from 300 eV to 5000 eV. Distorted-wave calculations for electron-impact ionisation by Jonauskas [374] have also reported ionisation from the $1s$ orbital to be insignificant. Hence, errors in our TICS from excluding ionisation from this orbital are expected to be negligible for the considered energy range.

6.4.3 Positronium-formation and direct ionisation cross sections

Presented in Fig. 6.4 is the positronium-formation cross section calculated with our CCC scaled complex model potential approach alongside the calculations of Singh and Antony [34]. We find that the results of Singh and Antony [34] are significantly larger than the present calculation. Although

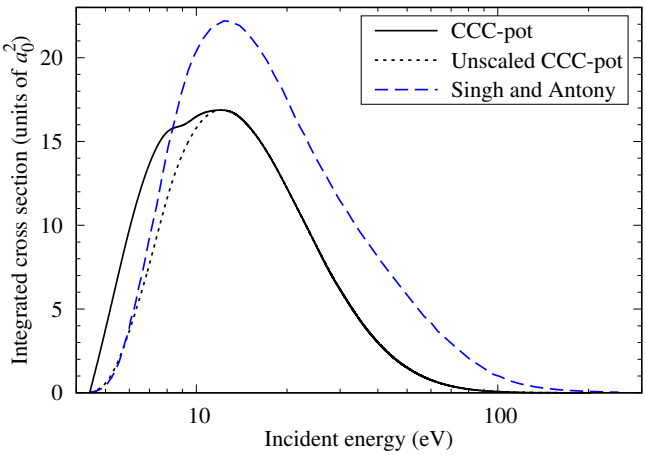

Figure 6.4: Positronium-formation cross section for a positron incident upon carbon. CCC-pot results are presented alongside theoretical results of Singh and Antony [34].

their results are also from a complex model potential calculation, we are able to fit our results to accurate single-centre calculations. For energies below 33 eV, we expect errors of within 20% for the positronium-formation cross section for the unscaled calculation, while for energies above this, we expect increasing errors with increasing energy. As σ_{Ps} rapidly decreases for higher energies, the impact of these larger errors will be minimal. For the scaled calculation the error for energies under the maximum cross section is expected to be within 10%. For energies towards threshold there is good agreement between our unscaled calculation and the results of Singh and Antony [34].

We present in Fig. 6.5 our current results for direct ionisation alongside the theoretical results of Singh and Antony [34] and the measurements for the incident electron case from Brook *et al.* [35] and Wang and Crawford [36]. For direct ionisation, the CCC-pot results are lower than those of Singh and Antony [34] above 20 eV, while good agreement is found below 20 eV down to the ionisation threshold. Both calculations predict a cross-section peak at 60 eV. For energies above approximately 150 eV, direct ionisation is by far the dominant component of the ELCS; hence, the same observations at high energy can be made here as for ELCS. The disagreement between the electron experiments of Brook *et al.* [35] with the results of Singh and Antony [34] at high energies is likely a result of the inaccuracies associated

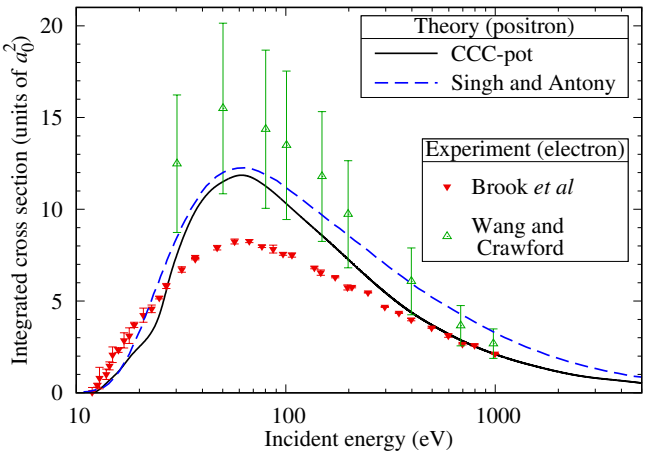

Figure 6.5: Direct ionisation cross section of positron incident upon carbon. Results calculated from our CCC-pot approach are presented alongside the calculation of Singh and Antony [34] and the experimental results for electrons incident on carbon measured by Brook *et al.* [35] and Wang and Crawford [36].

with the CSP-ic method, in which $\sigma_{\rm ion}$ is predicted from $\sigma_{\rm in}$ based on an expectation that $\sigma_{\rm ion}$ will be between 70-80% of $\sigma_{\rm in}$ at its maximum, and 100% for large energies. From our calculations we predict the direct ionisation cross-section to be 66% of $\sigma_{\rm in}$ at the peak at 60 eV, and by 5000 eV we find that ionisation still only comprises 71% of $\sigma_{\rm in}$.

6.4.4 Born extrapolation

Our total and direct ionisation cross section were extrapolated using the 4571-state Born calculation for energies above 55 eV. This was accomplished by multiplying the CCC results by the ratio between the 4571- and 943-state Born TICS. To confirm the validity of the 4571-state Born calculation, we utilised the scaling method developed by Kim [272] to compare TICS results with both electron experiments and BEB calculations [45], as shown in Appendix B. The agreement for scaled Born results with the more accurate experiment of Brook *et al.* [35] and other theory provides direct evidence of the accuracy of our structure model.

In Fig. 6.6, we present the 943- and 4571-state Born calculations utilised for our extrapolation procedure, along with the single-centre 943-state CCC result and the extrapolated cross section. The extrapolation has the great-

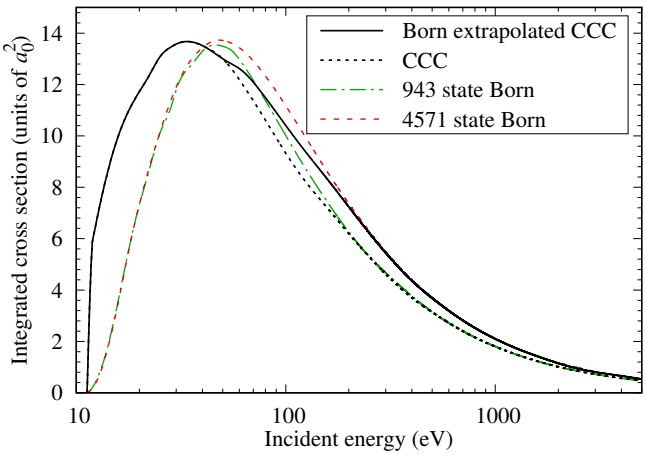

Figure 6.6: 4571- and 943-state plane-wave Born alongside 943-state single-centre CCC and Born extrapolated CCC results for the electron-loss cross section of a positron incident upon carbon.

est effect for energies between 100 and 1000 eV, with the Born and CCC results converged for energies above 300 eV. The 943-state model contains all excitations up to 40 eV above the ionisation threshold. We can see this reflected in the figure, with the 4571- and 943-state models being in near perfect agreement up to 40 eV, in close agreement up to 60 eV, and then above 60 eV, the 4571-state model is noticeably larger. Using the Born extrapolation procedure, we can capture the states which become energetically accessible at incident energies above 52 eV without requiring close-coupling calculations, which would be unfeasible with this number of states.

6.4.5 Inelastic cross section

In Fig. 6.7 we present the inelastic cross section. This result was calculated using the CCC-pot approach, with values above 20 eV obtained from the single-centre CCC calculation and values below 20 eV calculated with the CCC-scaled complex model potential technique. Also included in this figure are the total excitation, direct ionisation, and positronium-formation cross sections, which make up the total inelastic cross section. To reiterate, the positronium-formation results are obtained directly from the CCC-scaled complex model potential calculation. The direct ionisation result is obtained from subtracting these results from the ELCS, and using the CSP-ic method below 20 eV. As with the inelastic result, the total bound excita-

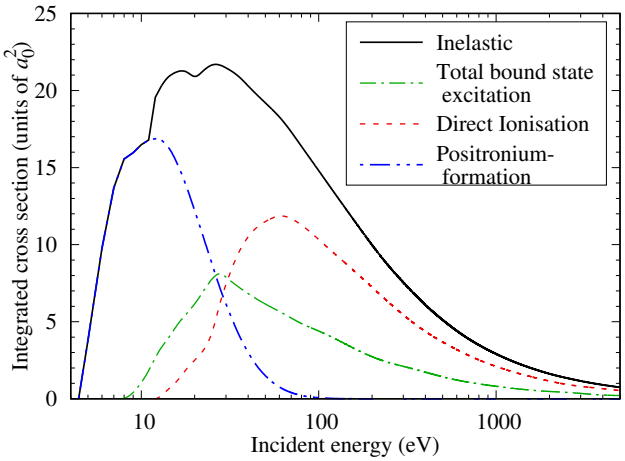

Figure 6.7: The inelastic cross section and its components calculated through the combination of our single-centre CCC and CCC-scaled complex model potential. Exact details are provided in the text. Results are presented from the positronium-formation threshold to 5000 eV.

tion is obtained below 20 eV with the CCC-scaled complex model potential and above from the single-centre CCC calculation. The dominant inelastic process is positronium-formation for energies under 25 eV, excitation from 25 eV to 31 eV, and direct ionisation for energies above 31 eV. There are no previous measurements or calculations to which the total inelastic cross section can be compared.

6.4.6 Frozen core model

In this section, we investigate the importance of including non-frozen-core configurations in the structure calculations by comparing the present CCC calculations with CCC calculations utilising a frozen-core model. In Fig. 6.8 we compare the 943-state CCC TCS and ELCS with results obtained from a frozen-core 248-state CCC model which contains only the $2s^2 2pn\ell$ configuration continuum, with $n = 18 - \ell$ and $\ell_{\max} = 8$. As previously mentioned, the single-centre method is unstable between the positronium-formation and ionisation thresholds due to mismatched boundary conditions. Therefore, results are not presented for this energy region in this figure. Between the ionisation threshold and 14 eV, the frozen-core TCS sharply decreases, whereas the 943-state cross section softly increases. These differences are likely a result of the frozen-core approach not being stable at energies so close

to the ionisation threshold. Above 14 eV, the frozen-core model underestimates the TCS by up to 25%. The same is true for the ELCS results above 20 eV. However, below this, the frozen-core model predicts a higher ELCS cross section with a sharper peak. The differences below the positronium-formation energy between the two models can largely be ascribed to the insufficient number of available states in the frozen core model resulting in a dipole polarisability value of 9.44 a_0^3, which is 23% lower than in the 943-state model.

Another significant discrepancy between these two models is that the frozen-core approach predicts an ionisation threshold at 10.5 eV, which is almost 10% lower than our 943-state calculation. This discrepancy also extends to excitation energies, with the first excitation having a difference of 10% in its threshold; for each subsequent excitation, this difference consistently increases. From these observations, it is clear that the frozen-core structure model is insufficient for this system, and non-frozen-core configurations are necessary to obtain accurate results, particularly below the positronium-formation energy.

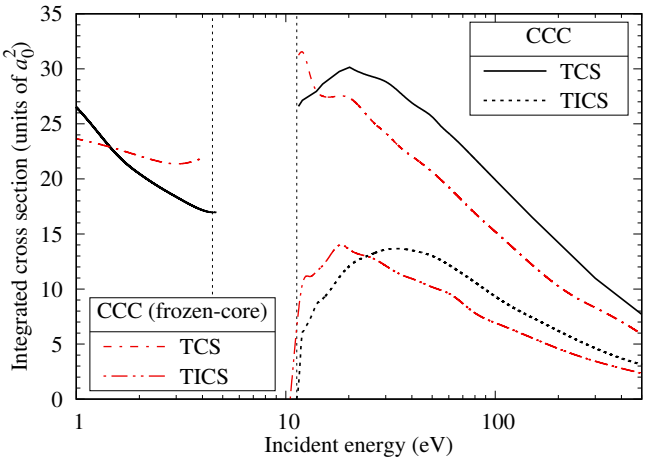

Figure 6.8: Comparison of total cross section and electron-loss cross section between 248-state frozen-core CCC model and 943-state CCC model. Results are presented from 1 to 500 eV.

6.4.7 Elastic cross section

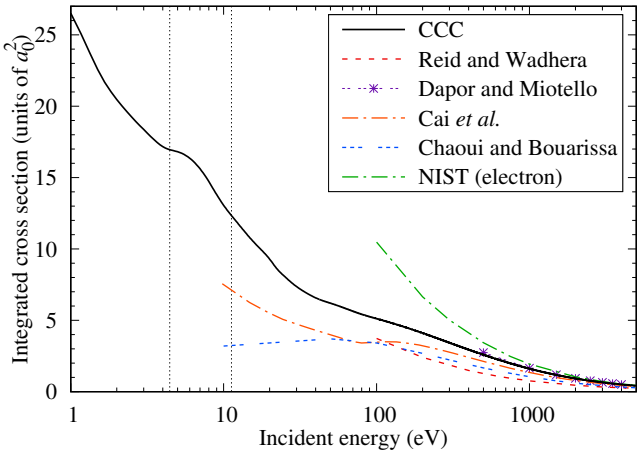

Figure 6.9: Elastic scattering cross section results for a positron scattering on carbon. CCC results are compared with the theoretical results of Reid and Wadehera [32], Dapor and Miotello [37], Cai *et al.* [38], and Chaoui and Bouarissa [39]. Also shown are the NIST elastic cross section results for the electron case [40]. The vertical lines represent the positronium-formation and ionisation thresholds, note that between these thresholds the single-centre calculation does not yield convergent results.

In Fig. 6.9, the single-centre CCC elastic cross section is compared with the calculations of Reid and Wadehra [32], Dapor and Miotello [37], Cai *et al.* [38], Chaoui and Bouarissa [39], and results obtained for the electron case from the NIST electron elastic-scattering cross-section database [40]. For energies below the positronium-formation and above the ionisation threshold, the single-centre CCC will converge to the true result; however, the calculation is unstable between these energies. To address these instabilities in the $\ell_{\max} = 8$ calculation, the CCC results between 6 eV and 11.26 eV are taken from an $\ell_{\max} = 4$ calculation. As the single-centre calculation cannot yield converged results for this energy range, the structure present within this range is likely a result of these instabilities and not a physical occurrence. Differences between the CCC calculation and those of Reid and Wadehra [32] are similar to those in the total cross section, with their results underestimating CCC over their entire energy range. The results of Cai *et al.* [38] agree with CCC above 2000 eV but are significantly lower for energies below this. This calculation also predicts a dip in the cross section at 80 eV, which is not seen in the CCC calculation. The calculations of

Chaoui and Bouarissa [39] are between the calculations of Cai *et al.* [38] and Reid and Wadehra [32] for energies above 150 eV, while below this energy they predict a lower cross section than CCC and Cai *et al.* [38]. The calculations of Dapor and Miotello [37] are in excellent agreement with the CCC results over their calculated energy range of 500 eV to 4000 eV. The electron results from NIST agree with CCC results above 2000 eV, a much higher energy for electron/positron projectile agreement than in the total ionisation cross section case.

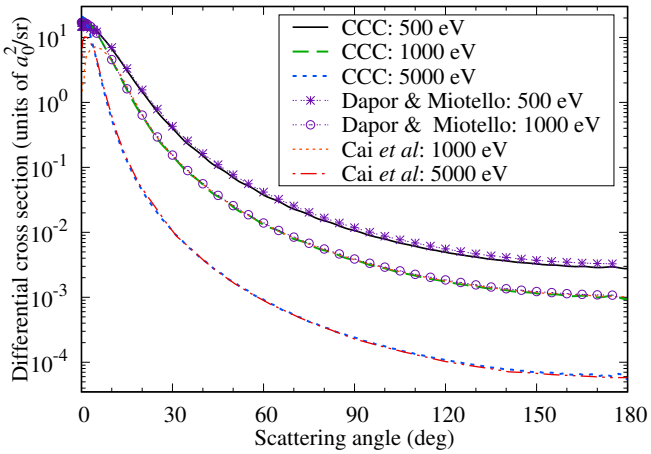

Figure 6.10: Elastic scattering differential cross section results for a positron incident upon carbon at 500, 1000 and 5000 eV. CCC results are presented against the theoretical results of Dapor and Miotello [37] and Cai *et al.* [38].

Differential cross sections for elastic scattering at incident energies of 500, 1000, and 5000 eV are presented in Fig. 6.10, alongside the calculations of Dapor and Miotello [37] and Cai *et al.* [38]. There is good agreement between the two calculations except for angles below 15° for 500 eV and 10° for 1000 eV. In both these cases, Cai *et al.* [38] predicts a decrease in the DCS, whereas the CCC DCS has a maximum value at 0°. The calculations of Dapor and Miotello [37] are also in excellent agreement with the CCC results, and predict the same forwards-scattering behaviour as CCC. The calculations of Cai *et al.* [38] were performed with the ELSEPA [291] code, which performs Dirac partial-wave calculations for scattering systems. The method of Dapor and Miotello [37] also solved the Dirac equation but used a non-relativistic Hartree-Fock potential for the target structure calculations.

In Fig. 6.11, we present a selection of CCC elastic DCS for incident ener-

gies between 0.1 and 5 eV. No previous calculations have been performed for these incident energies. Calculations were completed to ensure convergence in the partial wave expansion, using a technique similar to Green *et al.* [89], which uses analytical properties of the long-range polarisation potential. This allows us to describe the cusp present at low scattering angles for energies ≥ 1 eV. This feature is not present for lower energies as p-wave scattering is dominant for the triplet ground state of C.

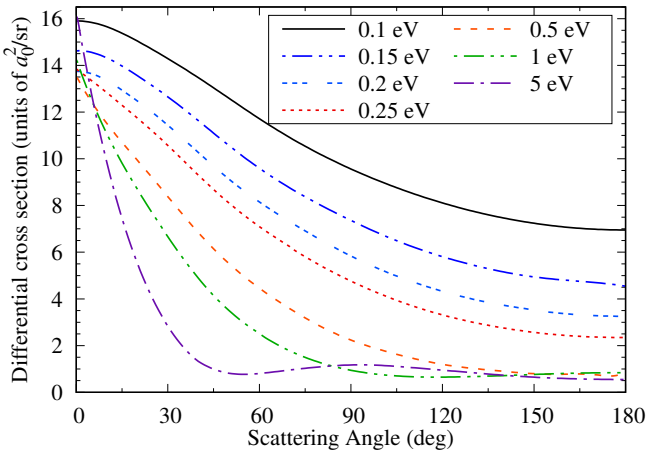

Figure 6.11: CCC elastic scattering differential cross section results for a positron incident upon carbon at 0.1, 0.2, 0.25, 0.5, 1 and 5 eV.

6.4.8 Momentum-transfer cross section

A useful quantity for Monte Carlo and other simulations is the MTCS, which measures the average momentum-transferred between the positron and C atom during the elastic scattering process. As with the elastic cross section, the CCC results between 6 eV and 11.26 eV are taken from an $\ell_{\max} = 4$ calculation. We present the results of our calculation alongside those of Dapor and Miotello [37] and Cai [41] in Fig. 6.12. We find excellent agreement between all calculations above 500 eV. Of the other theoretical methods, only Cai [41] performed calculations below 500 eV, and their calculation is slightly higher than CCC down to 30 eV, below which CCC predicts an increase in this cross section. An analysis of the low energy behaviour of this cross section is provided later.

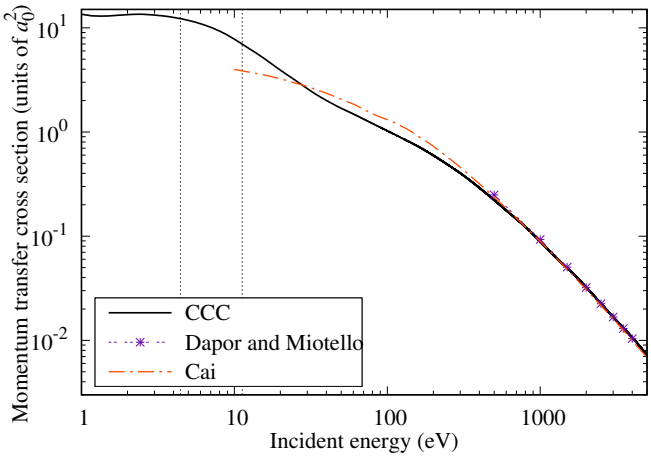

Figure 6.12: Momentum-transfer cross section results for a positron incident upon carbon. CCC results are presented against the theoretical results of Dapor and Miotello [37] and Cai [41]. The vertical lines represent the positronium-formation and direct ionisation thresholds. Note that between these thresholds the single-centre calculation does not yield convergent results.

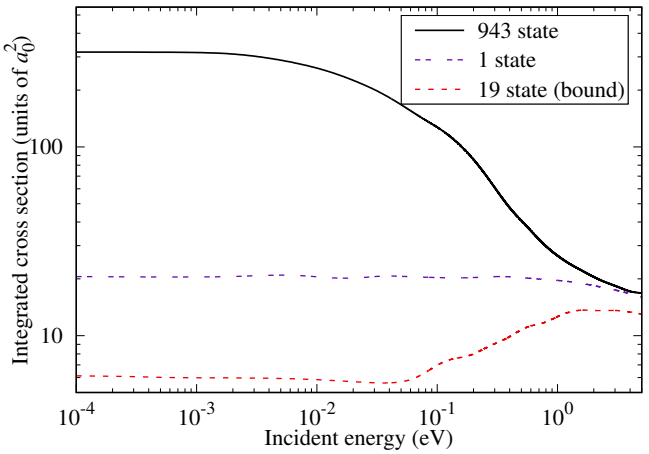

Figure 6.13: Low energy elastic scattering cross section results for positron scattering on carbon. CCC results are presented for several different models from energies of 10^{-4} eV to 5 eV.

6.4.9 Low energy study

To demonstrate the impact of polarisability and virtual positronium-formation on the elastic cross section and to enable calculation of the scattering length, we have calculated the elastic scattering cross section

down to incident energies of 10^{-4} eV. Calculations were performed using three CCC models, the first being a single-state model in which the target polarisability is not accounted for, the second a model containing all 19 bound states which accounts for the major part of the polarisability but not virtual positronium-formation, and lastly the full 943-state CCC model in which virtual positronium-formation and polarisability are both fully accounted for. In Fig. 6.13, we compare the three models, which allows us to illustrate the effects of including various reaction channels. For the 943-state model, the elastic cross section rapidly rises and reaches an asymptotic value of 318 a_0^2. However, the single-state model is comparatively flat from 1 eV to lower energies, and the bound-state model decreases before reaching a constant value of 6.13 a_0^2.

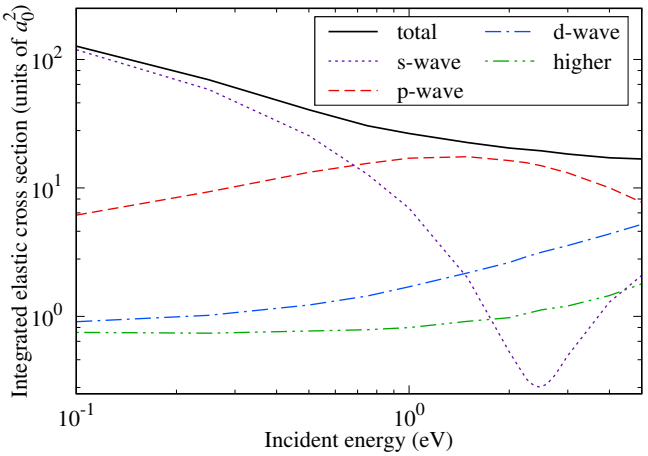

Figure 6.14: Cross section for elastic total, s-, p-, d-, and higher L wave positron scattering from carbon for the energy range 0.1 eV to 5 eV.

From the asymptotic value of the 943-state low-energy elastic cross section, we can determine the scattering length for the e^+-C system to be $A = \pm 5.03\ a_0$. To determine the sign, we can use Eq. 2.67. Using our δ_0 value at 10^{-4} eV we obtain $A = -5.03\ a_0$. The negative value indicates that this system has a strongly attractive nature at low energies [109]. The magnitude of A is larger than the mean radius of C, and the scattering cross section is much greater than the geometric size of the atom at low energies. This enhancement of the elastic cross section occurs due to the existence of a virtual level of the positron projec-

tile [311], the energy of which can be obtained using Eq. 2.69. From our calculated A the energy of the e^+-C virtual level is found to be $\epsilon = 0.537$ eV.

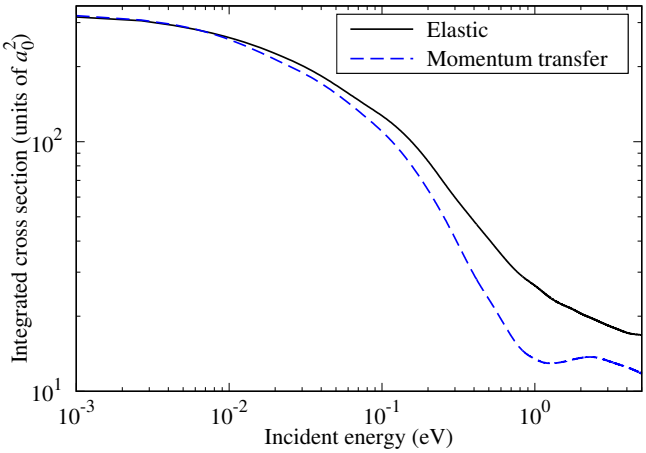

Figure 6.15: Elastic and momentum-transfer cross section for positron scattering from carbon for the energy range 10^{-3} eV to 5 eV.

As our scattering length is negative this implies the existence of a Ramsauer-Townsend minimum which will occur at incident energy given by Eq. 2.68. Using our calculated A and α_{D} values we find E_{min} to be 2.34 eV. Our integrated elastic cross section does not exhibit a minimum structure at this energy. However, it is observable when examining the s-wave contribution. This is shown in Fig. 6.14 alongside the p, d and higher Ł contributions for 0.1 to 5 eV. Here, L represents the incident angular momenta of the positron for which its contributions to the elastic cross section are extracted from the relevant partial-wave J. It has been demonstrated in the literature that for positron scattering from noble gas atoms, the contributions of higher partial waves can result in the minimum in the s-wave being hidden in the elastic cross section [82, 89, 310]. We observe this for carbon with the p, d, and higher L cross sections supplementing the decreased s-wave contribution. Over the energy range considered, we can see that s-wave scattering is dominant for incident energies below 0.6 eV. Above this, the p wave is dominant, with the peak p-wave cross section occurring at 1.5 eV. The $\mathrm{RT}_{\mathrm{min}}$ we find in our integrated s-wave cross-section occurs at an incident energy of approximately 2.45 eV, 0.11 eV higher than the value predicted by Eq. 2.68. This difference is small and likely due to the omission

of higher-order terms in Eqs. (2.68) and (2.67). From this difference, we can predict an uncertainty in our A of 2%.

Unlike the elastic cross section, in which the occurrence of a minimum solely depends on the s-wave phase shift becoming 0 while higher contributions are small, for the momentum-transfer cross section, the presence of a minimum depends on the difference between the s- and p-wave phase shifts [82]. As a result, even with a minimum hidden by higher contributions in the elastic cross section, it can be present in the MTCS. This is the case for e^+-C scattering, where a minimum can be observed at approximately 1.25 eV in Fig. 6.15. The elastic and momentum-transfer cross sections become equal when energies are low enough that scattering is isotropic, which our calculations predict to occur at energies below 0.01 eV.

6.4.10 Excitation cross sections

Cross sections for several excitations from the $2s^2 2p^2\ ^3P$ carbon ground state are presented in Fig. 6.16. The oscillator strengths for the $2p3d\ ^3D^o$ and $2s2p^3\ ^3P^o$ transitions had differences over 20% with the results of NIST. We have therefore scaled the positron-impact CCC cross section by the ratio between these oscillator strengths and those of NIST for these excitations, a process we refer to as OOS scaling. The scaled and unscaled results for these transitions are presented in the figure. As results for these excitations are unstable below the direct ionisation threshold, these calculations have been linearly interpolated between their threshold and the direct ionisation threshold. Since there are no previous positron-impact results for these processes, our results are presented alongside electron-impact scattering calculations. Due to the different scattering dynamics for positron and electron projectiles, the results are only expected to be equal at high energies, typically greater than 500 eV [118, 264, 375]. As results for these excitations have only been calculated to a maximum of 150 eV for electron-impact, comments can only be made regarding general differences between our positron-impact calculation and the electron-impact calculations.

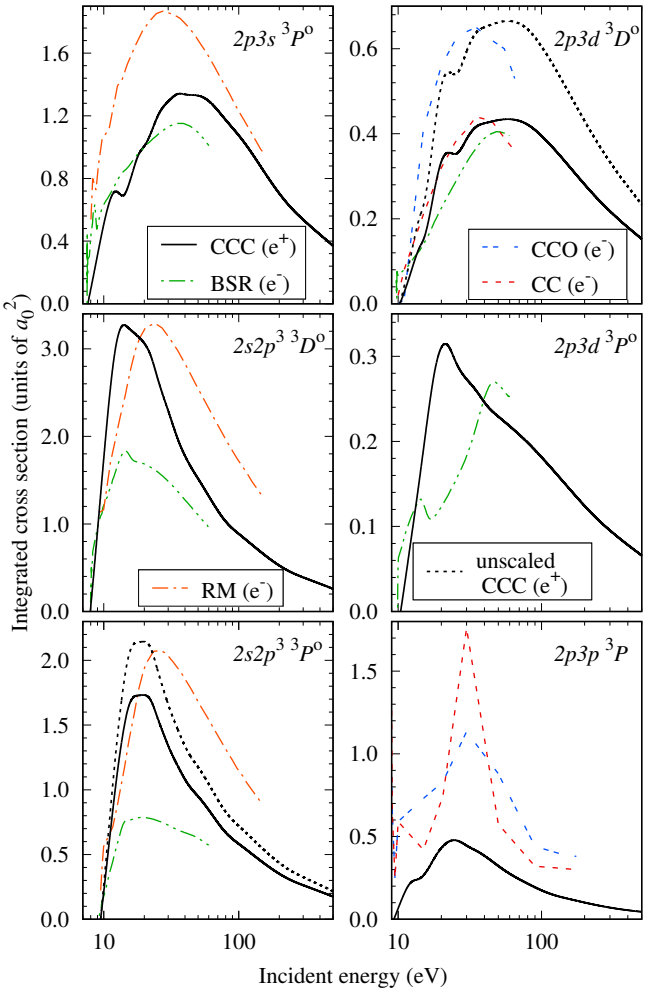

Figure 6.16: Cross section for excitations from the ground state of carbon to several excited states from threshold to 500 eV. Positron-impact CCC results are shown alongside electron-impact calculations from the BSR [42] (-···-), R-matrix (RM) [43] (-·-·-), CCO [44] (-- ·-), and CC [44] (- - -) methods. For CCC results which have been OOS scaled, the unscaled result is shown by (·····) and the scaled by (——).

For these excitations positron-impact CCC results are typically closer in magnitude with the 696-state electron-impact BSR calculations [42] than other electron calculations, a reflection of our closer agreement in oscillator strengths. As expected, differences largely decrease with increasing energy between the BSR and CCC results, particularly in the $2s2p^3\ ^3D^o$ and $2s2p^3\ ^3P^o$ excitations. After scaling of the $2p3d\ ^3D^o$ excitation with the NIST oscillator strengths, we find our positron-impact results to be closer in

magnitude to the CC [44] and BSR electron-impact models.

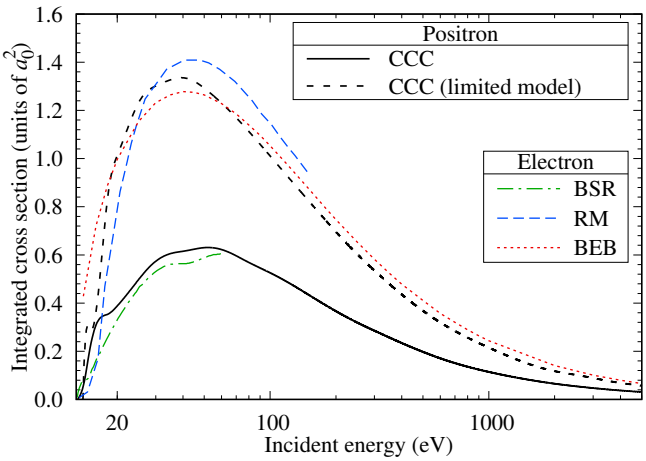

Figure 6.17: Cross section of excitation from the ground state to the $2s2p^3$ $^3S^0$ autoionising state. Positron-impact CCC and limited model CCC results are shown alongside electron-impact results calculated with BSR [42], R-matrix (RM) [43], and BEB [45] methods.

Our positron-impact CCC results for the $2s2p^3$ $^3S^o$ autoionising-state excitation from the ground state can be viewed in Fig. 6.17 with previous theoretical electron-impact results for this excitation. We have included results for a positron-impact model in which excitations from $2s2p^2n\ell$ were bound to $n\ell \leq 5s$, denoted as CCC (limited model). The results of this limited model are similar in magnitude to the electron-impact BEB [45] result at low energy and converge with it for energies above 2000 eV. The electron-impact R-matrix calculation of Dunseath *et al.* [43] is larger than both the BEB results and our CCC results above 25 eV. The 943-state CCC results are almost a factor of 2 lower than our limited model values and are larger than the BSR results up to 60 eV, where they appear to meet. The discrepancy between this calculation of Dunseath *et al.* [43] and the 943-state model is not surprising as their oscillator strength for this transition is almost twice the value we predict. Comparing our two CCC models, it is likely that the difference between the BSR and other electron-impact theoretical methods results from an inadequate description of the $2s2p^2n\ell$ continuum in the other approaches.

6.4.11 Stopping power and mean excitation energy

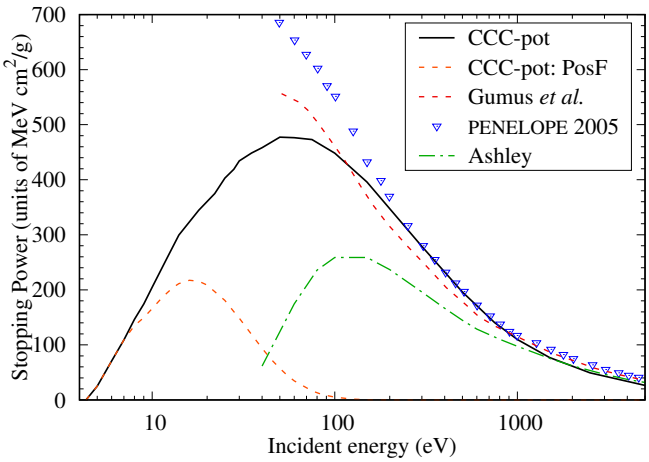

Figure 6.18: Stopping power of a positron incident on carbon. CCC results are compared against those of Gumus *et al.* [46], the PENELOPE 2005 program [47], and Ashley [48]. Also presented is the positronium-formation (PosF) component of the CCC stopping power. These results are presented from threshold to 5000 eV.

In Fig. 6.18, we present the stopping power, calculated from threshold to 5000 eV using Eq. 2.61. The positronium-formation component of the stopping power was calculated with the method outline in Section. 2.2.6, the bound-state excitation component for energies below 21 eV was obtained from an ℓ_{max}=2 calculation, and the direct ionisation component was found from scaling the electron-loss stopping power from the single-centre CCC calculation. Alongside the CCC results are those from the Gumus *et al.* [46], PENELOPE program [47], and Ashley [48]. As was done for ionisation, the results were extrapolated using our 4571 Born calculation for energies above 50 eV. In these results, we cannot utilise the CCC-pot approach as it does not calculate the cross-section for each specific excitation. Therefore, positronium-formation is only included implicitly. From 250 eV to 1000 eV, there is excellent agreement between the CCC and PENELOPE results. Below 250 eV, the PENELOPE results are significantly higher than the CCC, with a difference of approximately 200 MeV cm^2/g at 50 eV, whereas above 1000 eV, the PENELOPE result is only slightly larger than the CCC. The PENELOPE program is a Monte-Carlo program that calculates stopping power using a plane-wave Born approximation

with the Sternheimer-Liljequist generalised oscillator strength model [376]. Therefore, the large differences at low energies are not surprising as this approach becomes increasingly inaccurate for energies below 1000 eV [47]. The results of the GOS model agree with PENELOPE for energies above 800 eV. Below this, the GOS model has lower values than both these models, except for energies below 100 eV, where it is larger than the CCC results. The calculations of Ashley [48] follow a similar shape to the CCC calculation but underestimate all other theoretical results below 1500 eV. Above this energy, however, there is excellent agreement with the CCC results.

The other theoretical approaches applied to stopping power are simpler

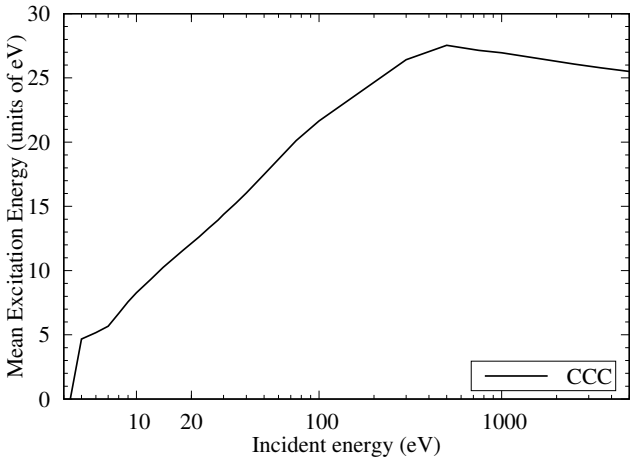

Figure 6.19: Mean excitation energy of a positron scattering on carbon. Results are presented from threshold to 5000 eV.

methods that do not directly model the target structure of the atom or account for positronium-formation. Therefore, while accurate for high energies, with all models practically equivalent above 1500 eV, they will be inaccurate at lower energies where scattering is more complex. As a result of the accurate structure model, the large number of included states, and the inclusion of positronium-formation, the CCC method is expected to model stopping power over the considered energy range more accurately than these other methods.

Following directly from the stopping power, we can obtain the mean excitation energy per Eq. 2.65. We present our results from threshold to 5000 eV in Fig. 6.19. We can observe that our mean excitation energy

steadily increases to 500 eV, after which it plateaus and slowly decreases to 5000 eV. The sharp rise near the threshold is a result of positronium-formation. We could not find any other calculations of mean excitation energy for the e^+-C system in the literature.

6.4.12 Chapter summary

In this chapter, the specific details of the calculation utilised for positron scattering on atomic carbon are outlined. The target wave functions of this structure model are in good agreement with NIST and previous theory for oscillator strengths and excitation energies. Cross sections associated with the total, elastic, momentum-transfer, direct ionisation, positronium-formation, electron-loss, inelastic, excitation, and stopping power scattering processes are presented for this system over energies ranging from 10^{-5} eV to 5000 eV. Several quantities of interest have also been determined. These include the scattering length, the energy of the virtual positron-carbon state, and the hidden Ramsauer-Townsend minimum.

The present results have been compared with existing experimental and theoretical results for both positron and electron scattering on atomic carbon. Total, elastic, momentum-transfer, and stopping power cross sections were all in good agreement with previous calculations at high energies. Substantial differences exist between the cross sections calculated by the SCOP and CCC methods for positron scattering at low energies. This is expected to result from the potential utilised by the previous SCOP approach which also significantly overestimate the ELCS across almost the entire calculated energy range. The current CCC calculations, however, are in excellent agreement with the existing electron-carbon experiment above 500 eV. Consequently we expect that our results to be of sufficient accuracy across the calculated energy range. The differences between positron and electron scattering are minimal for high energies, and their results are practically identical. The main source of the differences present between CCC ELCS and previous model potential approach calculations is the positronium-formation process, with the previous theory being a factor of 1.5 larger than our results at the maximum for this cross section.

Chapter 7

Positron scattering from oxygen

This chapter presents the single-centre CCC and CCC-scaled complex model potential calculations for positron scattering from atomic oxygen. First, the calculation details are provided, and comparisons are made with quantities such as excitation energies, oscillator strengths, and dipole polarisability with existing theoretical and experimental values to verify the quality of the utilised structure model. Following this, the results for the total elastic, momentum-transfer, excitation, direct ionisation, electron-loss, total inelastic, positronium-formation, stopping power, and total cross sections from threshold to 5000 eV are shown. We also present the scattering length, the hidden Ramsauer-Townsend minimum, the energy of the positron-oxygen virtual state, and the mean excitation energy. These results are compared with existing positron calculations, electron experiment, and halved positron-O_2 experiment. Some sections in this chapter text or figures are adapted from a published work by the candidate [2]. The publishers of this article (EDP Sciences, Società Italiana di Fisica, and Springer Berlin Heidelberg) provide the right to use an article or a portion of an article in a thesis or dissertation without requesting permission.

7.1 Calculation

Orbitals $1s$ to $2p$ were obtained from a HF calculation of the oxygen ion (O^+), optimised on its ground state. All other orbitals were obtained from

the Laguerre basis. For this calculation, $N_\ell = 18 - \ell$ with $\alpha_\ell = 0.4$ for $0 \leq \ell \leq 4$ and $\alpha_\ell = 1.0$ for $\ell \leq 8$. The present close-coupling expansion includes $2s^2np^4$, $2snp^5$, and np^6. The $2s^22p^3n\ell$ continuum is included for $\ell \leq 8$. We also include the $2s2p^4n\ell$ continuum, but with $\ell \leq 4$, and $2s2p^3n\ell^2$ configurations for orbitals $n\ell$ between $3s$ and $5s$. To limit the size of the calculation the only $2s2p^3n\ell n'\ell'$ configurations included were $2s2p^34s4p$, $2s2p^34s4d$, $2s2p^34d4f$, $2s2p^34p4d$, and $2s2p^34d5s$. The restriction of these configurations is expected to slightly decrease the accuracy of the current structure model. States were included with energies up to 75 eV above ionisation, resulting in a total of 1543 states.

For energies above 500 eV, calculations were completed with $\ell_{\max} = 4$, which is sufficient to obtain convergent results at these energies. Below the positronium-formation threshold, a 1409 state model with $\alpha_\ell = 5.0$ and N_ℓ=$25 - \ell$ containing all states with energies up to 300 eV was used. For energies above 100 eV, ELCS and stopping power were extrapolated using a Born model with the same configuration structure as the CCC model but with N=$25 - \ell$, the $2s2p^4n\ell$ continuum extended to $\ell \leq 8$, and all 3863 generated states included. Calculations are completed to $J = 10$ for all energies, except for presented DCS results which were obtained with $J \leq 50$ and for low energies where convergence can be achieved for $J \leq 5$.

A convergence study for the ELCS is presented in Fig. 7.1. Calculations are fully converged for $\ell_{\max} = 7$ for energies ≥ 20 eV, $\ell_{\max} = 6$ for energies ≥ 100 eV, and $\ell_{\max} = 4$ for energies ≥ 300 eV.

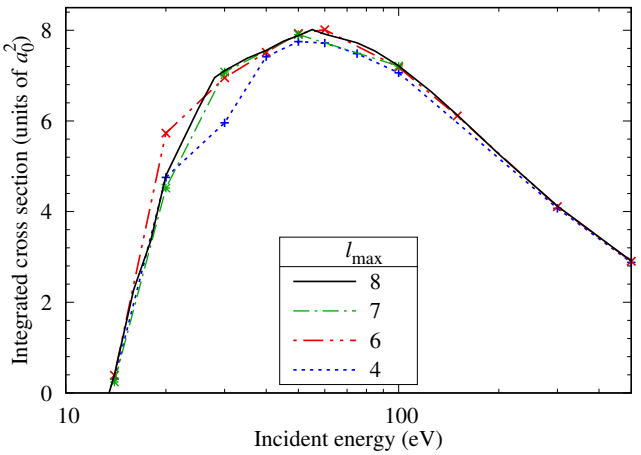

Figure 7.1: Convergence study for the electron-loss cross section of O where $\ell_{\max}$ represents the maximum ℓ in which calculations are completed.

7.2 Structure

Excitation energies for triplet target states of the atomic oxygen atom are presented in Table 7.1. Agreement between the current calculation and past theory and experiment is satisfactory, with differences between NIST [59] and CCC ranging from 0.002 eV to 0.278 eV. Oscillator strengths for several transitions between triplet bound states are shown in Table 7.2. Good agreement is found with NIST and past theory for all presented transitions except for the $2p^3 3s\ ^3D^0$ transition, though this is a weak transition with a small oscillator strength.

For oxygen, the experimental value of α_D is $5.2 \pm 0.4 a_0^3$ [377]. Our largest 3863 state Born model had $\alpha_D = 5.50\ a_0^3$, which is within experimental error and slightly higher than other theory [331]. Our 1543 state model had a dipole polarisability of $6.00\ a_0^3$ and our small-energy 1490 state model of $5.31\ a_0^3$, which is within 3 % of the largest model and within experimental uncertainty. The difference between the polarisabilities of these models results from the differences in their structure models, as described previously. As the charge distribution for oxygen is spherically symmetric only α_D is relevant for the scattering calculations. For completeness, however, we provide the quadrupole and octupole polarisability results of our small-energy model. The quadrupole polarisability was $18.91\ a_0^5$, which is within 12% of CEPA-NO value for α_Q of $21.2\ a_0^3$ [372]. For the octupole polarisability, our result was $159.80\ a_0^7$ and there exists no other calculations of α_O to compare with.

7.3 Scattering

7.3.1 Total cross section

The total cross section arising in the CCC calculation of atomic oxygen is presented in Fig. 7.2 alongside the calculations of Singh *et al.* [33], Reid and Wadehra [32], and Pindariya *et al.* [49]. In this case, the CCC-pot is equivalent to the 1490 state CCC calculation below the positronium-formation threshold and the 1543 state model above 23.5 eV. The calculation is equivalent to the CCC-scaled complex model potential between these two energies. Due to the lack of existing experimental data for electron and positron scattering from atomic oxygen, we compare against experimental

Table 7.1: Excitation energies (eV) for atomic oxygen triplet target bound states.

	State	Term	CCC	Ref. [61]	Ref. [63]	Ref. [331]	NIST [59]
1	$2s^2 2p^4$	^3P	0.000	0.000	0.000	0.000	0.000
2	$2s^2 2p^3 3s$	$^3S^0$	9.523	9.608	9.67	9.592	9.521
3	$2s^2 2p^3 3p$	^3P	11.002	11.025	11.24	11.156	10.989
4	$2s^2 2p^3 4s$	$^3S^0$	11.938	12.035	12.07	12.000	11.930
5	$2s^2 2p^3 3d$	$^3D^0$	12.075	12.119	12.23	12.150	12.087
6	$2s^2 2p^3 4p$	^3P	12.355		12.59	12.504	12.359
7	$2s^2 2p^3 3s$	$^3D^0$	12.744	12.653	12.82	12.694	12.540
8	$2s^2 2p^3 5s$	$^3S^0$	12.692		12.89		12.697
9	$2s^2 2p^3 4d$	$^3D^0$	13.037		13.01	12.762	12.759
10	$2s^2 2p^3 4f$	^3F	12.752		13.16	12.830	12.766
Ion. Limit			13.513	13.597			13.618

Table 7.2: Oscillator strengths for bound triplet states of O.

Lower level	Upper level	CCC	Ref. [61]	NIST [59]
$2p^4\ ^3P$	$2p^3 3s\ ^3P^0$	0.052	0.051	0.052
	$2p^3 4s\ ^3S^0$	0.0090	0.0087	0.0092
	$2p^3 3d\ ^3D^0$	0.024	0.022	0.020
	$2p^3 3s\ ^3D^0$	0.011	0.056	0.056
$2p^3 3s\ ^3S^0$	$2p^3 3p\ ^3P$	1.091	1.050	1.030
$2p^3 3p\ ^3P$	$2p^3 4s\ ^3S^0$	0.182	0.186	0.186
	$2p^3 3d\ ^3D^0$	0.956	0.960	0.990

results for positron and electron results for O_2, which are divided by 2, in accordance with the additivity rule. This rule is expected only to be relevant for higher energies. Therefore, only qualitative comparisons can be made for lower energies. A more accurate comparison between the current theoretical calculations for O and the experimental data for O_2 can be accomplished using the IAM-SCAR approach. This approach was applied to the current atomic data to calculate O_2 cross sections in Section. 11.2 for all presented cross sections.

CCC results are higher than the halved positron O_2 experimental results of Charlton *et al.* [50] and Dababneh *et al.* [52] for energies above 40 eV. However, comparison with the more recent measurements of Chiari *et al.* [51], shows near-perfect agreement. For high incident energies, positron and electron results are expected to become equal to the Born approximation, which is independent of the projectile charge. We observe this for energies above 1000 eV, with excellent agreement found with the halved electron O_2 measurements of García *et al.* [53].

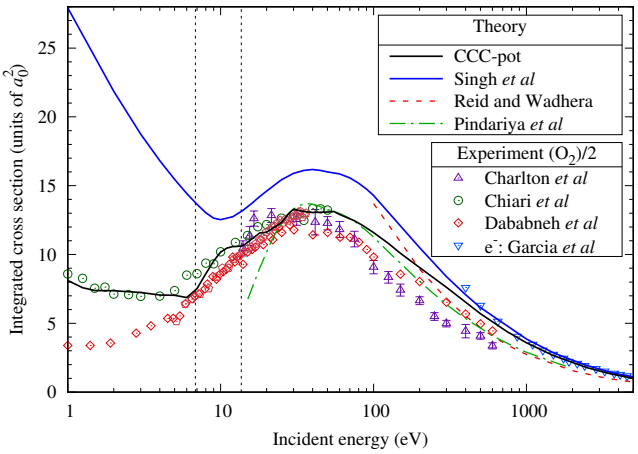

Figure 7.2: Total cross section for positron scattering on oxygen. Theoretical CCC results are shown alongside optical potential calculations by Singh *et al.* [33], Reid and Wadehra [32], and Pindariya *et al.* [49]. Experimental O_2 results for positron scattering are from Charlton *et al.* [50], Chiari *et al.* [51], and Dababneh *et al.* [52]. Electron O_2 results are by García *et al.* [53]. The vertical dotted lines represent the positronium-formation and direct ionisation thresholds.

The peak cross section of the CCC TCS is of similar magnitude to the

calculation of Pindariya *et al.* [49] and the halved positron O_2 experiment of Chiari *et al.* [51]. However, the results of Singh *et al.* [33] are much larger than our CCC result at the peak TCS and also depicts significantly different behaviour for lower energies. At low energies, our results behave similarly to O_2 experiment, with results flat from 1 eV to the positronium-formation threshold. On the other hand, Singh *et al.* [33] predict the cross section to decrease significantly from 1 eV to the positronium threshold and the experiment of Dababneh *et al.* [52] predict the cross section to increase over this energy range. Consequently, this calculation predicts a value at 1 eV over five times higher than the CCC result. We expect that CCC results converge to exact results at energies below the positronium-formation threshold, given in Fig. 7.2. Therefore, the discrepancy is likely due to the polarisation potential being too high in the model potential or from the exclusion of virtual positronium-formation in the SCOP approach. A similar discrepancy was noted between the CCC and results of Singh *et al.* [33] for the carbon atom [1], but not as pronounced.

7.3.2 Electron-loss cross section

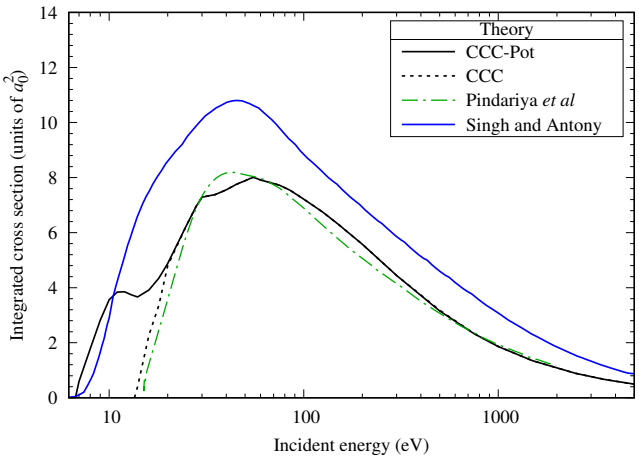

Figure 7.3: Electron-loss cross section for positron scattering on oxygen. Current CCC results are presented alongside the calculations of Singh and Antony [34] and Pindariya *et al.* [49]. The CCC-pot calculations incorporate an estimate of the Ps-formation cross section contribution from its threshold, see text.

The ELCS for positron scattering on oxygen, which is equivalent to the sum of direct ionisation and positronium-formation, is shown in Fig. 7.3. As with the total cross section, for energies below 23.5 eV the CCC-pot results are from the CCC-scaled complex model potential, whereas, for energies above this energy they are from the single-centre CCC calculation. The results of Pindariya *et al.* [49] are in close perfect agreement with those of CCC from near the direct ionisation threshold through to high energies. The results of Singh and Antony [34] are considerably higher for energies above 10 eV.

7.3.3 Direct ionisation and positronium-formation cross section

The e^+-O direct ionisation cross section is presented in Fig. 7.4. This includes the current CCC-pot results alongside the theoretical result of Singh and Antony [34] and e^--O experiment. At high energies, electron and positron results are expected to become equal. We find this to occur by 1000 eV, with excellent agreement between the CCC and electron experiment above this energy. Similar to the ELCS, the calculation of Singh and Antony [34] is significantly larger than the CCC calculation for incident energies above 35 eV.

Cross sections for positronium-formation in e^+-O scattering are presented in Fig. 7.5. Current CCC-pot results are presented together with the only other calculation, by Singh and Antony [34]. The experimental results are for the O_2, and have therefore been divided by two. The positronium-formation threshold energy of O_2 is lower than that of O, which is why near-threshold energies, there is a discrepancy in the behaviour of the O_2 experiment and theoretical values for O. Compared to the halved O_2 experiment, we find agreement with the measurements of Marler and Surko [56] for energies above 40 eV, and Griffith [58] above 100 eV. Apart from the lower energies the results of Singh and Antony [34] are generally considerably above those of CCC-pot. A similar disagreement was found comparing these approaches for atomic carbon [1]. The absence of existing experiment for atomic oxygen makes it difficult to judge the true accuracy of the CCC-pot calculations, particularly at the lower energies. However, as our calculation is scaled directly to the *ab-initio* CCC calculation and is in agreement with halved O_2 experiment at the higher energies, we believe lower energy CCC-pot cross section uncertainty is no more than 20%.

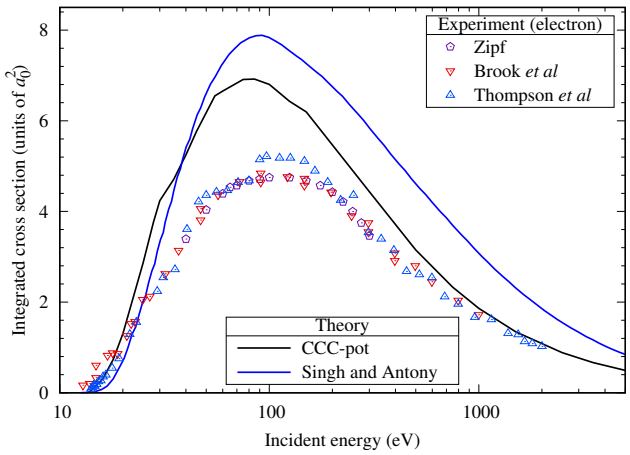

Figure 7.4: Direct ionisation cross section for positron scattering on oxygen. Theoretical results include CCC-pot and Singh and Antony [34] calculations. Experimental results for electron scattering from Zipf [54], Brook *et al.* [35], and Thompson *et al.* [55] are expected to converge to positron scattering ones at high energies.

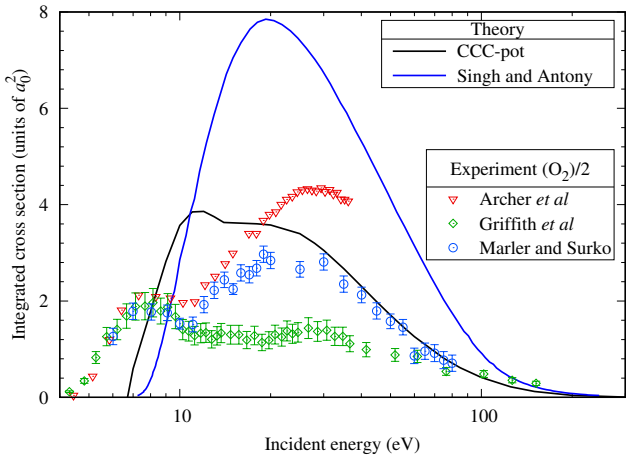

Figure 7.5: Positronium-formation cross section for positron scattering on oxygen. Theoretical results include CCC-pot and Singh and Antony [34] calculations. Halved experimental O_2 measurements are from Marler and Surko [56], Archer *et al.* [57], and Griffith [58].

7.3.4 Inelastic cross section

Fig. 7.6 presents the total inelastic cross section for positron scattering on oxygen from its threshold to 5000 eV. Above 500 eV, close agreement is found between the CCC and the calculation of Pindariya *et al.* [49]. The

CCC is slightly above the results of Pindariya *et al.* [49] between 100 eV and 500 eV. Below this, Pindariya *et al.* [49] are notably larger than the CCC results, except for below 20 eV, where they are smaller. The calculation of Reid and Wadehra [32] overestimates other theory over their calculated energy range of 100 eV to 5000 eV.

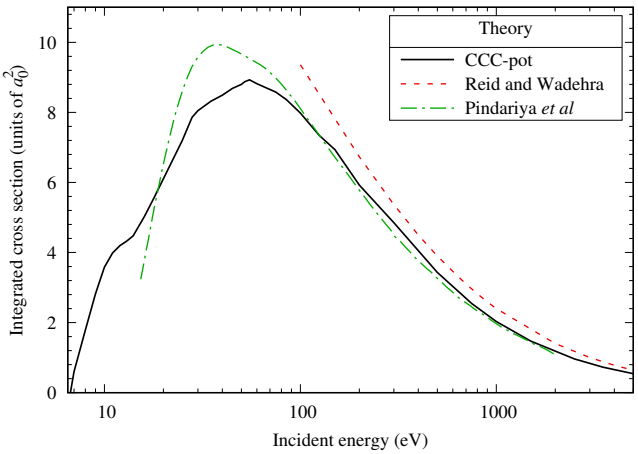

Figure 7.6: Total inelastic cross section for positron scattering on oxygen. CCC results are shown alongside those of Pindariya *et al.* [49] and Reid and Wadehra [32].

7.3.5 Elastic and momentum-transfer cross section

The integrated elastic cross section is shown in Fig. 7.7 alongside the calculations of Reid and Wadehra [32], Pindariya *et al.* [49], Dapor and Miotello [37], and, for the electron case, NIST. Above 500 eV, we find near-perfect agreement with the calculations of Dapor and Miotello [37] and above 3000 eV with the NIST electron results. Comparisons are also made with the halved electron experimental results of Iga *et al.* [60] for O_2. At 1000 eV, the electron and positron theory lies within the experimental uncertainty.

In Fig. 7.8 we present the momentum-transfer cross section for this system. Current results are compared with the calculations of Dapor and Miotello [37], the electron calculations of NIST, and halved electron-O_2 experimental data of Iga *et al.* [60]. As with the elastic cross section, for energies above 500 eV excellent agreement is observed between the CCC and the calculations of Dapor and Miotello [37]. The NIST results for

the electron case are larger than the positron theoretical results, with no agreement viewed by 5000 eV. The experimental data is found to lie between the positron and electron calculations.

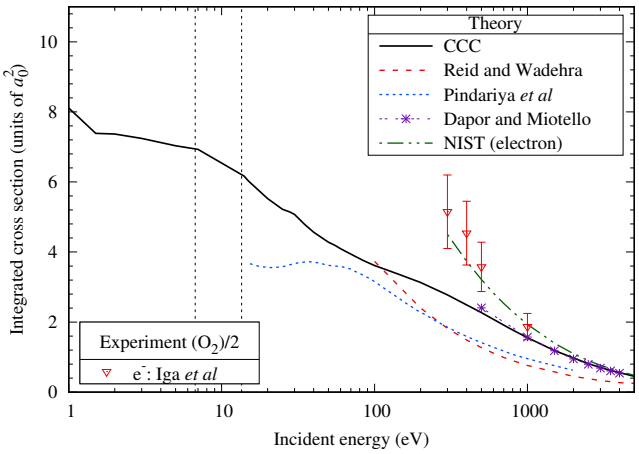

Figure 7.7: Total elastic cross section for positron scattering on oxygen. Theoretical results for positrons include the CCC, Reid and Wadehra [32], Pindariya *et al.* [49], and Dapor and Miotello [37]. Theoretical results for electrons are from NIST [59]. Halved O_2 experimental results for electrons are from Iga *et al.* [60]. The vertical dotted lines represent the positronium-formation and direct ionisation thresholds.

The DCS for various energies between 500 and 3500 eV are shown in Fig. 7.9. As with the integrated cross section, excellent agreement is viewed with the calculations of Dapor and Miotello [37] for each of these energies. In Fig. 7.10 we present a selection of elastic DCS for incident energies between 1 and 100 eV. A technique similar to Green *et al.* [89] is used to ensure convergence in the partial wave expansion, resulting in a cusp at low scattering angles for incident energies above 1 eV. As with carbon [1], this feature is not present at lower energies due to the triplet ground state resulting in p-wave scattering being dominant at low energies.

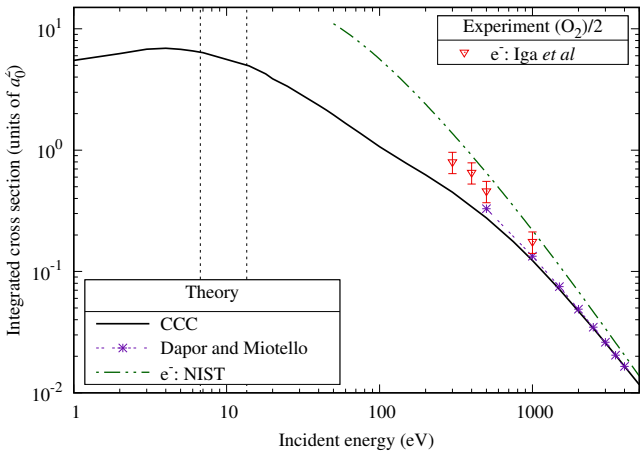

Figure 7.8: Momentum-transfer cross section for positron scattering on oxygen. CCC results are presented alongside the positron calculation of Dapor and Miotello [37] and the NIST electron results [59]. Halved O_2 experimental results for electrons are from Iga *et al.* [60]. The vertical dotted lines represent the positronium-formation and direct ionisation thresholds.

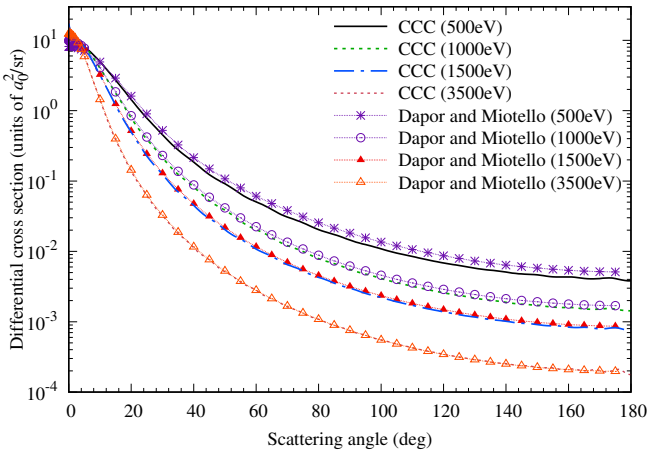

Figure 7.9: High energy elastic differential cross sections for positron scattering on oxygen. CCC results are presented alongside the calculations of Dapor and Miotello [37].

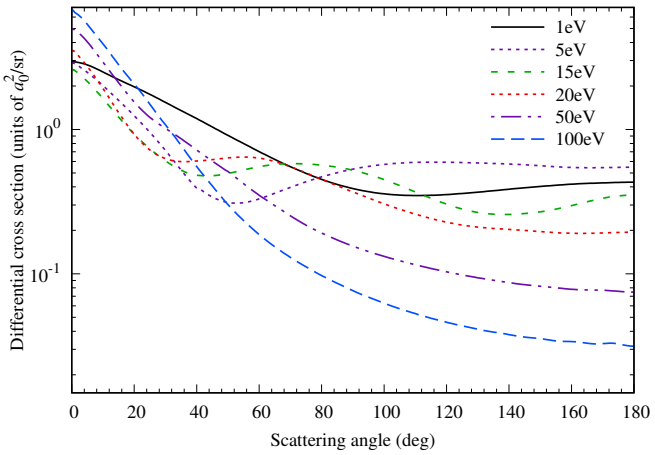

Figure 7.10: Elastic differential cross sections for positron scattering on oxygen for energies between 1 and 100 eV.

7.3.6 Low-energy study

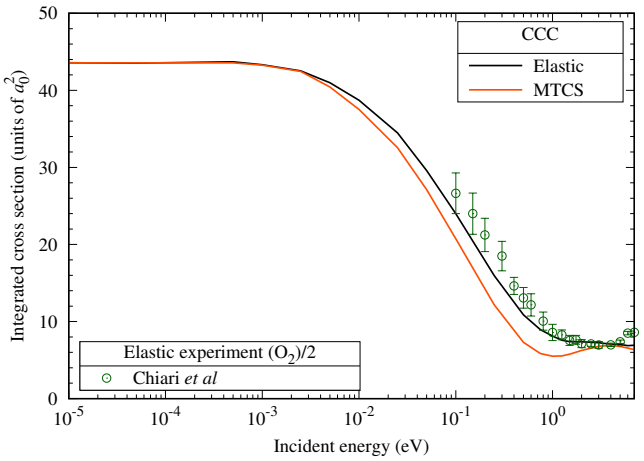

Figure 7.11: Elastic and momentum-transfer cross sections for positron scattering on atomic oxygen at energies below 1 eV. Halved O_2 experimental results are from Chiari *et al.* [51].

Elastic and momentum-transfer cross sections for energies below 1 eV are shown in Fig. 7.11. Although the IAM approximation does not hold for low energies, we find good agreement with the halved O_2 experiment from Chiari *et al.* [51], this experiment does not have forward-scattering corrections so likely underestimates the actual result for O_2. However, the similar behaviour exhibited provides some evidence of the accuracy

of the current results. At lower energies, as scattering becomes isotropic, the elastic and momentum-transfer cross sections are expected to become equal. We observe this for energies below 10^{-3} eV.

Using the asymptotic value of our elastic cross section at 10^{-5} eV, we determine $A = -1.862$ a_0 for this system. Where the sign is derived from our phase shift at low energies, per Eq. 2.67. As $|A|$ is larger than the mean radius of O, the scattering cross section is greater than the geometric size of the atom at low energies. This is due to the existence of a virtual level of the positron projectile, which has energy $\epsilon = 3.92$ eV.

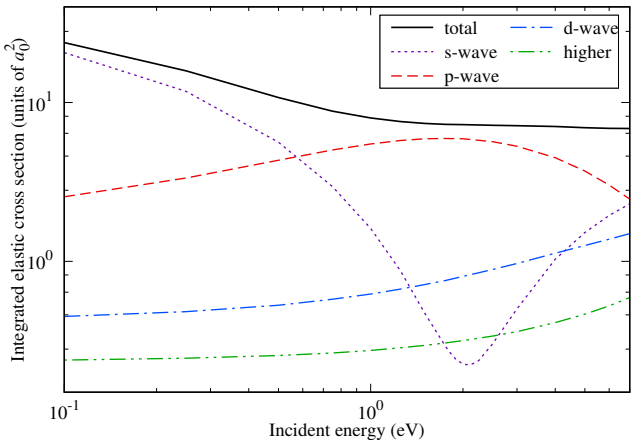

Figure 7.12: Elastic cross sections for positron scattering on atomic oxygen and its s-, p-, d- and higher L-wave contributions. Here, L refers to the angular momentum of the incident positron.

As the scattering length is negative this implies a Ramsauer-Townsend minimum that occurs at an energy of $E_{\text{min}} = 1.53$ eV, per Eq. 2.68, which (due to neglected higher order terms in Eq. 2.68) is 0.5 eV lower than the value of 2.05 eV observed in the s-wave scattering component of the elastic cross section in Fig. 7.12. In this figure, the s-, p-, d-, and higher-wave cross sections refer to the angular momentum of the incident positron L for which their contributions to the elastic cross section are extracted from the relevant partial-waves J. A Ramsauer-Townsend minimum is not observed in the total elastic cross section as the magnitude of the s-wave component becomes small relative to other partial waves as the incident energy increases. This process can be observed in Fig. 7.12, with the peak of the p-wave and

increasing values of the d- and higher-wave cross-sections supplementing the decreased s-wave contribution at its minimum. As we observed in carbon, although the effect of the minimum in the s-wave is hidden for the elastic cross-section, its impact can be observed for the momentum-transfer cross section, which has a minimum at 1 eV due to this effect.

7.3.7 Bound-state excitation cross section

There is no other existing positron theory or experiment for specific bound-state excitations. Therefore, we compare against existing electron theory and experiment, which are expected to be equivalent to positron results for high incident energies. To obtain stable results for energies below 20 eV, values were obtained for calculations with $\ell_{\max} = 2$ and only bound states included.

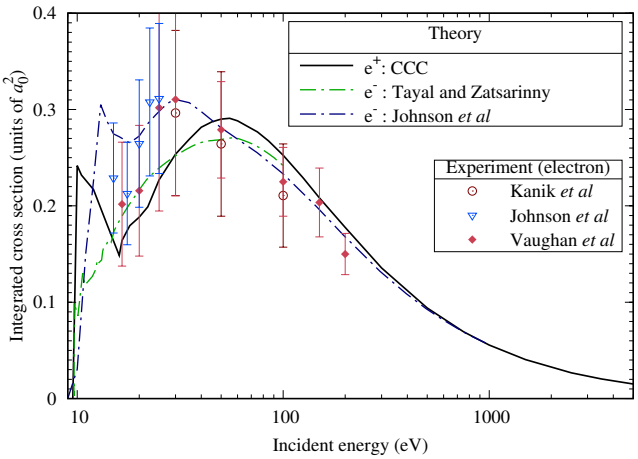

Figure 7.13: The $2p^4\ ^3P \rightarrow 2p^3 3s\ ^3S^o$ excitation cross section for positron scattering on oxygen. Theoretical results for incident electrons are from Tayal and Zatsarinny [61] and the recommended values from Johnson *et al.* [62]. Experimental electron measurements are from Johnson *et al.* [63], Kanik *et al.* [64], and Vaughan and Doering [65].

Fig. 7.13 presents the excitation of the ground state to $2p^3 3s\ ^3S^o$. Excellent agreement is found for energies above 500 eV with the recommended electron theoretical results of Johnson *et al.* [62]. At lower energies, our positron calculation lies within the experimental error of existing electron measurements and is close to the BSR calculation of [61].

Fig. 7.14 presents the $2p^4\ ^3P \rightarrow 2p^3 3s\ ^3S^o$ excitation cross section. Comparing with the BSR results, we find that differences decrease with increasing energy and that they become close by 100 eV. The CCC results lie within the uncertainty of the experiment of Gulcicek *et al.* [66] below 20 eV.

The $2p^3 3d\ ^3D^o$ excitation cross section is shown in Fig. 7.15. Due to the differences observed with the oscillator strength for this transition and those of NIST, we have applied OOS scaling, which is the scaling of the CCC cross section by the ratio between these two oscillator strengths. Agreement is observed after this scaling with the recommended electron results of Johnson *et al.* [62] for energies above 500 eV. Closer agreement is observed with the BSR calculation for the unscaled result of this excitation.

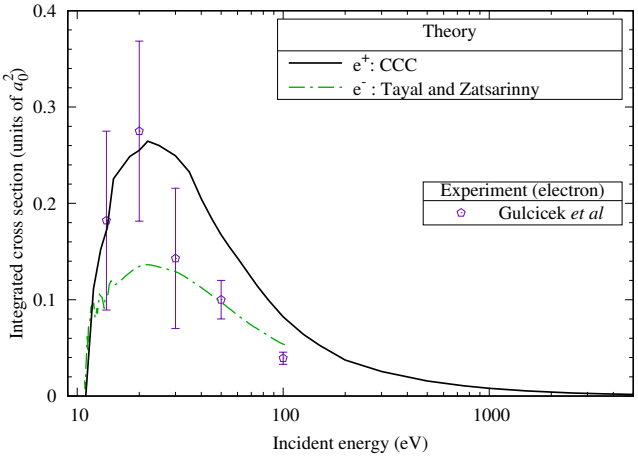

Figure 7.14: The $2p^4\ ^3P \rightarrow 2p^3 3p\ ^3P$ excitation cross section for positron scattering on oxygen. Theoretical results for incident electrons are from Tayal and Zatsarinny [61]. Experimental electron measurements are from Gulcicek *et al.* [66].

Fig. 7.16 shows the $2p^3 3s\ ^3D^o$ excitation cross section. After OOS scaling we find excellent agreement with the recommended electron results of Johnson *et al.* [62] at high energies. At lower energies our positron calculation is found to be lower than the electron theory, but within the uncertainty of electron experiment.

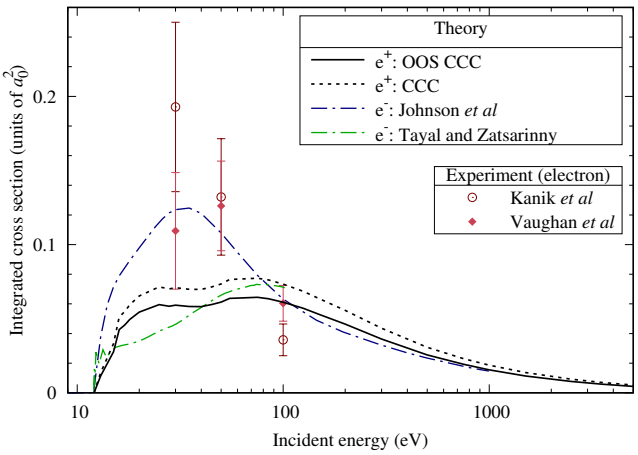

Figure 7.15: The $2p^4\ ^3P \rightarrow 2p^3 3d\ ^3D^o$ excitation cross section for positron scattering on oxygen. Theoretical results for incident electrons are from Tayal and Zatsarinny [61] and recommended from Johnson *et al.* [62]. Experimental electron measurements are from Kanik *et al.* [64]

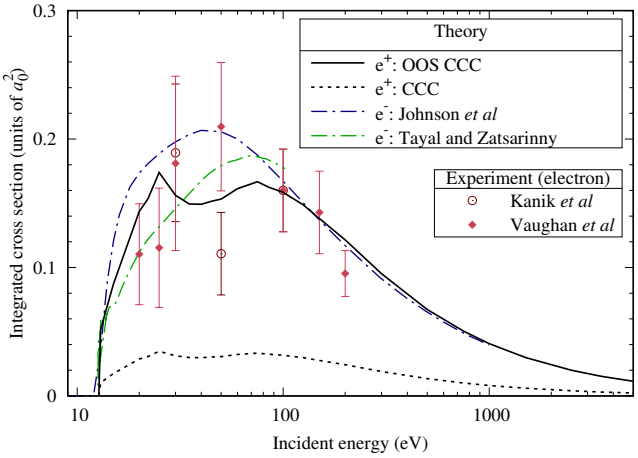

Figure 7.16: The $2p^4\ ^3P \rightarrow 2p^3 3s\ ^3D^o$ excitation cross section for positron scattering on oxygen. Theoretical results for incident electrons are from Tayal and Zatsarinny [61] and recommended results from Johnson *et al.* [62]. Experimental electron measurements are from Vaughan and Doering [65] and Kanik *et al.* [64].

The total bound-state excitation cross section is presented in Fig. 7.17. The CCC-pot calculation is equivalent to the CCC-scaled complex model potential calculation for energies below 23.5 eV and the CCC for energies above this. Little agreement is observed with the only existing positron

calculation of Pindariya *et al.* [49], which is significantly larger than the CCC result for energies below 300 eV. However, both calculations find a maximum at $\approx$ 20 eV. For energies above 500 eV, the electron results of Joshipura and Patel [67] agree with the positron results of Pindariya *et al.* [49] above 500 eV, but both are lower than the CCC results. The presented calculation of Johnson *et al.* [62] is a sum of only the three previously presented excitations. Therefore, it is expected to underestimate the total as it does not contain enough states to approximate the full excitation spectrum. Consequently, the summed recommended values follow the shape of the CCC calculation, which contains 28 bound states, for energies above 100 eV but is much lower even at 1000 eV. As the summed Johnson *et al.* [62] results are higher than the other presented electron and positron calculation at this energy, this suggests they underestimate the total bound-state excitation cross section at higher energies.

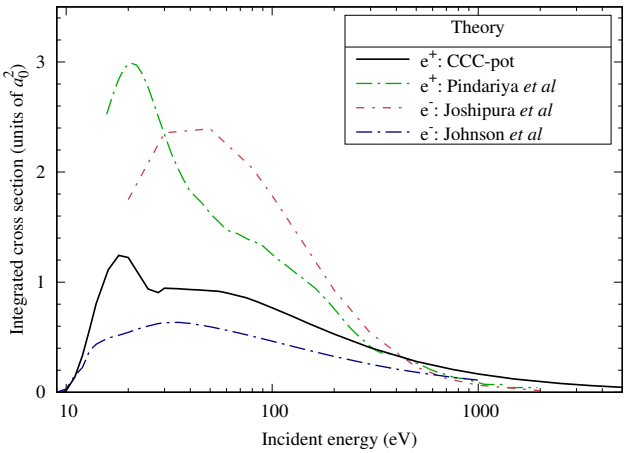

Figure 7.17: Total bound-state excitation cross section for positron scattering on oxygen. Theoretical results are from the CCC, Pindariya *et al.* [49], and, for the electron case, Joshipura and Patel [67] and Johnson *et al.* [62].

7.3.8 Mean excitation energy and stopping power

In Fig. 7.18, we present the stopping power for a positron incident on atomic oxygen. The calculation of stopping power requires the cross section and excitation energy for each reaction channel. The stopping power for the positronium-formation channel was obtained from the total positronium-formation cross sections, as discussed in Section. 2.2.6. Reaction channels

corresponding to bound-state excitation and ionisation are treated in the following way. Below 23.5 eV, for bound-state excitation, we have used the present estimates for the cross sections. For ionisation, we have used cross sections for positive-energy pseudostates from the single-centre CCC model scaled to obtain the present direct ionisation cross section. For energies above 23.5 eV, the stopping power is obtained directly from the single-centre CCC calculation.

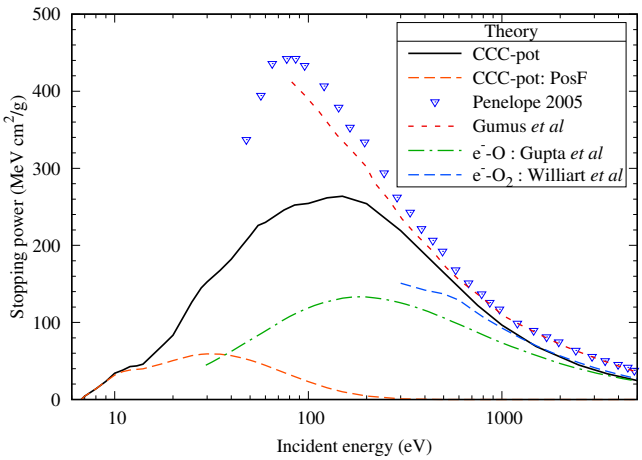

Figure 7.18: Stopping power for positron scattering on oxygen. Current CCC-pot calculations are shown alongside the calculations of the PENELOPE code [47], and Gumus *et al.* [46] for e^+-O_2. Calculations for e^--O by Gupta *et al.* [68] and semi-empirical results for the e^--O_2 system by Williart *et al.* [69] are also presented. The positronium-formation component of the stopping power (PosF) is also shown for the CCC-pot calculation.

According to Bragg's additivity rule [378], which is accurate for high energies, the stopping power of O_2 is expected to be equal to that of O. CCC calculations of stopping power for H and H_2 [13] targets found this rule accurate for energies above 100 eV. As electron and positron results are equivalent for high energies, we also present the e^--O calculation of Gupta *et al.* [68] and the e^--O_2 semi-empirical calculations of Williart *et al.* [69]. For energies above 1000 eV, we find excellent agreement between the current CCC results and those of Williart *et al.* [69]. The calculations of Gupta *et al.* [68] are in close agreement with the CCC results and those of Williart *et al.* [69] for energies above 3000 eV.

For energies above 200 eV, CCC, the GOS model of Gumus *et al.*

[46] and the PENELOPE code [47] predict similar behaviour, with the CCC results slightly below these other models. Below 200 eV, the CCC-pot calculation is in significant disagreement with these other approaches and predicts a substantially lower stopping power. As the models used for these positron calculations apply simple approximations, do not account for processes such as positronium-formation, and do not directly model the atom's target structure, the current CCC calculation is expected to be more accurate for the presented energies.

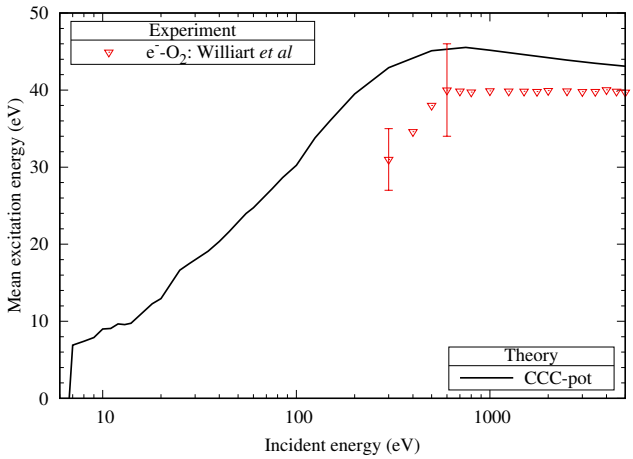

Figure 7.19: Mean excitation energy for positron scattering on oxygen. CCC-pot theoretical results are presented alongside experimental results for the e^--O_2 system from Williart *et al.* [69].

The mean excitation energy, directly obtained from the stopping power and the inelastic cross section, is shown in Fig. 7.19. There are no existing calculations of mean excitation energies for positron scattering on atomic oxygen or O_2. Williart *et al.* [69] only provide measurements and their uncertainty for incident energies of 300 eV and 600 eV for the e^--O_2 system. As their stopping power result was obtained with their measurements of mean excitation energy, we have extracted the experimental values for other energies using their presented stopping power and inelastic cross section. There is no discussion provided of the experimental uncertainty for these other incident energies.

The mean excitation energy between atomic oxygen and O_2 is expected to be similar at higher energies. For CCC calculations of e^- and e^+ scatter-

ing on H_2 [13], the e^+ mean excitation energy was found to follow similar behaviour as the e^- result but at a magnitude $\approx$ 20 % higher. A similar trend is found here but with a smaller difference between the e^+ and e^- result. At 600 eV, the CCC results lies just within the electron experimental uncertainty. Above this energy, as our results decrease, the difference between them and this experiment decreases to be within 10 % at 5000 eV. This experiment and the CCC results exhibit similar behaviour, with the mean excitation energy increasing to 600 eV. Above this energy, the mean excitation energy becomes nearly constant in the experiment and slowly decreases in the CCC-pot calculation. The sharp rise observed in the CCC-pot at threshold is due to positronium-formation.

7.3.9 Chapter summary

An outline is given for the target structure model and scattering calculation utilised to calculate cross sections for the positron-oxygen scattering system. The target structure in the present calculations is in good agreement with the energy levels and oscillator strengths of NIST and previous theory, reflecting its accuracy. A comprehensive set of cross sections and other quantities have been calculated for positron scattering from atomic oxygen within the current approach. These include total, elastic, momentum-transfer, direct ionisation, positronium-formation, electron-loss, inelastic, excitation, and stopping power cross sections for energies between threshold and 5000 eV. Quantities such as the scattering length, mean excitation energy, hidden Ramsauer-Townsend minimum, and the energy of the virtual positron-oxygen state were also calculated.

Good agreement is observed between current results and high-energy electron atomic oxygen experiment and theory for total ionisation, total, elastic, and bound- state excitations. Halved O_2 experiments for both positron and electrons are also in good agreement with the present calculations. For past positron calculations, agreement is observed at high energies with some available approaches. However, large differences are observed at lower energies and for the positronium-formation cross section.

Chapter 8

Positron scattering from neon and argon

This chapter presents the single-centre CCC and CCC-scaled complex model potential calculations for positron scattering from the noble gas atoms neon and argon. We present cross sections for both atoms for total, direct ionisation, electron-loss, elastic, positronium-formation, momentum-transfer, and total bound state excitation processes. The scattering length for each atom is also obtained from the low-energy elastic cross sections. Comparisons are made with previous frozen-core CCC calculations and other existing theory and experiment. Some sections in this chapter text or figures are adapted from a published work by the candidate [3]. The publishers of this article (EDP Sciences, Società Italiana di Fisica, and Springer Berlin Heidelberg) provide the right to use an article or a portion of an article in a thesis or dissertation without requesting permission.

8.1 Calculation

First, atomic orbitals are obtained for the ground state of each target's singly-charged ion using the HF method. For the Ar case, a MCHF calculation is then used to obtain the outer orbitals $4s$ to $5f$ for Ar^+. This HF, MCHF, and subsequent CCC calculations, have all orbitals below the outermost s and p orbitals frozen. For the Laguerre basis, the exponential fall-off (α_ℓ) was 2.0 for Ar and 1.5 for Ne. In the configuration structure for each noble gas atom, along with the ground configuration (ns^2np^6), we have

included $ns^2np^5n'\ell$ and $nsnp^6n'\ell$ configurations for $n'_\ell = 25 - \ell$ and $\ell \leq 8$, where the n is the outermost orbital for each noble gas ground state. To account for electron correlations more accurately we have included $np^4n'\ell n''\ell'$ configurations, where $n'\ell$ and $n''\ell'$ are all possible combinations of the orbitals $3d$ to $5f$ for Ne and $3d$ to $5f$ for Ar. We have also included $np^4n'\ell^2$ configurations for $4s \leq n'\ell \leq 5f$ for both Ne and Ar. We apply the non-relativistic LS-coupling scheme which is satisfactory for these relatively light atoms. Such a scheme results in 1034 and 1025 singlet states for Ne and Ar, respectively.

8.2 Structure

Table. 8.1 presents the excitation energies from the ground state to the first 12 LS-coupled singlet states of Ne. Compared to the previous frozen-core calculation, better agreement is observed with the reference data [59]. Almost all errors are less than 0.1 eV.

Table 8.1: Excitation energies (eV) for first 12 singlet Ne target states from the ground state, in the LS-coupling scheme.

	State	Term	CCC	CCC (FC)	NIST. [59]
1	$2s^22p^6$	^1S	0.000	0.000	0.000
2	$3s^22p^54s$	$^1P^o$	16.949	15.994	16.848
3	$2s^22p^53p$	^1D	18.659	17.681	18.636
4	$2s^22p^53p$	^1P	18.708	17.742	18.612
5	$2s^22p^53p$	^1S	18.996	18.035	18.966
6	$2s^22p^54s$	$^1P^o$	19.788	18.940	19.779
7	$2s^22p^53d$	$^1P^o$	20.083	19.098	20.040
8	$2s^22p^53d$	^1F	20.087	19.102	20.048
9	$2s^22p^53d$	$^1D^o$	20.104	19.120	20.048

Table 8.1: Excitation energies (eV) for first 12 singlet Ne target states from the ground state, in the LS-coupling scheme.

	State	Term	CCC	CCC (FC)	NIST. [59]
10	$2s^2 2p^5 4p$	^1D	20.264	19.340	20.297
11	$2s^2 2p^5 4p$	^1P	20.276	19.354	20.211
11	$2s^2 2p^5 4p$	^1S	20.379	19.515	20.368
Ion. limit			21.597	20.573	21.564

For Ar, excitation energies for the first 12 LS-coupled states are shown in Table. 8.2. Good agreement is found with our current calculation, the past theoretical results of Zatsarinny *et al.* [211], Ballance *et al.* [340], and the reference data [59]. Differences between our energies and the reference data are all within 0.2 eV for these 12 states.

Table 8.2: Excitation energies (eV) for first 12 Ar target states from the ground state, in the LS-coupling scheme.

	State	Term	CCC	Ref. [211]	Ref. [340]	NIST. [59]
1	$3s^2 3p^6$	^1S	0.000	0.000	0.000	0.000
2	$2s^2 2p^5 4s$	$^3P^o$	11.596	11.717	11.547	11.548
3	$3s^2 3p^5 4s$	$^1P^o$	11.786	11.998	11.805	11.828
4	$3s^2 3p^5 4p$	^3S	12.852	12.974	12.879	12.907
5	$3s^2 3p^5 4p$	$^3D^o$	13.099	13.134	13.045	13.076
6	$3s^2 3p^5 4p$	^1P	13.241	13.206	13.160	13.153
7	$3s^2 3p^5 4p$	^3P	13.239	13.229	13.160	13.172
8	$3s^2 3p^5 4p$	^1D	13.163	13.348	13.104	13.302
9	$3s^2 3p^5 4p$	^1S	13.467	13.534	13.440	13.480

Table 8.2: Excitation energies (eV) for first 12 Ar target states from the ground state, in the LS-coupling scheme.

	State	Term	CCC	Ref. [211]	Ref. [340]	NIST. [59]
10	$3s^2 3p^5 3d$	$^3P^o$	13.818	13.999	13.741	13.854
11	$3s^2 3p^5 3d$	$^3F^o$	13.980	14.079	13.768	13.979
12	$3s^2 3p^5 3d$	$^1F^o$	14.119	14.109	14.000	14.067
Ion. limit			15.713			15.760

The static dipole polarisability (α_D), quadrupole polarisability (α_Q), and octupole polarisability (α_O) of each noble gas structure model is provided in Table 8.3. The dipole polarisability (α_D) obtained was 2.85 a_0^3 for Ne and 12.9 a_0^3 for Ar. These values, although higher than experiment and other theory, are improved from the previous frozen-core calculations [70]. As α_D are a little above that of experiment and other theory we have followed the approach suggested in [379] where the reduced matrix elements for dipole transitions are scaled to obtain α_D equal to the experimental value. This scaling was utilised in both the structure and scattering calculations. The α_Q value for Ne is within the range of theoretical results, whereas, for Ar, α_Q is within 5% of the upper limits. For α_O, the value for Ne is within 3% of other calculations and for Ar is within 7%. The values of α_Q and α_O are expected to have minimal impact on the calculations as Ne and Ar have spherically symmetric charge distributions, however, the good agreement of these values with past theory give further support of the accuracy of the current structure model.

The calculations were conducted for partial waves up to $J = 10$. To obtain elastic differential cross sections (DCS) for energies above 100 eV, we utilised calculations with a simpler structure by including configurations with only $\ell \leq 4$, and performing the partial-wave expansion up to $J = 100$.

For elastic DCS at the forward scattering angles, an analytical extrapolation of these DCS is utilised based on the long-range polarisation potential, which is necessary to describe the cusp present at these angles [89]. Between the positronium-formation and direct ionisation threshold the elastic cross

section was linearly interpolated for each atom.

Table 8.3: Multipole polarisabilities for Ne and Ar. The α_D value for the CCC is scaled to be equal to the experimental value within the scattering calculation for both atoms. CCC results are presented alongside the range of theoretical values and experiment.

α	Atom	CCC	Theory [380, 381]	Exp [382]
α_D	Ne	2.67	2.37 - 2.71	2.67
	Ar	11.1	10.59 - 11.22	11.1
α_Q	Ne	7.33	6.41 - 7.52	
	Ar	54.50	49.54 - 52.8	
α_O	Ne	43.66	42.07	
	Ar	591.27	536.4 - 553.1	

8.3 Scattering

8.3.1 Total cross section

In Figs. 8.1 and 8.2, we present the total cross sections for positron scattering on neon and argon, respectively, for incident energies ranging from 0.1 eV to 5000 eV. The theoretical results shown are the current CCC-pot result and the previous frozen-core CCC calculations of Fursa and Bray [70], labelled as CCC (FC). The CCC-pot result is equivalent to the current single-centre CCC calculation for energies below the positronium-formation and for energies 10 eV above the ionisation threshold of each atom. CCC-pot results are obtained from the CCC-scaled complex model potential between these energies.

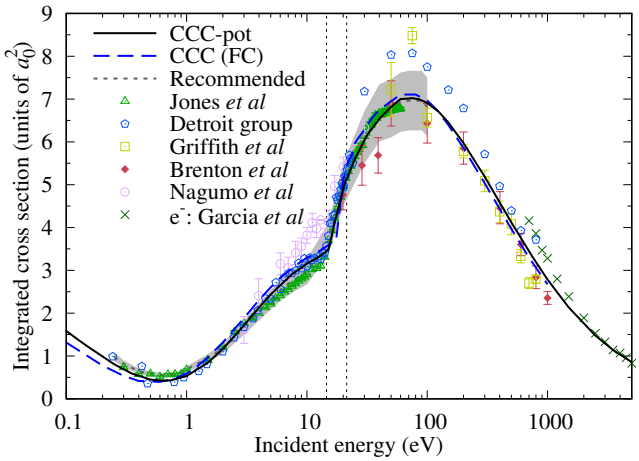

Figure 8.1: Total cross section for positron scattering on neon. Current CCC and CCC-pot calculations are compared with the previous CCC calculation of Fursa and Bray [70]. Also presented are experimental results for positrons by Jones *et al.* [71], the Detroit group [72, 73], Griffith *et al.* [74], Brenton *et al.* [75] and Nagumo *et al.* [76]. The grey shaded area represents the uncertainty of the recommended results of Ratnavelu *et al.* [15]. Experimental results for incident electrons are by García *et al.* [77]. Vertical dotted lines represent the positronium-formation and direct ionisation thresholds.

For the current CCC calculations for Ne, there is little difference with the previous frozen-core CCC calculations for energies above 0.6 eV. The current calculations are slightly lower than the frozen-core approach below 100 eV and slightly larger above this energy. For energies below 0.6 eV, the current calculations are also larger than the frozen-core calculations. For energies above 1 eV, the current CCC-pot results are in close agreement with the recommended results of Ratnavelu *et al.* [15]. Between 1 eV and the positronium-formation threshold the current and frozen-core CCC results agree well with the measurements of the Detroit group [72, 73], but are above the results of Jones *et al.* [71] and below those of Nagumo *et al.* [76]. The measurements of Nagumo *et al.* [76] agree with our calculation at low energies and between the positronium-formation and ionisation thresholds but elsewhere are notably larger than our calculation and the other experiments. Between the ionisation threshold and 300 eV, the Detroit group results are larger than our calculation and most other experiments. For energies above 100 eV, our calculation is mostly within the uncertainties of the measurements of Brenton *et al.* [75] and

Griffith *et al.* [74]. As a consistency check, we also compare with the electron-impact measurements of García *et al.* [77] at high energies, and find good agreement for energies above 2000 eV. Here the Born approximation is valid, which is the same for both electron and positron scattering.

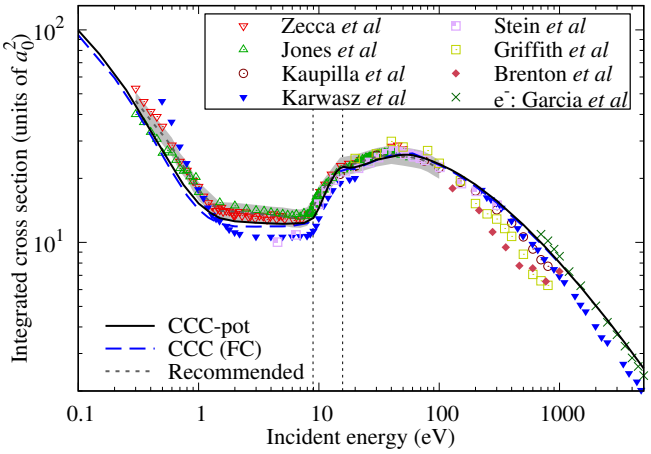

Figure 8.2: Total cross section for positron scattering on argon. Current CCC and CCC-pot calculations are compared with the previous CCC calculation of Fursa and Bray [70]. Also presented are experimental results for positrons by Zecca *et al.* [78], Jones *et al.* [71], Brenton *et al.* [75], Griffith *et al.* [74], Karwasz *et al.* [20, 79], and Kauppila *et al.* [73]. The grey shaded area represents the uncertainty of the recommended results of Ratnavelu *et al.* [15]. Measurements for incident electrons are by García *et al.* [77]. Vertical dotted lines represent the positronium-formation and direct ionisation thresholds.

From Fig. 8.2 we see that there is little difference between the current and frozen-core CCC calculations for Ar, except for energies below the positronium-formation threshold, where the current results are slightly larger. For energies above 10 eV, the current results are within the 10% uncertainty of the recommended results of Ratnavelu *et al.* [15]. The best agreement with these recommended results is found for energies above the direct ionisation threshold. For energies below 1 eV, the current results are slightly lower than the lower limits of the recommended values. Very close agreement is also found between the majority of the presented experiments and the current calculations for energies above the positronium-formation threshold and below 300 eV. The CCC-pot and frozen-core CCC results

are slightly larger than positron experiments for incident energies above 600 eV. This difference is likely a result of the measurements of Karwasz *et al.* [79] lacking an energy-loss discriminator, which causes forward scattered positrons to be measured as non-scattered, resulting in a systematic underestimation at high energies. Excellent agreement, however, is found between the CCC-pot calculation and the electron experiment of García *et al.* [77] above 1000 eV, which gives us confidence in the CCC-pot results at the lower energies.

Due to the high $\ell_{\max}$ and large number of states included in the current calculations we expect the errors associated with convergence to be within 2%. Based on the excellent agreement with excitation energies and multipole polarisabilities with past theory and experiment, the current structure models are estimated to contribute errors of within 2%. The single-centre CCC approach has very good numerical stability and we expect errors associated with this to be under 2%. The errors associated with the model potential approach will be most significant for the direct ionisation and positronium-formation cross sections. Therefore, for the total cross section, we expect an uncertainty of 10% in the energy region where model potential calculations were utilised. Outside of this region, where results are obtained directly from the CCC calculations, the uncertainty for the total cross section is expected to be within 5%. As the recommended results are only available between 0.25 eV and 100 eV, we provide accurate theoretical results for energies in which recommended values are unavailable.

8.3.2 Elastic cross section

The elastic cross sections for Ne and Ar are shown in Figs. 8.3 and 8.4 for energies between 0.1 eV to 5000 eV. In the energy region between the two given thresholds, where single-centre CCC calculations are unable to converge, the elastic cross section is linearly interpolated between the positronium-formation and ionisation thresholds. The instability in this energy region is a result of mismatched boundary conditions which occur due to the channels corresponding to positive-energy pseudostates being closed while positronium-formation channels are open. This means convergent results cannot be obtained between the positronium-formation and ionisation thresholds. Below the positronium-formation threshold, the elastic cross section is convergent and is the same as the total cross section. We, there-

fore, expect the uncertainty of the current results to be within 5% for all energies besides between the two thresholds, where results are expected to be within 10%.

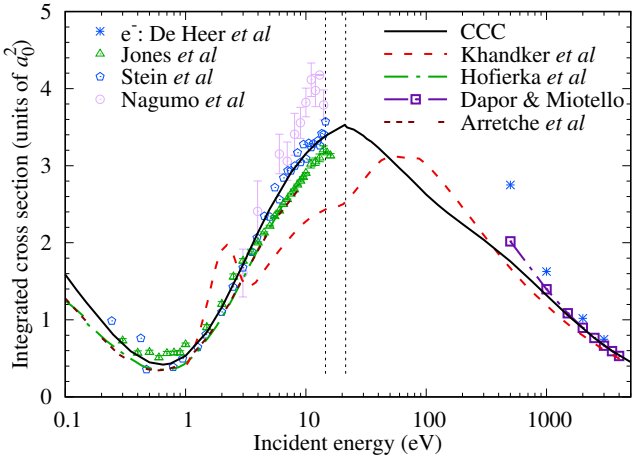

Figure 8.3: Elastic cross section for positron scattering on neon. CCC results are presented alongside the calculations of Khandker *et al.* [80], Hofierka *et al.* [81], Arretche *et al.* [82] and Dapor and Miotello [37]. Measurements of Nagumo *et al.* [76], Jones *et al.* [71], and Stein *et al.* [72] are shown alongside the electron results of De Heer *et al.* [83]. Vertical dotted lines represent the positronium-formation and direct ionisation thresholds.

In Fig. 8.3, we show the elastic cross section for positron scattering from neon. Calculations by Khandker *et al.* [80], Arretche *et al.* [82], Hofierka *et al.* [81], and Dapor and Miotello [37] are shown alongside the CCC results. The calculations of Arretche *et al.* [82] and Hofierka *et al.* [81] are lower than the CCC results across their calculated range, although they follow a similar shape. The results of Khandker *et al.* [80] have numerous features that are not found in the CCC calculation, with agreement only found above 2000 eV. The results of Dapor and Miotello [37] agree with the CCC calculation for energies above 1500 eV. We have also presented the electron-impact measurements of De Heer *et al.* [83] for energies above 500 eV, which agree with the current positron calculations above 3000 eV. All theoretical methods and experiments agree on the position of the minimum (≈ 0.6 eV), however, not on the magnitude of the cross section at the minimum. This minimum is a Ramsauer-Townsend minimum which occurs due the $J = 0$ partial wave yielding a near-zero cross section at this energy.

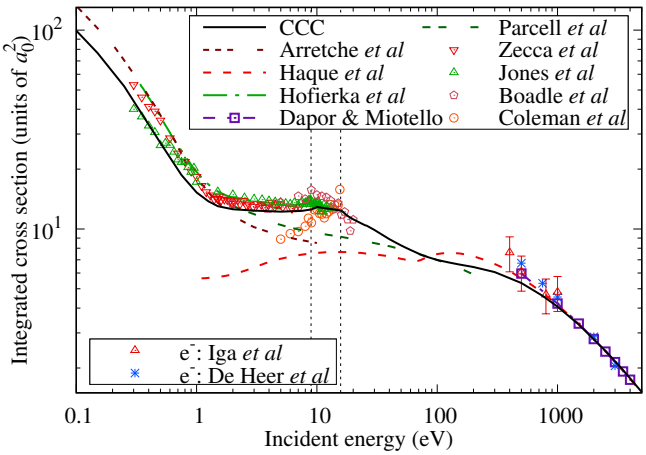

Figure 8.4: Elastic cross section for positron scattering on argon. CCC results are presented alongside the calculations of Arretche *et al.* [82], Haque *et al.* [84], Parcell *et al.* [85], and Hofierka *et al.* [81]. Measurements of Jones *et al.* [71], Zecca *et al.* [78], Boadle *et al.* [86] and Coleman *et al.* [87] alongside the electron results of Iga *et al.* [60] and De Heer *et al.* [83].

For argon, the elastic cross section for positron scattering is shown in Fig. 8.4. Here, alongside the CCC calculation, we present the calculations of Haque *et al.* [84], Hofierka *et al.* [81], and Dapor and Miotello [37]. We also show the experiments of Jones *et al.* [71, 108], Zecca *et al.* [78], Boadle *et al.* [86], Coleman *et al.* [87], and the electron experiment results of Iga *et al.* [60]. The calculations of Hofierka *et al.* [81] are higher than the current CCC results over its calculated range. The calculations of Haque *et al.* [84] are significantly lower than the CCC calculation up to 100 eV; however, for energies above 700 eV, there is excellent agreement between these calculations. The CCC calculation also has excellent agreement above 1000 eV with the results of Dapor and Miotello [37]. Comparison of CCC positron-impact results with the electron-impact experiments of Iga *et al.* [60] shows excellent agreement above 500 eV, and with De Heer *et al.* [83] agreement is seen for energies above 1000 eV. All of the experimental results predict a rise in the elastic cross section at the positronium-formation threshold.

Experimental results for the elastic cross section of noble gas atoms contain Wigner cusps at the positronium-formation threshold [87, 108], which are expected to result from virtual positronium formation. The current calculations have a small rise near the positronium-formation, but do not

exhibit this feature to the same extent as observed in experiment. This discrepancy is expected to result from the single-centre approximation utilised in the current calculations which causes instabilities at, and between, the positronium-formation and direct ionisation thresholds. To properly model this feature, two-centre calculations would be required.

Recommended results are not available for the elastic cross sections and there are no existing positron experiments for intermediate and high energies. We expect the current calculations to provide accurate results across the entire energy range.

8.3.3 Elastic differential cross sections: positron-Neon

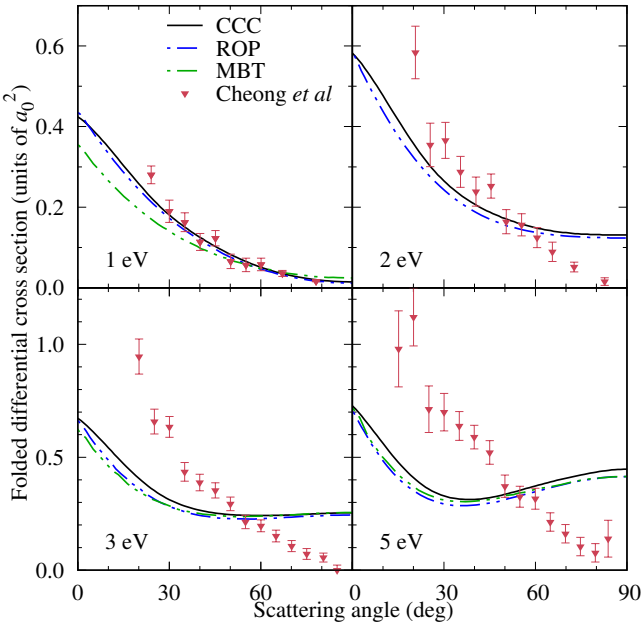

Figure 8.5: Elastic folded differential cross sections for positron scattering on neon with energies ranging from 1 eV to 5 eV. CCC results are presented alongside relativistic optical potential (ROP) [88] and many-body theory (MBT) calculations [89], and the measurements of Cheong *et al.* [88].

We present folded elastic DCS for Ne in Figs. 8.5 and 8.6 for energies between 0.4 eV and 40 eV. These cross sections are "folded" at 90° to allow comparison with existing positron beam experiments, where positrons with angles $> 90°$ are backscattered resulting in the measurement at angle θ also including the DCS of angle $180 - \theta$ [86]. For 1 eV and 2 eV, the CCC

results are within the uncertainty of most of the measurements of Cheong *et al.* [88] and is slightly above the ROP and MBT calculations of [88] and [89]. For 3 eV and 5 eV, the measurements are in significant disagreement with the theoretical results, while a good agreement is observed between the CCC results and other presented theory for angles above 30°. The reason for the discrepancy between theoretical and experimental DCS for 3 eV and 5 eV is unknown. An experimental and theoretical investigation undertaken by Cheong *et al.* [88] found that neither systematic error or multiple scattering effects could have resulted in this difference. For energies between 10 eV and 40 eV, there is generally good agreement between the presented theory, measurements, and current CCC calculations.

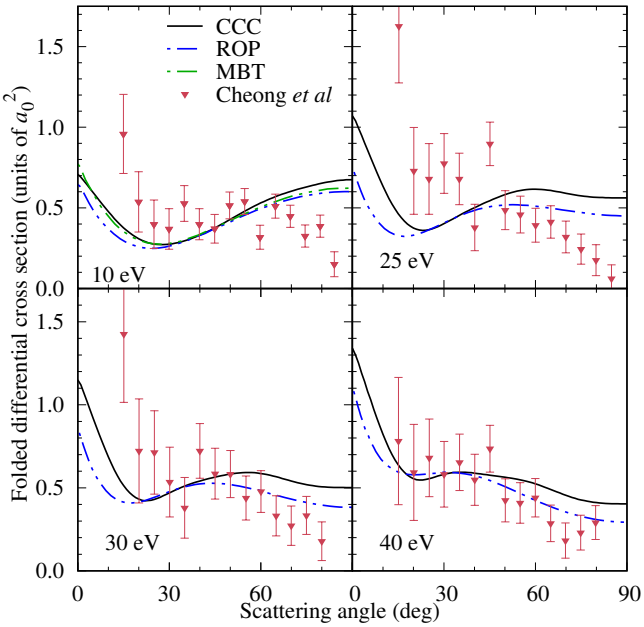

Figure 8.6: Elastic folded differential cross sections for positron scattering on neon with energies ranging from 10 eV to 40 eV. CCC results are presented alongside relativistic optical potential (ROP) [88] and many-body theory (MBT) calculations [89], and the measurements of Cheong *et al.* [88].

Elastic differential cross sections for energies between 50 eV and 300 eV are shown in Fig. 8.7 over the full angular range. The measurements of Kauppila *et al.* [93] were normalised to the existing theoretical results of the time, therefore, to facilitate comparison with the current results we

have renormalised them to the CCC at 90°. At 50 eV, the CCC calculation follows a similar shape to the experimental results of Kauppila *et al.* [93] and is higher than the other presented theory. For 100 eV, the closest agreement is found with the CCC calculation and those of Byron Jr and Joachain [91] for angles above 100°. For this energy, the different theoretical methods predict very different behaviour and magnitudes of the cross section. At 200 eV, the CCC calculation finds different behaviour from the previous calculations and experiment of Kauppila *et al.* [93], however, the shape of the calculation follows that of the electron measurement of Gupta and Rees [94] for angles below 60°. For 300 eV, on the other hand, very similar behaviour is observed between the current and other calculations, with the CCC cross sections being larger at higher angles. As with 200 eV, the shape of the CCC results resembles that of the electron measurement of Gupta and Rees [94] for angles below 60°.

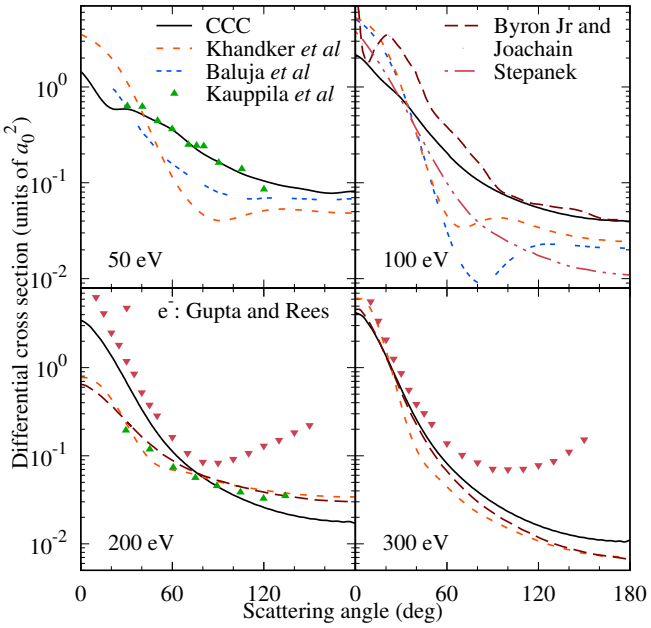

Figure 8.7: Elastic differential cross sections for positron scattering on neon with energies ranging from 50 eV to 300 eV. Theoretical results include the current CCC calculation and those of Khandker *et al.* [80], Baluja *et al.* [90], Byron Jr and Joachain [91], and Stepanek [92]. The measurements of Kauppila *et al.* [93] are shown for 50 eV and 200 eV, electron measurements by Gupta and Rees [94] are shown for 200 and 300 eV.

8.3.4 Elastic differential cross sections: positron-Argon

For Ar, folded elastic DCS are shown in Fig. 8.8 for energies between 0.4 eV and 1.5 eV. For 0.4 eV, the CCC calculation passes within the range of experimental values; for 0.7 eV, the CCC calculation agrees with two experimental points. For 1 eV, the CCC results are within the uncertainty of all the absolute measured points of Sullivan *et al.* [95], and for 1.5 eV, good agreement is found with the absolute measurements of Gilbert *et al.* [96].

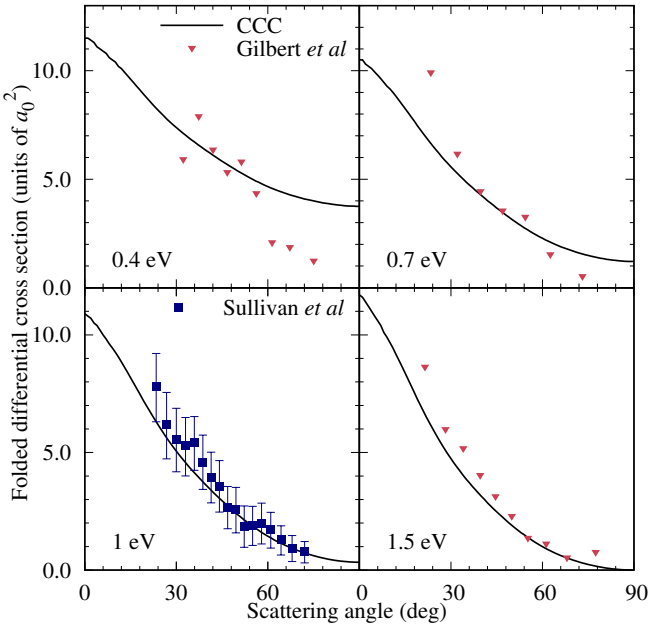

Figure 8.8: Elastic differential cross sections for positron scattering on argon with energies ranging from 0.4 eV to 1.5 eV. CCC results are shown alongside the measurements of Sullivan *et al.* [95] and Gilbert *et al.* [96].

In Fig. 8.9 the folded elastic DCS are presented for energies between 2 eV and 10 eV. We present the experimental results of Boadle *et al.* [86], Coleman and McNutt [97], Floeder *et al.* [98], and Smith *et al.* [99]. For which, the results of Boadle *et al.* [86] are absolute measurements and the latter three were rescaled by Boadle *et al.* [86]. The theoretical ROP results of Boadle *et al.* [86] are also presented. For these energies, we find very close agreement with the shape of the ROP results, however, the CCC results are slightly higher for all energies except 2 eV. The current results

are typically in the range of experiment, however, for large angles the behaviour predicted by Boadle *et al.* [86] differs from the other experiment and theoretical results.

In Fig. 8.10 the folded elastic DCS are presented for energies between 15 eV and 50 eV. As with the previous results, the older experiments have been rescaled by Boadle *et al.* [86]. Very close agreement is found with the shape of the current CCC results and the measurements of Smith *et al.* [99] for each of these considered energies. The ROP calculation finds very different behaviour for angles $> 30°$ to the CCC calculations for these energies. Current results are also within the uncertainty of Boadle *et al.* [86] for the majority of experimental points.

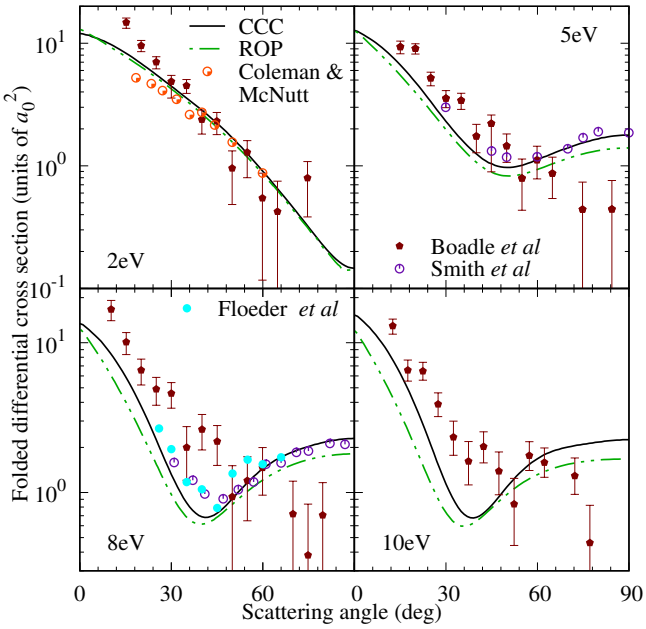

Figure 8.9: Elastic differential cross sections for positron scattering on argon with energies ranging from 2 eV to 10 eV. CCC results are shown alongside the ROP theoretical results of Boadle *et al.* [86] and the experimental results of Boadle *et al.* [86], Coleman and McNutt [97], Floeder *et al.* [98], and Smith *et al.* [99].

Fig. 8.11 presents elastic DCS for incident energies between 100 eV and 500 eV. For positron experiments we show the normalised measurements of Hyder *et al.* [101] and the absolute measurements of Dou *et al.* [102]. As the measurements of Hyder *et al.* [101] were normalised to theory and

experiment at the time, we have renormalised this experiment at 100 eV and 200 eV to the current calculations at 90°. At 100 eV, we find the CCC calculation to be a similar shape to both experiments and slightly above the results of Dou *et al.* [102]. The DCS for this energy is also below the theoretical results of Haque *et al.* [84] and Nahar and Wadehra [100], for all angles except below 15°. For 200 eV, the current DCS follows the shape of the results of Hyder *et al.* [101] and is below the other presented theory for angles above 10°. For 300 eV, there is good agreement with the measurements of Hyder *et al.* [101] and Dou *et al.* [102], with the CCC results again lower than the other theory.

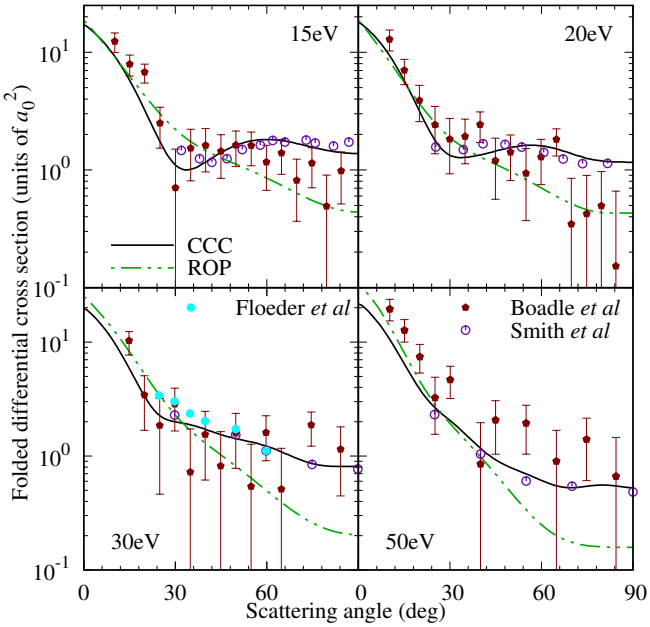

Figure 8.10: Elastic differential cross sections for positron scattering on argon with energies ranging from 15 eV to 50 eV. CCC results are shown alongside the ROP theoretical results of Boadle *et al.* [86] and the experimental results of Boadle *et al.* [86], Floeder *et al.* [98], and Smith *et al.* [99].

There is no existing positron experiment for 500 eV, so we instead compare our calculations with existing electron measurements and the theoretical results of Dapor and Miotello [37]. The remarkable agreement between the two theories indicates that 500 eV is close to the Born approximation regime.

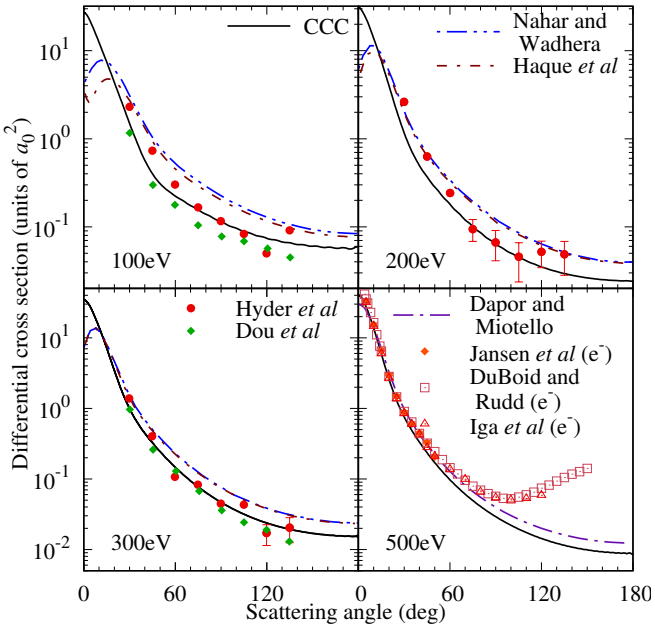

Figure 8.11: Elastic differential cross sections for positron scattering on argon with energies ranging from 100 eV to 500 eV. CCC results are shown alongside the theoretical results of Nahar and Wadehra [100], Haque *et al.* [84], and Dapor and Miotello [37] and the experimental results of Hyder *et al.* [101] and Dou *et al.* [102]. For 500 eV, the experimental results of Iga *et al.* [60], DuBois and Rudd [103], and Jansen *et al.* [104] for the electron case are shown.

8.3.5 Momentum-transfer cross section

The momentum-transfer cross section for the considered noble gas systems are presented in Figs. 8.12 and 8.13. For these cross sections we expect the uncertainty to be the same as the elastic cross section. A dip at low energies can be observed in the momentum-transfer cross section for each atom, which is due to the minimum in the s-wave. For elastic scattering, a Ramsauer-Townsend minimum occurs due to the s-wave phase shift becoming 0 while higher J-wave phase shifts are small, as occurs for Ne. The presence of the minimum in the s-wave can also be hidden due to the contributions of higher J-waves counteracting the minimum in the s-wave, as occurs for Ar. This can be observed in the J-wave contributions to the elastic cross sections presented in Figs. 8.16 and 8.17. For the momentum-transfer cross section, a minimum occurs when the s- and p-wave phase shifts are equal and the contributions from the higher J-wave

phase shift differences are small [82]. Therefore, a minimum can occur in the momentum-transfer cross section even if none is present for the elastic case.

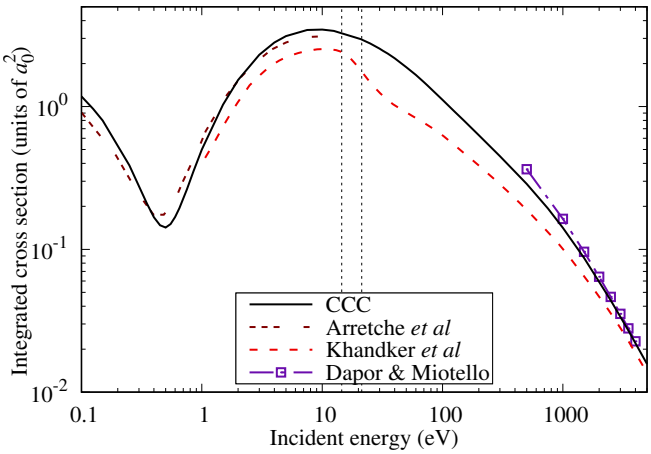

Figure 8.12: Momentum-transfer cross section for positron scattering on neon. CCC results are shown alongside the theoretical results of Arretche *et al.* [82], Khandker *et al.* [80], and Dapor and Miotello [37]. Vertical dotted lines represent the positronium-formation and direct ionisation thresholds.

In Fig. 8.12, the momentum-transfer cross section for positron scattering on neon is shown. The current CCC calculations are compared with the theoretical results of Arretche *et al.* [82], Khandker *et al.* [80], and Dapor and Miotello [37]. The calculations of Arretche *et al.* [82] are close to the CCC calculations from 2 eV to 10 eV; below 2 eV, these calculations follow a similar shape to the CCC results, but with a minimum at a slightly lower energy. Across the calculated energy range, Khandker *et al.* [80] follows a similar shape to CCC, but predicts lower values and has a much steeper decrease in the cross section at the positronium-formation threshold. The results of Dapor and Miotello [37] are in excellent agreement with CCC for energies above 1000 eV.

Fig. 8.13 shows the momentum-transfer cross section for positron scattering on argon. Alongside the current CCC calculations we show the calculations of Haque *et al.* [84], Dapor and Miotello [37], Arretche *et al.* [82], Šuvakov *et al.* [105], and the electron experimental results of Iga *et al.* [60]. The results of Šuvakov *et al.* [105] follow a similar shape to CCC, but the

minimum occurs at a higher energy and, instead of sharply decreasing above 30 eV, follows a linear path. Calculations of Arretche *et al.* [82] yield similar results to those of Šuvakov *et al.* [105], but with a shallower minimum. The results of Haque *et al.* [84] are similar in shape to CCC with excellent agreement above 1000 eV. The CCC cross sections are slightly below the measurements of Iga *et al.* [60]. As with neon, we find excellent agreement with the calculation of Dapor and Miotello [37] for energies above 1000 eV.

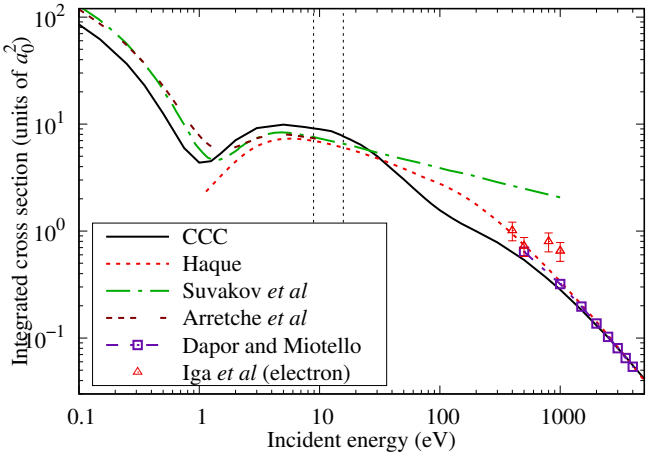

Figure 8.13: Momentum-transfer cross section for positron scattering on argon. CCC results are shown alongside the theoretical results of Arretche *et al.* [82], Haque *et al.* [84], Šuvakov *et al.* [105], Dapor and Miotello [37] and the electron experiment of Iga *et al.* [60]. Vertical dotted lines represent the positronium-formation and direct ionisation thresholds.

8.3.6 Low-energy scattering

The elastic cross section for incident energies below 1 eV is shown in Fig. 8.14 for positron scattering from Ne. Compared to the frozen-core CCC [70], the current calculation predicts a higher cross section for these energies, and is almost indistinguishable from the calculations of Poveda *et al.* [107]. The calculations of McEachran *et al.* [106] are around 20% higher.

In Fig. 8.15, we show the positron-argon elastic cross section for energies between 10^{-4} eV and 1 eV. The current CCC calculation is in close agreement with the frozen-core CCC calculation, with it slightly higher across the presented range. The calculations of Poveda *et al.* [107] and McEachran *et al.* [109] are significantly larger than the two CCC

calculations across the presented energy range. The calculation of Green *et al.* [89] is in excellent agreement with the current CCC calculation for energies below 0.4 eV.

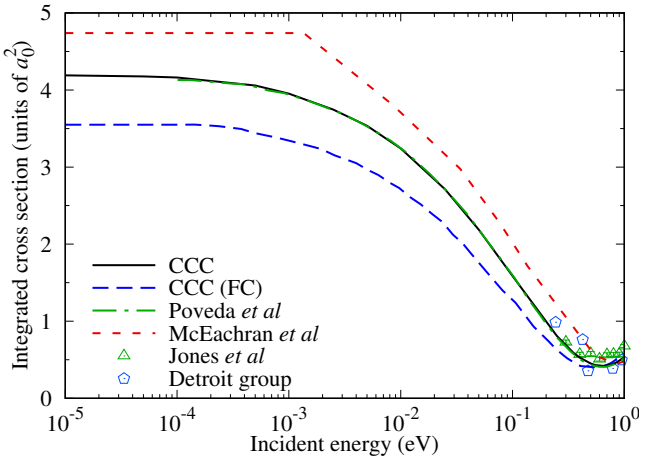

Figure 8.14: Total cross section for positron scattering on neon for energies below 1 eV. Theoretical results include the CCC and frozen-core CCC calculations alongside those of McEachran *et al.* [106], and Poveda *et al.* [107]. Measurements are from the Detroit group [72, 73] and Jones *et al.* [108].

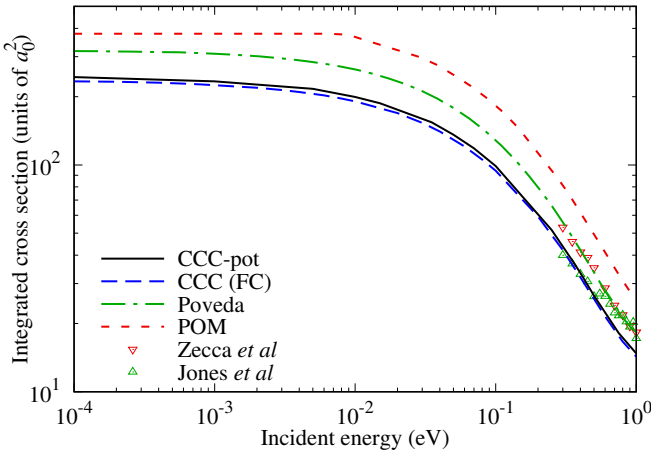

Figure 8.15: Total cross section for positron scattering on argon for energies below 1 eV. Theoretical results include the CCC and frozen-core CCC calculations alongside those of McEachran *et al.* [109], and Poveda *et al.* [107]. Measurements are from Zecca *et al.* [78] and Jones *et al.* [108].

The scattering length was obtained from the asymptote for low-energy

elastic cross section through Eq. 2.66. The values for Ne and Ar are given in Table 8.4 alongside the results from past theory and the experimental value of Zecca *et al.* [78] for Ar, which was extrapolated to low energies with the frozen-core CCC calculation. The current scattering length result for Ne is in good agreement with other calculations. For Ar, close agreement is found with the MBT calculations, and within the uncertainty of the experimental estimate.

Table 8.4: Scattering length (a_0) for neon and argon. Current results are from CCC, frozen-core CCC (FC), model potential (MP), many-body theory (MBT), polarised orbitals method (POM) and experiment.

Atom	CCC	CCC (FC)	MP [107]	MBT [81]	POM	Exp.
Ne	-0.58	-0.53	-0.57	-0.53	-0.61 [106]	
Ar	-4.42	-4.30	-5.05	-4.90	-5.30 [109]	-4.9 ± 0.7 [78]

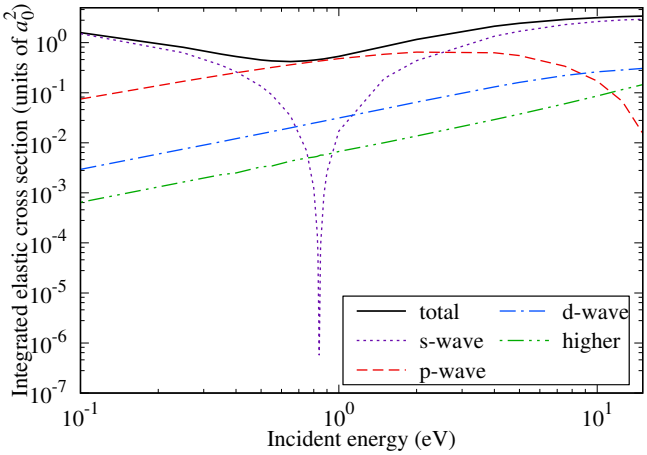

Figure 8.16: Elastic cross sections for positron scattering on neon and its *s*-, *p*-, *d*-, and higher *L*-wave contributions for the energy range 0.1 eV to 15 eV.

In Fig. 8.16 we show the partial-wave components of the elastic scattering of Ne for energies between 0.1 eV and 15 eV. The minimum in the *s*-wave component can be clearly observed at 0.84 eV. For comparison, we present this result with other theoretical calculations in Table. 8.5. The current calculation is in agreement with the POM calculations of McEachran *et al.*

[106], close to the semi-empirical model potential (SEMP) calculation of Arretche *et al.* [82], and 0.18 eV higher than the MBT calculation of Green *et al.* [89]. The s-wave component of the cross section is dominant for energies below 0.4 eV and above 2 eV, with the p-wave component dominant between these two energies.

For Ar, the partial-wave components for the elastic scattering are shown in Fig. 8.17. The minimum can be observed in the s-wave component of the cross section at 2.14 eV. In this case, the current result is lower than all other theory, with closest agreement observed with the MBT calculation [89]. Similar to Ne, the s-wave component is dominant for energies below 0.4 eV and above 2.5 eV, with the p-wave component dominant between these two energies. In this case, as previously observed [82, 89], it is clear that the contributions of the higher J-waves counteract the decreased s-wave and, therefore, hide the presence of the s-wave minimum in the elastic cross section.

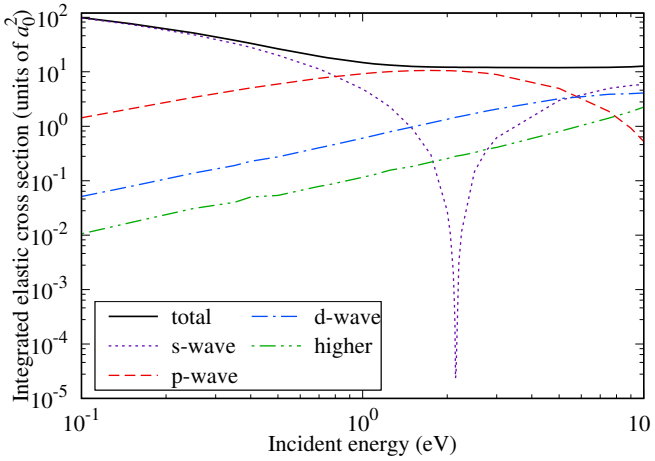

Figure 8.17: Elastic cross sections for positron scattering on argon and its s-, p-, d-, and higher L-wave contributions for the energy range 0.1 eV to 10 eV.

8.3.7 Electron-loss cross section

The electron-loss cross section (ELCS) is the sum of positronium-formation and direct ionisation. The single-centre CCC calculation yields this cross section directly by summing the cross sections for all positive-energy pseudostates. The CCC-pot separation of Ps-formation and direct

Table 8.5: Energy of the s-wave minimum for neon and argon.

Atom	CCC	SEMP [82]	MBT [89]	POM
Ne	0.84	0.79	0.66	0.85 [106]
Ar	2.14	3.05	2.35	2.76 [109]

ionisation is constrained by this result at energies a little above the ionisation threshold. For the region where results are obtained from the model potential calculation the error is expected to be within 10%. Outside of this region, errors are again expected to be within 5%. Hence, we expect the CCC method to be particularly accurate for this cross section.

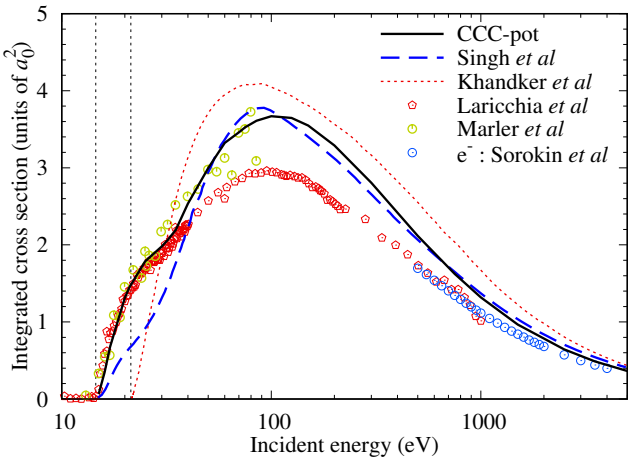

Figure 8.18: Electron-loss cross section for positron scattering on neon. The current CCC-pot and previous frozen-core CCC [70] results are shown alongside the calculations of Singh *et al.* [110]. Measurements for positrons are from Marler *et al.* [111], Laricchia *et al.* [112] and those for electrons are by Sorokin *et al.* [113]. Vertical dotted lines represent the positronium-formation and ionisation thresholds.

In Fig. 8.18, results are shown for the ELCS of positron-neon scattering. Excellent agreement is found between the CCC-pot calculation and the experiment of Marler *et al.* [111] below 30 eV, and above 30 eV agreement is found with the upper measurements of this experiment. Agreement is found with the current calculation and the measurements of Laricchia *et al.* [112] for energies below 30 eV; above this energy, this experiment is lower

than the current calculation and that of Singh *et al.* [110]. This difference, however, decreases with increasing energy and is most significant at the peak cross section, where the measurements of Laricchia *et al.* [112] are more than 20% lower than the current theory. The calculation of Singh *et al.* [110] is in close agreement with the CCC-pot results for energies above 1000 eV but typically is lower than the CCC-pot for energies below this. On the other hand, the results of Khandker *et al.* [80] are larger than those of the CCC-pot for all energies above 30 eV. We also compare with the frozen-core CCC results of Fursa and Bray [70]. These are marginally smaller than the present results at the higher energies as they do not include ejection of the 2s electrons.

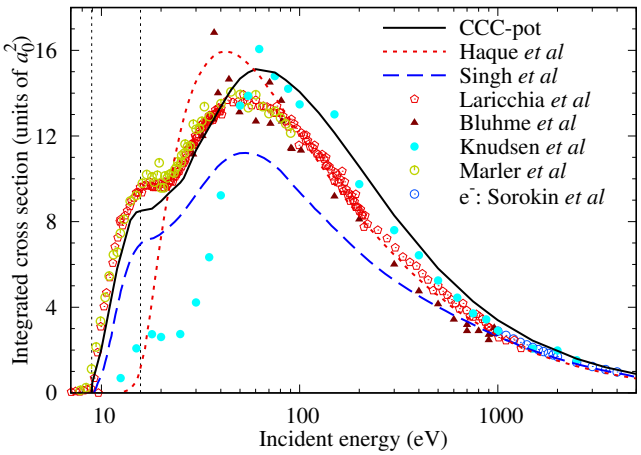

Figure 8.19: Electron-loss cross section for positron scattering on argon. The current CCC-pot and previous frozen-core CCC [70] results are shown alongside the calculations of Singh *et al.* [110] and Haque *et al.* [84]. Measurements for positrons are from Marler *et al.* [111], Laricchia *et al.* [112], Knudsen *et al.* [29], Marler *et al.* [111], and Bluhme *et al.* [114]. Electrons measurements are by Sorokin *et al.* [113]. Vertical dotted lines represent the positronium-formation and ionisation thresholds.

The ELCS results for positron-argon scattering are shown in Fig. 8.19. For energies below 25 eV, the CCC-pot calculation is slightly below experiment. Between 25 eV and 50 eV, there is good agreement with experiment and the CCC-pot calculation. Above 50 eV, however, the CCC-pot result is notably higher than most experimental results, with agreement only found, again, above 2000 eV. The CCC-pot calculation predicts a similar shape to

those of Singh *et al.* [110], and both calculations predict a peak at approximately 60 eV. The CCC-pot results, however, are significantly larger across the entire calculated energy range. Haque *et al.* [84] predict a peak cross section lower than the other calculations, and above 60 eV is between the current calculation and those of Singh *et al.* [110], except for above 1000 eV where it converges with the Singh *et al.* [110] calculation. As for the neon target, the present CCC results at energies above 100 eV are a little higher than the CCC (FC) [70]. This time this is due to the inclusion of the ejection of the 3s electrons.

The consistency of the present CCC results and the CCC(FC) ones for both targets gives us confidence in the latest CCC results for the electron-loss cross section. Due to the discrepancies that exist between theory and experiment at intermediate energies, further experimental investigation would be most welcome.

8.3.8 Positronium-formation cross section

The positron-neon positronium-formation cross section is presented in Fig. 8.20. The recommended values of Ratnavelu *et al.* [15] are in agreement with the current calculations for energies below 30 eV. For energies above 30 eV, the current results are larger than the recommended results and the available measurements but follow the shape of the data obtained by Laricchia *et al.* [112]. The CCC-pot calculation is higher than the calculations of Singh *et al.* [110] and McEachran and Stauffer [115] over the entire presented energy range, whereas the calculation of Gilmore *et al.* [116] is higher at energies below 22 eV. Given the discrepancy with the corresponding experiment for the ELCS above, we expect the CCC-pot results to be somewhat higher than experiment, and the recommended cross sections.

The positron-argon positronium-formation cross section is shown in Fig. 8.21. Compared to the recommended values of Ratnavelu *et al.* [15] the current CCC-pot calculations are sufficiently close to the recommended values and experiment over most of the energy range. Comparison with other theory shows that the CCC-pot results are roughly in between the calculations of Singh *et al.* [110] and McEachran and Stauffer [115] over much of the energy range of interest.

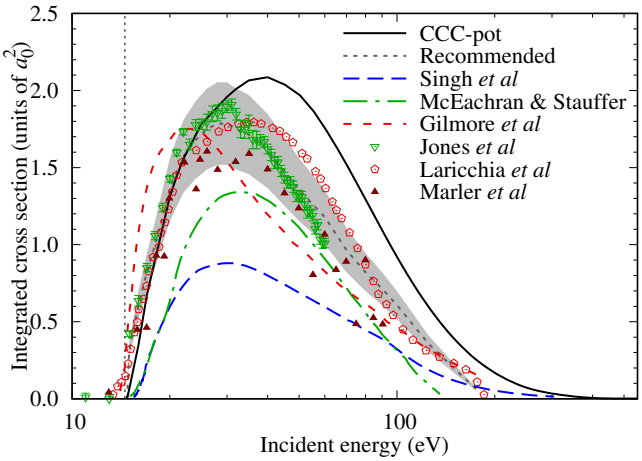

Figure 8.20: Positronium-formation cross section for positron scattering on neon. CCC-pot results are presented alongside the results of the calculations of Singh *et al.* [110], McEachran and Stauffer [115], and Gilmore *et al.* [116], and the recommended results of Ratnavelu *et al.* [15]. The grey shaded area represents the uncertainty of the recommended results. Measurements are from Jones *et al.* [71], Marler *et al.* [111], and Laricchia *et al.* [112]. The threshold is indicated by the vertical dotted line.

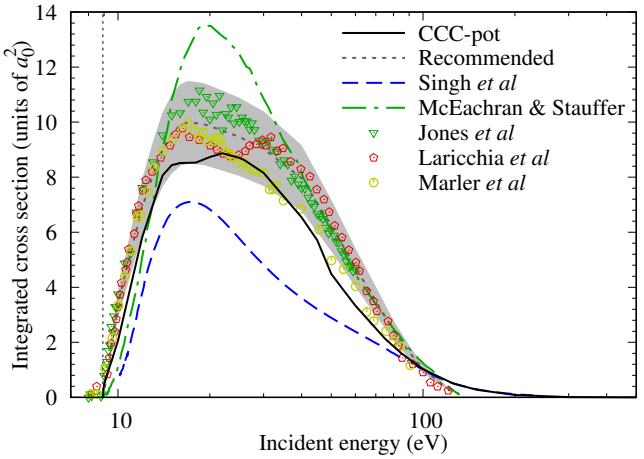

Figure 8.21: Positronium-formation cross section for positron scattering on argon. CCC-pot results are presented alongside the results of the calculations by Singh *et al.* [110], Gilmore *et al.* [116], and McEachran and Stauffer [115], and the recommended results of Ratnavelu *et al.* [15]. The grey shaded area represents the uncertainty of the recommended results. Measurements are from Jones *et al.* [71], Marler *et al.* [111], and Laricchia *et al.* [112]. The threshold is indicated by the vertical dotted line.

The above two comparisons between CCC-pot results and the recommended data for Ar and Ne are rather different. The first thing to note is that the Ps-formation cross section at its maximum is around five times higher than for Ne, and so the discrepancy for Ne has to be seen in that context. Due to the inclusion of scaling procedures to increase the accuracy of the positronium-formation cross section for energies below its maximum, we expect errors for these energies to be within 10%. For higher energies, we estimate an uncertainty of 20%.

8.3.9 Direct ionisation cross section

The direct ionisation cross sections are obtained as the difference of the ELCS and Ps-formation, and are given for positron scattering on neon in Fig. 8.22. The current CCC-pot result is within the uncertainty limits of the recommended results of Ratnavelu *et al.* [15] for energies above 50 eV. For energies between 100 eV and 1000 eV, the CCC-pot calculation agrees within uncertainty with the measurements of Jacobsen *et al.* [10]. For energies between 50 eV and 80 eV, the CCC-pot calculation is within the uncertainty of the experiment of Mori and Sueoka [11], slightly above that of Laricchia *et al.* [112], and below other experiments. Below 50 eV, the CCC-pot cross sections are below the existing experiment and theory. There is good agreement with the calculation of Bartschat [117] above 50 eV to its maximum calculated energy of 100 eV. The CCC-pot is substantially larger than the calculation of McEachran and Stauffer [119] for energies above 110 eV and that of Singh *et al.* [110] between 150 eV and 700 eV. The calculation of Montanari and Miraglia [118] is significantly larger than that of the CCC for energies below 300 eV, with a peak cross section over 15% larger than the CCC calculation. The peak direct ionisation cross section is predicted to occur at 150 eV by the CCC-pot, slightly above the energy predicted by Montanari and Miraglia [118], approximately 50 eV above that of McEachran and Stauffer [119] and almost twice that of Singh *et al.* [110]. Very close agreement is found between the CCC-pot calculation and that of Singh *et al.* [110] above 700 eV, and for Montanari and Miraglia [118] above 300 eV.

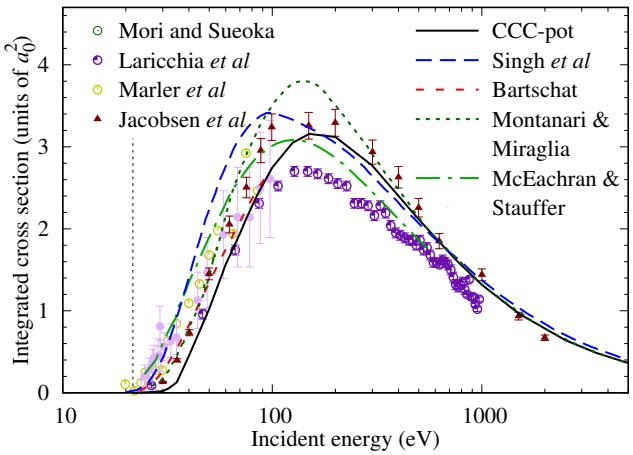

Figure 8.22: Direct ionisation cross section for positron scattering on neon. CCC-pot results are compared with the calculations of Bartschat [117], Singh *et al.* [110], Montanari and Miraglia [118], McEachran and Stauffer [119], and the recommended results of Ratnavelu *et al.* [15]. The grey shaded area represents the uncertainty of the recommended results. Measurements are from Laricchia *et al.* [112], Marler *et al.* [111], Mori and Sueoka [11], and Jacobsen *et al.* [10]. The threshold is indicated by the vertical dotted line.

The corresponding results for the argon target are presented in Fig. 8.23. The current CCC-pot calculations follow a similar shape to the recommended results of Ratnavelu *et al.* [15] but are a little outside the upper uncertainty limits for energies above 30 eV. CCC-pot results are within the error of the experiment of Laricchia *et al.* [112] for energies below 30 eV and above 500 eV. Between these energies, the CCC-pot results overestimate this experiment and that of [111], but follow the shape of these experiments with a peak at 100 eV. The CCC-pot calculation, however, is within the uncertainty of Mori and Sueoka [11] from 30 to 100 eV. The calculation of Singh *et al.* [110] is significantly lower than the CCC-pot results for energies above 40 eV and is below experiment between 60 and 300 eV. On the other hand, the calculation of Montanari and Miraglia [118] is notably larger than other theory to 70 eV, with a peak cross section at 60 eV. The calculation of Bartschat [117] follows a similar shape to the CCC-pot result and predicts a similar peak cross section at slightly lower energy. The CCC-pot results are slightly higher than these other calculations for energies above 1000 eV, but by 5000 eV the differences between each method are minimal.

As the positronium-formation rapidly decreases above its maximum, the

impact of the higher uncertainty at these energies is not expected to significantly contribute to the calculation of the direct ionisation cross section, which we estimate to be within 15% of the true result for both targets.

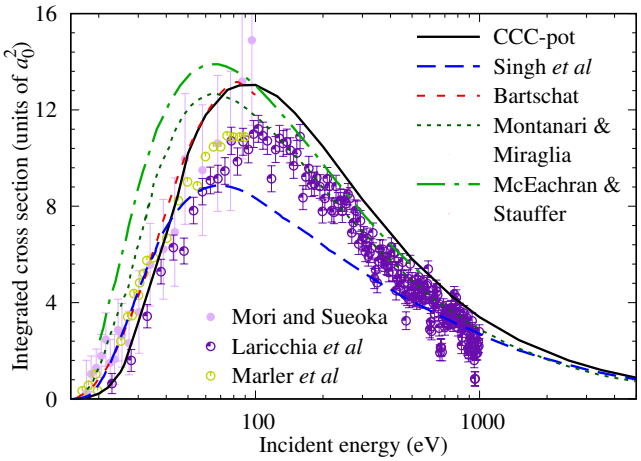

Figure 8.23: Direct ionisation cross section for positron scattering on argon. CCC-pot results are compared against the calculations of Bartschat [117], Singh *et al.* [110], Montanari and Miraglia [118], and the recommended results of Ratnavelu *et al.* [15]. The grey shaded area represents the uncertainty of the recommended results. Measurements are from Laricchia *et al.* [112], Marler *et al.* [111], and Mori and Sueoka [11]. The threshold is indicated by the vertical dotted line.

8.3.10 Total bound excitation cross section

We present the positron-impact total bound excitation cross section (labelled CCC-pot) for Ne and Ar in Figs. 8.24 and 8.25, respectively, from the excitation energy threshold to 5000 eV. For energies higher than 10 eV above the direct ionisation threshold, results are obtained directly from the CCC calculation, whereas, below this point, results are calculated with a CCC model containing only bound states and the CCC-scaled complex model potential. The bound state CCC model is used for energies closer to the excitation threshold and the CCC-scaled complex model potential is used for energies closer to the direct ionisation threshold, with these two models smoothly connected at their intersection. The instability of the single-centre CCC model, which contains both bound and continuum states, can be observed towards the direct ionisation threshold, where it rapidly increases, demonstrating the benefit of using the complex model potential. For ener-

gies below the direct ionisation threshold the uncertainty is expected to be within 15%, whereas, above this threshold, uncertainty is within 10%.

Starting with Fig. 8.24, we see that from threshold to 100 eV the CCC-pot results are within the error bars of the experiments of Coleman *et al.* [121] and Mori and Sueoka [11]. The CCC-pot calculation predicts this cross section to rise to a maximum at 30 eV before slowly descending to 5000 eV. The calculation of Kothari and Joshipura [120] agrees with the CCC-pot result below 30 eV, but not above until around 1000 eV. For energies above 200 eV, the current calculation is in excellent agreement with the electron semi-empirical results of De Heer *et al.* [83], as we would expect at the higher energies.

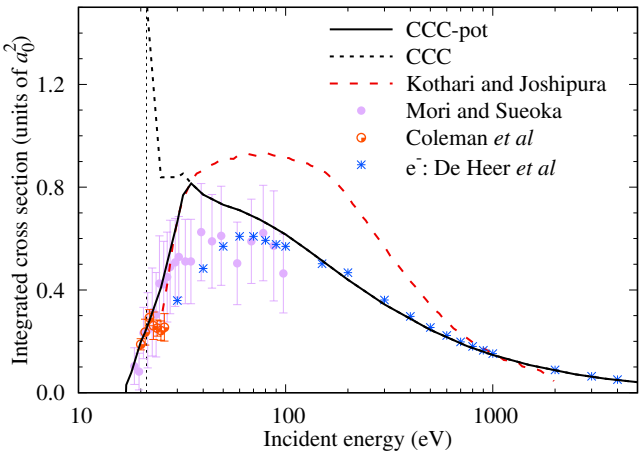

Figure 8.24: Total bound excitation cross section for positron scattering on neon. CCC results are presented alongside the calculations of Kothari and Joshipura [120] and the measurements of Mori and Sueoka [11] and Coleman *et al.* [121]. Semi-empirical results of De Heer *et al.* [83] for incident electrons are also shown. The vertical dotted line represents the direct ionisation threshold.

The corresponding results for argon are given in Fig. 8.25. Our current CCC and CCC-pot results are shown alongside the calculations of Kothari and Joshipura [122] and Parcell *et al.* [85], and the experiment of Mori and Sueoka [11], Coleman *et al.* [121], and Sullivan *et al.* [23]. The calculation of Kothari and Joshipura [122] exhibits very different behaviour to the CCC calculation, peaking at almost twice the largest value of the CCC and decreasing far more rapidly at higher energies. The calculation of Parcell *et al.* [85] is smaller than the CCC result, particularly at lower energies, and

has its peak cross section approximately 40 eV above the other two calculations. Good agreement is found between the experimental data of Mori and Sueoka [11] and the CCC-pot results, within the error bars of most points. The measurements of Sullivan *et al.* [23] and Coleman *et al.* [121] are significantly lower than both the CCC and the experiment of Mori and Sueoka [11] for energies above 15 eV. This is expected for the measurements of Sullivan *et al.* [23] as their results are of only excitation to the $4s$ state and, therefore, are only equivalent to the total bound-state excitation cross section near-threshold. On the other hand, the results of Coleman *et al.* [121] are expected to underestimate the true result due to under-counting of the positrons. For energies above 300 eV, we find close agreement between the current positron-impact and the electron-impact semi-empirical results of De Heer *et al.* [83].

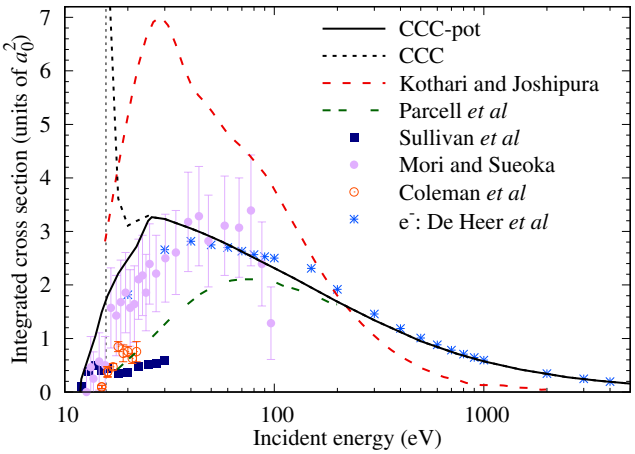

Figure 8.25: Total bound excitation cross section for positron scattering on argon. CCC results are presented alongside the calculations of Kothari and Joshipura [122] and Parcell *et al.* [85]. Measurements are by Mori and Sueoka [11], Sullivan *et al.* [23], and Coleman *et al.* [121]. Semi-empirical results of De Heer *et al.* [83] for incident electrons are also shown. The vertical dotted line represents the direct ionisation threshold.

8.4 Chapter summary

In this chapter, the structure models utilised for the positron scattering calculations from neon and argon are described. Results for the excitation energy and dipole polarisabilities are then shown alongside existing theory,

NIST, and previous frozen-core CCC calculations. Following this, single-centre CCC calculations of positron scattering from Ne and Ar noble gases are presented for energies between 10^{-5} eV and 5000 eV. Compared to previous frozen-core CCC calculations, quantities such as the dipole polarisability and excitation energy are significantly improved due to the opening of the upper s and p shells in these calculations. Due to the implementation of the MCHF and large CI expansions, the current structure model is expected to give more reliable and accurate results than the frozen-core approximation. However, differences between the open- and frozen-core cross sections were mostly minimal. The one exception was the elastic cross section for neon for energies below 0.6 eV, in which the current approach leads to significantly larger cross sections. Through the use of the complex model potential procedure outlined in Chapter. 3, we have also obtained cross sections for positronium-formation, direct ionisation, and inelastic scattering between the positronium-formation and direct ionisation thresholds.

Overall, the CCC-pot calculations are found to be in satisfactory agreement with experiment. Exceptions include the electron-loss cross section for both atoms at intermediate energies, and some elastic differential cross sections. Agreement with previous calculations is rather mixed. Previous review articles have presented several recommended cross sections for these systems. However, these have been limited in both the incident energies and scattering processes considered. Therefore, the current calculations have addressed an existing gap in the literature for accurate theoretical results at intermediate and high energies and provides results for scattering processes in which previous theoretical and experimental work is limited. Another benefit of the current approach is that it allows the extraction of individual bound-state excitation cross sections, which will be a focus of future work.

Chapter 9

Positron scattering from boron

This chapter first describes the structure and scattering calculations undertaken for positron scattering on boron. To validate the structure models comparisons are made with existing values for the excitation energies, oscillator strengths, and multipole polarisabilities. Then, cross sections are provided for the significant scattering processes of this system. An analysis is also provided for low-energy scattering, with results for the scattering length and energy of the virtual positron level given.

9.1 Structure

9.1.1 Calculation details

A MCHF calculation was used to obtain orbitals up to $4d$. The current model contained $N_\ell = 20 - \ell$ with $\alpha_\ell = 1.0$. Configurations included $1s^2 2s^2 n\ell$ and $1s^2 2p^2 n\ell$ for $\ell \leq \ell_{\max}$. Also included was $1s^2 2s 2p n\ell$ for $\ell \leq 4$, $1s^2 2p^3$, and $1s^2 2s n\ell^2$ for all orbitals between $2p$ and $3d$. Above the direct ionisation threshold, a 1559-state $\ell_{\max} = 9$ was used to 15 eV. Above 15 eV, a 1353-state $\ell_{\max} = 8$ model was used. Both of these previous models contained all states with energies up to 100 eV relative to the B^+ direct ionisation threshold. For energies below the positronium-formation, a 1673-state model with $\alpha_\ell = 3.0$, $\ell_{\max} = 20$, and energies up to 350 eV above the direct ionisation threshold was used. This larger model was required to obtain convergent results at low energies due to the slow convergence with

ℓ for energies below the positronium-formation threshold. The electron-loss cross section was extrapolated above 50 eV using a 3832 state Born model containing the above configurations, in addition to $1s^2 2s 2pn\ell$, $1s^2 2s 3sn\ell$ and $1s^2 2s 3pn\ell$ for $\ell \leq 8$, $1s^2 2s 3dn\ell$ and $1s 2s^2 2pn\ell$ configurations.

9.1.2 Convergence study

A convergence study of the electron-loss (positronium-formation plus direct ionisation) cross section for different $\ell_{\max}$ for e^+-B is shown in Fig. 9.1. This cross section converges quickly with calculations fully converged for $\ell_{\max} \geq 8$ for energies above 10 eV, and $\ell_{\max} \geq 4$ above 50 eV.

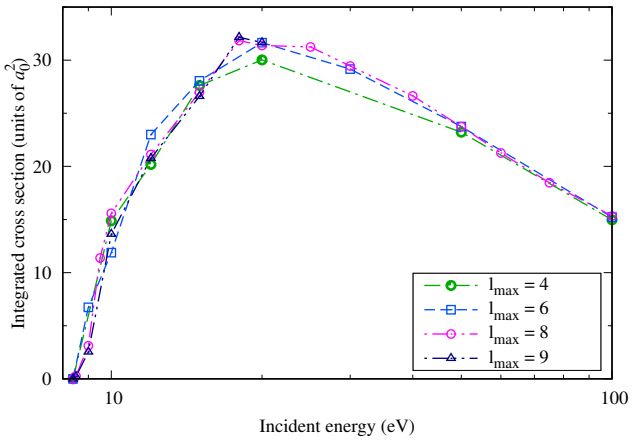

Figure 9.1: Convergence study of electron-loss cross section of Be for models of different $\ell_{\max}$.

In Fig. 9.2 a convergence study is presented for the scattering length for the B models used below the positronium-formation. Convergence of this value is found to occur by $\ell_{\max} = 20$. The slow convergence at low energies in relation to $\ell_{\max}$ leads to the requirement of very large scattering calculations. This was also found to be the case in CCC calculations for positron scattering from magnesium [230, 261], which also has a low positronium-formation threshold (0.8 eV).

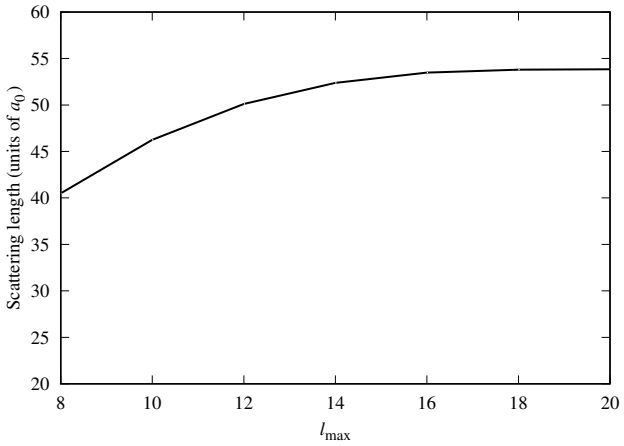

Figure 9.2: Convergence study of scattering length of B for models of different $\ell_{\max}$.

9.1.3 Excitation energies, oscillator strengths, and polarisabilities

We present the excitation energies of the current calculation for B alongside those of the BSR [123], MCHF [383, 384], and NIST [59] in Table. 9.1. There is excellent agreement between these results, with all excitations within 0.1 eV of the NIST values. In Table. 9.2 we present the oscillator strengths for transitions from the ground state of B. Close agreement is typically observed between the calculations for the presented oscillator strengths, with minor discrepancies present for the weaker transitions.

Table 9.1: Excitation energies (eV) for the first 10 B doublet target states.

	State	Term	CCC	BSR [123]	NIST [59]
1	$2s^2 2p$	$^2P^o$	0.000	0.000	0.000
2	$2s^2 3s$	^2S	4.898	4.916	4.964
3	$2s 2p^2$	^2D	5.931	5.939	5.933
4	$2s^2 3p$	$^2P^o$	6.006	5.974	6.027
5	$2s^2 3d$	^2D	6.761	6.725	6.790

Table 9.1: Excitation energies (eV) for the first 10 B doublet target states.

	State	Term	CCC	BSR [123]	NIST [59]
6	$2s^2 4s$	^2S	6.773	6.752	6.820
7	$2s^2 4p$	$^2P^o$	7.117	7.097	7.165
8	$2s^2 4d$	^2D	7.399	7.374	7.438
9	$2s^2 4f$	$^2F^o$	7.397	7.370	7.443
10	$2s^2 5s$	^2S	7.427	7.387	7.457
Ion. Limit			8.383	8.222	8.298

The dipole polarisability (α_D) of both models utilised for B is 20.3 a_0^3, within 1 % of the accepted value of 20.5 a_0^3. This quantity must be accurate to calculate cross sections at low energies correctly. Due to the relatively low ionisation energy of boron, the majority of the dipole polarisability originates from the continuum rather than the bound-states. Therefore, to accurately model boron the impact of the continuum must be correctly accounted for. The close agreement of α_D, oscillator strengths, and energy levels with past theory and experiment provides strong evidence for the accuracy of the current B structure model.

Higher multipole polarisabilities are expected to have negligible impact for these atoms, however the α_Q and α_O results of our small-energy models are included for completeness. Our calculation of B had α_Q = 135.89 a_0^5 and α_O = 2243.2 a_0^7. The current α_Q result is within 8 % of the CEPA-NO result of 145.7 [372].

Table 9.2: Oscillator strengths for transitions from the ground state of B.

Lower level	Upper level	CCC	BSR. [123]	MCHF [383, 384]	NIST [59]
$2s^2 2p\ ^2P^o$	$2s^2 3s\ ^2S$	0.0770	0.0803	0.0797	0.0785
	$2s2p^2\ ^2D$	0.0304		0.0290	0.0471
	$2s^2 3d\ ^2D$	0.167	0.0172	0.104	0.170
	$2s^2 4s\ ^2S$	0.0132	0.0162	0.0161	0.0154
	$2s^2 4d\ ^2D$	0.0759	0.0762	0.0428	0.0723
	$2s^2 5s\ ^2S$	0.0069	0.0117	0.0097	0.0082

9.2 Scattering

9.2.1 Total cross section

In Fig. 9.3 the CCC-pot results for the total cross section of positron scattering on B are presented alongside the electron scattering BSR calculation of Wang *et al.* [123]. Typically for atomic targets below 500 eV, the electron and positron total cross sections differ significantly due to the different scattering dynamics present for each projectile. In this case, however, we see unexpected agreement between the electron BSR and positron CCC-pot results for energies above 15 eV. From considering the components of excitation (Fig. 9.10), ionisation (Fig. 9.6), and elastic scattering (Fig. 9.7) the reason for this agreement is because the difference in elastic scattering between the two projectiles is almost equivalent to the difference in inelastic scattering. The significantly larger elastic cross section for the electron case is a result of electron exchange, a process which does not occur in positron scattering.

Unlike the other atoms considered in this thesis, when completing the CCC-scaled complex model potential calculations the direct inelastic component of the CCC-pot for B was fit to 100 eV, where the positronium-formation becomes near-zero, instead of at high-energies. This was done to prevent discontinuities in the inelastic cross section between the CCC and

CCC-pot approaches.

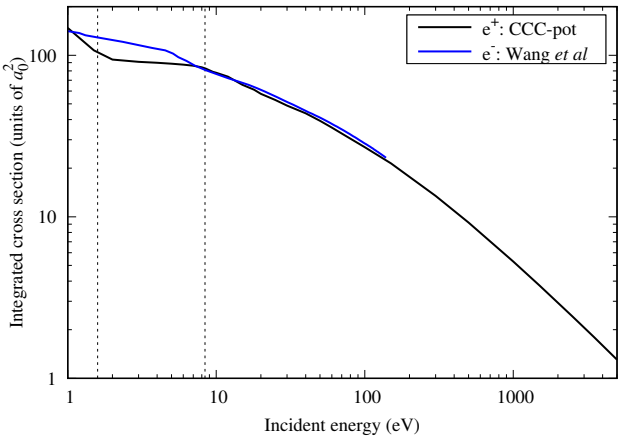

Figure 9.3: Total cross sections for positron scattering from boron. CCC-pot results are presented alongside the theoretical results for the incident electron by Wang *et al.* [123]. The vertical dotted lines represent the positronium-formation and direct ionisation thresholds.

9.2.2 Positronium-formation, direct, and electron-loss cross section

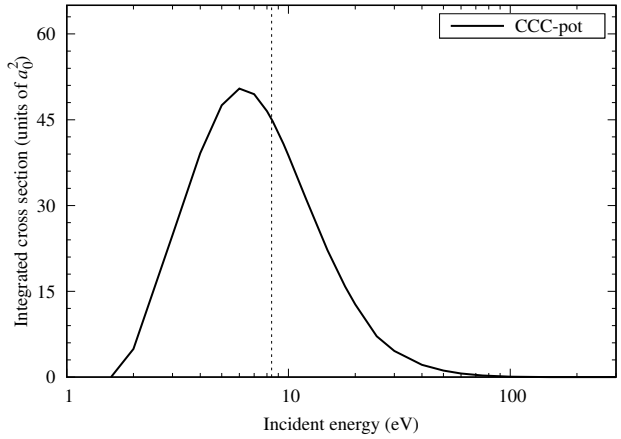

Figure 9.4: CCC-pot positronium-formation cross sections for positron scattering from boron. The vertical dotted line represents the direct ionisation threshold.

In Fig. 9.4, positron-boron CCC-pot results are presented without comparison as there is no existing theory or experiment for this transition.

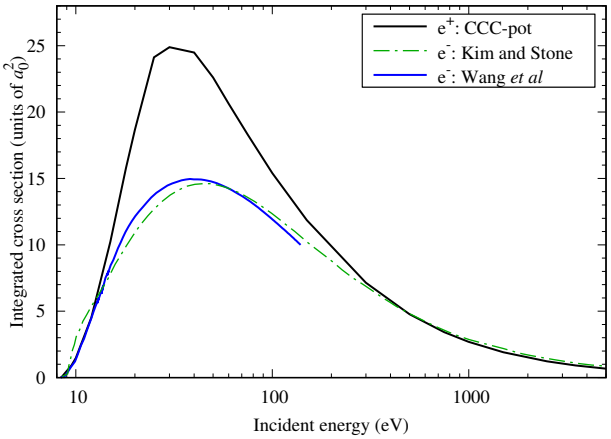

Figure 9.5: Direct ionisation cross sections for positron scattering from boron. CCC-pot results are presented alongside the theoretical results for the incident electron by Wang *et al.* [123] and Kim and Stone [124].The vertical dotted lines represent the positronium-formation and direct ionisation thresholds.

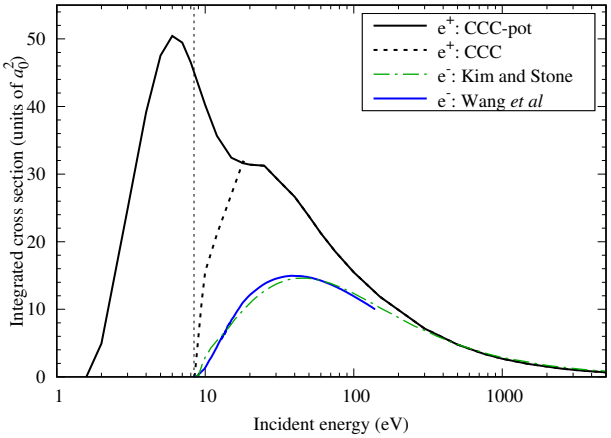

Figure 9.6: Electron-loss cross sections for positron scattering from boron. CCC-pot results are presented alongside the theoretical results for the incident electron by Wang *et al.* [123] and Kim and Stone [124]. The vertical dotted line represents the direct ionisation threshold.

Direct ionisation results for boron are shown in Fig. 9.5. Due to the absence of previous positron results, we present current CCC results alongside the BSR calculation of Wang *et al.* [123] and BEB calculation of Kim and

Stone [124]. At high incident energies CCC results become equal to that of the Born approximation, which is equal for positrons and electrons. We find this to be valid for energies above 300 eV, with close agreement between the electron BEB calculation and the current CCC result above this energy. The results for the electron-loss cross section are shown in Fig. 9.6

9.2.3 Elastic cross section

In Fig 9.7 we present the elastic cross section for boron. Positron results from the CCC calculations and Dapor and Miotello [37] are shown alongside the electron scattering BSR calculations of Wang *et al.* [123] and NIST [125]. As previously mentioned, the electron results for elastic scattering are significantly greater than the positron calculation across most of the energy range due to the electron exchange process. Above 500 eV, near-perfect agreement is found between the CCC calculation and the results of Dapor and Miotello [37]. For energies above 1000 eV, the electron elastic results of NIST [125] are close to the positron results, with them nearly the same by 5000 eV.

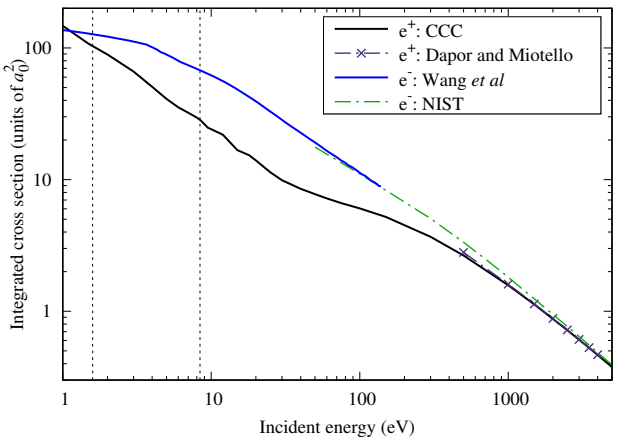

Figure 9.7: Elastic cross sections for positron scattering from boron. CCC results are presented alongside the theoretical results of Dapor and Miotello [37] and electron scattering results of Wang *et al.* [123] and NIST [125]. The vertical dotted lines represent the positronium-formation and direct ionisation thresholds.

9.2.4 Momentum-transfer cross section

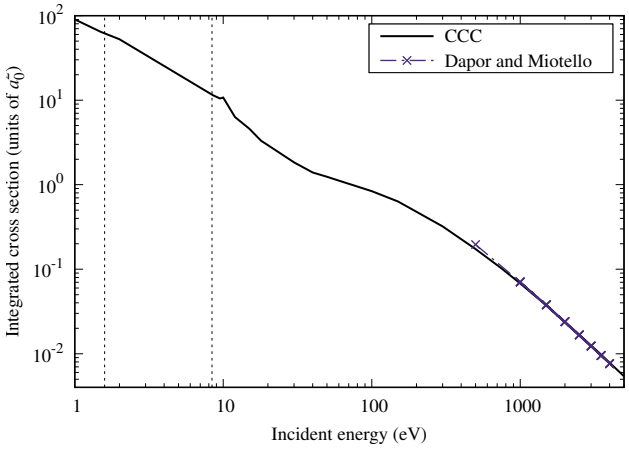

Figure 9.8: Momentum-transfer cross sections for positron scattering from boron. CCC results are presented alongside the theoretical results of Dapor and Miotello [37]. The vertical dotted lines represent the positronium-formation and direct ionisation thresholds.

The CCC momentum-transfer cross section for boron is presented in Fig. 9.8 alongside the only other calculation of Dapor and Miotello [37]. As with the elastic cross section, excellent agreement is observed between these calculations. Above 1000 eV, the NIST [125] results are close to the positron results.

9.2.5 Low energy scattering

Due to the absence of other theoretical results, we present only CCC low-energy results for both momentum-transfer and elastic scattering in Fig. 9.9. We find the scattering length of B to be $53.85a_0$. As scattering becomes isotropic for low energies, the momentum-transfer and elastic cross section become equivalent, in this case, for energies below 10^{-2} eV.

As the scattering length for B is significantly greater than its geometric size, a positron virtual level will exist. The energy of this level can be obtained using the scattering length and Eq. 2.69. For boron, we find this energy to be $\epsilon = 4.69\times10^{-3}$ eV.

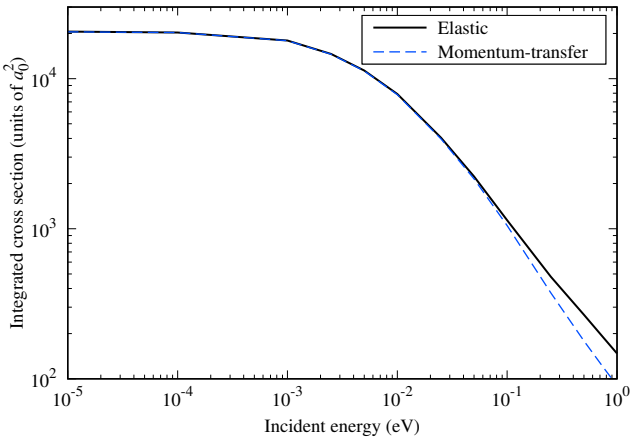

Figure 9.9: CCC elastic and momentum-transfer cross sections for positron scattering from boron for energies below 1 eV.

9.2.6 Excitation cross sections

The single-centre CCC formalism is unable to obtain convergence in the small energy region (6.8 eV) between positronium-formation and the ionisation threshold. This is due to the inability to approximate positronium-formation with the positive-energy atomic pseudostates, which are closed in this energy region. In our experience, running small eigenstate-only calculations are likely to provide more accurate results in this energy region.

The total and first nine individual bound-state excitation cross sections for boron are shown in Fig. 9.10. For the total excitation cross section, there are no other results to compare against within the literature. The sharp spike at the lower energies in the CCC result for the total excitation is unphysical and a result of a lack of convergence in the single-centre approach. The CCC-pot total excitation result does not exhibit this unphysical behaviour, however, this approach can not discretise the individual excitations. Therefore, for the lower energies, the current results for individual excitations are instead from a 10-state CCC model. For the $2s^2 4f\ ^2\mathrm{F}^o$ and $2s^2 5s\ ^2\mathrm{S}$ excitations, this smaller model was significantly larger than the 1353-state CCC model. This discrepancy is likely due to the strong coupling of these states to the continuum in the larger model, therefore, the 10-state model was uniformly scaled to agree with the larger model at 18 eV for these excitations. This process better approximates

the low-energy behaviour of these excitations by minimising the unphysical behaviour that results from positronium-formation in the single-centre technique.

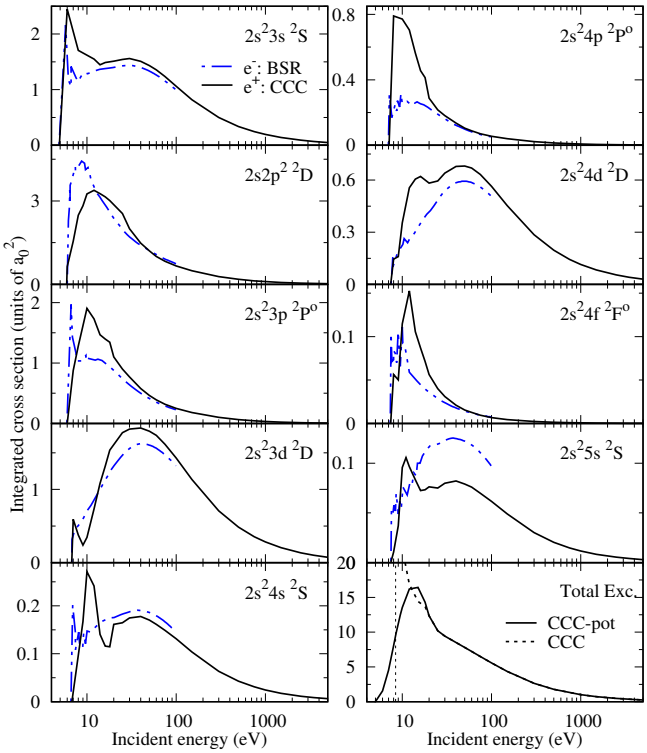

Figure 9.10: The first nine and the total bound-state excitation cross sections for positron scattering from boron. Current CCC results are presented alongside the BSR electron calculations of Wang *et al.* [123]. For the total excitation cross section, the CCC and CCC-pot results are presented. The vertical dotted line in the total excitation figure represents the direct ionisation threshold.

For low energies the results for each projectile are not expected to be equal due to the impact of the different Coulomb forces. However, there is close agreement between the current positron results and the electron BSR [123] results by 100 eV for almost all transitions. The one exception is the $2s^2 5s\ ^2\mathrm{S}$ excitation, which differs significantly at high energies between the CCC and BSR due to the different oscillator strengths found by these models for this transition.

9.2.7 Stopping power and mean excitation energy

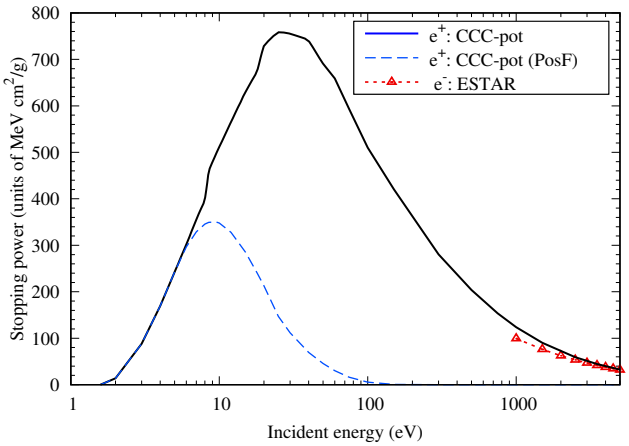

Figure 9.11: Stopping power CCC-pot calculations for boron. Also shown are the positronium-formation (PosF) component of the stopping power and the electron calculations from the ESTAR database [126].

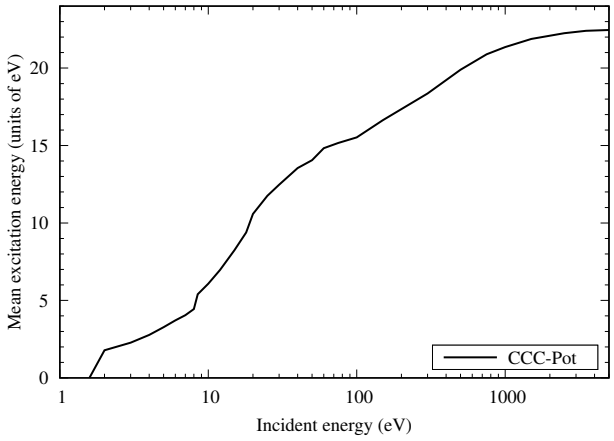

Figure 9.12: Mean excitation energy CCC-pot calculations for positron scattering from boron.

Current CCC-pot results for the positron stopping power of B are shown in Fig. 9.11 alongside the ESTAR database [126] results for the electron stopping power. We also present the positronium-formation component of the stopping power which is estimated from the CCC-pot result using the same approach utilised for oxygen in Chapter. 7. At 1000 eV, these electron stopping power results are slightly below the positron stopping power, but the

difference between the electron and positron calculations becomes negligible for higher energies.

The mean excitation CCC-pot results for B are shown in Fig. 9.12. The mean excitation energy generally slowly rises across the entire energy range before plateauing by 5000 eV.

9.3 Chapter summary

In this chapter the structure model and details of the current calculations for positron scattering on boron are provided. The excitation energies, oscillator strengths, and multipole polarisabilities derived from the current atomic structure models are then compared with previous theory and experiment. A comprehensive set of cross-sections is presented for positron scattering from boron. An analysis is also performed for the low-energy scattering of this system to calculate the scattering length and energy of the positron virtual level.

Good agreement was found between the current results and the only other existing positron calculation for elastic and momentum transfer cross sections which were available at high energies only. Excellent agreement is found with past theory and experiment for the polarisabilities, oscillator strengths, and excitation energies, with differences only present for weak transitions. Due to the absence of positron results, other cross sections have been compared to existing electron theoretical results. In particular, excellent agreement was found for the direct ionisation and electron-loss cross section for energies above 300 eV. There was also good agreement between previous electron and current positron results for most of the first nine bound-state excitations by 100 eV. Above the positronium-formation threshold, there was an unexpected agreement between the current positron results and previous electron calculations for the total cross section. This is a result of the differences between the elastic cross section of the different projectiles being approximately equal to their differences in the inelastic cross section.

Chapter 10

Positron scattering from fluorine

This chapter presents the single-centre CCC and CCC-scaled complex model potential calculations for positron scattering from atomic fluorine. First, details of the calculation and structure model are provided, comparisons are then made with the excitation energies, weighted oscillator strengths, and multipole polarisabilities of the current calculation with existing theoretical and experimental values. This is followed with the results for the total elastic, momentum-transfer, excitation, direct ionisation, electron-loss, positronium-formation, stopping power, and total cross sections from threshold to 5000 eV. These results are compared against existing positron and electron theory and experiment.

10.1 Structure

10.2 Calculation details

The Laguerre basis utilised in these calculations had $N = 25$ for $\ell \leq 2$ and $N = 22 - \ell$ for $\ell > 2$, with $\ell_{\max} = 8$ and $\alpha_\ell = 2$ for all ℓ. The $1s$ core is frozen while one-electron excitations are allowed from the $2s$ and $2p$ shells for these calculations. The structure model includes the ground configuration $2s^2 2p^5$, the one-electron excitation configurations of $2s^2 2p^4 n\ell$ and $2s^1 2p^5 n\ell$ for all possible n and ℓ within the Laguerre basis, and the configuration $2s2p^6$. For each symmetry, states were included with energies

up to 50 eV above ionisation, except for the S^o, P, and D^o symmetries for which all states were included with energies up to 100 eV. These states were required to obtain an accurate dipole polarisability. This model generated a total of 1246 target states. For energies below 1 eV, a 1175 state model with $\alpha_\ell = 5$ and all states with energies up to 300 eV was required to achieve convergence at low energies. The electron-loss cross section was extrapolated for high energies with a Born calculation with the same structure model but containing all 2446 generated states.

10.3 Excitation energies, oscillator strengths, and polarisabilities

Good agreement is observed between the present bound-state excitation energies, those of Gedeon *et al.* [127], and NIST [59], which are presented in table 10.1. All current results are within 0.1 eV of this previous theory and NIST, except for the $2p^4 3s^2 D$ and $2p^4 5s^2 P$ states, which are within 0.4 eV of NIST.

Weighted oscillator strengths are presented for the doublet target states in Table. 10.2. We find typically good agreement across all these transitions with the BSR calculations of Gedeon *et al.* [127], the MCHF calculations of Fischer and Tachiev [385], and NIST [59]. The best agreement is found for transitions from the ground state, which are the only transitions considered within our scattering calculation. The structure model of Gedeon *et al.* [127] contained more configuration states and continuums than the present model, which had to be limited due to the high $\ell_{\max}$ required to accurately model positron scattering. The close agreement between our current excitation energies and oscillator strengths with their results is, therefore, indicative of the current model's accuracy.

Other quantities we can use to evaluate the quality of our structure model are the multipole polarisabilities. The value of α_D is found to be 3.75 a_0^3 for the model used above the direct ionisation threshold, and $3.78 a_0^3$ for the model used below the positronium-formation threshold. These values are within 1 % of the experimental result of $3.76 a_0^3$ and are close to our 2764 state result of $3.78 a_0^3$.

The model used below the positronium-formation had $\alpha_Q = 12.05$ and $\alpha_O = 85.79$. This value of α_Q is close to the CEPA-NO calculation of

12.69 [372] and B-Spline CI calculation of 12.69 [358]. The current octupole result for this model is within 3% of the B-spline CI value of 88.43 [358]. For the model used above the direct ionisation threshold $\alpha_Q = 11.78$ and $\alpha_O = 84.57$. These results are close to our 2446-state model result of $\alpha_Q = 12.05$ and $\alpha_O = 85.48$.

Table 10.1: Excitation energies (eV) for F bound doublet target states.

	State	Term	CCC	Ref. [127]	NIST [59]
1	$2p^5$	$^2P^o$	0.000	0.000	0.000
2	$2p^4 3s$	^2P	13.101	13.092	12.982
3	$2p^4 3p$	$^2D^o$	14.603	14.584	14.579
4	$2p^4 3p$	$^2S^o$	14.699	14.670	14.680
5	$2p^4 3p$	$^2P^o$	14.785	14.728	14.735
6	$2p^4 3s$	^2D	15.748	15.496	15.347
7	$2p^4 4s$	^2P	15.671	15.628	15.653
8	$2p^4 3d$	^2D	15.884	15.836	15.874
9	$2p^4 3d$	^2F	15.900	15.836	15.906
10	$2p^4 3d$	^2P	15.915	15.868	15.934
11	$2p^4 4p$	$^2D^o$	16.124	16.063	16.109
12	$2p^4 4p$	$^2S^o$	16.154	16.086	16.136
13	$2p^4 4p$	$^2P^o$	16.182	16.099	16.152
14	$2p^4 5s$	^2P	16.709	16.426	16.482
Ion. Limit			17.335	17.367	17.406

Table 10.2: Weighted oscillator strengths for F.

Lower level	Upper level	CCC	Ref. [127]	Ref. [385]	NIST [59]
$2p^5\ ^2P^o$	$2p^4 3s\ ^2P$	0.580	0.559	0.586	
	$2p^4 3s\ ^2D$	0.281	0.286	0.306	
	$2p^4 4s\ ^2P$	0.113	0.106	0.585	
	$2p^4 3d\ ^2D$	0.147	0.125	0.150	
	$2p^4 3d\ ^2P$	0.029	0.028	0.041	
	$2p^4 5s\ ^2P$	0.058	0.039		
$2p^4 3s\ ^2P$	$2p^4 3p\ ^2D^o$	3.265	3.303	3.166	3.18
	$2p^4 3p\ ^2S^o$	0.660	0.662	0.661	0.660
	$2p^4 3p\ ^2P^o$	2.168	2.158	2.060	2.04
	$2p^4 4p\ ^2P^o$	0.042	0.030		
$2p^4 3p\ ^2D^o$	$2p^4 4s\ ^2P$	1.667	1.662		
	$2p^4 3d\ ^2D$	1.408	1.421	1.388	
	$2p^4 3d\ ^2F$	7.863	7.875	7.859	
	$2p^4 3d\ ^2P$	0.079	0.081	0.107	
	$2p^4 5s\ ^2P$	0.226	0.167		
$2p^4 3p\ ^2S^o$	$2p^4 4s\ ^2P$	0.389	0.379		
	$2p^4 3d\ ^2P$	1.876	1.880	1.809	
	$2p^4 5s\ ^2P$	0.010	0.032		
$2p^4 3p\ ^2P^o$	$2p^4 3s\ ^2D$	0.061	0.023	0.009	
	$2p^4 4s\ ^2P$	1.154	1.121		
	$2p^4 3d\ ^2D$	4.271	4.282	3.751	
	$2p^4 3d\ ^2P$	1.492	1.465	1.255	
	$2p^4 5s\ ^2P$	0.207	0.096		
$2p^4 4s\ ^2P$	$2p^4 4p\ ^2D^o$	4.834	4.889		
	$2p^4 4p\ ^2S^o$	1.020	1.015		
	$2p^4 4p\ ^2P^o$	2.976	2.945		
$2p^4 3d\ ^2D$	$2p^4 4p\ ^2D^o$	0.435	0.422		
	$2p^4 4p\ ^2P^o$	1.429	1.324		
$2p^4 3d\ ^2F$	$2p^4 4p\ ^2D^o$	2.365	2.285		
$2p^4 3d\ ^2P$	$2p^4 4p\ ^2D^o$	0.015	0.016		
	$2p^4 4p\ ^2S^o$	0.566	0.544		
	$2p^4 4p\ ^2P^o$	0.515	0.467		

10.4 Scattering

10.4.1 Convergence study

In Fig. 10.1, we present a convergence study of the electron-loss cross section for positron scattering on fluorine. From this, we find that this model is converged for $\ell_{\max} \geq 6$ for energies above 30 eV and for $\ell_{\max} \geq 4$ for energies above 300 eV.

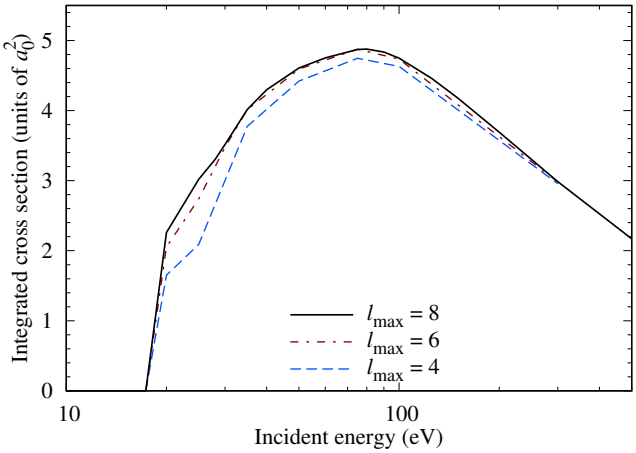

Figure 10.1: CCC convergence study for the electron-loss cross section of positron scattering on fluorine.

10.4.2 Total cross section

In Fig. 10.2 the CCC-pot calculations for positron scattering from fluorine for energies between 0.1 eV and 5000 eV are presented. As no other results exist in the literature for the positron total cross sections, we present these results alongside the BSR calculations of Gedeon *et al.* [127] for incident electrons. The BSR calculations were only conducted to 100 eV; therefore, comparisons can only be qualitative as electron and positron calculations are not expected to be equivalent below incident energies of 500 eV. The electron results are significantly larger than the positron results above 0.25 eV, with a maximum almost twice that of the positron result. However, the electron TCS decreases above quickly for energies above its peak and is only 50 % larger by 100 eV. The electron cross section is notably higher for intermediate energies due to electron exchange, which causes a substantial increase of the e^--F elastic cross section.

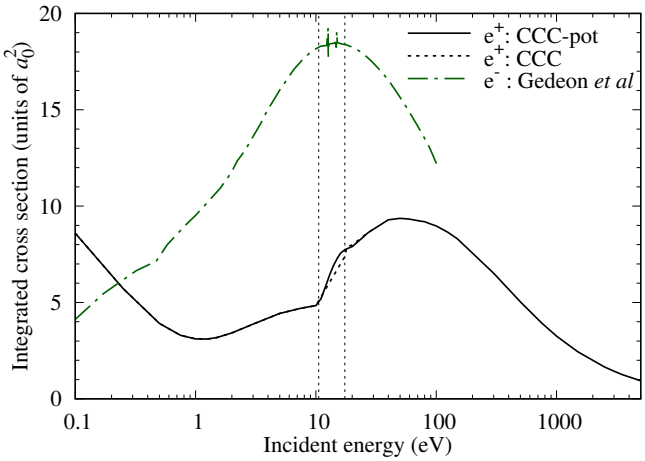

Figure 10.2: Total cross sections for positron scattering from fluorine. CCC-pot results are presented alongside the BSR calculations of Gedeon *et al.* [127] for incident electrons.

10.4.3 Electron-loss, direct ionisation, and positronium-formation cross sections

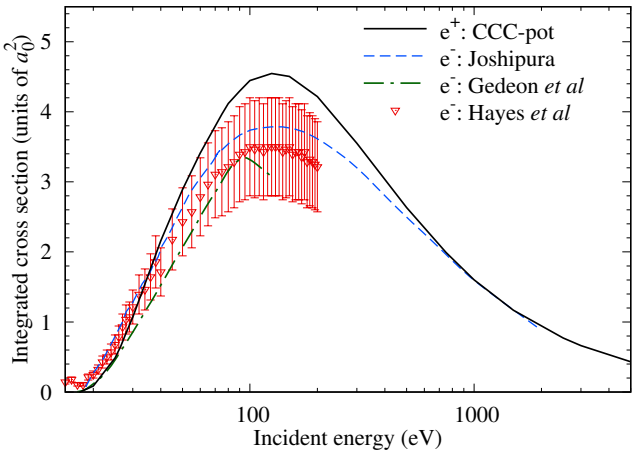

Figure 10.3: Direct ionisation cross sections for positron scattering from fluorine. CCC-pot results are presented alongside the theoretical results for the incident electron by Joshipura and Limbachiya [128] and Gedeon *et al.* [127]. Measurements for electron scattering are from Hayes *et al.* [129].

The direct ionisation cross section for positron scattering is shown in Fig. 10.3. We present the CCC-pot results for e^+-F alongside the e^--F theoretical results of Joshipura and Limbachiya [128] and Gedeon *et al.* [127].

Experimental results for the electron case by Hayes *et al.* [129] are also presented. The BSR calculations of Gedeon *et al.* [127] are lower than the other theory, except near threshold. The positron calculations are equivalent to the electron results for energies above 1000 eV and close to them below 40 eV. The electron theoretical results are within the uncertainty of experiment over its measured range, and the positron results for energies below 50 eV. The peak cross section at 125 eV occurs at the same energy for the current CCC-pot positron calculation, experimental results, and the electron calculations of Joshipura and Limbachiya [128].

In Fig. 10.4, we present the positronium-formation cross sections from threshold to 500 eV. As no other theoretical or experimental results exist for this scattering process, we present CCC-pot results by themselves. This cross section exhibits a shoulder formation with a peak at 15 eV followed by a slightly larger peak at 25 eV. For energies above 30 eV, this cross section steadily decreases and is found to be negligible by 300 eV.

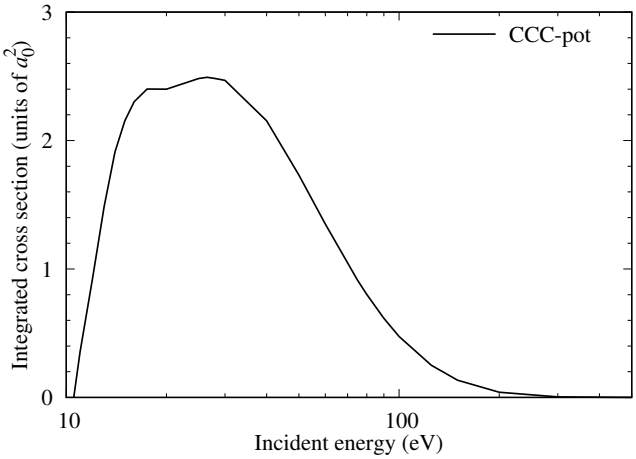

Figure 10.4: CCC-pot positronium-formation cross sections for positron scattering from fluorine.

The electron-loss cross section is presented in Fig. 10.5. The current CCC-pot results are shown alongside the same theory and experiment as for direct ionisation. This cross section exhibits two peaks, one at 15 eV and the other at 85 eV.

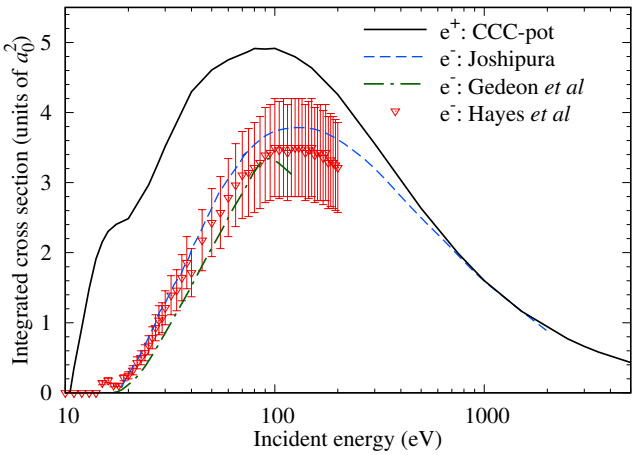

Figure 10.5: Electron-loss cross sections for positron scattering from fluorine. CCC-pot results are presented alongside the theoretical results for the incident electron by Joshipura and Limbachiya [128] and Gedeon *et al.* [127]. Measurements for electron scattering are from Hayes *et al.* [129].

10.4.4 Bound-state excitation cross sections

The CCC and CCC-pot total bound-state excitation cross section for positron scattering on fluorine is shown in Fig. 10.6. There are no existing positron results for the excitation cross sections of e^+-F in the literature. Alongside the total, the excitation cross sections of the first two excited states, $2p^4 3s^2 P$ and $2p^4 3p^2 D$, from the ground state are also presented. These cross sections were smoothly connected from 20 eV to their thresholds, as the CCC calculation is unstable for these energies. The presented ^2P excitation is found to peak at 60 eV, whereas the ^2D excitation peaks at 30 eV. The total bound excitation cross section peaks at 25 eV and then plateaus to 60 eV, after which it steadily decreases to 5000 eV.

10.4.5 Elastic and momentum-transfer cross sections

The elastic cross section for positron scattering on fluorine is shown in Fig. 10.7 for energies between 0.01 eV and 5000 eV. The current CCC results are presented alongside three theoretical models of Tenfen *et al.* [130] and the calculations of Dapor and Miotello [37]. Compared to these, we find the shape of our current calculation matches closest with the MCF-PD model of Tenfen *et al.* [130] but with a higher magnitude. The other two models are significantly higher than the current calculation for incident energies below

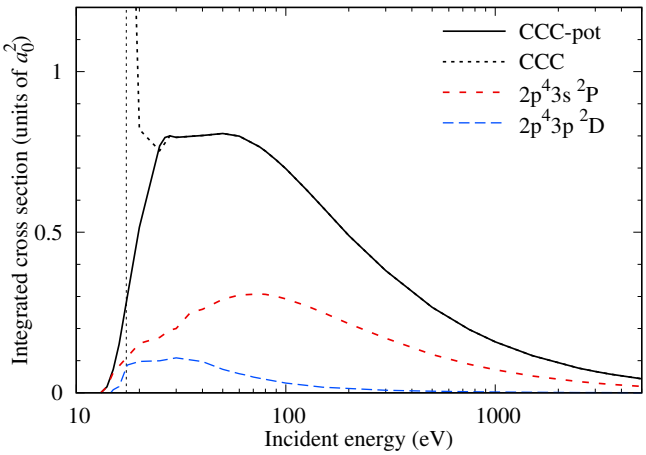

Figure 10.6: Total bound-state excitation cross sections for positron scattering from flourine. CCC and CCC-pot results are presented. Also shown are the excitation cross section of the $2p^4 3s^2 P$ and $2p^4 3p^2 D$ states from the ground state.

1 eV. Each of these models contain different approximations for the polarisation of F. The MCF-PD model includes only the dipole polarisability, MCF-PQ includes the dipole and quadrupole polarisability, and MCF-PG accounts for the dipole, quadrupole, mixed dipole-quadrupole hyperpolarisability, and pure dipole hyperpolarisability. The quadrupole polarisability is particularly important in this system as fluorine contains a permanent quadrupole moment [131]. Below the positronium-formation threshold, the CCC calculation is expected to converge to the true result. Evidence for this is provided through our calculations of α_D, which is within 1% of experimental results, α_Q, which is within 2% of previous calculations, and α_O, which is within 3% of the previous calculation. Due to the excellent agreement of these polarisabilities, the current elastic cross sections are expected to be accurate. The calculations of Dapor and Miotello [37] are indistinguishable from the CCC results for energies above 500 eV. The CCC calculations exhibit a minimum at 1 eV, which is a Ramsauer-Townsend minimum.

Momentum-transfer cross sections for e^+-F are presented in Fig. 10.8 for energies between 0.1 eV and 5000 eV. The current CCC calculation is shown alongside the calculations of Dapor and Miotello [37]. Similar to the elastic cross section, we find that these results are indistinguishable from the CCC calculations for energies above 500 eV. The momentum-transfer

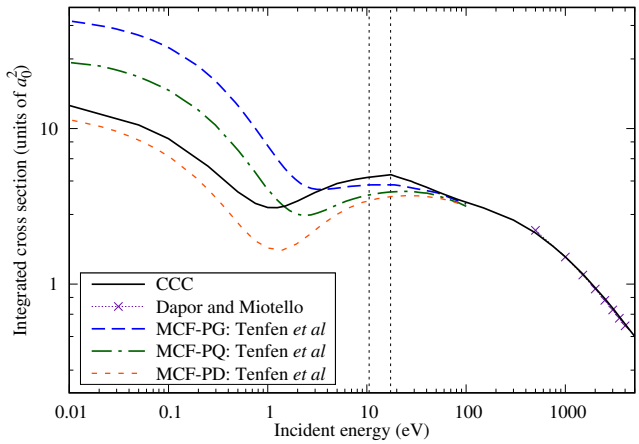

Figure 10.7: Elastic cross sections for positron scattering from flourine. CCC results are presented alongside the calculations of Dapor and Miotello [37] and Tenfen *et al.* [130].

cross section also exhibits a minimum resulting from the s- and p-wave shifts being equal, while higher-wave contributions are small, at ≈ 0.7 eV.

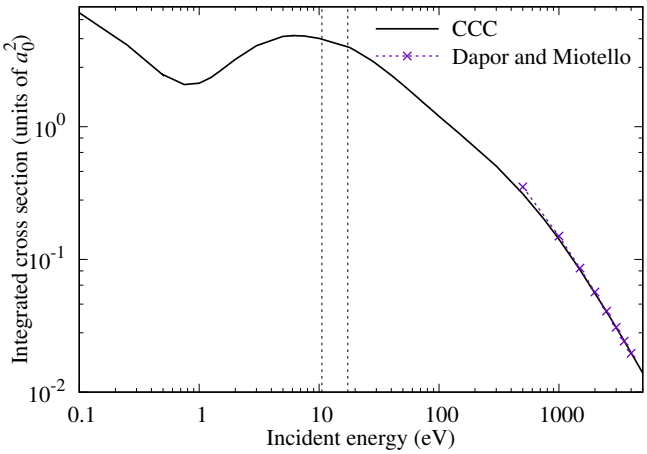

Figure 10.8: Momentum-transfer cross sections for positron scattering from flourine. CCC results are presented alongside the calculations of Dapor and Miotello [37].

10.4.6 Elastic differential cross sections

The elastic differential cross section for the positron-F scattering system is shown in Fig. 10.9 for incident energies between 0.5 eV and 10 eV. The

current CCC calculations are shown alongside the MCF-PG and MCF-PD models of Tenfen *et al.* [130]. Compared to these two models, the current CCC calculation follows the shape of the MCF-PD models for each of the presented energies but with a higher magnitude. The MCF-PG model, on the other hand, is larger than the CCC for all angles at 0.5 eV and below 40° for the other energies. This model also consistently finds the minimum of the DCS to occur at a larger angle than the CCC and MCF-PD models for the presented energies. The CCC and MCF-PD models are in agreement for the location of these minima.

In Fig. 10.10, the differential cross section is presented for energies

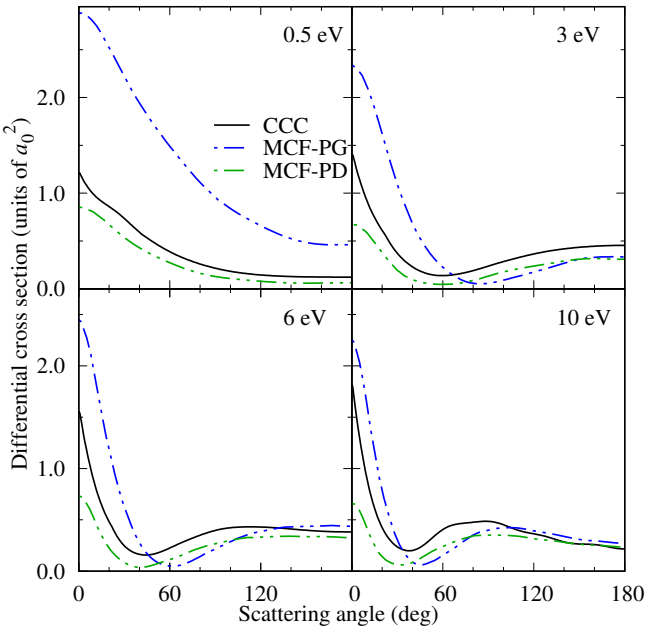

Figure 10.9: Elastic differential cross section for positron scattering on fluorine for incident energies between 0.5 eV and 10 eV. CCC results are presented alongside the MCF-PG and MCF-PD models of Tenfen *et al.* [130].

between 50 eV and 1000 eV. The current CCC results are shown alongside the MCF-PG model of Tenfen *et al.* [130] and the calculations of Dapor and Miotello [37]. For 50 eV and 100 eV, we find good agreement between the CCC calculation and the MCF-PG model for higher angles; however, very different behaviour is found at the low angles. The MCF-PG is found to have a dip at $\approx 10°$ before rising again towards 0°. The CCC result, on the other hand, smoothly increases to 0°. As with the elastic cross section,

we find very close agreement with the DCS of Dapor and Miotello [37] for 500 eV and 1000 eV.

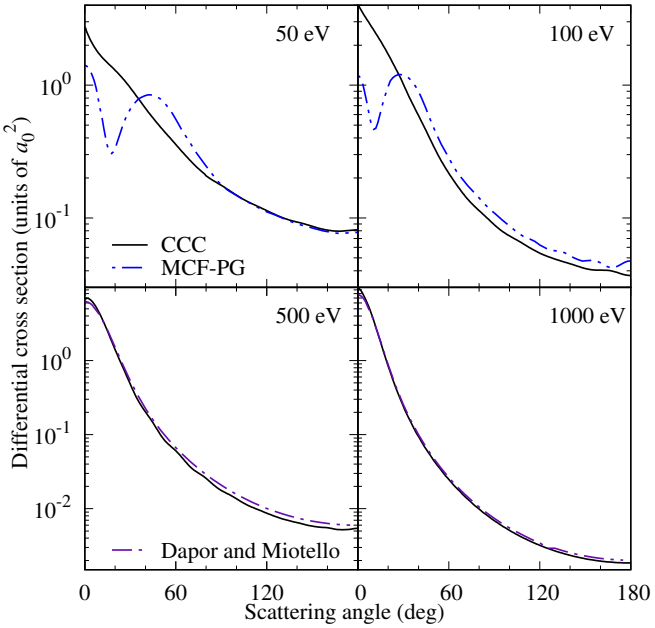

Figure 10.10: Elastic differential cross section for positron scattering on fluorine for incident energies between 50 eV and 1000 eV. CCC results are presented alongside the MCF-PG model of Tenfen *et al.* [130] and the calculations of Dapor and Miotello [37].

10.4.7 Low energy scattering

The elastic cross section from 10^{-5} eV to 5 eV is presented in Fig. 10.11. This cross section is asymptotic for energies below 10^{-3} eV. Above 10^{-3} eV the cross section decreases to the minimum at 1 eV. Using Eq. 2.66 we find the scattering length of this system to be 1.108 a_0.

In Fig. 10.12 we present the L-wave components of the elastic cross section, where L is the orbital angular momentum of the incident positron. The minimum in the s-wave component that results in the Ramsauer-Townsend minimum can be observed at approximately 1.5 eV.

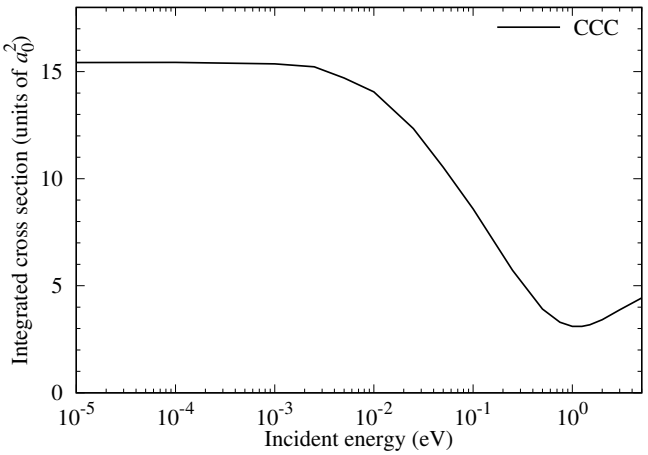

Figure 10.11: Elastic CCC cross sections of positron scattering from flourine for energies below 5 eV.

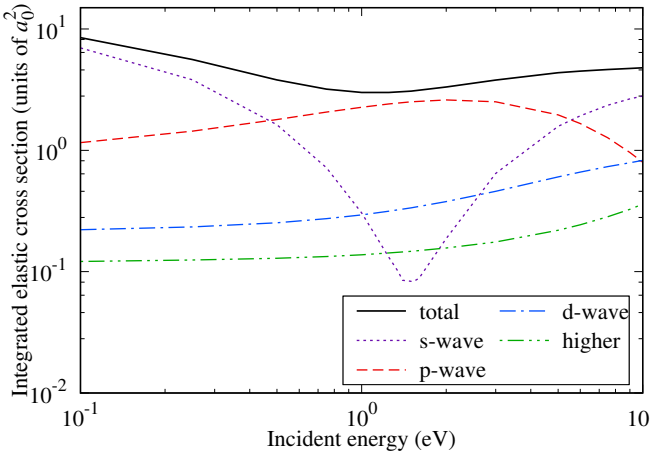

Figure 10.12: Elastic CCC cross sections of positron scattering from fluorine for energies below 5 eV.

10.4.8 Inelastic cross section

The total inelastic cross section and its components are presented in Fig. 10.13 for the current calculation. Positronium-formation is the dominant inelastic scattering process to 40 eV. Above 40 eV, direct ionisation is the dominant inelastic process. Excitation of the bound-states is minimal compared to the other scattering processes. The total inelastic cross section has a maximum at 80 eV, between that of the positronium-formation and

direct ionisation maximums.

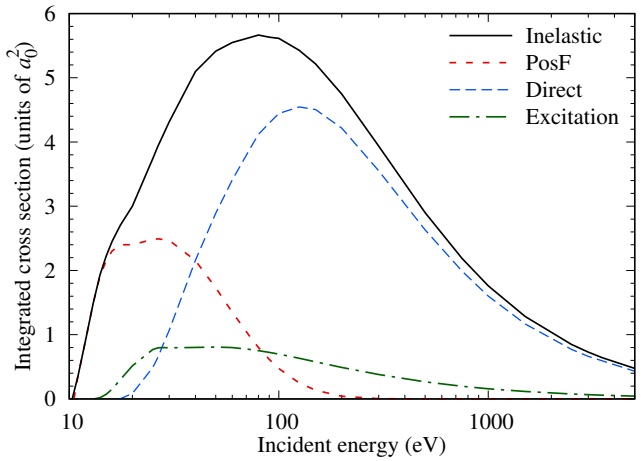

Figure 10.13: Total inelastic CCC cross sections of positron scattering from fluorine The positronium-formation (PosF), direct ionisation, and total bound-state excitation components are also shown.

10.4.9 Stopping power and mean excitation energy

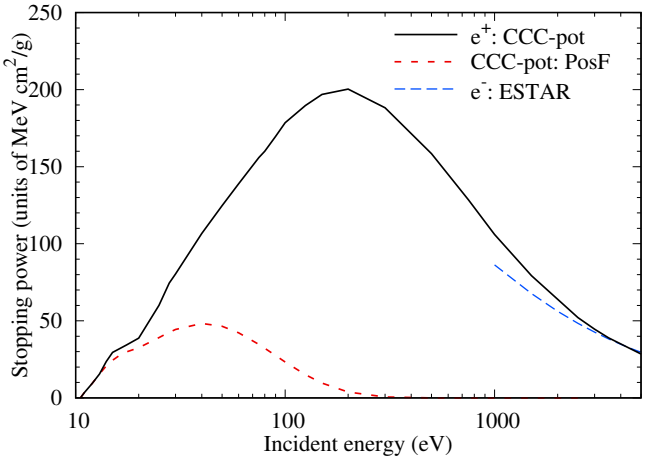

Figure 10.14: Stopping power for positron scattering from fluorine CCC results are presented alongside the electron calculations of ESTAR [126]. The positronium-formation (PosF) component of the stopping power is also presented.

In Fig. 10.14 the stopping power of a positron incident on fluorine is presented for energies between 10 eV and 5000 eV. The e^+-F CCC-pot results are presented alongside the e^--F results of the ESTAR database [126]. There

is close agreement between the current CCC-pot calculation and the ESTAR calculations for energies above 3000 eV. Below this energy, the ESTAR results are slightly lower. This is expected as, at lower energies, electrons have a lower stopping power than positrons due to their decreased inelastic cross sections.

The mean excitation energy for positron scattering from fluorine is shown in Fig. 10.15. There is a sharp rise near the threshold due to the opening of the positronium-formation channel. Above this, the mean excitation energy steadily increases to 1000 eV. For energies over 1000 eV, the mean excitation energy slightly decreases to 5000 eV. The CCC-pot calculations are presented by themselves as there are no other theoretical or experimental results for this quantity within the literature.

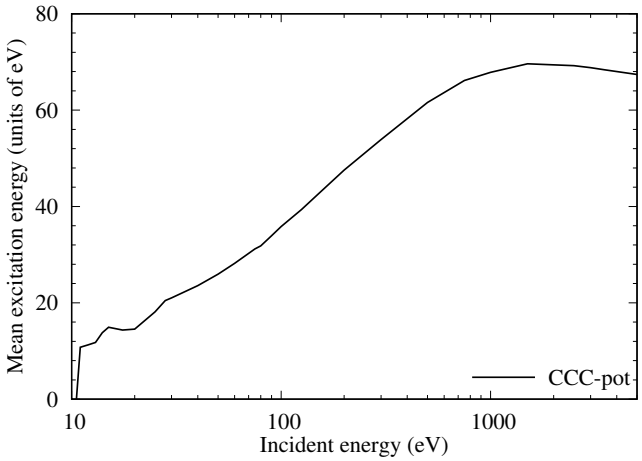

Figure 10.15: CCC-pot results for the mean excitation energy for positron scattering from fluorine

10.5 Chapter summary

An outline is given for the structure model and scattering calculations utilised to calculate cross sections for the positron-fluorine scattering system. The current target structure model for atomic fluorine is in excellent agreement with the energy levels and weighted oscillator strengths of NIST and previous theory. A comprehensive set of cross sections, including the total, elastic, momentum-transfer, direct ionisation, positronium-formation, electron-loss, inelastic, excitation, and stopping power cross sections, have been calculated for energies between threshold and 5000 eV. Quantities

such as the scattering length and the mean excitation energy were also calculated.

Good agreement is observed between current results and previous positron theory for the elastic and momentum-transfer cross sections for energies above 500 eV. There is disagreement between the current calculation and other theoretical models for energies below the positronium-formation. However, the CCC calculation is within the range of these models. For ionisation, agreement is found for energies above 1000 eV with previous electron calculations. For the stopping power, agreement was found between the current positron calculation and previous electron results for energies above 3000 eV.

As calculations have been conducted to high orbital angular momentum and there is close agreement with excitation energies, oscillator strengths, and multipole polarisabilities to previous results, we expect that errors associated with structure will be within 5 %. We, therefore, expect that elastic, momentum-transfer, elastic differential, and total bound-state excitation cross sections will be within 5 % of their true results. The model potential calculations are expected to have higher inaccuracies than the CCC results. However, positronium-formation is fairly small for fluorine. Therefore, we expect that the total cross section and direct ionisation cross sections to have an uncertainty within 10 %. For the positronium-formation cross section, we expect errors to be within 10 % to its maximum value and 20 % for energies above this.

Chapter 11

Molecules

To calculate positron scattering from complex molecular targets with *ab-initio* close-coupling calculations, such as those completed for the considered atomic targets, would require extensive theoretical and code development well outside the scope of this thesis. Furthermore, the computational resources required for these calculations would also be considerable. A far less intensive approach is to follow the independent atom modelling method (CCC-SCAR) outlined in Chapter. 4. With the atomic cross sections calculated within the preceding chapters and previous calculations for atomic hydrogen, we can therefore calculate cross sections for molecules that contain H, C, O, B, and F atoms with this method.

In this chapter, results are provided for the CCC-SCAR calculations of positrons from C_2, O_2, CO, CO_2, O_3, H_2O, CH_4, and CF_4. These molecules were selected due to both their importance within biological, plasma, atmospheric, and astrophysical research and the existence of previous calculations and experiments. For each molecule, results are presented for the total, elastic, total electronic excitation, direct ionisation, positronium-formation, electron-loss, and total inelastic cross section from 0.1 eV to 5000 eV. Due to the difficulties found in this approach for modelling molecules containing H, the hydrogen-scaling method described in Section. 4.3 is utilised for the H_2O and CH_4 molecular targets. Current results are compared to existing positron theory and experiment and, where appropriate, electron theory and experiment. Some sections in this chapter text or figures are adapted from a published work by the candidate [4]. The publishers of this article (EDP Sciences, Società Italiana di Fisica, and Springer Berlin Heidelberg) provide

the right to use an article or a portion of an article in a thesis or dissertation without requesting permission.

11.1 Molecular inelastic thresholds and geometrical distances

For the CCC-SCAR method, we require the accepted values for the thresholds of inelastic processes because molecular inelastic thresholds can differ considerably from those of their constituent atoms. Once an inelastic cross section is calculated, we can use these accepted thresholds to shift this cross section to its correct molecular threshold, improving the accuracy of the calculated results. Table. 11.1 presents the currently accepted direct ionisation and electronic excitation thresholds for several of the molecules considered within this chapter. Direct ionisation thresholds were obtained from the CCCB database of NIST [368]. The source of the electronic excitation thresholds are provided in Table. 11.1. For each molecule, the electronic excitation, direct ionisation, positronium-formation, and electron-loss cross sections were shifted according to these values. The geometrical distances between atomic components within a molecule required to calculate the screening coefficients for each molecular target (Eq. 4.3) were also obtained from the CCCB database of NIST [368].

Table 11.1: Direct ionisation and electronic excitation threshold for some of the considered molecules.

Threshold	H_2	C_2	O_2	CO	CO_2	O_3	H_2O	CH_4	CF_4
Ion. [368]	15.43	11.40	12.07	14.01	13.78	12.53	12.62	12.61	14.70
Exc.	12.73 [13]	6.30 [386]	7.05 [56]	8.07 [387]	11.04 [141]	1.6 [388]	7.54 [389]	10.58 [390]	12.6 [391]

11.2 O_2 scattering

11.2.1 Total cross section

The total cross section of a positron incident upon molecular oxygen is presented in Fig. 11.1. CCC-SCAR calculations are lower than the IAM-SCAR+I calculations of Ellis-Gibbings *et al.* [133], the IAM-SCAR calculations of Chiari *et al.* [51], and the SCOP calculations of Singh *et al.*

[33]. Close agreement is found between the CCC-SCAR and the experiment of Chiari *et al.* [51] for energies between 1 eV and 10 eV. Although the results of Chiari *et al.* [51] are not corrected for forward scattering effects, as O_2 is a non-polar molecule this correction is not expected to be significant. Therefore, the CCC-SCAR agrees fairly well with the experiment of Chiari *et al.* [51] but underestimates for energies below 1 eV. The IAM-SCAR approach is of least accuracy at these low energies where the impact of a molecule's polarisability and structure are at their most significant.

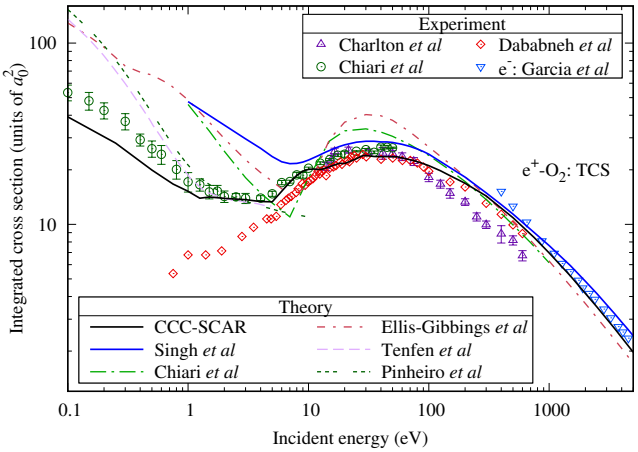

Figure 11.1: Total cross section for positron scattering on molecular oxygen. Theoretical CCC-SCAR results are shown alongside calculations by Singh *et al.* [33], Tenfen *et al.* [131], Pinheiro *et al.* [132], Ellis-Gibbings *et al.* [133]. Experimental O_2 results for positron scattering are from Charlton *et al.* [50], Chiari *et al.* [51], and Dababneh *et al.* [52]. Electron O_2 results are by García *et al.* [53].

There is good agreement with the CCC-SCAR results and those of Tenfen *et al.* [131] and Pinheiro *et al.* [132] for energies between 1 eV and the positronium-formation threshold. Both of these calculations utilised model potential based approaches in which higher-order polarisabilities are accounted for, with Pinheiro *et al.* [132] also including adiabatic corrections. The calculations of Singh *et al.* [33], on the other hand, employed the SCOP method, where the polarisation component of the potential is obtained via the approach of Padial and Norcross [392]. It has been demonstrated by Jain [393] that model correlation potentials which model electron impact, such as the one utilised by Singh *et al.* [33], are inadequate to describe positron scat-

tering, particularly at low energy. This is due to the fundamental differences in the correlation between both projectiles, which are more pronounced at lower energies. Chiari *et al.* [51] and Ellis-Gibbings *et al.* [133] calculations also utilised the IAM-SCAR approach, with the underlying atomic cross sections calculated through model potential calculations. These other theoretical calculations agree at 1 eV and are substantially higher than the current results and those of Tenfen *et al.* [131] and Pinheiro *et al.* [132].

The CCC-SCAR results are in agreement with positron experiment for energies up to 100 eV. In contrast, the other theoretical calculations predict substantially higher cross sections in this energy range. Above 100 eV, the CCC-SCAR results are slightly higher than the measurements of Dababneh *et al.* [52] and much higher than those of Charlton *et al.* [50]. For energies above 1000 eV, the current calculations are slightly below the electron measurements of García *et al.* [53]. The results of Singh *et al.* [33] are above this experiment, whereas the other calculations are below the CCC-SCAR result.

11.2.2 Elastic cross section

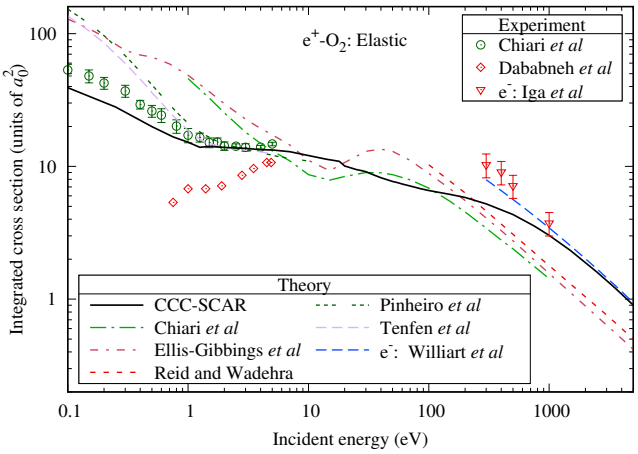

Figure 11.2: Elastic cross section for positron scattering on molecular oxygen. Theoretical results include those of the CCC-SCAR, Reid and Wadehra [32], Pinheiro *et al.* [132], Tenfen *et al.* [131], Ellis-Gibbings *et al.* [133], and Chiari *et al.* [51] for positrons and Williart *et al.* [69] for the electron case. Experimental results are from Chiari *et al.* [51], Dababneh *et al.* [52], and Iga *et al.* [60] for the electron case.

The elastic cross section for e^+-O_2 is shown in Fig. 11.2. CCC-SCAR results below the positronium-formation are equivalent to the TCS. The IAM-SCAR+I calculations of Ellis-Gibbings *et al.* [133], the IAM-SCAR calculations of Chiari *et al.* [51], and the IAM calculations of Reid and Wadehra [32] follow similar behaviours but at different magnitudes. The CCC-SCAR results, however, are notably different, with a more gradual descent. Compared to the experimental e^- results of Iga *et al.* [60], our results lie within the error bars of the 1000 eV measurement. The CCC-SCAR results are also in close agreement with the theoretical e^- calculations of Williart *et al.* [69] for energies above 2000 eV. As e^+ and e^- scattering are expected to be close for these high incident energies, with the e^- results providing an upper limit for the e^+ result, this lends validity to our results at high energy.

11.2.3 Total electronic excitation cross section

The total electronic excitation cross sections for O_2 are presented in Fig. 11.3. The current CCC-SCAR results are lower than the experimental data of Katayama *et al.* [135], which measures positron excitations to the Schumann-Runge continuum, even if the CCC-SCAR reproduces well the near-to-threshold resonant-like dependence of the cross section. This continuum represents excitations from the ground state $X^3\Sigma_g^-$ to the $B^3\Sigma_u^-$ state. The other existing theoretical results of Ellis-Gibbings *et al.* [133] are significantly larger than the CCC-SCAR results across the calculated energy range.

To facilitate comparison with O_2 excitations for incident electrons at high energies, we present the summed theoretical and experimental results of Suzuki *et al.* [134] and Newell *et al.* [136] for excitations to the Schumann-Runge continuum and the longest band state. The longest band state represents excitations of O_2 from the ground state to $E^3\Sigma_u^-$. Compared to this summed experiment, the positron measurements and current calculations are within error for all values in their measured range of 15 eV to 200 eV. The CCC-SCAR is higher than high-energy theoretical results of Suzuki *et al.* [134] for energies above 100 eV. This difference is expected as the CCC-SCAR should approximate the sum of all electronic excitations, whereas the summed theoretical results of Suzuki *et al.* [134] contains only two transitions.

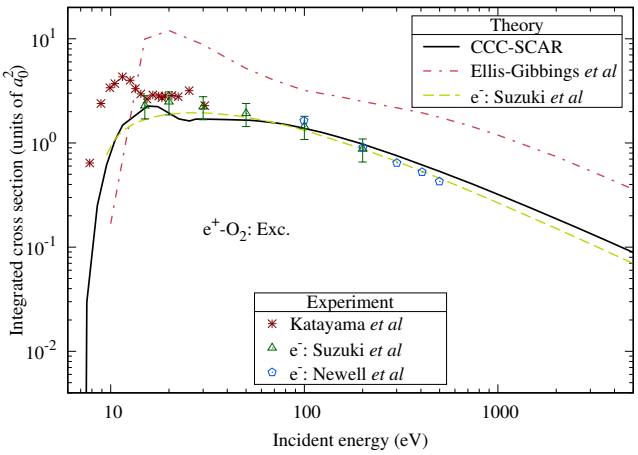

Figure 11.3: Total electronic excitation cross section for positron scattering on molecular oxygen. Theoretical results include the CCC-SCAR and the IAM-SCAR calculations of Ellis-Gibbings *et al.* [133] for positrons and the calculations of Suzuki *et al.* [134] for electrons. Experimental results for positrons are of excitations to the Schumann-Runge continuum from Katayama *et al.* [135]. Electron experimental results are from Newell *et al.* [136] and Suzuki *et al.* [134].

11.2.4 Electron-loss, direct ionisation and positronium-formation cross section

In Fig. 11.4 the results for the positronium-formation cross section of e^+-O_2 are presented. The theoretical calculations of Singh and Antony [34] and Ellis-Gibbings *et al.* [133] predict higher peaks than the CCC-SCAR. These calculations also predict that σ_{Ps} increases to a maximum and then steadily decreases, smoothly in the case of Singh and Antony [34] and sharply in that of Ellis-Gibbings *et al.* [133]. All theoretical methods agree for energies above 100 eV, however the CCC-SCAR results are lower than the other theory for energies between 10 and 100 eV but in better agreement with experiments of Marler and Surko [56], Archer *et al.* [57], and Laricchia *et al.* [137]. Compared to all of the experiments, the CCC-SCAR is in good agreement for energies below 7 eV, with all experiment, and above 30 eV, with that of Marler and Surko [56]. Experimental results predict a first maximum between 7-9 eV, which is expected to result from coupling between the positronium-formation and excitation to the Schumann-Runge continuum [137]. A second maximum is predicted by experiment to occur at 30 eV. The CCC-SCAR results are in a qualitative agreement with more

recent experiments.

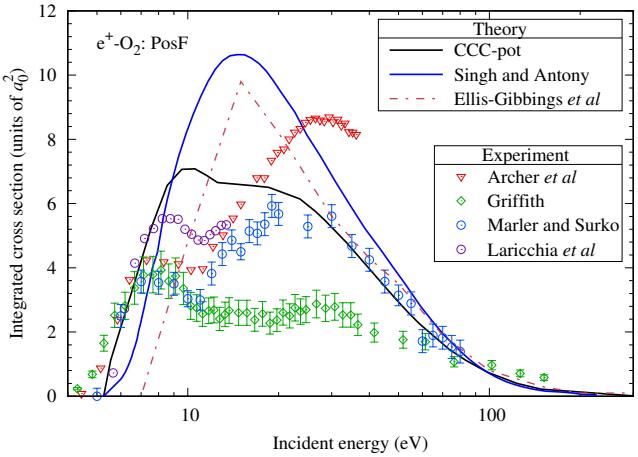

Figure 11.4: Positronium-formation cross section for positron scattering on molecular oxygen. Theoretical results include CCC-SCAR and the calculations of Ellis-Gibbings *et al.* [133] and Singh and Antony [34]. Experimental O_2 measurements are from Marler and Surko [56], Archer *et al.* [57], Laricchia *et al.* [137], and Griffith [58].

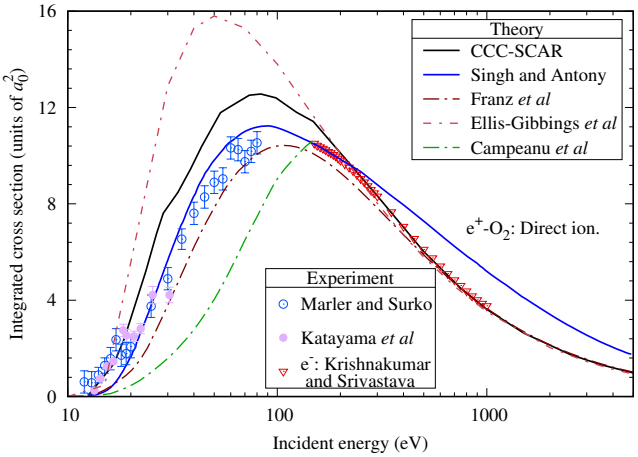

Figure 11.5: Direct ionisation cross section for positron scattering on molecular oxygen. Theoretical results include CCC-SCAR, Ellis-Gibbings *et al.* [133], Singh and Antony [34], Franz *et al.* [138], and Campeanu *et al.* [139]. Experimental results for positrons are from Marler and Surko [56] and Katayama *et al.* [135], electron results are from Krishnakumar and Srivastava [140].

Results for the direct ionisation cross section for the e^+-O_2 system are

shown in Fig. 11.5. Excellent agreement is found between the calculations of Ellis-Gibbings *et al.* [133] and the CCC-SCAR results for energies above 150 eV. For energies above 500 eV, there is agreement between the CCC-SCAR, [133], and Franz *et al.* [138] calculations. The calculations of Singh and Antony [34], on the other hand, are almost double that of the other calculations for incident energies above 500 eV. At lower energies, there is no agreement between different theoretical methods, with all varying in their magnitude. For energies below 20 eV, the results of the CCC-SCAR and Ellis-Gibbings *et al.* [133] are within the range of experimental results. For energies between 20 and 60 eV, the experiments are typically between the calculations of Singh and Antony [34] and Franz *et al.* [138] with these calculations lying with the error of some points. For this same energy range, the CCC-SCAR results are above the calculations of Singh and Antony [34] and much lower than the calculations of Ellis-Gibbings *et al.* [133].

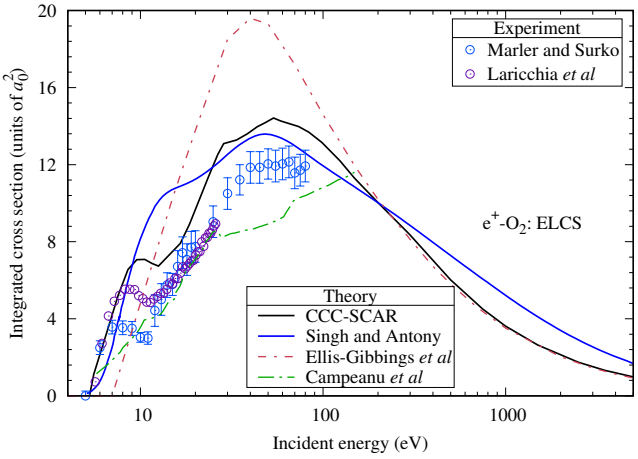

Figure 11.6: Electron-loss cross section for positron scattering on molecular oxygen. Theoretical results include CCC-SCAR and Singh and Antony [34], and Ellis-Gibbings *et al.* [133] calculations. Experimental O_2 measurements are from Marler and Surko [56] and Laricchia *et al.* [137].

The electron-loss cross sections are presented in Fig. 11.6. The σ_{EL} is equivalent to the direct ionisation cross section for high energies. The CCC-SCAR results predict a similar shape to the experiments of Marler and Surko [56] and Laricchia *et al.* [137] but have a larger magnitude for energies above 7 eV. The local minima at 12 eV results from the positronium-formation decreasing while the direct ionisation increases. The calculations

of [34] are also higher than experiment but predict a very different shape. The results of Ellis-Gibbings *et al.* [133] predict a rise in this cross section to a peak at 30 eV, approximately 1.5 times larger than the other calculations and experiment, followed by a rapid decrease after which there is excellent agreement with the CCC-SCAR results for energies above 200 eV.

11.3 C_2 scattering

11.3.1 Total cross section

The total cross section for a positron scattering on diatomic carbon is shown in Fig. 11.7. Current CCC-SCAR results are compared to the results of Singh *et al.* [33] and Reid and Wadehra [32]. For energies above 20 eV, good agreement is found between the CCC-SCAR results and those of Singh *et al.* [33]. Above 1000 eV, however, the results of Singh *et al.* [33] are slightly above the CCC-SCAR results. For energies between 6 and 25 eV, the CCC-SCAR results are larger than those of Singh *et al.* [33]. Below 6 eV, the CCC-SCAR results are instead lower, and its minimum at 5 eV is lower than that of Singh *et al.* [33] at 7 eV. The IAM calculations of Reid and Wadehra [32] are significantly lower than the other calculations over its entire range.

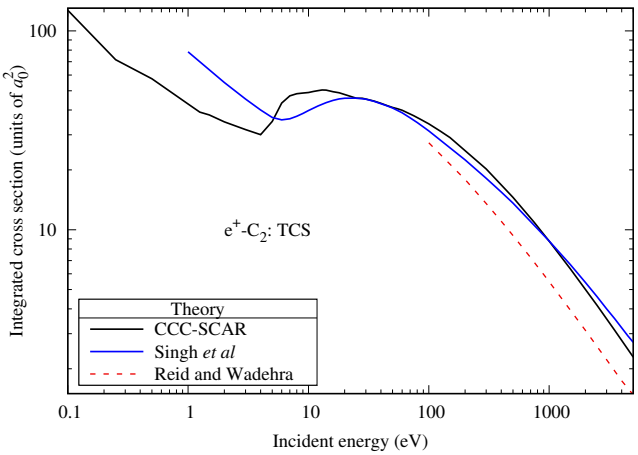

Figure 11.7: Total cross section for positron scattering on diatomic carbon. Theoretical results include the CCC-SCAR and those of Singh *et al.* [33] and Reid and Wadehra [32].

11.3.2 Elastic cross section

The elastic cross section for this system is presented in Fig. 11.8. The only existing theoretical calculations are those of Reid and Wadehra [32]. As with the total cross section, these results are significantly lower than the CCC-SCAR results, except for energies below 100 eV.

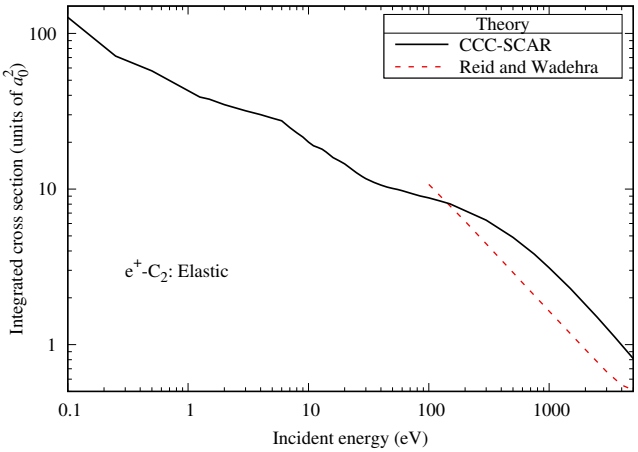

Figure 11.8: Elastic cross section for positron scattering on diatomic carbon. Theoretical results include those of the CCC-SCAR and Reid and Wadehra [32].

11.3.3 Total inelastic and electronic excitation cross section

For the total inelastic cross section for a positron scattering on diatomic carbon, shown in Fig. 11.9, the CCC-SCAR results are presented with the only other results of Reid and Wadehra [32]. Again, we find the calculations of Reid and Wadehra [32] to be lower than the CCC-SCAR results, although the differences between these results decrease with increasing incident energy. Also presented in this figure are the electronic excitation cross section which, due to there being no previous theoretical or experimental work, are presented without comparison.

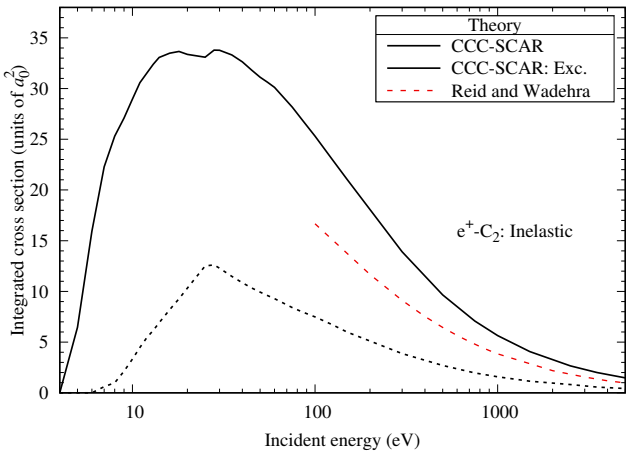

Figure 11.9: Total inelastic cross section for positron scattering on diatomic carbon. Theoretical results include those of the CCC-SCAR and Reid and Wadehra [32]. Also shown are the CCC-SCAR total electronic excitation cross section (Exc.) for this scattering system.

11.3.4 Electron-loss, direct ionisation, and positronium-formation cross sections

The positronium-formation cross section for positron scattering on diatomic carbon is shown in the bottom segment of Fig. 11.10. CCC-SCAR results are shown alongside the calculations of Singh and Antony [34]. Here, we find the CCC-SCAR results to be much higher than those of Singh and Antony [34] for energies below 35 eV. Above 35 eV, the CCC-SCAR results fall off substantially faster than this approach.

For the direct ionisation cross section of this system, shown in the middle segment of Fig. 11.10, CCC-SCAR results are again shown alongside those of Singh and Antony [34]. There is very close agreement between these calculations for energies below 20 eV. Between 20 eV and 250 eV, the CCC-SCAR results are higher and predict a larger peak than that of Singh and Antony [34]. Above 250 eV, the CCC-SCAR results are lower than the results of Singh and Antony [34] to 5000 eV.

In the top segment of Fig. 11.10 we present the σ_{EL} for both the CCC-SCAR and Singh and Antony [34] results for e^+-C_2. The CCC-SCAR calculations follow a similar shape to the calculations of Singh and Antony [34] but with a substantially higher peak at 10 eV due to the higher positronium-formation predicted by the CCC-SCAR. The second peak, resulting from the

direct ionisation, is also higher in the CCC-SCAR calculation. For higher energies, as with direct ionisation, the CCC-SCAR results for σ_{EL} are below those of Singh and Antony [34].

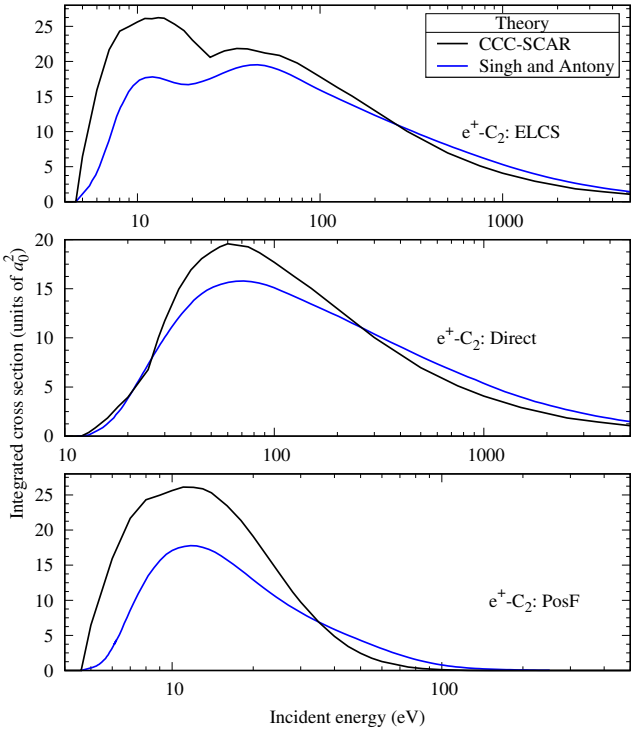

Figure 11.10: Electron-loss (top), direct ionisation (middle), and positronium-formation (bottom) cross section for positron scattering on diatomic carbon. Theoretical results include CCC-SCAR and those of Singh and Antony [34].

11.4 CO scattering

11.4.1 Total cross section

The total cross section for positron scattering on carbon monoxide is shown in Fig. 11.11. The current CCC-SCAR calculations are shown alongside the theoretical results of Billah *et al.* [143], which utilise the IAM-SCAR+I approach, Gianturco *et al.* [142], that use the BF-VCC, and those of Singh *et al.* [141]. Experimental results for electrons are from Karwasz *et al.* [148] and García *et al.* [149] and for positrons are from Zecca *et al.* [144], Sueoka and Mori [145], Coleman *et al.* [146], and Kwan *et al.* [147]. For energies

below the positronium-formation, our results find similar behaviour to the measurements of Zecca *et al.* [144] but at a larger magnitude. As CO is polar it is likely that the results of Zecca *et al.* [144] underestimate due to not accounting for forward scattering. The calculations of Billah *et al.* [143], on the other hand, predict a minimum at 4 eV and are significantly lower than the current result. The results of Gianturco *et al.* [142] were calculated only below the positronium-formation threshold and have a similar shape to the CCC-SCAR results but with a lower magnitude and steeper rise below 1 eV. For energies above the positronium-formation our results are between the calculations of Billah *et al.* [143] and Singh *et al.* [141] to 60 eV. Above this energy, the current results are larger than these theoretical approaches. However, above 1500 eV, the current results are close to those of Singh *et al.* [141]. Our calculations are generally above the positron measurements across the calculated energy range. Agreement is found with the electron measurements of Karwasz *et al.* [148] and the CCC-SCAR results for energies between 200 eV and 1000 eV. Above 1000 eV, the results of Karwasz *et al.* [148] underestimate the current results and the electron measurements of García *et al.* [149]. Therefore, the current theory is expected to be more reliable at high energies

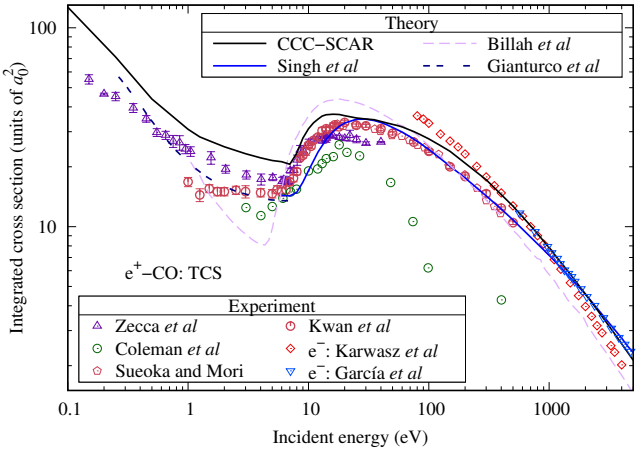

Figure 11.11: Total cross section for positron scattering on carbon monoxide. Theoretical results include those of the CCC-SCAR and those of Singh *et al.* [141], Gianturco *et al.* [142], and Billah *et al.* [143]. Experimental results for positrons are from Zecca *et al.* [144], Sueoka and Mori [145], Coleman *et al.* [146], and Kwan *et al.* [147]. For electrons the experimental measurements are from Karwasz *et al.* [148] and García *et al.* [149].

11.4.2 Elastic cross section

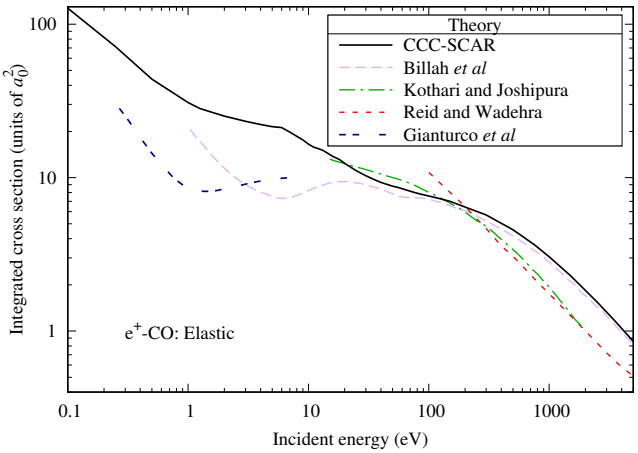

Figure 11.12: Elastic cross section for positron scattering on carbon monoxide. Theoretical results include those of the CCC-SCAR, Singh *et al.* [141], Billah *et al.* [143], Kothari and Joshipura [150], Reid and Wadehra [32], and Gianturco *et al.* [142].

The elastic cross section for a positron incident on carbon monoxide is shown in Fig. 11.12. CCC-SCAR results are shown alongside the theoretical calculations of Billah *et al.* [143] and Singh *et al.* [141], and Gianturco *et al.* [142]. Very close agreement is found with the calculations of Billah *et al.* [143] above 100 eV. Below this energy, these results, and those of Gianturco *et al.* [142], exhibit very different behaviour and are at a lower magnitude than the CCC-SCAR calculation. The calculations of Reid and Wadehra [32] are lower than the CCC-SCAR results for energies above 200 eV, and at high energies, are in agreement with the calculations of Kothari and Joshipura [150].

11.4.3 Total electronic excitation cross section

In Fig. 11.13, we present the e^+-CO total electronic excitation cross section. Current CCC-SCAR results are shown alongside the calculations of Kothari and Joshipura [150] for the total excitation, the calculations of da Silva *et al.* [151] for excitation to the $A^1\Pi$ state, and the measurements for excitation to the $A^1\Pi$ state from Marler and Surko [56]. The calculations of Kothari and Joshipura [150] are below the CCC-SCAR results across almost the entire energy range. Over its calculated energies the SMC results of da Silva *et al.*

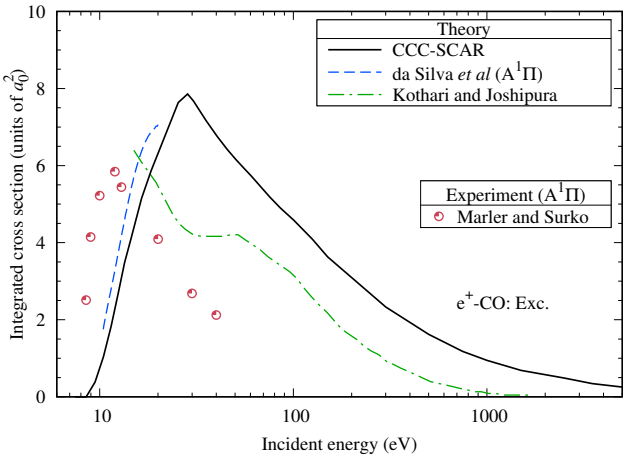

Figure 11.13: Total electronic excitation cross section for positron scattering on carbon monoxide. Theoretical results include those of the CCC-SCAR and Kothari and Joshipura [150] for the total excitation and da Silva *et al.* [151] for excitation to the $A^1\Pi$ state. Experimental results for excitation to the $A^1\Pi$ state are from Marler and Surko [56].

[151] are slightly higher than the CCC-SCAR results. The current results, and those of da Silva *et al.* [151], have a similar shape to the experiment of Marler and Surko [56]. However, both theoretical results predict a maximum that occurs at a higher energy, with the peak of the CCC-SCAR results is 20 eV above that predicted by this experiment. Towards threshold, the SMC and CCC-SCAR results predict lower values than that of the experiment.

11.4.4 Electron-loss, direct ionisation, and positronium-formation cross sections

The CCC-SCAR calculations for the e^+-CO positronium-formation cross section are presented in Fig. 11.14 alongside the theoretical calculations of Singh and Antony [24] and experiment of Marler and Surko [56]. The current results are in agreement with Singh and Antony [24] for energies above 80 eV. For lower energies, the CCC-SCAR results, however, are significantly higher. As with O_2, agreement is found with experiment for energies above 30 eV. Below 30 eV, the current results are significantly larger than experiment.

For the direct ionisation cross section, presented in Fig. 11.15, the CCC-SCAR results are larger than other theory and experiment for energies

between 30 and 200 eV. Above 200 eV, the CCC-SCAR results lie within the uncertainty of the experiment of Bluhme *et al.* [154] and is between the calculations of Kothari and Joshipura [150] and Singh and Antony [24], and those of Tóth *et al.* [152] and Campeanu *et al.* [153]. Below 30 eV, the CCC-SCAR results are close to other presented theory and experiment.

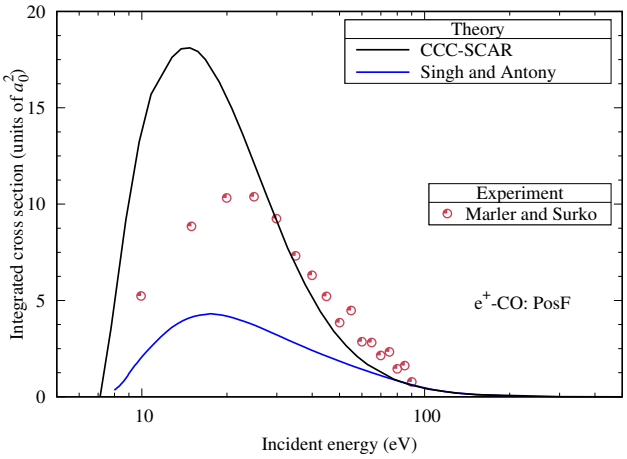

Figure 11.14: Positronium-formation cross section for positron scattering on carbon monoxide. Theoretical results include CCC-SCAR and the calculations of Singh and Antony [24]. Experimental measurements are from Marler and Surko [56].

Due to the large values for positronium-formation in the CCC-SCAR results, the σ_{EL}, shown in Fig. 11.16, features a first maximum not present in other theory or experiment. For energies between 30 and 80 eV, the CCC-SCAR results lie within the uncertainty of the experiment of Bluhme *et al.* [154]. For higher energies, the CCC-SCAR results are above the experiment of Bluhme *et al.* [154] and between the calculations of Billah *et al.* [143] and Singh and Antony [24].

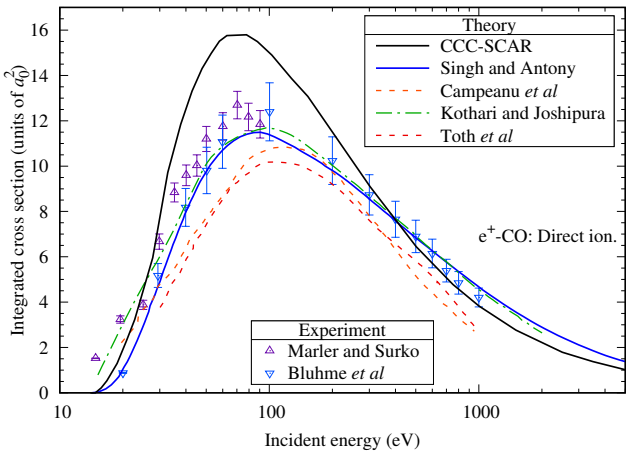

Figure 11.15: Direct ionisation cross section for positron scattering on carbon monoxide. Theoretical results include CCC-SCAR, Singh and Antony [24], Kothari and Joshipura [150], Tóth *et al.* [152], and Campeanu *et al.* [153]. Experimental results are from Marler and Surko [56] and Bluhme *et al.* [154].

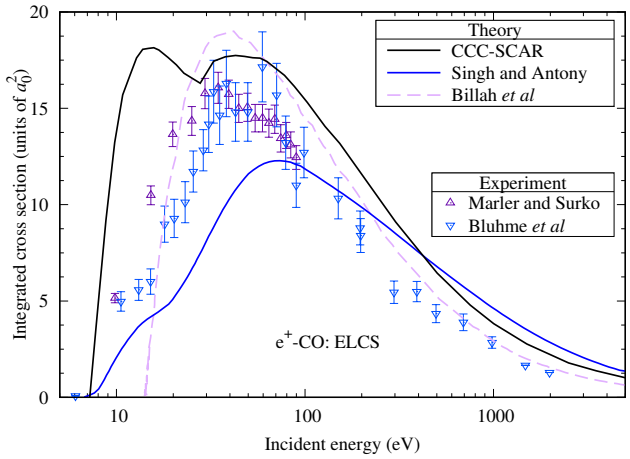

Figure 11.16: Electron-loss cross section for positron scattering on carbon monoxide. Theoretical results include CCC-SCAR and Singh and Antony [34], and Ellis-Gibbings *et al.* [133] calculations. Experimental O_2 measurements are from Marler and Surko [56] and Bluhme *et al.* [154].

11.4.5 Total inelastic cross section

The total inelastic cross section for e^+-CO is presented in Fig. 11.17. As there are no experimental results for this scattering process, we present current CCC-SCAR results alongside the calculations of Singh *et al.* [141],

Billah *et al.* [143], Reid and Wadehra [32], and Kothari and Joshipura [150]. For energies above 1000 eV, there is excellent agreement between all of the theoretical results, except for Billah *et al.* [143], which is lower than other theory. Below this energy, the CCC-SCAR results are larger than other theoretical results, except for below 70 eV, where the CCC-SCAR results are between the other theoretical calculations and the results of Billah *et al.* [143].

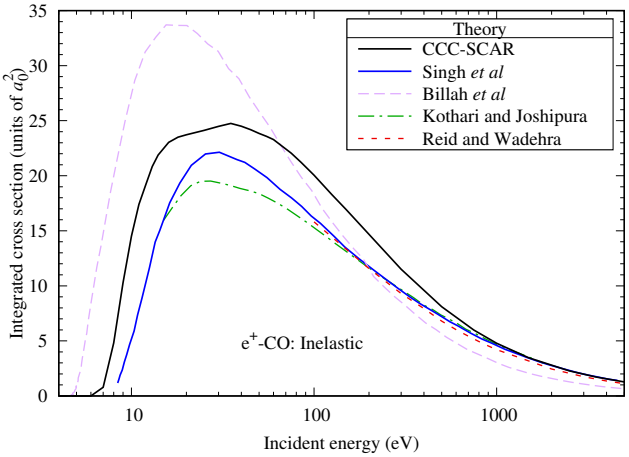

Figure 11.17: Total inelastic cross section for positron scattering on carbon monoxide. Theoretical results include those of the CCC-SCAR, Singh *et al.* [141], Billah *et al.* [143], Reid and Wadehra [32], and Kothari and Joshipura [150].

11.5 CO_2 scattering

11.5.1 Total cross section

In Fig. 11.18, we present the results for the total cross section of e^+-CO_2. Current CCC-SCAR results are presented alongside a several theoretical results [131, 141, 155, 156] and measurements for positrons [145, 147, 159, 160] and electrons [158]. As was found for CO, the current calculations are larger than the positron experiments, except below the positronium-formation energy where good agreement is found with the measurements of Zecca *et al.* [160]. This discrepancy is likely a result of the experiments of Sueoka and Mori [145], Kwan *et al.* [147], and Charlton *et al.* [159] having used strong guiding magnetic fields. Therefore, their results will underestimate the true

result as no corrections were made for forward scattering. For energies above 400 eV, however, excellent agreement is found with the electron experiment of García and Manero [158] and the theoretical calculations of Lozano *et al.* [155]. For energies above 2500 eV, there is also close agreement between these two calculations and those of Singh *et al.* [141]. Besides these agreements, large discrepancies exist between the different theoretical calculations, with all differing in magnitudes and behaviour.

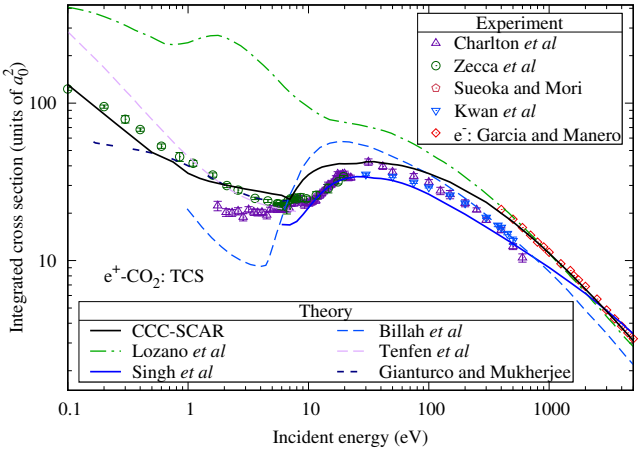

Figure 11.18: Total cross section for positron scattering on carbon dioxide. Theoretical results include those of the CCC-SCAR, Lozano *et al.* [155], Singh *et al.* [141], Billah *et al.* [156], Gianturco and Mukherjee [157], and Tenfen *et al.* [131]. Experimental results for incident electrons are from García and Manero [158] and for positrons are from Charlton *et al.* [159], Zecca *et al.* [160], Sueoka and Mori [145], Kwan *et al.* [147].

11.5.2 Elastic cross section

The elastic cross section for carbon dioxide is shown in Fig. 11.19. The current CCC-SCAR calculations are presented alongside the same theoretical calculations as the σ_{tot} and the experimental measurements of Charlton *et al.* [159] and Zecca *et al.* [160]. Excellent agreement is found between the CCC-SCAR results and the IAM-SCAR calculations of Billah *et al.* [156] for energies above 100 eV. Good agreement is also found with the current results and the SCOP calculations of Singh *et al.* [141] for energies between 20 and 80 eV. Outside of these cases, little agreement is found between the different theoretical calculations.

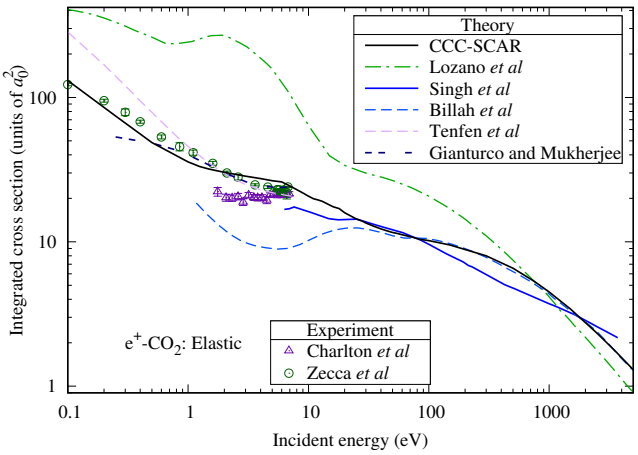

Figure 11.19: Elastic cross section for positron scattering on carbon dioxide. Theoretical results include those of the CCC-SCAR, Lozano *et al.* [155], Singh *et al.* [141], Billah *et al.* [156], Gianturco and Mukherjee [157], and Tenfen *et al.* [131]. Experimental results for incident electrons are from Charlton *et al.* [159] and Zecca *et al.* [160].

11.5.3 Total electronic excitation cross section

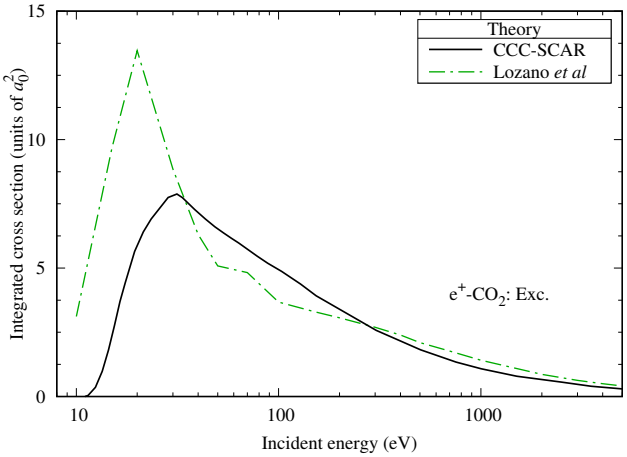

Figure 11.20: Total electronic excitation cross section for positron scattering on carbon dioxide. Theoretical results include those of the CCC-SCAR and the recommended results of Lozano *et al.* [155].

In Fig. 11.20, the CCC-SCAR results and those of Lozano *et al.* [155] for the total electronic excitation cross section are shown for e^+-CO_2. Both of these calculations are in close agreement for energies above 300 eV. Below this energy, different behaviour is found between the different calculations

with that of Lozano *et al.* [155] exhibiting a much larger peak than the CCC-SCAR at a slightly lower energy.

11.5.4 Electron-loss, direct ionisation, and positronium-formation cross sections

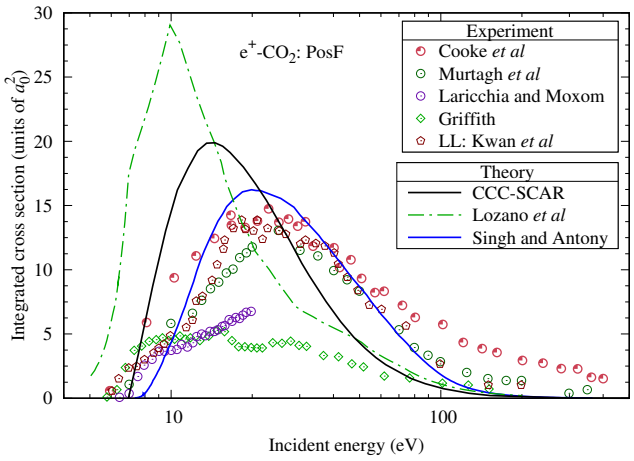

Figure 11.21: Positronium-formation cross section for positron scattering on carbon dioxide. Theoretical results include the CCC-SCAR and the calculations of Singh and Antony [24] and Lozano *et al.* [155]. Experimental CO_2 measurements are from Cooke *et al.* [161], Murtagh *et al.* [162], Laricchia and Moxom [163], Griffith [58], and the lower limits of Kwan *et al.* [147].

In Fig. 11.21, the positronium-formation cross section is shown for e^+-CO_2. Current CCC-SCAR results are presented with the calculations of Singh and Antony [24] and the measurements of Cooke *et al.* [161], Murtagh *et al.* [162], Laricchia and Moxom [163], Griffith [58], and Kwan *et al.* [147] (for the lower limits). Close agreement is found between the CCC-SCAR and the measurements from threshold to 8 eV. Beyond this, however, agreement is only found again above 80 eV with the measurements of Griffith [58]. The other presented measurements and the theoretical calculations of Singh and Antony [24] predict a maximum at an energy 10 eV above that of the CCC-SCAR and a much slower drop-off in this cross section. The calculations of Lozano *et al.* [155] utilised an IAM-SCAR+I approach for their calculations and have similar behaviour at high energies to the CCC-SCAR results, with close agreement between these calculations for energies above 50 eV. The large difference in their threshold for the results of Lozano

et al. [155] and the other results is because they did not shift the threshold of their inelastic processes as was done in the CCC-SCAR approach. The discrepancies found between the current calculations and the experiments is expected to result from the IAM-SCAR approach being insufficient to model positronium-formation for CO_2.

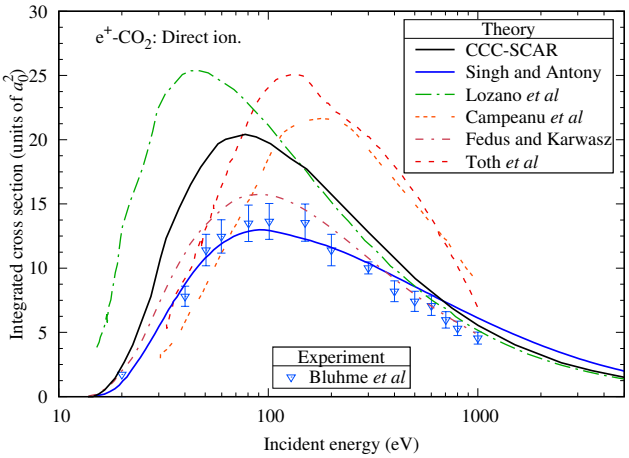

Figure 11.22: Direct ionisation cross section for positron scattering on carbon dioxide. Theoretical results include CCC-SCAR, Singh and Antony [24], Lozano *et al.* [155], Tóth *et al.* [152], Fedus and Karwasz [28], and Campeanu *et al.* [153]. Experimental results are from Bluhme *et al.* [154].

The direct ionisation cross section for e^+-CO_2 is presented in Fig. 11.22. Current CCC-SCAR results are shown alongside the theoretical calculations of Singh and Antony [24], Lozano *et al.* [155], Tóth *et al.* [152], Fedus and Karwasz [28], and Campeanu *et al.* [153]. The closest agreement is found between the current calculations and those of Lozano *et al.* [155] for energies above 100 eV, with these results slightly above the experiment of Bluhme *et al.* [154] for energies above 500 eV. The results of Singh and Antony [24] are in good agreement with this experiment, except for at high energies where it is larger than both the experimental and the CCC-SCAR results. The BEB results of Fedus and Karwasz [28] are between the CCC results and those of Singh and Antony [24] for intermediate energies and are lower than other theory above 700 eV. For these high energies, the IAM-SCAR approach is equivalent to the IAM method, and therefore, the current high-energy results are expected to be accurate. The calculations of Tóth *et al.* [152] and Campeanu *et al.* [153] both utilise distorted-wave based models

and predict similar behaviour to each other. However, this behaviour is very different from the other presented theory.

The electron-loss cross section is shown in Fig. 11.23 for the e^+-CO_2 scattering system. The CCC-SCAR results are shown alongside the theoretical calculations of Singh and Antony [24] and Billah *et al.* [156] and the experimental results of Bluhme *et al.* [154] and Laricchia and Moxom [163]. The CCC-SCAR results are higher than these experiments, except for energies near-threshold and at 40 eV. At higher energies, the CCC-SCAR is between the results of Billah *et al.* [156] and Singh and Antony [24].

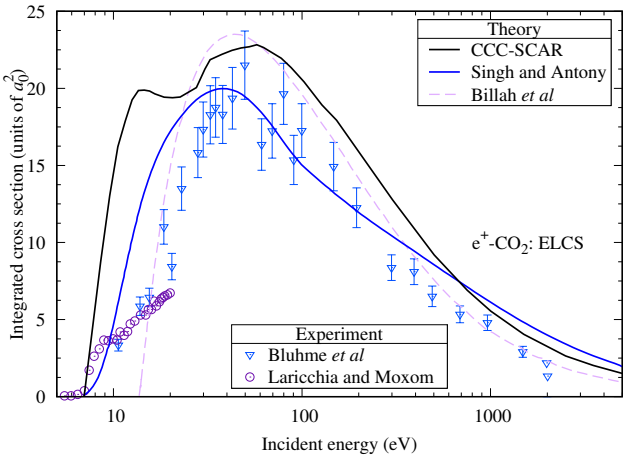

Figure 11.23: Electron-loss cross section for positron scattering on carbon dioxide Theoretical results are from the CCC-SCAR, Singh and Antony [24], and Billah *et al.* [156]. Experimental measurements are from Bluhme *et al.* [154] and Laricchia and Moxom [163].

11.5.5 Total inelastic cross section

In Fig. 11.24, the total inelastic cross section is shown for e^+-CO_2. CCC-SCAR results are presented alongside the calculations of Singh and Antony [24], Billah *et al.* [156], and Lozano *et al.* [155]. The results of all the theoretical calculations except for Billah *et al.* [156] follow a similar shape but at varying magnitudes. Between 50 eV and 300 eV, close agreement is found between the CCC-SCAR and the calculations of Lozano *et al.* [155]. For energies above 1000 eV, the CCC-SCAR is slightly higher than the other theoretical approaches.

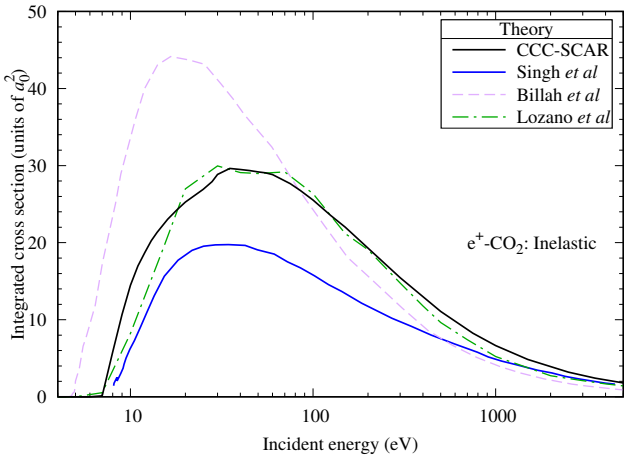

Figure 11.24: Total inelastic cross section for positron scattering on carbon dioxide. Theoretical results are from CCC-SCAR, Singh and Antony [24], Billah *et al.* [156], and Lozano *et al.* [155].

11.6 O_3 scattering

11.6.1 Total cross section

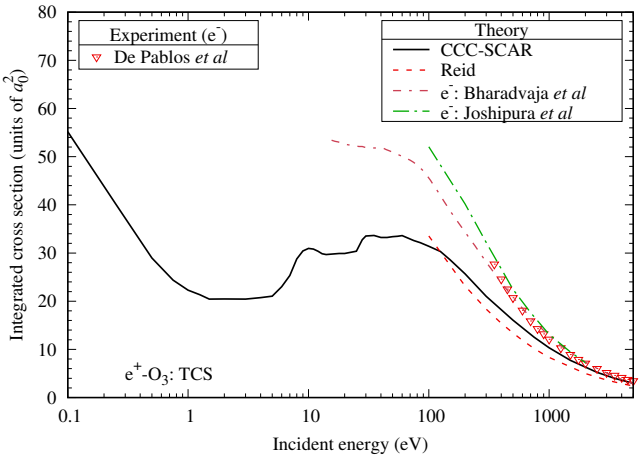

Figure 11.25: Total cross section for positron scattering on ozone. Theoretical CCC-SCAR results are shown alongside the calculations of Reid [164]. Electron theoretical results are from Bharadvaja *et al.* [165] and Joshipura *et al.* [166] and electron experimental results are from De Pablos *et al.* [167].

The total cross section for positron scattering on ozone is presented in Fig. 11.25. Current CCC-SCAR results are shown alongside the only other

positron results of Reid [164], which is an IAM calculation. We also present theoretical results by Bharadvaja *et al.* [165] and Joshipura *et al.* [166] and experimental results from De Pablos *et al.* [167] for electron scattering on ozone at high energies. Close agreement is found between the current calculations and the electron experiment for energies above 2000 eV. Below this energy, the electron experimental and theoretical results are larger than the positron calculations. The CCC-SCAR results feature a local maximum at 10 eV, followed by a second maximum at 30 eV. The CCC-SCAR then smoothly decreases for energies above 100 eV, similar to the calculations of Reid [164] but at a slightly higher magnitude.

11.6.2 Elastic cross section

The elastic cross section for a positron scattering on ozone is shown in Fig. 11.26. There are substantial differences between the current calculations and the IAM results of [164], with the CCC-SCAR almost an order of magnitude higher. The electron theoretical and experimental results are higher than the CCC-SCAR for the entire energy range but become relatively close by 5000 eV.

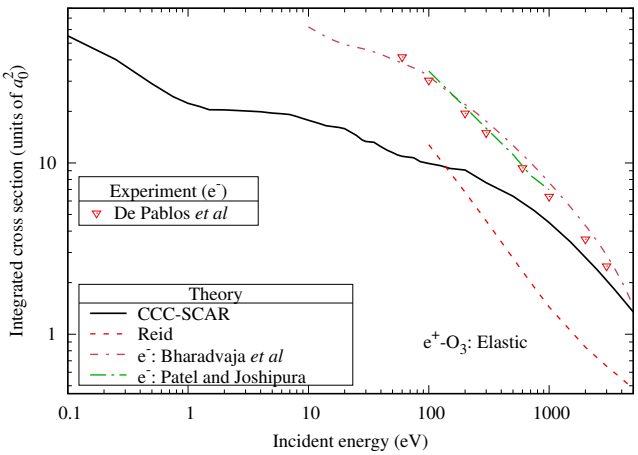

Figure 11.26: Elastic cross section for positron scattering on ozone. Theoretical CCC-SCAR results are shown alongside the calculations of Reid [164]. Electron theoretical results are from Bharadvaja *et al.* [165] and Patel and Joshipura [168] and electron experimental results are from De Pablos *et al.* [167].

11.6.3 Total electronic excitation cross section

In Fig. 11.27, the CCC-SCAR results for the total electronic excitation cross section for e^+-O_3 are shown alongside the calculations of Bharadvaja *et al.* [165] for e^--O_3. Both of these calculations find very different behaviour for this cross section. The electron calculations predict a rapid decrease in this cross section after 5 eV. The CCC-SCAR results feature a peak at 10 eV and decrease far slower than the electron calculation.

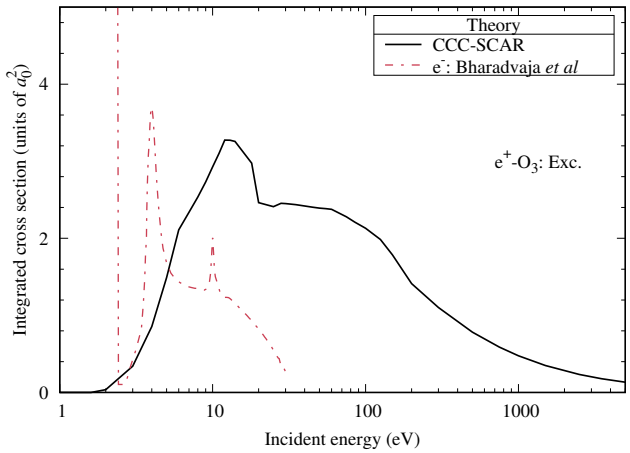

Figure 11.27: Total electronic excitation cross section for positron scattering on ozone. Theoretical CCC-SCAR results are shown alongside the electron theoretical results of Bharadvaja *et al.* [165].

11.6.4 Electron-loss, direct ionisation, and positronium-formation cross section

The positron-impact direct ionisation cross section for ozone is shown in Fig. 11.28. As there are no existing positron measurements or calculations, the CCC-SCAR is compared to existing electron-impact theory and experiment. These include the calculations of Bharadvaja *et al.* [165] and Joshipura *et al.* [166] and the experiments of Newson *et al.* [169] and Siegel [170]. For energies above 1000 eV and below 30 eV, we find good agreement with the calculations of Bharadvaja *et al.* [165]. The electron experiments are significantly lower than the electron and positron theoretical results.

As there is no existing theory or experiment for positronium-formation or electron-loss for positron scattering on ozone, we present these cross sections alongside the direct ionisation cross section in Fig. 11.29. At high energies,

the electron-loss cross section is equivalent to the direct ionisation cross section, so the comparisons with electron theory and experiment will be the same here. The positronium-formation features a peak at 10 eV, followed by a smooth descent to 200 eV where it becomes minimal.

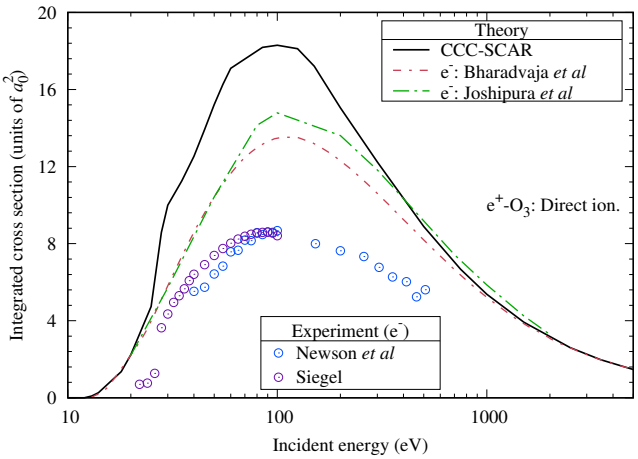

Figure 11.28: Direct ionisation cross section for positron scattering on ozone. Theoretical CCC-SCAR results are shown alongside the electron calculations of Bharadvaja *et al.* [165] and Joshipura *et al.* [166]. Electron experimental results are from Newson *et al.* [169] and Siegel [170].

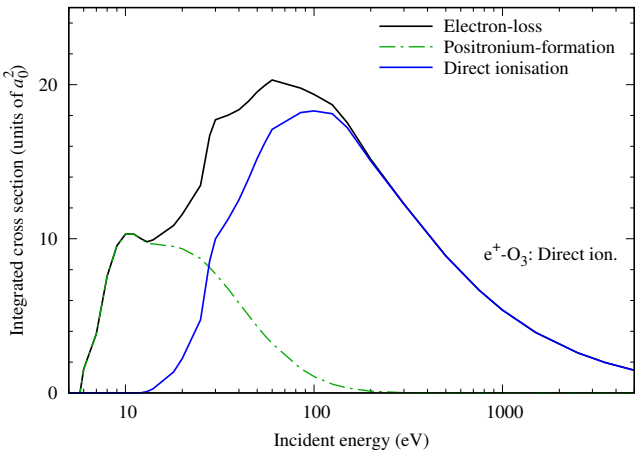

Figure 11.29: CCC-SCAR calculation of electron-loss, positronium-formation, and direct ionisation cross section for positron scattering on ozone.

11.6.5 Total inelastic cross section

The total inelastic cross section for positron scattering on ozone is shown in Fig. 11.30. The CCC-SCAR results are compared against the only existing theoretical calculations of Reid [164]. The two calculations follow a similar shape above 300 eV, with the CCC-SCAR slightly lower.

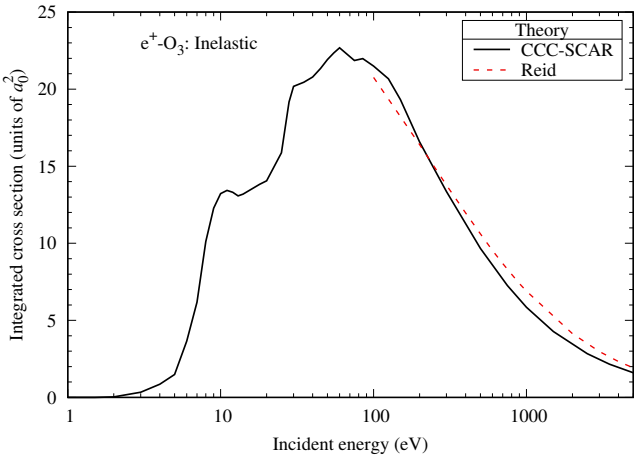

Figure 11.30: Total inelastic cross section for positron scattering on ozone. Theoretical CCC-SCAR results are shown alongside the calculations of Reid [164].

11.7 H_2O scattering

11.7.1 Total cross section

In Fig. 11.31 the total cross section for positron scattering on H_2O is shown. Current CCC-SCAR and CCC-SCAR+ROT results are presented alongside the theoretical results of Blanco *et al.* [171], Baluja *et al.* [394], and Sinha *et al.* [172]. Experimental results for positrons are from Makochekanwa *et al.* [173], Sueoka *et al.* [175], Kimura *et al.* [174], Loreti *et al.* [176], and Zecca *et al.* [177]. For energies above 50 eV, we also present the electron experimental results of Muñoz *et al.* [178]. Similar to the process taken for our H_2 results, we have scaled the H component of the current calculations to give agreement with the high energy σ_{tot} of Muñoz *et al.* [178]. This approach is described in detail in Section. 4.3.

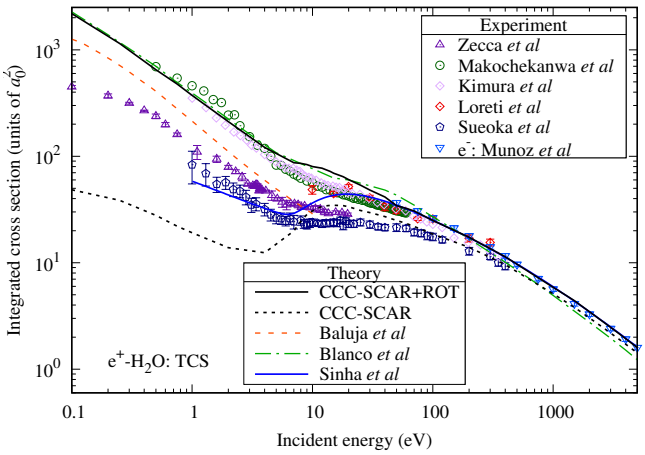

Figure 11.31: Total cross section for positron scattering on H_2O. Theoretical CCC-SCAR and CCC-SCAR+ROT results are shown alongside the calculations of Blanco *et al.* [171] and Sinha *et al.* [172]. Experimental results for positrons are from Makochekanwa *et al.* [173], Kimura *et al.* [174], Sueoka *et al.* [175], Loreti *et al.* [176], and Zecca *et al.* [177]. For incident electrons the experimental results of Muñoz *et al.* [178] are shown.

The rotational cross section must be accounted for to calculate the total cross section of H_2O accurately. This results from this molecule being both polar and non-linear, which results in it having an extra degree of freedom. The impact of this cross section is most notable at low energies, where the calculations of Blanco *et al.* [171] found it to represent almost 99% of their total cross section. In our CCC-SCAR+ROT calculations, we have summed the rotational cross sections that were obtained from the Born calculations of Blanco *et al.* [171] to our CCC-SCAR calculation.

For energies above 40 eV, excellent agreement is found between the current CCC-SCAR+ROT calculations and those of Sinha *et al.* [172]. The CCC-SCAR+ROT results are almost equivalent to the results of Blanco *et al.* [171] to 10 eV, lower between 30 eV and 150 eV, and then higher above 150 eV. Compared to the positron experiment, the current calculations are close to most of the experimental results for energies below 7 eV and above 40 eV. Between 7 eV and 40 eV, the current results are higher than the presented experiment.

11.7.2 Elastic cross section

The elastic cross section for e^+-H_2O is shown in Fig. 11.32. There are large discrepancies between the theoretical results for low and intermediate energies. There is also little agreement observed between the positron experiments. At 1000 eV, the CCC-SCAR and the calculations of Aouchiche *et al.* [181] and Sinha *et al.* [172] are within the error bars of the measurement of Katase *et al.* [183]. Above 1000 eV, these three theoretical methods are also in close agreement.

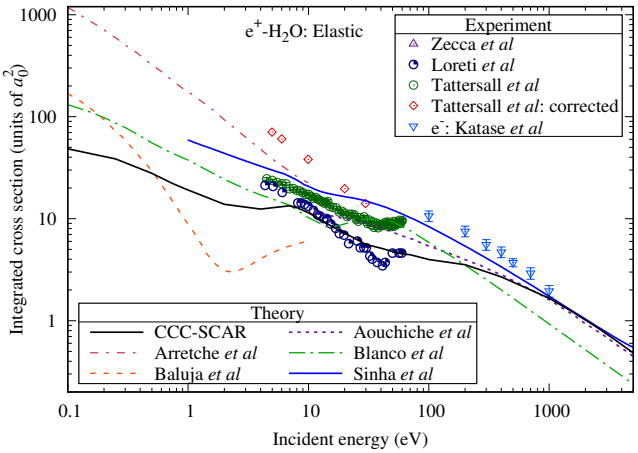

Figure 11.32: Elastic cross section for positron scattering on H_2O. Theoretical CCC-SCAR results are shown alongside the calculations of Blanco *et al.* [171], Sinha *et al.* [172], Baluja *et al.* [179], Arretche *et al.* [180], and Aouchiche *et al.* [181]. Experimental results are from Tattersall *et al.* [182] and Loreti *et al.* [176] for positrons and Katase *et al.* [183] for electrons.

11.7.3 Total electronic excitation cross section

The total electronic excitation cross section for e^+-H_2O is presented in Fig. 11.33. CCC-SCAR results are presented alongside the theoretical results of Blanco *et al.* [171] and Arretche *et al.* [302] and the experiment of Tattersall *et al.* [182]. The current results are significantly higher than the previous theory by almost a factor of four. Good agreement, however, is observed with the experiment of Tattersall *et al.* [182] to 10 eV.

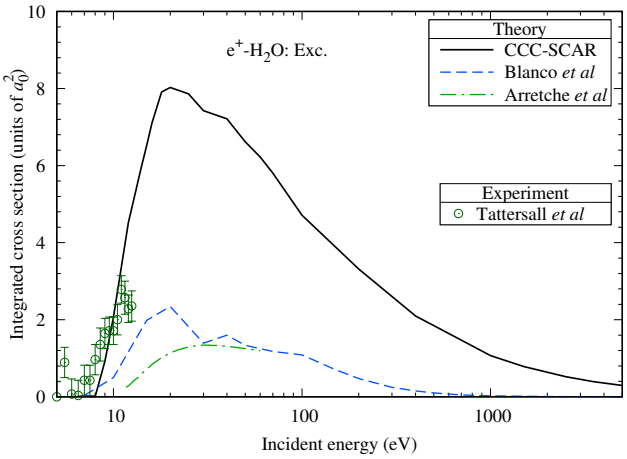

Figure 11.33: Total electronic excitation cross section for positron scattering on H_2O. Theoretical CCC-SCAR results are shown alongside the calculations of Blanco *et al.* [171] and Arretche *et al.* [184]. Experimental results for Tattersall *et al.* [182] are shown for energies below the direct ionisation threshold.

11.7.4 Electron-loss, direct ionisation, and positronium-formation cross section

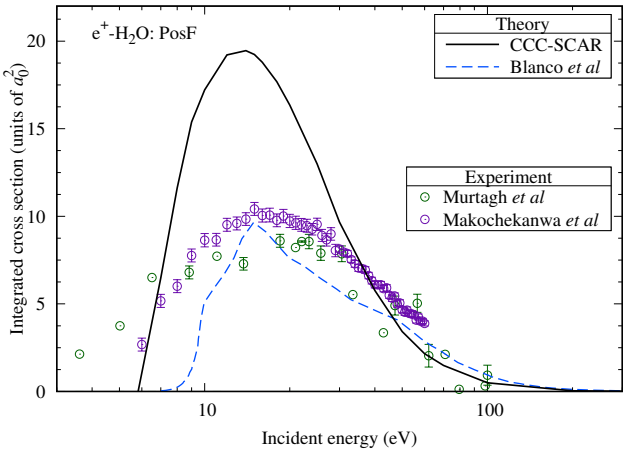

Figure 11.34: Positronium-formation cross section for positron scattering on H_2O. Theoretical CCC-SCAR results are shown alongside those of Blanco *et al.* [171]. Experimental results are from Makochekanwa *et al.* [173] and Murtagh *et al.* [162].

The positronium-formation cross section for the e^+-H_2O scattering system is shown in Fig. 11.34. The CCC-SCAR and Blanco *et al.* [171] theoretical

calculations are shown alongside the experimental results of Murtagh *et al.* [9] and Makochekanwa *et al.* [173]. The current results are within the range of experiment below 7 eV and above 35 eV. Between these energies, the CCC-SCAR results are significantly higher than experiment and the calculations of Blanco *et al.* [171]. The calculations of Blanco *et al.* [171] are slightly higher than the CCC-SCAR for energies above 50 eV.

In Fig. 11.35, the direct ionisation cross section is shown for e^+-H_2O. Current CCC-SCAR results are shown alongside the calculations of Blanco *et al.* [171] and the Coulomb plus plane waves with full energy range (CPE) and electron-screening (ES) distorted-wave models of Tóth *et al.* [152]. There are no positron experimental results for direct ionisation. Therefore, results are shown alongside the e^--H_2O experiments of Bolorizadeh and Rudd [186], Khare and Meath [187], Muñoz *et al.* [178], Straub *et al.* [188], and Rao *et al.* [189]. For energies above 150 eV, there is excellent agreement between the different theoretical methods. Below 150 eV, the current results are in closest agreement with the ES model of Tóth *et al.* [152] with the other theoretical results lower. There is excellent agreement between the measurements of Bolorizadeh and Rudd [186] and the CCC-SCAR results from 150 eV to 5000 eV.

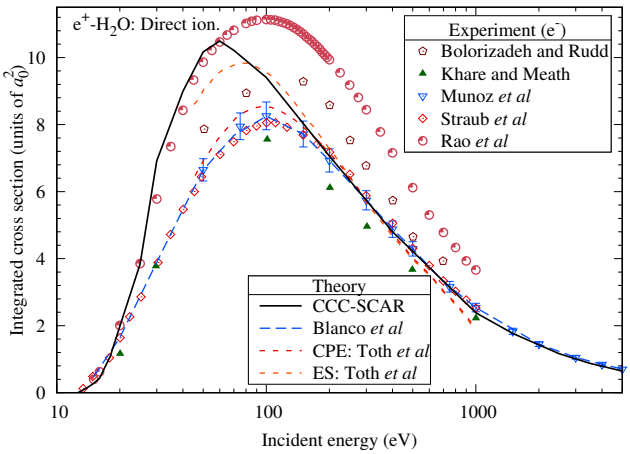

Figure 11.35: Direct ionisation cross section for positron scattering on H_2O. Theoretical CCC-SCAR results are shown alongside those of Blanco *et al.* [171] and Tóth *et al.* [185]. Experimental results for electrons are from Bolorizadeh and Rudd [186], Khare and Meath [187], Muñoz *et al.* [178], Straub *et al.* [188], and Rao *et al.* [189].

The electron-loss cross section is shown in Fig. 11.36 for e^+-H_2O. The CCC-SCAR results are shown with the calculations of Blanco *et al.* [171] and the electron experiments that were presented for the direct ionisation cross section [178, 186–189]. Below 150 eV, the CCC-SCAR results are larger than the calculations of Blanco *et al.* [171]. This results mainly from the larger positronium-formation cross sections found within the current calculation.

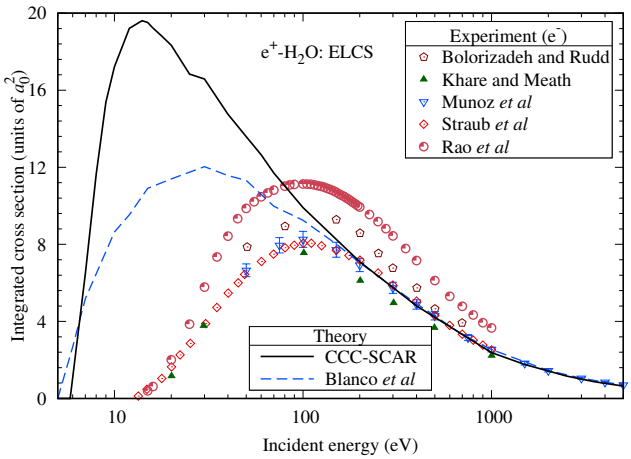

Figure 11.36: Electron-loss cross section for positron scattering on H_2O. Theoretical CCC-SCAR results are shown alongside those of Blanco *et al.* [171]. Experimental results for electrons are from Bolorizadeh and Rudd [186], Khare and Meath [187], Muñoz *et al.* [178], Straub *et al.* [188], and Rao *et al.* [189].

11.7.5 Total inelastic cross section

The total inelastic and direct inelastic cross section are shown in Fig. 11.37 for positron scattering on H_2O. The total inelastic cross section is the sum of the direct ionisation, total electron excitation, and positronium-formation cross sections. The direct inelastic cross section, on the other hand, is the sum of the total electron excitation and direct ionisation cross sections. As with the total electron excitation cross section (Fig. 11.33) the direct inelastic results are significantly larger than the calculations of Blanco *et al.* [171]. For this cross section, the current CCC-SCAR calculations follow a similar shape to the results of Tattersall *et al.* [182], however, have a higher magnitude. For the total inelastic cross section, the current results are close to those of Blanco *et al.* [171] for energies above 100 eV. Below 100 eV, different behaviour is found between both of these calculations.

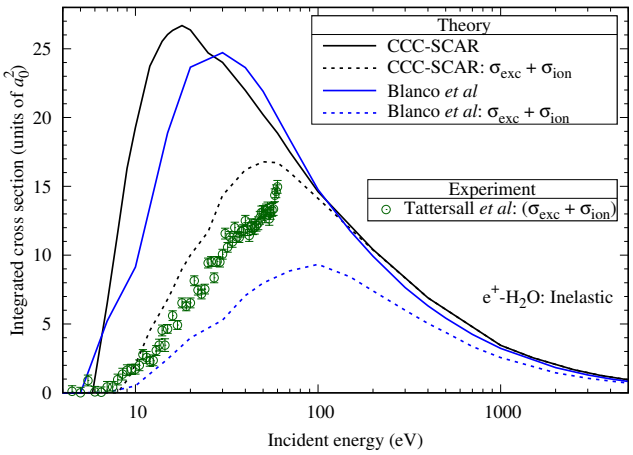

Figure 11.37: Total inelastic and direct inelastic cross section for positron scattering on H_2O. Theoretical CCC-SCAR results are shown alongside the calculation of Blanco *et al.* [171] and the direct inelastic experiment of Tattersall *et al.* [182].

11.8 CH_4 scattering

11.8.1 Total cross section

The total cross section for positron scattering on CH_4 is shown in Fig. 11.38. CCC-SCAR results are shown alongside the theoretical results of Singh *et al.* [141], Baluja and Jain [190], Rawlins *et al.* [193], Zecca *et al.* [192], Jain and Gianturco [191], and De-Heng *et al.* [194]. The measurements of Charlton *et al.* [195], Sueoka and Mori [196], Zecca *et al.* [192], and Dababneh *et al.* [52] and the high-energy results from the recommended results of Song *et al.* [197] are also included. As was done for H_2O, the H components of the CCC-SCAR calculations have been scaled to give agreement with the high-energy electron results of Song *et al.* [197]. The CCC-SCAR results are close to those of Singh *et al.* [141] for energies between 100 eV and 500 eV. Above 500 eV, the CCC-SCAR follows a similar shape as the results of Singh *et al.* [141] but with a higher magnitude. The SMC results of Zecca *et al.* [192] and the model potential results of Jain and Gianturco [191] are both significantly lower than the current calculation for energies above 0.4 eV. Compared to the calculations of Baluja and Jain [190] the CCC-SCAR is larger for energies below 50 eV and above 500 eV. For the results of De-Heng *et al.* [194] the CCC-SCAR results are larger for energies above 500 eV and lower

for energies under 500 eV. The CCC-SCAR results are in good agreement with experiment for energies below 1 eV [192] and above 80 eV [52].

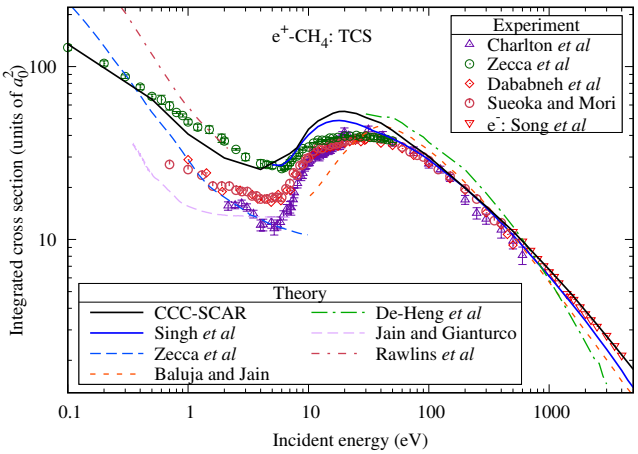

Figure 11.38: Total cross section for positron scattering on CH_4. Theoretical CCC-SCAR results are shown alongside the calculations of Singh *et al.* [141], Baluja and Jain [190], Jain and Gianturco [191], Zecca *et al.* [192], Rawlins *et al.* [193], and De-Heng *et al.* [194]. Experimental results for positrons are from Charlton *et al.* [195], Sueoka and Mori [196], Zecca *et al.* [192], and Dababneh *et al.* [52]. The recommended results of Song *et al.* [197] for electron scattering on methane are also given.

11.8.2 Elastic cross section

The elastic cross section for e^+-CH_4 is shown in Fig. 11.39. CCC-SCAR results are presented alongside the calculations of Jain [198], Zecca *et al.* [192], and Rawlins *et al.* [193]. For energies below the positronium-formation threshold, the $\sigma_{\rm tot}$ experimental results of Charlton *et al.* [195], Zecca *et al.* [192], and Dababneh *et al.* [52] are also shown. The measurements for electrons of Sakae *et al.* [199], which were conducted for energies up to 700 eV, have also been included. For energies above 200 eV, excellent agreement is found between the CCC-SCAR results and those of Jain [198]. Below 200 eV, the results of Jain [198] are lower than the CCC-SCAR results. The experimental results of Sakae *et al.* [199] have not been completed to high enough energies for the electron and positron elastic scattering to become equivalent. However, the results follow a similar shape to the current calculations, and differences decrease with increasing energy.

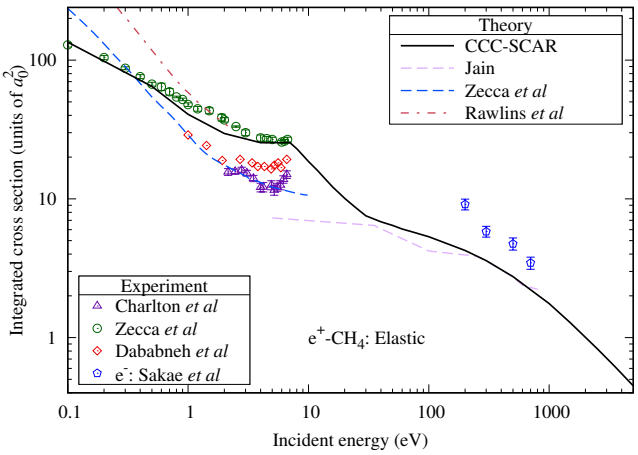

Figure 11.39: Elastic cross section for positron scattering on CH_4. Theoretical CCC-SCAR results are shown alongside the calculations of Jain [198], Zecca *et al.* [192], and Rawlins *et al.* [193]. Experimental results for electrons are from Sakae *et al.* [199] and for positrons are from Charlton *et al.* [195], Zecca *et al.* [192], and Dababneh *et al.* [52].

11.8.3 Electron-loss, direct ionisation, and positronium-formation cross section

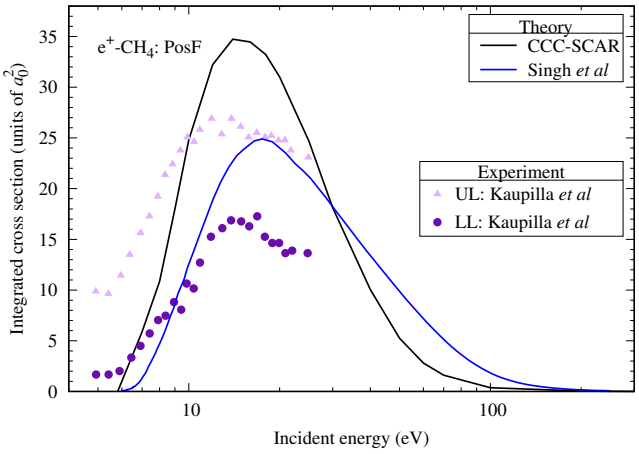

Figure 11.40: Positronium-formation cross section for positron scattering on CH_4. Theoretical CCC-SCAR results are shown alongside the results of Singh and Antony [24] and the upper and lower limit measurements of Kauppila *et al.* [200].

The CCC-SCAR results for the positronium-formation cross section of e^+-CH_4 are shown in Fig. 11.40 alongside the calculations of Singh and Antony

[24] and upper and lower limit measurements of Kauppila *et al.* [200]. The CCC-SCAR calculations are within the experimental limits for energies below 10 eV. The calculations of Singh and Antony [24] are smaller than the CCC-SCAR results to 30 eV. Above 30 eV, these calculations are higher than the CCC-SCAR results.

Results for the direct ionisation cross section are shown in Fig. 11.41. This cross section has had the most theoretical investigation for this molecule with CCC-SCAR results shown alongside the calculations of Singh and Antony [24], Tóth *et al.* [152], Campeanu *et al.* [201], and Fedus and Karwasz [28]. No measurements have been conducted for positron scattering for this process; therefore, we also present the recommended electron results of Song *et al.* [197]. For energies between 100 eV and 300 eV, the current CCC-SCAR calculations are lower than other theoretical results. From 300 eV to 700 eV, the CCC-SCAR results are in close agreement with the calculations of Tóth *et al.* [152] but are higher for energies above 700 eV. From threshold to 25 eV, there is good agreement between the CCC-SCAR and the results of Singh and Antony [24]. Between 15 eV and 300 eV, the different theoretical calculations are in disagreement for the magnitude of this cross section. The experimental results of Song *et al.* [197] are above the current CCC-SCAR results for energies above 100 eV.

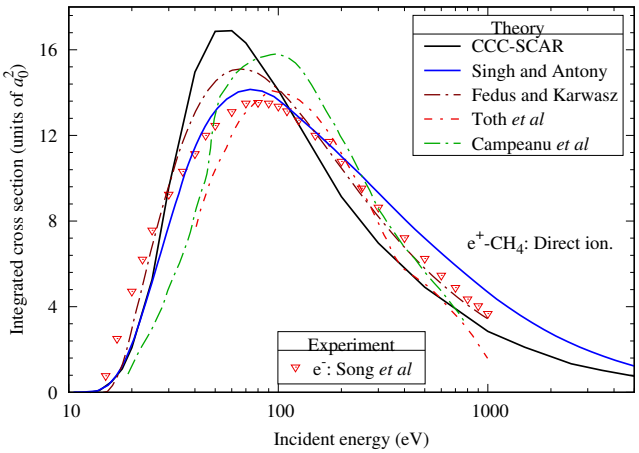

Figure 11.41: Direct ionisation cross section for positron scattering on CH_4. The CCC-SCAR results are shown alongside the theoretical results of Singh and Antony [24], Tóth *et al.* [152], Campeanu *et al.* [201], and Fedus and Karwasz [28]. Experimental results for incident electrons are from Song *et al.* [197].

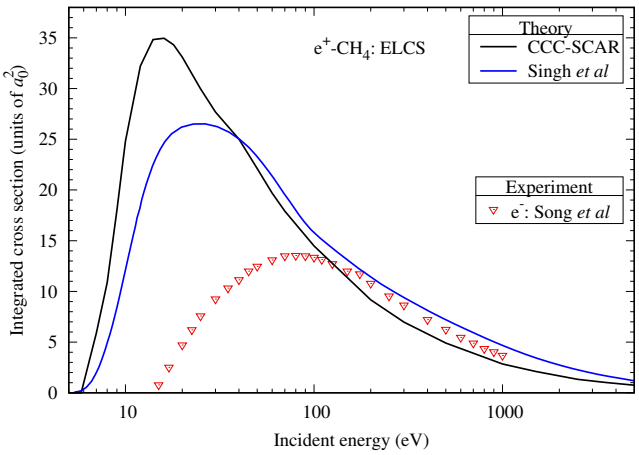

Figure 11.42: Electron-loss cross section for positron scattering on CH_4. Theoretical CCC-SCAR results are shown alongside the results of Singh and Antony [24].

In Fig. 11.42, the electron-loss cross section for e^+-CH_4 is shown. Current CCC-SCAR results are shown alongside the calculations of Singh and Antony [24] and the recommended electron results of Song *et al.* [197]. For energies above 50 eV, the CCC-SCAR follows a similar shape to the calculations of Singh and Antony [24] but are lower. Below 30 eV, the CCC-SCAR results are larger than those of Singh and Antony [24] and have a maximum at 15 eV, whereas the results of Singh and Antony [24] have a maximum at 25 eV.

11.8.4 Total inelastic and excitation cross section

The e^+-CH_4 total inelastic cross section is shown in Fig. 11.43. The current CCC-SCAR results are shown alongside those of Singh *et al.* [141]. Similar shapes are found for both calculations, but the CCC-SCAR results are significantly higher than those of Singh and Antony [24] for energies above 15 eV. Also shown in this figure is the CCC-SCAR total electronic excitation cross section, due to the absence of previous theoretical or experimental work these are presented without comparison.

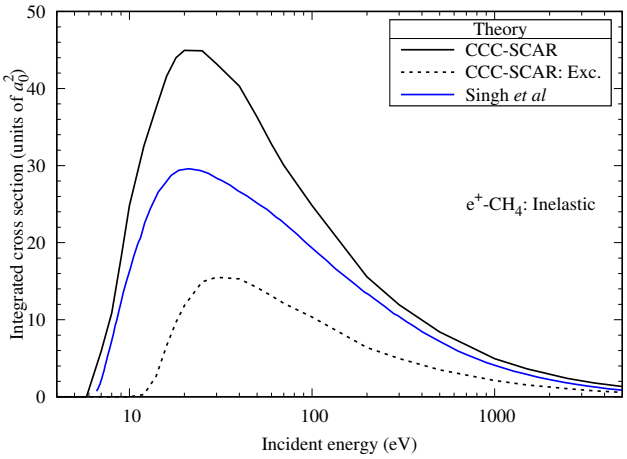

Figure 11.43: Total inelastic cross section for positron scattering on CH_4. Theoretical CCC-SCAR results are shown alongside the results of Singh *et al.* [141]. The CCC-SCAR total electronic excitation cross section (Exc.) is also shown.

11.9 CF_4

11.9.1 Total cross section

The total cross section for positron scattering on CF_4 is shown in Fig. 11.44. Current CCC-SCAR results are shown alongside the positron calculations of Baluja and Jain [190] and experiment of Sueoka *et al.* [202]. Experimental results for e^--CF_4 by Zecca *et al.* [203] are also shown for energies above 150 eV. The CCC-SCAR results are higher than the calculations of Baluja and Jain [190] for energies above 10 eV, with differences between the two calculations increasing with increasing energy. Good agreement is found with the experiment of Sueoka *et al.* [202] for energies between 6 eV and 10 eV and above 100 eV. At sufficiently high incident energies, the cross sections for electrons and positrons are expected to become equal as the Born approximation becomes valid. This occurs above 1000 eV, with close agreement between the CCC-SCAR and the electron experiment of Zecca *et al.* [203] for these energies.

For energies below 6 eV, there is markedly different behaviour between the current calculation and the experiment of Sueoka *et al.* [202]. This experiment was not corrected for the forward angle scattering effect, which can result in measured cross sections undercounting the true result [248].

Furthermore, for energies below 30 eV, these positron measurements are not expected to be accurate as they exhibit an unphysical energy dependence [248]. These errors are likely the source of the discrepancy between the current results and this experiment.

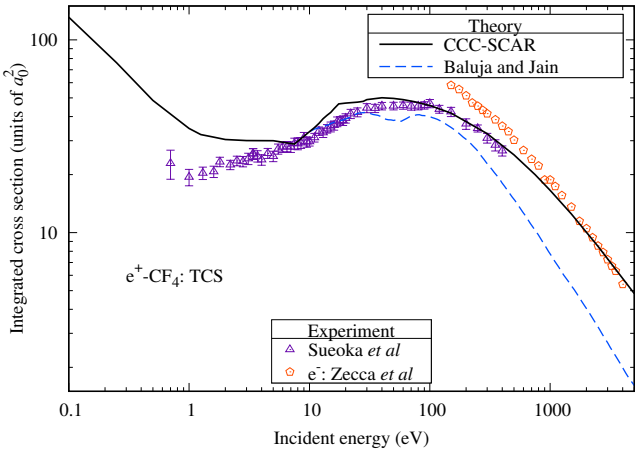

Figure 11.44: Total cross section for positron scattering on CF_4. Theoretical CCC-SCAR results are shown alongside the calculations of Baluja and Jain [190] and the measurements of Sueoka *et al.* [202] for positrons, and Zecca *et al.* [203] for electrons.

11.9.2 Direct ionisation cross section

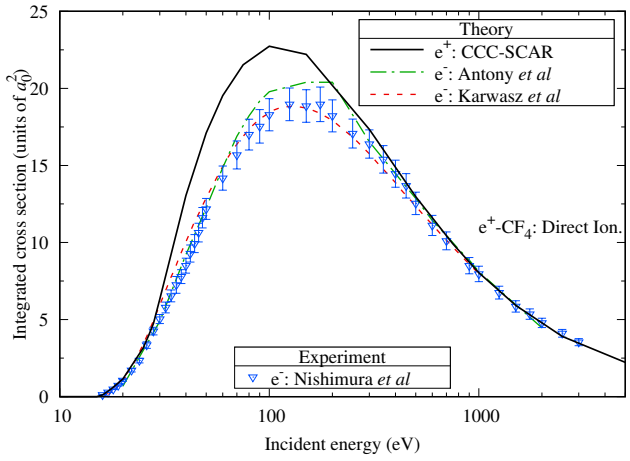

Figure 11.45: Direct ionisation cross section for positron scattering on CF_4. Theoretical positron CCC-SCAR results are shown alongside the electron calculations of Antony *et al.* [204] and Karwasz *et al.* [205], and the measurements of Nishimura *et al.* [206].

In Fig. 11.45, we present direct ionisation cross sections for e^+-CF_4. As no other positron theory or experiment exist, the current CCC-SCAR results are shown alongside the theoretical calculations of Antony *et al.* [204] and Karwasz *et al.* [205], and the experiment of Nishimura *et al.* [206] for e^--CF_4. For direct ionisation, the differences between positron and electron results will be similar to that of atomic fluorine, with results for both projectiles being similar at low and high incident energies and positron results higher in between. As expected, the current CCC-SCAR is in close agreement with the electron theory and experiment for energies above 200 eV, and is larger than the electron results at lower energies.

11.9.3 Inelastic cross sections

In the absence of other calculations or experiments to compare against, we have presented the total inelastic cross section and its components in Fig. 11.46. The positronium-formation has a peak at 15 eV and is the major component of inelastic scattering to 25 eV. Above 25 eV, direct ionisation is the major component to 5000 eV. The total electronic excitation cross section has its maximum at 20 eV.

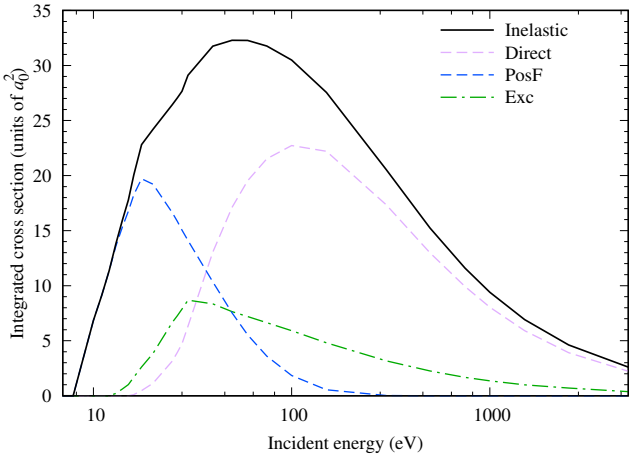

Figure 11.46: CCC-SCAR total inelastic cross section and the positronium-formation (PosF), total electronic excitation (Exc), and direct ionisation components for positron scattering on CF_4.

11.10 Chapter summary

In this chapter CCC-SCAR calculations are presented for positron scattering from the H_2, C_2, O_2, CO, CO_2, O_3, H_2O, CH_4, and CF_4 molecules. In general, good agreement is found with the current results and previous theory and experiment. The current results were generally within the range of positron experiment and theory for intermediate to high energies and in agreement with electron measurements and theory for high energies. Significant differences, however, were found for the positronium-formation cross section for energies up to 30 eV, with the current approach generally considerably higher than other calculations and experiments for this energy range. Other discrepancies between theoretical results were found for the total electronic excitation cross sections of several molecules, for which there is a notable absence of experimental results.

In this case, we have applied the IAM-SCAR method to cross sections that were first demonstrated to be accurate for the corresponding atomic systems. Through the provision of the obtained cross sections for the wide range of considered molecules, we aim to provide results from which more advanced theoretical approaches can follow. It is recommended that further work is undertaken for the results in which significant disagreements exist between different methods and experiment, such as the positronium-formation and total electronic excitation cross sections.

The present work has demonstrated the advantages and limitations of using the IAM-SCAR approach to model positron collisions with molecules. The current modified IAM-SCAR approach produces accurate molecular cross sections at intermediate and high energies, especially when the underlying atomic cross sections are of high accuracy. This methodology however, is less accurate in the low-energy regime, most notably below 1 eV, where the impact of the molecule's structure has the most influence. Furthermore, the current approach systematically overestimates the positronium-formation cross section for energies below 30 eV. Further progress in improving the accuracy of the collision data, particularly at low projectile energies, has to come from a complete treatment of the molecular target as a whole.

Chapter 12

Conclusions

This thesis has presented single-centre CCC results for positron scattering on carbon, oxygen, neon, argon, boron, and fluorine atomic targets. Apart from neon and argon, this is the first time the CCC method has been applied to positron scattering from these targets. To validate the structure models utilised for each atom the results for oscillator strengths, excitation energies, and multipole polarisabilities are directly compared to previous theoretical and experimental values. For each of these targets, cross sections of all major elastic and inelastic scattering transitions have been computed. For most transitions, good agreement has been observed between current results and previous theory and experiment. Large discrepancies, however, have been found between current and previous results for some atom's low-energy, elastic, positronium-formation, and direct ionisation cross sections. We hope that the current results will spur further theoretical and experimental work to address these discrepancies.

To conduct these calculations the frozen-core atomic CCC code has been extended to allow for scattering on targets with any number of active electrons. This code was validated through comparisons between frozen-core calculations with this new code and the existing CCC code for a range of different target atoms, angular momenta, and spin. To calculate the direct ionisation and positronium-formation cross sections a new approach has been developed in which the results of complex model potential calculations are scaled directly to those of the single-centre CCC. Through comparison with existing two-centre calculations this method is found to be reasonably accurate for the considered transitions.

The IAM-SCAR approach has also been applied to the cross sections calculated within this thesis and previous results for atomic H. Through comparisons with single- and two-centre CCC calculations of positron scattering on H_2 we have modified this approach to produce better agreement with these molecular calculations. These CCC-SCAR calculations have then been completed for positron scattering from the O_2, CO, CO_2, O_3, H_2O, CH_4, and CF_4 molecules. Through the provision of the obtained cross sections for the wide range of considered molecules, we aim to provide results from which more advanced theoretical approaches can follow.

12.1 Data availability

The positron-atom cross sections calculated within this thesis are available online at the atomic CCC database: https://atom.curtin.edu.au/CCC-WWW/.

12.2 Future work

The next steps for this project will be to calculate cross sections from other important light atoms such as nitrogen, calcium, phosphorous, and sulphur. The obtained cross sections for these atoms can then be utilised alongside existing results to calculate positron scattering from important biomolecules, such as the bases of DNA, with the IAM-SCAR method.

For positron scattering, extensions can be made to the methodology to allow calculation of annihilation. The current positron code could also be extended to electron scattering through the addition of exchange V-matrix elements. Calculations for electron scattering can use the same structure models as for the positron case and, therefore, could be readily undertaken for all atomic targets considered within this thesis. Furthermore, GPU acceleration can be implemented into the current CCC code to increase its speed and allow for larger scattering calculations to be conducted.

Appendix A

Computational implementation

A.1 Input files

A description is provided here of the input files utilised by the current code to provide a better understanding of the code.

A.1.1 Calculation data

The file "data.in" includes a range of different values required for the calculation. This includes structure information such as the Z value, the number and ℓ of the core orbitals, the incident energy of the positron, and the energy of the ion. It is from this inputted ion energy and the calculated energy of the states from which the ionisation threshold is calculated.

The Laguerre basis functions are also listed with the value of N_ℓ and α_ℓ given for each considered ℓ. Other inputs include the maximum total angular momentum J the calculation is conducted to and the k-grid utilised within the calculation.

A.1.2 Configurations

Configurations to be included in the calculation are listed in a file named "conf.inp" as shown below for the example of argon. Here, frozen orbitals are listed in the first line and in subsequent lines configurations containing active orbitals are listed. The numbers in brackets for these active orbitals

represent the number of active electrons present within each orbital. The "99" term generates all possible orbitals based on the limits of the Laguerre basis, .e.g. in the case of $N_\ell = 30$ for each ℓ then all possible configurations with n up to $n = 30$ will be included in the calculation.

```
Ar
1s   2s   2p
3s(2)   3p(6)
3s(2)   3p(5)   99s(1)
3s(2)   3p(5)   99p(1)
3s(2)   3p(5)   99d(1)
```

A.1.3 F5 file

The "F5" file allows you to list all states that will be included in the calculation. In the below example for Ar we see that 30 s states, 25 p states, and 20 d states will be included in the calculation. This file can be edited to include a range of states of different spins, ℓ_{max}, and parity.

```
1   ! iSmax number of spin values target: Ar
0   ! spin values
2   ! Lmaxst
30   0   20   ! nstate(...) par = +1, spin 0
0   25   0   ! nstate(...) par = -1, spin 0
```

A.1.4 Input wavefunctions

When using the HF or MCHF code, wavefunctions are output into a file called "wfn.inp". This file is stored in binary and read by the current code during the structure calculations.

A.2 CCC code outline

The CCC code used to calculate positron scattering from atomic targets in this thesis is written in Fortran and utilises the OpenMP and MPI parallelisation processes to increase computational efficiency. On a supercomputer calculations are completed on nodes, which contain one or more CPUs and an attachment of memory. These CPUs contain a number of CPU cores which can be run in parallel. With the use of OpenMP, sections of a computer code can be parallelised up to the maximum number of available processes on a node. This parallelisation is limited to one node and cannot be distributed between different nodes. MPI parallelisation, on the other hand, runs a copy of the code on each available node and, therefore, by distributing a calculation across nodes can perform calculations utilising the combined memory of available nodes. OpenMP can be utilised alongside MPI parallelisation to parallelise a calculation to all the processes on all available nodes.

Due to the shared memory and speed increases resulting from this parallelisation scheme, the feasible size of atomic scattering calculations that can be completed is significantly increased. During code development, the current code was further optimised with the Arm MAP profiler to identify bottlenecks and other inefficiencies. Furthermore, this code has been tested and ran on a number of different machines which required different profilers.

In the following outline of the code, we have split the CCC code into the structure and scattering components. In practise, these two sections are connected and directly after the completion of structure calculations the code moves onto the scattering calculations.

A.2.1 Structure

The section of the code that calculates the structure of the target atom is described here and is depicted as a schematic in Fig. A.1. This section of the code is completed on the first process of each available node. First, the input file "data.in" is read to establish the required data for the calculation. Following this, the HF/MCHF wavefunctions are read from "wfn.inp," and the local potential is constructed. The Laguerre basis is produced and diagonalised to produce an orthonormal basis of one-electron functions, and corresponding one-electron Hamiltonian matrix elements, which are stored in

an object file. This basis is then combined with the HF/MCHF radial functions and relevant one-electron Hamiltonian matrix elements are recalculated. This final basis is stored in the Orbitals object. The Gramm-Schmidt orthogonalisation procedure is then utilised to ensure orthonormality of the final basis.

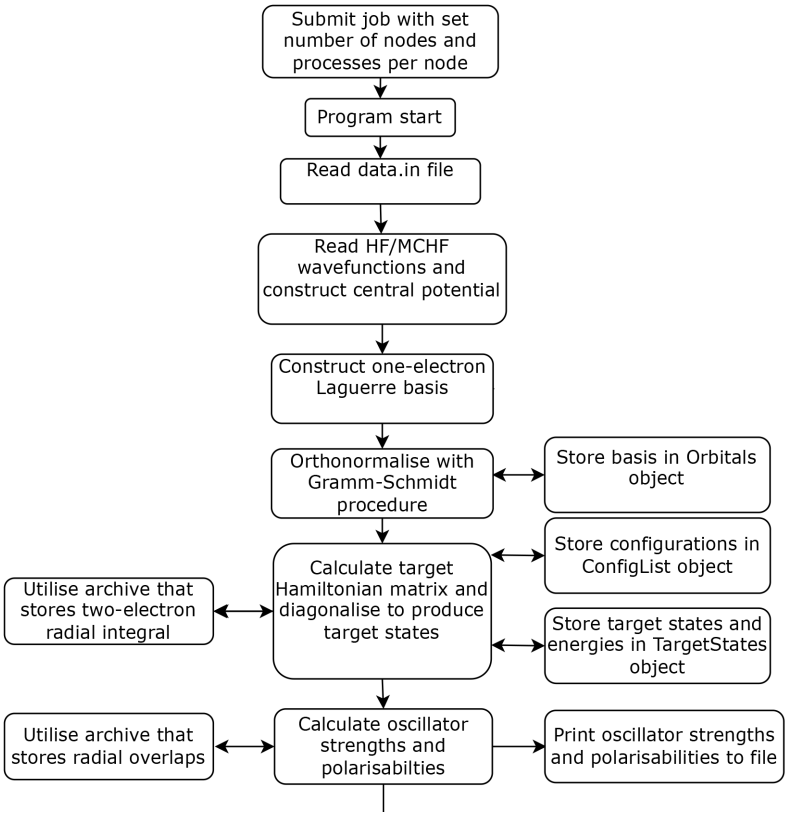

Figure A.1: Schematic of the program start and structure component of current CCC code.

Using the configurations listed in "conf.inp," the configuration functions are created from the one-electron basis and stored in the TargetConfigs object. The target Hamiltonian matrix is then calculated through use of the BSR subroutines and one-electron basis. OpenMP parallelisation and an archive that stores the two-electron radial integral (Eq. 2.19) are utilised to speed up the calculation of this matrix. The target Hamiltonian matrix is then diagonalised by using the *rsg* subroutine (from the eispack package) to obtain the CI coefficients, target states, and energy of the target states. The target states and all associated information is stored in the TargetStates

object.

The target atom's oscillator strengths and dipole/quadrupole/octupole polarisabilities can then be calculated with these target states. The calculation of these values is optimised by applying OpenMP parallelisation to existing loops and an archive that stores the overlaps between one-electron orbitals. These results are then written to file.

A.2.2 Scattering

Following the structure calculations, we describe here the scattering component of the code through to the end of the program. This process is also shown as a schematic in Fig. A.2. First, analytical Born cross sections are calculated, printed to file, and saved for use in the analytical Born completion near the end of the calculation. The angular coefficients that are calculated during this process by the BSR subroutines are stored, as they are also used in the V-matrix calculation. After this, a loop is begun over the total angular momentum J and parity. For each loop, a list of scattering channels are produced and the required continuum waves are calculated. All of these calculations are completed on the first process of each available node. Consequently, the continuum wavefunctions and target wavefunctions are stored on each of the nodes utilised in the calculation.

Due to the large number of states included in the calculations completed in this thesis, the V-matrix elements require significant memory and time to be computed. The memory requirements are far beyond that available on a single node, and therefore, MPI parallelisation is utilised to distribute this calculation among a set of nodes. Furthermore, by increasing the number of nodes in the calculation the time taken by the calculation is also reduced. The V-matrix calculation for the current J is therefore distributed equally between the available nodes. OpenMP parallelisation is used on each node to further parallelise the calculation of the V-matrix elements distributed to that node.

After calculating the V-matrix elements, the partial-wave Lippmann-Schwinger equations are solved with the ScaLAPACK routines for the current scattering symmetry. These routines utilise openMP and MPI parallelisation to distribute the calculation among every process on every node. The partial-wave T-matrix elements and other required observables are then obtained on the first node. Once the loop over total angular momentum and

parity is complete, the final cross sections and observables are calculated and printed to file by the first node.

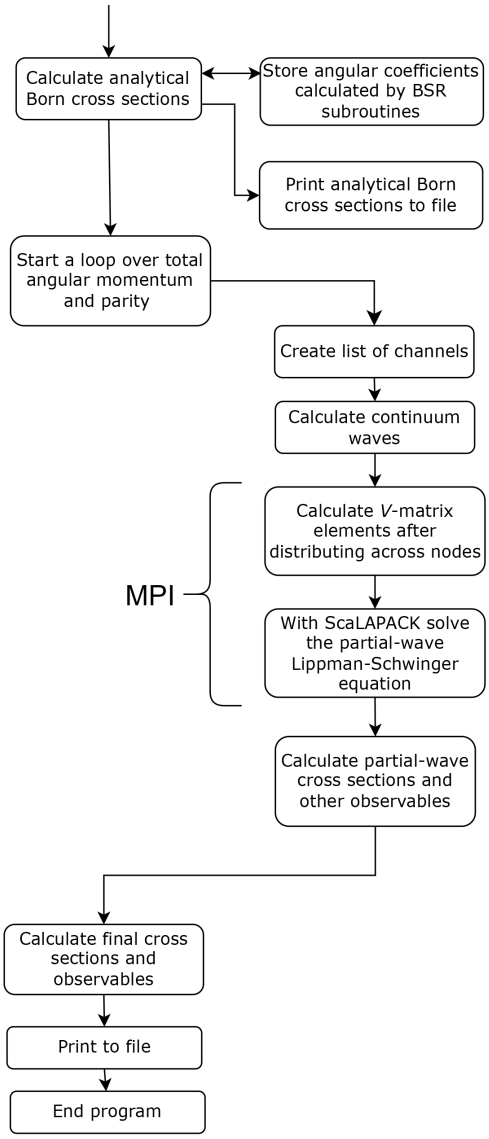

Figure A.2: Schematic of scattering component to end of program of the current CCC code. The section labelled as MPI is where MPI parallelisation is used to distribute the calculation among each of the available nodes.

Appendix B

Scaled Born cross sections

Once an accurate structure model is obtained Born calculations can be completed with relative ease. Through the scaling approach of Kim [272], accurate results for the total ionisation cross section for electrons can then be obtained. The accuracy of these scaled Born calculations is directly related to the accuracy of the structure used to calculate them [124]. The structure model of each Born calculation is the largest model described in the relevant chapters. Below, we provide results for the atomic targets considered within this thesis.

B.1 Carbon

In Fig. B.1 we present the Born and scaled Born cross section for electron scattering for carbon alongside existing theory and experiment. For energies above 200 eV, the scaled Born results are within the error of the experiment by Brook *et al.* [35]. For the range 30 eV to 200 eV, these scaled Born results are marginally larger than this experiment, and below 30 eV, they are somewhat lower. The unscaled results are significantly larger than this experiment for energies below 500 eV. Above 200 eV, the BEB results are in close agreement with the scaled Born results. The experimental results of Wang and Crawford [36] significantly overestimate the current and BEB results, with it in closer agreement with the Born result.

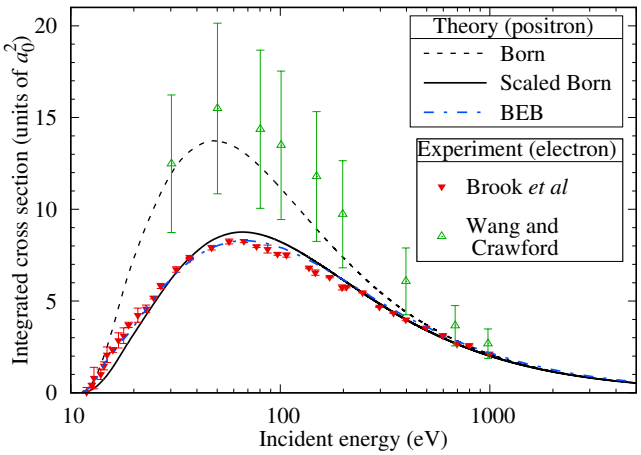

Figure B.1: Born and scaled Born calculations for the total ionisation cross section of an electron scattering on carbon. These results are compared against the BEB calculations [45] and the measurements by Brook *et al.* [35] and Wang and Crawford [36].

B.2 Oxygen

We compare the scaled Born cross section for oxygen with that of existing experiment and theory for electron scattering in Fig. B.2. This is a useful test as the accuracy of this approach is directly related to the accuracy of the model used [272]. We find excellent agreement with the measurements of Thompson *et al.* [55], with our scaled Born result within error for most measured points. The peak of our scaled cross section lies within the uncertainty of the measurements of Thompson *et al.* [55], above that of the other experiments. The BEB calculation also lies within the uncertainty of Thompson *et al.* [55]. The discontinuity observed in the measurements of Thompson *et al.* [55] below 90 eV is due to a lack of O^{2+} data at low energies [395].

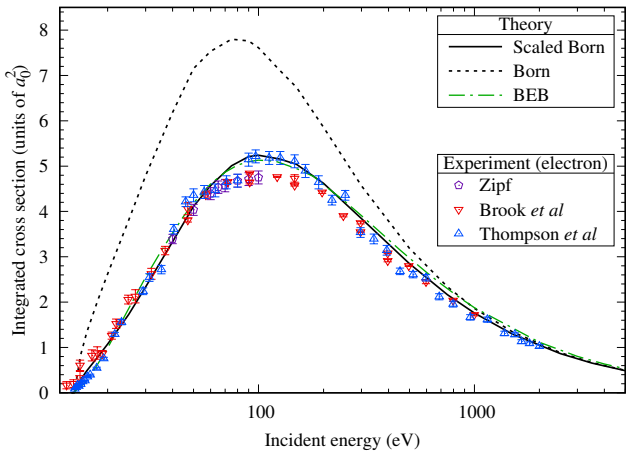

Figure B.2: Total ionisation cross section for electron scattering on oxygen. Theoretical results include Born, Scaled Born, and BEB [45] calculations. Experimental results are from Zipf [54], Brook *et al.* [35], and Thompson *et al.* [55].

B.3 Neon

In Fig. B.3, we present our scaled Born calculations for the total ionisation cross section of electrons incident on neon. Compared to the experimental results, we find the closest agreement with those of Rejoub *et al.* [208], with the current calculation within the uncertainty of these results from threshold to 1000 eV. Above 1000 eV, our calculation is higher than the experiment of Sorokin *et al.* [210], but in close agreement with the calculations of Montanari and Miraglia [118]. At lower energies, the calculation of Montanari and Miraglia [118] is significantly higher than our scaled Born calculation. The BSR calculation of Zatsarinny and Bartschat [207] is in excellent agreement with the current calculation to 30 eV and is slightly lower above this energy.

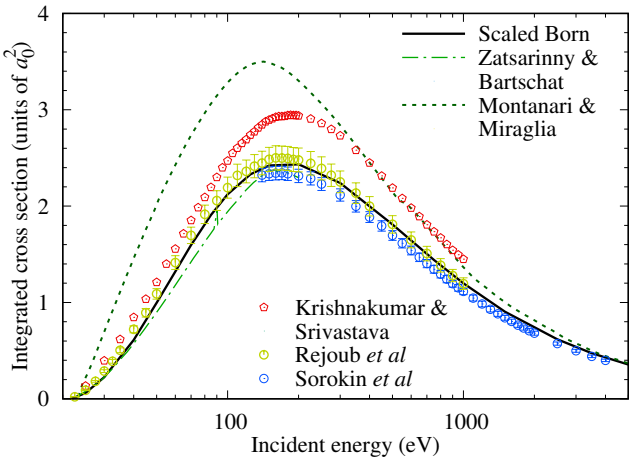

Figure B.3: Total ionisation cross section for electron scattering on neon. The current scaled Born calculations are shown alongside the calculations of Montanari and Miraglia [118] and Zatsarinny and Bartschat [207]. Measurements are from [208], Krishnakumar and Srivastava [209], and Sorokin *et al.* [210].

B.4 Argon

In Fig. B.4, we present our scaled Born calculations for the total ionisation cross section of electrons incident on argon. Close agreement is found with the experiment of Krishnakumar and Srivastava [209] for energies above 60 eV to 1000 eV. Compared to the experimental results, the current calculation is significantly lower below 60 eV but is similar in magnitude to the BSR calculation of Zatsarinny *et al.* [211] for this energy range. The calculation of Montanari and Miraglia [118] is significantly higher than our scaled Born calculation to 300 eV, above which excellent agreement is observed to 1000 eV. Above 1000 eV, this calculation is slightly lower than our scaled Born result. The BSR calculation is significantly lower than the current scaled Born calculation for energies above 50 eV.

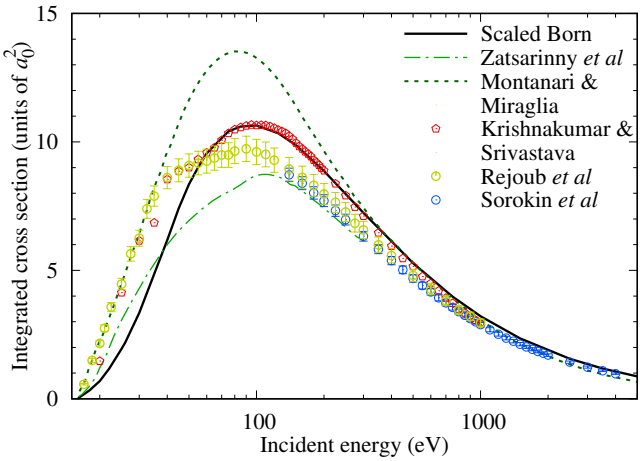

Figure B.4: Total ionisation cross section for electron scattering on argon. The current scaled Born calculations are shown alongside the calculations of Montanari and Miraglia [118] and Zatsarinny *et al.* [211]. Measurements are from Rejoub *et al.* [208], Krishnakumar and Srivastava [209], and Sorokin *et al.* [210].

B.5 Boron

In Fig. B.5, we present our scaled Born calculations for the total ionisation for electron scattering on boron alongside the calculations of Wang *et al.* [123] and Kim and Stone [124]. Our current scaled Born results are above other results for energies between 20 eV and 200 eV. Below 20 eV, all calculations are in close agreement to the ionisation threshold. For energies above 200 eV, there is close agreement with the current scaled Born results and those of Kim and Stone [124].

B.6 Fluorine

In Fig. B.6, we present our scaled Born calculations for the total ionisation cross section of electrons incident on fluorine. There is excellent agreement with the results of Joshipura *et al.* [332] and those of the scaled Born across the presented energy range. The BSR calculations of Gedeon *et al.* [127] are lower than the other theory, except near threshold. The electron theoretical results are within the uncertainty of experiment over its measured range.

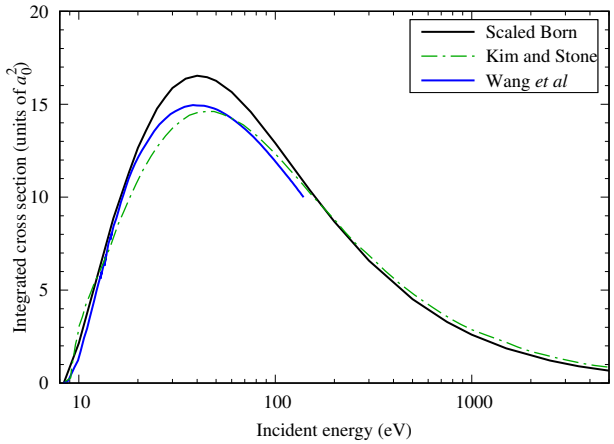

Figure B.5: Total ionisation cross sections for electron scattering from boron. The scaled Born calculation is presented alongside the theoretical results for the incident electron by Wang *et al.* [123] and Kim and Stone [124].

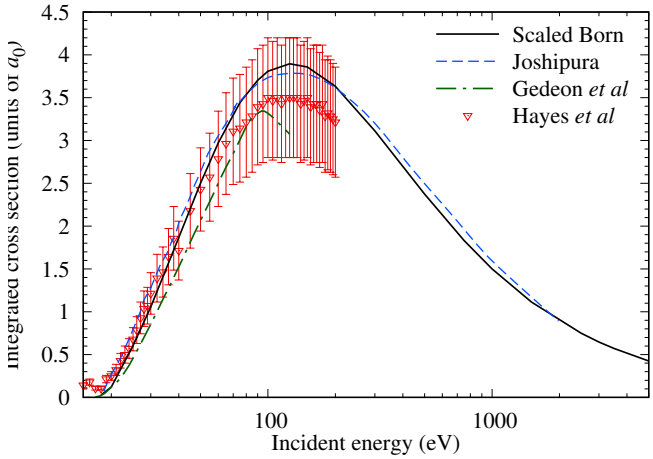

Figure B.6: Total ionisation cross sections for electron scattering from fluorine. The scaled Born calculation is presented alongside the theoretical results of Joshipura and Limbachiya [128] and Gedeon *et al.* [127]. Measurements for electron scattering are from Hayes *et al.* [129].

Appendix C

Publication co-authorship statements

To whom it may concern

I, Nicolas A. Mori, performed the code development and calculations, and prepared the figures and manuscript for the following publication:

N. A. Mori, L. H. Scarlett, I. Bray, and D.V. Fursa. *Convergent close-coupling calculations of positron scattering from atomic carbon.* Physical Review A 107 (3), 032817 (2023).

I, as a Co-Author, endorse that this level of contribution by the candidate indicated above is appropriate.

Liam H. Scarlett _____

Igor Bray _____

Dmitry V. Fursa _____

To whom it may concern

I, Nicolas A. Mori, performed the code development and calculations, and prepared the figures and manuscript for the following publication:

N. A. Mori, L. H. Scarlett, I. Bray, and D.V. Fursa. *Convergent close-coupling calculations of positron scattering from oxygen.* European Physical Journal D 77, 182 (2023).

I, as a Co-Author, endorse that this level of contribution by the candidate indicated above is appropriate.

Liam H. Scarlett _____

Igor Bray _____

Dmitry V. Fursa _____

To whom it may concern

I, Nicolas A. Mori, performed the code development and calculations, and prepared the figures and manuscript for the following publication:

N. A. Mori, L. H. Scarlett, I. Bray, and D.V. Fursa. *Convergent close-coupling calculations of positron scattering from neon and argon.* European Physical Journal D 78, 19 (2024).

I, as a Co-Author, endorse that this level of contribution by the candidate indicated above is appropriate.

Liam H. Scarlett _____

Igor Bray _____

Dmitry V. Fursa _____

To whom it may concern

I, Nicolas A. Mori, performed the code development and calculations, and prepared the figures and manuscript for the following publication:

N. A. Mori, I. Bray, and D.V. Fursa. *Calculations of positron scattering from small molecules.* European Physical Journal D 78, 58 (2024)

I, as a Co-Author, endorse that this level of contribution by the candidate indicated above is appropriate.

Igor Bray _____

Dmitry V. Fursa _____

Bibliography

[1] N. A. Mori, L. H. Scarlett, I. Bray, and D. V. Fursa, Physical Review A **107**, 032817 (2023).

[2] N. A. Mori, L. H. Scarlett, I. Bray, and D. V. Fursa, The European Physical Journal D **77**, 182 (2023).

[3] N. A. Mori, L. H. Scarlett, I. Bray, and D. V. Fursa, The European Physical Journal D **78**, 19 (2024).

[4] N. A. Mori, I. Bray, and D. V. Fursa, The European Physical Journal D **78**, 58 (2024).

[5] A. S. Kadyrov and I. Bray, Physical Review A **66**, 012710 (2002).

[6] S. Zhou, H. Li, W. Kauppila, C. Kwan, and T. Stein, Physical Review A **55**, 361 (1997).

[7] P. Caradonna, A. Jones, C. Makochekanwa, D. Slaughter, J. Sullivan, S. Buckman, I. Bray, and D. V. Fursa, Physical Review A **80**, 032710 (2009).

[8] L. Fornari, L. Diana, and P. Coleman, Physical review letters **51**, 2276 (1983).

[9] D. Murtagh, M. Szłuińska, J. Moxom, P. Van Reeth, and G. Laricchia, Journal of Physics B: Atomic, Molecular and Optical Physics **38**, 3857 (2005).

[10] F. Jacobsen, N. Frandsen, H. Knudsen, U. Mikkelsen, and D. Schrader, Journal of Physics B: Atomic, Molecular and Optical Physics **28**, 4691 (1995).

[11] S. Mori and O. Sueoka, Journal of Physics B: Atomic and Molecular Physics **27**, 4349 (1994).

[12] M. C. Zammit, J. S. Savage, D. V. Fursa, and I. Bray, Physical Review Letters **116**, 233201 (2016).

[13] R. Utamuratov, D. V. Fursa, N. Mori, A. S. Kadyrov, I. Bray, and M. C. Zammit, Physical Review A **99**, 042705 (2019).

[14] J.-S. Yoon, M.-Y. Song, J.-M. Han, S. H. Hwang, W.-S. Chang, B. Lee, and Y. Itikawa, Journal of Physical and Chemical Reference Data **37**, 913 (2008).

[15] K. Ratnavelu, M. J. Brunger, and S. J. Buckman, Journal of Physical and Chemical Reference Data **48**, 023102 (2019).

[16] I. Bray and A. T. Stelbovics, Physical Review A **46**, 6995 (1992).

[17] K. Hoffman, M. Dababneh, Y.-F. Hsieh, W. Kauppila, V. Pol, J. Smart, and T. Stein, Physical Review A **25**, 1393 (1982).

[18] A. Zecca, L. Chiari, A. Sarkar, K. L. Nixon, and M. J. Brunger, Physical Review A **80**, 032702 (2009).

[19] J. Machacek, E. Anderson, C. Makochekanwa, S. Buckman, and J. Sullivan, Physical Review A **88**, 042715 (2013).

[20] G. Karwasz, D. Pliszka, and R. S. Brusa, Nuclear Instruments and Methods in Physics Research Section B: Beam Interactions with Materials and Atoms **247**, 68 (2006).

[21] A. Deuring, K. Floeder, D. Fromme, W. Raith, A. Schwab, G. Sinapius, P. Zitzewitz, and J. Krug, Journal of Physics B: Atomic and Molecular Physics **16**, 1633 (1983).

[22] F. Arretche and M. Lima, Physical Review A **74**, 042713 (2006).

[23] J. P. Sullivan, J. P. Marler, S. J. Gilbert, S. J. Buckman, and C. M. Surko, Physical Review Letters **87**, 073201 (2001).

[24] S. Singh and B. Antony, Journal of Applied Physics **121**, 244903 (2017).

[25] P. Biswas, J. Germano, and T. Frederico, Journal of Physics B: Atomic, Molecular and Optical Physics **35**, L409 (2002).

[26] D. Fromme, G. Kruse, W. Raith, and G. Sinapius, Journal of Physics B: Atomic, Molecular and Optical Physics **21**, L261 (1988).

[27] R. Campeanu, V. Chis, L. Nagy, and A. Stauffer, Physics Letters A **310**, 445 (2003).

[28] K. Fedus and G. P. Karwasz, Physical Review A **100**, 062702 (2019).

[29] H. Knudsen, L. Brun-Nielsen, M. Charlton, and M. Poulsen, Journal of Physics B: Atomic and Molecular Physics **23**, 3955 (1990).

[30] P. Ashley, J. Moxom, and G. Laricchia, Physical review letters **77**, 1250 (1996).

[31] J. Moxom, G. Laricchia, and M. Charlton, Journal of Physics B: Atomic, Molecular and Optical Physics **26**, L367 (1993).

[32] D. D. Reid and J. Wadehra, Chemical Physics Letters **311**, 385 (1999).

[33] S. Singh, S. Dutta, R. Naghma, and B. Antony, The Journal of Physical Chemistry A **120**, 5685 (2016).

[34] S. Singh and B. Antony, Europhys. Lett. **119**, 50006 (2017).

[35] E. Brook, M. F. A. Harrison, and A. C. H. Smith, Journal of Physics B: Atomic and Molecular Physics **11**, 3115 (1978).

[36] K. I. Wang and C. K. Crawford, *Electron Impact Ionization Cross Sections Particle Optics Lab*, Tech. Rep. (MIT, Technical Report, 1971).

[37] M. Dapor and A. Miotello, Atomic Data and Nuclear Data Tables **69**, 1 (1998).

[38] L. H. Cai, B. Yang, C. C. Ling, C. D. Beling, and S. Fung, Journal of Physics: Conference Series **262**, 012009 (2011).

[39] Z.-E.-A. Chaoui and N. Bouarissa, Journal of Applied Physics **96**, 807 (2004).

[40] A. Jablonski, C. J. Powell, and A. Y. Lee, "Nist electron elastic-scattering cross-section database version 4.0, nist standard reference database number 64," https://srdata.nist.gov/srd64/ (2016), (retrieved 2022-04-26).

[41] L. Cai, *Induced Secondary Electrons In Thin Carbon Foils*, M.phil. thesis, University of Hong Kong, Pokfulam, Hong Kong (2010 [Online]).

[42] Y. Wang, O. Zatsarinny, and K. Bartschat, Physical Review A **87**, 012704 (2013).

[43] K. M. Dunseath, W. C. Fon, V. M. Burke, R. H. G. Reid, and C. J. Noble, Journal of Physics B: Atomic and Molecular Physics **30**, 277 (1997).

[44] J. Liu, Y. Wang, and Y. Zhou, Journal of Physics B: Atomic and Molecular Physics **39**, 861 (2006).

[45] Y.-K. Kim and J.-P. Desclaux, Physical Review A **66**, 012708 (2002).

[46] W. Gumus, T. Namdar, and A. Bentabet, International Journal of Molecular Biology: Open Access **3**, 87 (2018).

[47] F. Salvat, J. Fernández-Varea, and J. Sempau., "Penelope, a code systems for monte carlo simulation of electron and photon transport," France: NEA Databank (2005).

[48] J. Ashley, Journal of Electron Spectroscopy and Related Phenomena **50**, 323 (1990).

[49] M. Pindariya, A. S. Chaudhari, F. M. Joshi, K. N. Joshipura, and H. N. Kothari, Journal of Atomic, Molecular, Condensed Matter and Nano Physics **5**, 229–237 (2018).

[50] M. Charlton, T. Griffith, G. Heyland, and G. Wright, Journal of Physics B: Atomic and Molecular Physics **13**, L353 (1980).

[51] L. Chiari, A. Zecca, S. Girardi, E. Trainotti, G. García, F. Blanco, R. P. McEachran, and M. J. Brunger, Journal of Physics B: Atomic and Molecular Physics **45**, 215206 (2012).

[52] M. Dababneh, Y.-F. Hsieh, W. Kauppila, C. K. Kwan, S. J. Smith, T. Stein, and M. Uddin, Physical Review A **38**, 1207 (1988).

[53] G. García, F. Blanco, and A. Williart, Chemical Physics Letters **335**, 227 (2001).

[54] E. Zipf, Planet. Space Sci. **33**, 1303 (1985).

[55] W. Thompson, M. Shah, and H. Gilbody, Journal of Physics B: Atomic and Molecular Physics **28**, 1321 (1995).

[56] J. Marler and C. Surko, Physical Review A **72**, 062713 (2005).

[57] J. Archer, S. Trilov, and P. Coleman, in *Journal of Physics: Conference Series*, Vol. 443 (IOP Publishing, 2013) p. 012001.

[58] T. Griffith, *Positron Scattering in Gases*, edited by J. W. Humberston and M. R. C. McDowell (Plenum Press, New York, 1983) pp. 53–63.

[59] A. Kramida, Yu. Ralchenko, J. Reader, and and NIST ASD Team, NIST Atomic Spectra Database (ver. 5.10), [Online]. Available: `https://physics.nist.gov/asd` [2023, October 23]. National Institute of Standards and Technology, Gaithersburg, MD. (2022).

[60] I. Iga, L. Mu-Tao, J. Nogueira, and R. Barbieri, Journal of Physics B: Atomic and Molecular Physics **20**, 1095 (1987).

[61] S. Tayal and O. Zatsarinny, Physical Review A **94**, 042707 (2016).

[62] P. Johnson, I. Kanik, D. Shemansky, and X. Liu, Journal of Physics B: Atomic and Molecular Physics **36**, 3203 (2003).

[63] P. Johnson, I. Kanik, M. Khakoo, J. McConkey, and S. Tayal, Journal of Physics B: Atomic and Molecular Physics **36**, 4289 (2003).

[64] I. Kanik, P. Johnson, M. Das, M. Khakoo, and S. Tayal, Journal of Physics B: Atomic and Molecular Physics **34**, 2647 (2001).

[65] S. Vaughan and J. Doering, Journal of Geophysical Research: Space Physics **92**, 7749 (1987).

[66] E. Gulcicek, J. Doering, and S. Vaughan, Journal of Geophysical Research: Space Physics **93**, 5885 (1988).

[67] K. Joshipura and P. Patel, Physical Review A **48**, 2464 (1993).

[68] P. Gupta, B. Jhanwar, and S. Khare, Physica B+ C **79**, 311 (1975).

[69] A. Williart, P. Kendall, F. Blanco, P. Tegeder, G. García, and N. Mason, Chemical Physics Letters **375**, 39 (2003).

[70] D. V. Fursa and I. Bray, Journal of Physics: Conference Series **388**, 012020 (2012).

[71] A. C. Jones, C. Makochekanwa, P. Caradonna, D. S. Slaughter, J. R. Machacek, R. P. McEachran, J. P. Sullivan, S. J. Buckman, A. Stauffer, I. Bray, *et al.*, Physical Review A **83**, 032701 (2011).

[72] T. Stein, W. Kauppila, V. Pol, J. Smart, and G. Jesion, Physical Review A **17**, 1600 (1978).

[73] W. Kauppila, T. Stein, J. Smart, M. Dababneh, Y. Ho, J. Downing, and V. Pol, Physical Review A **24**, 725 (1981).

[74] T. Griffith, G. Heyland, K. Lines, and T. Twomey, Applied Physics **19**, 431 (1979).

[75] A. Brenton, J. Dutton, and F. Harris, Journal of Physics B: Atomic and Molecular Physics **11**, L15 (1978).

[76] K. Nagumo, Y. Nitta, M. Hoshino, H. Tanaka, and Y. Nagashima, The European Physical Journal D **66**, 1 (2012).

[77] G. García, F. Arqueros, and J. Campos, Journal of Physics B: Atomic and Molecular Physics **19**, 3777 (1986).

[78] A. Zecca, L. Chiari, E. Trainotti, D. V. Fursa, I. Bray, A. Sarkar, S. Chattopadhyay, K. Ratnavelu, and M. J. Brunger, Journal of Physics B: Atomic and Molecular Physics **45**, 015203 (2011).

[79] G. P. Karwasz, M. Barozzi, R. S. Brusa, and A. Zecca, Nuclear Instruments and Methods in Physics Research Section B: Beam Interactions with Materials and Atoms **192**, 157 (2002).

[80] M. H. Khandker, A. Haque, M. Maaza, and M. A. Uddin, Japanese Journal of Applied Physics **59**, SHHA05 (2020).

[81] J. Hofierka, C. M. Rawlins, B. Cunningham, D. T. Waide, and D. G. Green, Frontiers in Physics **11**, 1227652 (2023).

[82] F. Arretche, M. V. Barp, W. Tenfen, and E. P. Seidel, Brazillian Journal of Physics **50**, 844 (2020).

[83] F. De Heer, R. Jansen, and W. Van der Kaay, Journal of Physics B: Atomic and Molecular Physics **12**, 979 (1979).

[84] M. Haque, A. Haque, D. Jakubassa-Amundsen, M. A. R. Patoary, A. Basak, M. Maaza, B. Saha, and M. A. Uddin, Journal of Physics Communications **3**, 045011 (2019).

[85] L. Parcell, R. McEachran, and A. Stauffer, Nuclear Instruments and Methods in Physics Research Section B: Beam Interactions with Materials and Atoms **171**, 113 (2000).

[86] R. Boadle, T. Babij, J. Machacek, R. McEachran, J. Sullivan, and S. Buckman, Physical Review A **93**, 022712 (2016).

[87] P. G. Coleman, N. Cheesman, and E. Lowry, Physical Review Letters **102**, 173201 (2009).

[88] Z. Cheong, T. Babij, B. Anthouard, J. Machachek, R. McEachran, and J. Sullivan, Journal of Physics B: Atomic and Molecular Physics **54**, 065204 (2021).

[89] D. Green, J. Ludlow, and G. Gribakin, Physical Review A **90**, 032712 (2014).

[90] K. Baluja, A. Jain, H. Jones, C. Weatherford, and K. Karim, Journal of Physics B: Atomic and Molecular Physics **24**, L93 (1991).

[91] F. Byron Jr and C. J. Joachain, Physical Review A **15**, 128 (1977).

[92] J. Stepanek, Radiation Physics and Chemistry **66**, 99 (2003).

[93] W. Kauppila, C. Kwan, D. Przybyla, S. Smith, and T. Stein, Canadian Journal of Physics **74**, 474 (1996).

[94] S. Gupta and J. Rees, Journal of Physics B: Atomic and Molecular Physics **8**, 417 (1975).

[95] J. Sullivan, S. J. Gilbert, J. P. Marler, R. Greaves, S. Buckman, and C. M. Surko, Physical Review A **66**, 042708 (2002).

[96] S. J. Gilbert, J. Sullivan, R. Greaves, and C. Surko, Nuclear Instruments and Methods in Physics Research Section B: Beam Interactions with Materials and Atoms **171**, 81 (2000).

[97] P. Coleman and J. McNutt, Physical Review Letters **42**, 1130 (1979).

[98] K. Floeder, P. Höner, W. Raith, A. Schwab, G. Sinapius, and G. Spicher, Physical Review Letters **60**, 2363 (1988).

[99] S. J. Smith, G. Hyder, W. Kauppila, C. Kwan, and T. Stein, Physical Review Letters **64**, 1227 (1990).

[100] S. N. Nahar and J. Wadehra, Physical Review A **35**, 2051 (1987).

[101] G. Hyder, M. Dababneh, Y.-F. Hsieh, W. Kauppila, C. Kwan, M. Mahdavi-Hezaveh, and T. Stein, Physical Review Letters **57**, 2252 (1986).

[102] L. Dou, W. Kauppila, C. Kwan, and T. Stein, Physical Review Letters **68**, 2913 (1992).

[103] R. DuBois and M. Rudd, Journal of Physics B: Atomic and Molecular Physics **9**, 2657 (1976).

[104] R. Jansen, F. De Heer, H. Luyken, B. Van Wingerden, and H. Blaauw, Journal of Physics B: Atomic and Molecular Physics **9**, 185 (1976).

[105] M. Šuvakov, Z. L. Petrović, J. Marler, S. J. Buckman, R. E. Robson, and G. Malović, New Journal of Physics **10**, 053034 (2008).

[106] R. McEachran, A. Ryman, and A. Stauffer, Journal of Physics B: Atomic and Molecular Physics **11**, 551 (1978).

[107] L. A. Poveda, A. Dutra, J. R. Mohallem, and D. Assafrao, Physical Review A **87**, 052702 (2013).

[108] A. Jones, P. Caradonna, C. Makochekanwa, D. Slaughter, R. McEachran, J. Machacek, J. Sullivan, and S. Buckman, Physical Review Letters **105**, 073201 (2010).

[109] R. McEachran, A. Ryman, and A. Stauffer, Journal of Physics B: Atomic and Molecular Physics **12**, 1031 (1979).

[110] S. Singh, R. Naghma, J. Kaur, and B. Antony, The European Physical Journal D **72**, 1 (2018).

[111] J. P. Marler, J. Sullivan, and C. M. Surko, Physical Review A **71**, 022701 (2005).

[112] G. Laricchia, P. Van Reeth, M. Szluinska, and J. Moxom, Journal of Physics B: Atomic and Molecular Physics **35**, 2525 (2002).

[113] A. Sorokin, L. Shmaenok, S. Bobashev, B. Möbus, M. Richter, and G. Ulm, Physical Review A **61**, 022723 (2000).

[114] H. Bluhme, H. Knudsen, J. Merrison, and K. Nielsen, Journal of Physics B: Atomic and Molecular Physics **32**, 5835 (1999).

[115] R. McEachran and A. Stauffer, Journal of Physics B: Atomic and Molecular Physics **46**, 075203 (2013).

[116] S. Gilmore, J. E. Blackwood, and H. Walters, Nuclear Instruments and Methods in Physics Research Section B: Beam Interactions with Materials and Atoms **221**, 129 (2004).

[117] K. Bartschat, Physical Review A **71**, 032718 (2005).

[118] C. C. Montanari and J. E. Miraglia, Journal of Physics B: Atomic and Molecular Physics **48**, 165203 (2015).

[119] R. McEachran and A. Stauffer, Journal of Physics B: Atomic and Molecular Physics **43**, 215209 (2010).

[120] H. N. Kothari and K. Joshipura, Chinese Physics B **19**, 103402 (2010).

[121] P. Coleman, J. Hutton, D. Cook, and C. Chandler, Canadian Journal of Physics **60**, 584 (1982).

[122] H. N. Kothari and K. Joshipura, Pramana **79**, 435 (2012).

[123] K. Wang, O. Zatsarinny, and K. Bartschat, Physical Review A **93**, 052715 (2016).

[124] Y.-K. Kim and P. M. Stone, Physical Review A **64**, 052707 (2001).

[125] A. Jablonski, F. Salvat., C. J. Powell, and A. Lee, *NIST Electron Elastic-Scattering Cross-Section Database Version 4.0, NIST Standard Reference Database Number 64* (National Institute of Standards and Technology, Gaithersburg MD, 2016).

[126] M. J. Berger, J. S. Coursey, M. A. Zucker, and J. Chang, "Nist standard reference database 124," (2017).

[127] V. Gedeon, S. Gedeon, V. Lazur, E. Nagy, O. Zatsarinny, and K. Bartschat, Physical Review A **89**, 052713 (2014).

[128] K. Joshipura and C. G. Limbachiya, International Journal of Mass Spectrometry **216**, 239 (2002).

[129] T. R. Hayes, R. C. Wetzel, and R. S. Freund, Physical Review A **35**, 578 (1987).

[130] W. Tenfen, J. de Souza Glória, and F. Arretche, The Journal of Physical Chemistry A **126**, 7901 (2022).

[131] W. Tenfen, E. P. Seidel, M. V. Barp, and F. Arretche, Journal of Electron Spectroscopy and Related Phenomena **255**, 147160 (2022).

[132] J. G. Pinheiro, D. Assafrão, L. A. Poveda, and J. R. Mohallem, The European Physical Journal D **77**, 184 (2023).

[133] L. Ellis-Gibbings, F. Blanco, and G. García, The European Physical Journal D **73**, 1 (2019).

[134] D. Suzuki, H. Kato, M. Ohkawa, K. Anzai, H. Tanaka, P. Limão-Vieira, L. Campbell, and M. J. Brunger, The Journal of Chemical Physics **134**, 064311 (2011).

[135] Y. Katayama, O. Sueoka, and S. Mori, Journal of Physics B: Atomic and Molecular Physics **20**, 1645 (1987).

[136] W. Newell, M. Khakoo, and A. Smith, Journal of Physics B: Atomic and Molecular Physics **13**, 4877 (1980).

[137] G. Laricchia, J. Moxom, and M. Charlton, Physical Review Letters **70**, 3229 (1993).

[138] M. Franz, K. Wiciak-Pawłowska, and J. Franz, Atoms **9**, 99 (2021).

[139] R. Campeanu, V. Chis, L. Nagy, and A. Stauffer, Physics Letters A **325**, 66 (2004).

[140] E. Krishnakumar and S. Srivastava, International Journal of Mass Spectrometry and Ion Processes **113**, 1 (1992).

[141] S. Singh, S. Dutta, R. Naghma, and B. Antony, Journal of Physics B: Atomic, Molecular and Optical Physics **50**, 135202 (2017).

[142] F. Gianturco, T. Mukherjee, and P. Paioletti, Physical Review A **56**, 3638 (1997).

[143] M. M. Billah, M. H. Khandker, M. Shorifuddoza, M. Sayed, H. Watabe, A. Haque, and M. A. Uddin, Journal of Physics B: Atomic, Molecular and Optical Physics **54**, 095203 (2021).

[144] A. Zecca, L. Chiari, A. Sarkar, and M. Brunger, New Journal of Physics **13**, 115001 (2011).

[145] O. Sueoka and S. Mori, Journal of the Physical Society of Japan **53**, 2491 (1984).

[146] P. Coleman, T. Griffith, and G. Heyland, Applied Physics **4**, 89 (1974).

[147] C. K. Kwan, Y. Hsieh, W. Kauppila, S. J. Smith, T. Stein, M. Uddin, and M. Dababneh, Physical Review A **27**, 1328 (1983).

[148] G. Karwasz, R. S. Brusa, A. Gasparoli, and A. Zecca, Chemical physics letters **211**, 529 (1993).

[149] G. García, C. Aragon, and J. Campos, Phys. Rev. A **42**, 4400 (1990).

[150] H. N. Kothari and K. Joshipura, Pramana **76**, 477 (2011).

[151] E. P. da Silva, M. T. d. N. Varella, and M. A. Lima, Physical Review A **72**, 062715 (2005).

[152] I. Tóth, R. Campeanu, V. Chiş, and L. Nagy, Nuclear Instruments and Methods in Physics Research Section B: Beam Interactions with Materials and Atoms **267**, 362 (2009).

[153] R. Campeanu, V. Chis, L. Nagy, and A. Stauffer, Physics Letters A **344**, 247 (2005).

[154] H. Bluhme, N. Frandsen, F. Jacobsen, H. Knudsen, J. Merrison, R. Mitchell, K. Paludan, and M. Poulsen, Journal of Physics B: Atomic, Molecular and Optical Physics **32**, 5825 (1999).

[155] A. I. Lozano, A. García-Abenza, F. Blanco Ramos, M. Hasan, D. S. Slaughter, T. Weber, R. P. McEachran, R. D. White, M. J. Brunger, P. Limão-Vieira, *et al.*, The Journal of Physical Chemistry A **126**, 6032 (2022).

[156] M. M. Billah, M. M. Khatun, M. Haque, M. Y. Ali, M. H. Khandker, A. Haque, H. Watabe, and M. A. Uddin, Atoms **10**, 31 (2022).

[157] F. Gianturco and T. Mukherjee, Journal of Physics B: Atomic, Molecular and Optical Physics **30**, 3567 (1997).

[158] G. García and F. Manero, Physical Review A **53**, 250 (1996).

[159] M. Charlton, T. Griffith, G. Heyland, and G. Wright, Journal of Physics B: Atomic and Molecular Physics **16**, 323 (1983).

[160] A. Zecca, C. Perazzolli, N. Moser, D. Sanyal, M. Chakrabarti, and M. J. Brunger, Physical Review A **74**, 012707 (2006).

[161] D. Cooke, D. Murtagh, and G. Laricchia, in *Journal of Physics: Conference Series*, Vol. 199 (IOP Publishing, 2010) p. 012006.

[162] D. Murtagh, C. Arcidiacono, Z. Pešić, and G. Laricchia, Nuclear Instruments and Methods in Physics Research Section B: Beam Interactions with Materials and Atoms **247**, 92 (2006).

[163] G. Laricchia and J. Moxom, Physics Letters A **174**, 255 (1993).

[164] D. D. Reid, *Electron and positron scattering in atomic and molecular gases*, Ph.D. thesis (1995), copyright - Database copyright ProQuest LLC; ProQuest does not claim copyright in the individual underlying works; Last updated - 2023-07-26.

[165] A. Bharadvaja, S. Kaur, and K. L. Baluja, Pramana **95**, 167 (2021).

[166] K. Joshipura, B. Antony, and M. Vinodkumar, Journal of Physics B: Atomic, Molecular and Optical Physics **35**, 4211 (2002).

[167] J. De Pablos, P. Kendall, P. Tegeder, A. Williart, F. Blanco, G. Garcia, and N. Mason, Journal of Physics B: Atomic, Molecular and Optical Physics **35**, 865 (2002).

[168] P. Patel and K. Joshipura, Pramana **61**, 685 (2003).

[169] K. A. Newson, S. M. Luc, S. D. Price, and N. J. Mason, International Journal of Mass Spectrometry and Ion Processes **148**, 203 (1995).

[170] M.-W. Siegel, International Journal of Mass Spectrometry and Ion Physics **44**, 19 (1982).

[171] F. Blanco, A. Roldán, K. Krupa, R. McEachran, R. White, S. Marjanović, Z. L. Petrović, M. J. Brunger, J. Machacek, S. J. Buckman, *et al.*, Journal of Physics B: Atomic, Molecular and Optical Physics **49**, 145001 (2016).

[172] N. Sinha, D. Patel, and B. Antony, ChemistrySelect **4**, 4575 (2019).

[173] C. Makochekanwa, A. Bankovic, W. Tattersall, A. Jones, P. Caradonna, D. S. Slaughter, K. Nixon, M. J. Brunger, Z. Petrovic, J. P. Sullivan, *et al.*, New Journal of Physics **11**, 103036 (2009).

[174] M. Kimura, O. Sueoka, A. Hamada, and Y. Itikawa, Advances in Chemical Physics , 537 (1999).

[175] O. Sueoka, S. Mori, and Y. Katayama, Journal of Physics B: Atomic and Molecular Physics **19**, L373 (1986).

[176] A. Loreti, R. Kadokura, S. Fayer, Á. Kövér, and G. Laricchia, Physical Review Letters **117**, 253401 (2016).

[177] A. Zecca, D. Sanyal, M. Chakrabarti, and M. J. Brunger, Journal of Physics B: Atomic, Molecular and Optical Physics **39**, 1597 (2006).

[178] A. Muñoz, J. Oller, F. Blanco, J. Gorfinkiel, P. Limão-Vieira, and G. García, Physical Review A **76**, 052707 (2007).

[179] K. Baluja, R. Zhang, J. Franz, and J. Tennyson, Journal of Physics B: Atomic, Molecular and Optical Physics **40**, 3515 (2007).

[180] F. Arretche, W. Tenfen, K. Mazon, S. Michelin, M. Lima, M.-T. Lee, L. Machado, M. Fujimoto, and O. Pessoa, Nuclear Instruments and Methods in Physics Research Section B: Beam Interactions with Materials and Atoms **268**, 178 (2010).

[181] H. Aouchiche, C. Champion, and D. Oubaziz, Radiation Physics and Chemistry **77**, 107 (2008).

[182] W. Tattersall, L. Chiari, J. R. Machacek, E. Anderson, R. D. White, M. J. Brunger, S. J. Buckman, G. García, F. Blanco, and J. P. Sullivan, The Journal of Chemical Physics **140**, 044320 (2014).

[183] A. Katase, K. Ishibashi, Y. Matsumoto, T. Sakae, S. Maezono, E. Murakami, K. Watanabe, and H. Maki, Journal of Physics B: Atomic and Molecular Physics **19**, 2715 (1986).

[184] F. Arretche, M. V. Barp, E. P. Seidel, and W. Tenfen, The European Physical Journal D **74**, 1 (2020).

[185] I. Tóth, R. Campeanu, V. Chiş, and L. Nagy, in *Journal of Physics: Conference Series*, Vol. 199 (IOP Publishing, 2010) p. 012018.

[186] M. Bolorizadeh and M. E. Rudd, Physical Review A **33**, 882 (1986).

[187] S. Khare and W. Meath, Journal of Physics B: Atomic and Molecular Physics **20**, 2101 (1987).

[188] H. Straub, B. Lindsay, K. Smith, and R. Stebbings, The Journal of Chemical Physics **108**, 109 (1998).

[189] M. Rao, I. Iga, and S. Srivastava, Journal of Geophysical Research: Planets **100**, 26421 (1995).

[190] K. Baluja and A. Jain, Physical Review A **45**, 7838 (1992).

[191] A. Jain and F. Gianturco, Journal of Physics B: Atomic, Molecular and Optical Physics **24**, 2387 (1991).

[192] A. Zecca, L. Chiari, E. Trainotti, A. Sarkar, S. d. Sanchez, M. Bettega, M. d. N. Varella, M. Lima, and M. Brunger, Physical Review A **85**, 012707 (2012).

[193] C. Rawlins, J. Hofierka, B. Cunningham, C. Patterson, and D. Green, Physical Review Letters **130**, 263001 (2023).

[194] S. De-Heng, L. Yu-Fang, S. Jin-Feng, Z. Zun-Lue, and Y. Xiang-Dong, Chinese Physics **14**, 964 (2005).

[195] M. Charlton, T. Griffith, G. Heyland, and G. Wright, Journal of Physics B: Atomic and Molecular Physics **13**, L353 (1980).

[196] O. Sueoka and S. Mori, Journal of Physics B: Atomic and Molecular Physics **19**, 4035 (1986).

[197] M.-Y. Song, J.-S. Yoon, H. Cho, Y. Itikawa, G. P. Karwasz, V. Kokoouline, Y. Nakamura, and J. Tennyson, Journal of Physical and Chemical Reference Data **44**, 023101 (2015).

[198] A. Jain, The Journal of Chemical Physics **78**, 6579 (1983).

[199] T. Sakae, S. Sumiyoshi, E. Murakami, Y. Matsumoto, K. Ishibashi, and A. Katase, Journal of Physics B: Atomic, Molecular and Optical Physics **22**, 1385 (1989).

[200] W. Kauppila, E. Miller, K. Pipinos, T. Stein, and E. Surdutovich, in *APS Division of Atomic, Molecular and Optical Physics Meeting Abstracts*, Vol. 34 (2003) pp. D1–144.

[201] R. Campeanu, V. Chis, L. Nagy, and A. Stauffer, Nuclear Instruments and Methods in Physics Research Section B: Beam Interactions with Materials and Atoms **247**, 58 (2006).

[202] O. Sueoka, S. Mori, and A. Hamada, Journal of Physics B: Atomic, Molecular and Optical Physics **27**, 1453 (1994).

[203] A. Zecca, G. Karwasz, and R. Brusa, Physical Review A **46**, 3877 (1992).

[204] B. Antony, K. Joshipura, and N. Mason, Journal of Physics B: Atomic, Molecular and Optical Physics **38**, 189 (2005).

[205] G. P. Karwasz, P. Możejko, and M.-Y. Song, International Journal of Mass Spectrometry **365**, 232 (2014).

[206] H. Nishimura, W. M. Huo, M. Ali, and Y.-K. Kim, The Journal of Chemical Physics **110**, 3811 (1999).

[207] O. Zatsarinny and K. Bartschat, Physical Review A **85**, 062710 (2012).

[208] R. Rejoub, B. Lindsay, and R. Stebbings, Physical Review A **65**, 042713 (2002).

[209] E. Krishnakumar and S. Srivastava, Journal of Physics B: Atomic, Molecular and Optical Physics **21**, 1055 (1988).

[210] A. Sorokin, L. Shmaenok, S. Bobashev, B. Möbus, and G. Ulm, Physical Review A **58**, 2900 (1998).

[211] O. Zatsarinny, Y. Wang, and K. Bartschat, Physical Review A **89**, 022706 (2014).

[212] H. Watabe, Y. Ikoma, Y. Kimura, *et al.*, Annals of Nuclear Medicine **20**, 583 (2006).

[213] L. Menichetti *et al.*, Applied Radiation and Isotopes **67**, S351 (2009).

[214] Y. F. Taia and P. Piccini, Journal of Neurology, Neurosurgery, and Psychiatry **75**, 669 (2004).

[215] Y. Wang, M. Li, R. Diao, B. Tung, D. Zhang, and Y. Li, Oncotarget **8**, 51652 (2017).

[216] V. Caridad, M. Arsenak, M. J. Abad, R. Martin, N. Guillen, L. F. Colmenter, and P. Taylor, Cancer Biother. Radiopharm. **23**, 371 (2008).

[217] S. Fang, J. Wang, H. Jiang, Y. Zhang, W. Xi, C. Zhao, M. Tian, and H. Zhang, Cancer Biother. Radiopharm. **25**, 733 (2010).

[218] R. M. Moadel, R. H. Weldon, E. B. Katz, P. Lu, J. Mani, M. Stahl, M. D. Blaufox, R. G. Pestell, M. J. Charron, and E. Dadachova, Cancer Research **65**, 698 (2005).

[219] D. M. Paul, C. M. Ghiuzeli, J. Rini, C. J. Palestro, E. K. Fung, M. Ghali, E. Ben-Levi, A. Prideaux, S. Vallabhajosula, and E. C. Popa, American Journal of Nuclear Medicine and Molecular Imaging **10**, 334 (2020).

[220] C. Champion and C. Le Loirec, Physics in Medicine and Biology **52**, 6605 (2007).

[221] L. Jødal, C. L. Loirec, and C. Champion, Physics in Medicine and Biology **57**, 3931 (2012).

[222] N. Mott and H. Massey, *The Theory of Atomic Collisions. Nucl. Phys.* (Oxford University Press, 1966).

[223] H. Massey and E. Burhop, *Electronic and ionic impact phenomena* (Oxford University Press, 1969).

[224] F. Blanco and G. García, Physics Letters A **317**, 458 (2003).

[225] F. Blanco, L. Ellis-Gibbings, and G. García, Chemical Physics Letters **645**, 71 (2016).

[226] D. Liljequist, T. Liamsuwan, and H. Nikjoo, International Journal of Radiation Biology **88**, 29 (2012).

[227] R. Utamuratov, D. Fursa, A. Kadyrov, and et al., The European Physical Journal D **75**, 260 (2021).

[228] J. J. Bailey, A. S. Kadyrov, and I. Bray, Physical Review A **91**, 012712 (2015).

[229] A. S. Kadyrov and I. Bray, Journal of Physics B: Atomic and Molecular Physics **49**, 222002 (2016).

[230] R. Utamuratov, D. V. Fursa, A. S. Kadyrov, A. V. Lugovskoy, J. S. Savage, and I. Bray, Physical Review A **86**, 062702 (2012).

[231] A. V. Lugovskoy, A. S. Kadyrov, I. Bray, and A. T. Stelbovics, Physical Review A **85**, 034701 (2012).

[232] A. V. Lugovskoy, R. Utamuratov, A. S. Kadyrov, A. T. Stelbovics, and I. Bray, Physical Review A **87**, 042708 (2013).

[233] P. Helander and D. J. Ward, Physical Review Letters **90**, 135004 (2003).

[234] T. Fülöp and G. Papp, Physical Review Letters **108**, 225003 (2012).

[235] J. Liu, H. Qin, N. J. Fisch, Q. Teng, and X. Wang, Physics of Plasmas **21**, 064503 (2014).

[236] L. J. Leger and J. T. Visentine, Journal of Spacecraft and Rockets **23**, 505 (1986).

[237] H. Richter, C. Buchbender, R. Güsten, R. Higgins, B. Klein, J. Stutzki, H. Wiesemeyer, and H.-W. Hübers, Communications Earth & Environment **2**, 19 (2021).

[238] A. Li and S. Close, Advances in Space Research **56**, 1645 (2015).

[239] J. Picone, A. Hedin, D. P. Drob, and A. Aikin, Journal of Geophysical Research: Space Physics **107**, SIA (2002).

[240] O. Adriani, G. Barbarino, G. Bazilevskaya, R. Bellotti, M. Boezio, E. Bogomolov, M. Bongi, V. Bonvicini, S. Bottai, A. Bruno, *et al.*, Physics Reports **544**, 323 (2014).

[241] A. Gusev, U. Jayanthi, I. Martin, G. Pugacheva, and W. Spjeldvik, Journal of Geophysical Research: Space Physics **106**, 26111 (2001).

[242] V. Mikhailov, O. Adriani, G. Barbarino, G. Bazilevskaya, R. Bellotti, M. Boezio, E. Bogomolov, M. Bongi, V. Bonvicini, S. Bottai, *et al.*, in *Journal of Physics: Conference Series*, Vol. 675 (IOP Publishing, 2016) p. 032003.

[243] D. Sarria, P. Kochkin, N. Østgaard, N. Lehtinen, A. Mezentsev, M. Marisaldi, E. Carlson, Brant, C. Maiorana, K. Albrechtsen, T. Neubert, *et al.*, Journal of Geophysical Research: Space Physics **124**, 10497 (2019).

[244] Y. V. Mikhailova, A. Galper, and V. Mikhailov, Physics of Atomic Nuclei **81**, 520 (2018).

[245] G. Keating, J. Nicholson III, and L. Lake, Journal of Geophysical Research: Space Physics **85**, 7941 (1980).

[246] C. J. Hansen, D. E. Shemansky, and A. Hendrix, Icarus **176**, 305 (2005).

[247] C. Cardinaud, Comptes Rendus Chimie **21**, 723 (2018).

[248] M. J. Brunger, S. Buckman, and K. Ratnavelu, Journal of Physical and Chemical Reference Data **46**, 023102 (2017).

[249] M. Natisin, J. Danielson, and C. Surko, Journal of Physics B: Atomic, Molecular and Optical Physics **47**, 225209 (2014).

[250] D. Cassidy, S. Deng, R. Greaves, and A. Mills Jr, Review of Scientific Instruments **77**, 073106 (2006).

[251] A. Swann and D. Green, Physical Review Letters **130**, 033001 (2023).

[252] A. Banković, S. Dujko, S. Marjanović, R. D. White, and Z. L. Petrović, The European Physical Journal D **68**, 1 (2014).

[253] S. Marjanović, A. Banković, D. Cassidy, B. Cooper, A. Deller, S. Dujko, and Z. L. Petrović, Journal of Physics B: Atomic, Molecular and Optical Physics **49**, 215001 (2016).

[254] D. Le Bars, Journal of Fluorine Chemistry **127**, 1488 (2006).

[255] S. A. T. Bray I, Physical Review A. **48(6)**, 4787 (1993).

[256] R. Utamuratov, A. S. Kadyrov, D. V. Fursa, and I. Bray, Journal of Physics B: Atomic and Molecular Physics **43**, 031001 (2010).

[257] R. Utamuratov, A. S. Kadyrov, D. V. Fursa, I. Bray, and A. T. Stelbovics, Physical Review A **82**, 042705 (2010).

[258] H. Wu, I. Bray, D. V. Fursa, and A. T. Stelbovics, Journal of Physics B: Atomic, Molecular and Optical Physics **37**, 1165 (2004).

[259] H. Wu, I. Bray, D. V. Fursa, and A. T. Stelbovics, Journal of Physics B: Atomic and Molecular Physics **37**, L1 (2003).

[260] A. V. Lugovskoy, A. S. Kadyrov, I. Bray, and A. T. Stelbovics, Physical Review A **82**, 062708 (2010).

[261] J. S. Savage, D. V. Fursa, and I. Bray, Physical Review A **83**, 062709 (2011).

[262] O. Zatsarinny, Computer Physics Communications **174**, 273 (2006).

[263] C. F. Fischer, Computer Physics Communications **64**, 369 (1991).

[264] N. A. Mori, R. Utamuratov, L. H. Scarlett, D. V. Fursa, A. S. Kadyrov, I. Bray, and M. C. Zammit, Journal of Physics B: Atomic and Molecular Physics **53**, 015203 (2019).

[265] M. C. Zammit, D. V. Fursa, and I. Bray, Physical Review A **87**, 020701 (2013).

[266] R. Utamuratov, A. S. Kadyrov, D. V. Fursa, M. C. Zammit, and I. Bray, Physical Review A **92**, 032707 (2015).

[267] L. H. Scarlett, J. S. Savage, D. V. Fursa, I. Bray, M. C. Zammit, and B. I. Schneider, Physical Review A **103**, 032802 (2021).

[268] L. H. Scarlett, J. S. Savage, D. V. Fursa, I. Bray, and M. C. Zammit, The European Physical Journal D **74**, 1 (2020).

[269] M. C. Zammit, D. V. Fursa, J. S. Savage, and I. Bray, Journal of Physics B: Atomic and Molecular Physics **50**, 123001 (2017).

[270] L. H. Scarlett, U. S. Rehill, M. C. Zammit, N. A. Mori, I. Bray, and D. V. Fursa, Physical Review A **107**, 062804 (2023).

[271] L. H. Scarlett, M. C. Zammit, I. Bray, B. I. Schneider, and D. V. Fursa, Physical Review A **106**, 042818 (2022).

[272] Y.-K. Kim, Physical Review A **64**, 032713 (2001).

[273] E. P. Wigner and L. Eisenbud, Physical Review **72**, 29 (1947).

[274] P. Descouvemont and D. Baye, Reports on Progress in Physics **73**, 036301 (2010).

[275] J. Gorfinkiel and J. Tennyson, Journal of Physics B: Atomic, Molecular and Optical Physics **37**, L343 (2004).

[276] R. Zhang, K. Baluja, J. Franz, and J. Tennyson, Journal of Physics B: Atomic, Molecular and Optical Physics **44**, 035203 (2011).

[277] K. Higgins and P. Burke, Journal of Physics B: Atomic, Molecular and Optical Physics **24**, L343 (1991).

[278] K. Higgins and P. Burke, Journal of Physics B: Atomic, Molecular and Optical Physics **26**, 4269 (1993).

[279] C. Campbell, M. T. McAlinden, A. A. Kernoghan, and H. Walters, Nuclear Instruments and Methods in Physics Research Section B: Beam Interactions with Materials and Atoms **143**, 41 (1998).

[280] M. T. McAlinden and H. Walters, Hyperfine Interactions **73**, 65 (1992).

[281] M. T. McAlinden, A. A. Kernoghan, and H. Walters, Journal of Physics B: Atomic, Molecular and Optical Physics **29**, 555 (1996).

[282] A. A. Kernoghan, M. T. McAlinden, and H. Walters, Journal of Physics B: Atomic, Molecular and Optical Physics **29**, 3971 (1996).

[283] M. T. McAlinden, A. A. Kernoghan, and H. Walters, Journal of Physics B: Atomic, Molecular and Optical Physics **30**, 1543 (1997).

[284] G. Danby and J. Tennyson, Journal of Physics B: Atomic, Molecular and Optical Physics **24**, 3517 (1991).

[285] J. Tennyson and L. Morgan, Journal of Physics B: Atomic and Molecular Physics **20**, L641 (1987).

[286] G. Danby and J. Tennyson, Journal of Physics B: Atomic, Molecular and Optical Physics **23**, 1005 (1990).

[287] V. Graves and J. D. Gorfinkiel, The European Physical Journal D **76**, 43 (2022).

[288] O. Zatsarinny, K. Bartschat, and S. Tayal, Journal of Physics B: Atomic and Molecular Physics **39**, 1237 (2006).

[289] O. Zatsarinny, K. Bartschat, D. V. Fursa, and I. Bray, Journal of Physics B: Atomic and Molecular Physics **49**, 235701 (2016).

[290] O. Zatsarinny, K. Bartschat, L. Bandurina, and V. Gedeon, Physical Review A **71**, 042702 (2005).

[291] F. Salvat, A. Jablonski, and C. J. Powell, Computer Physics Communications **165**, 157 (2005).

[292] D. D. Reid and J. Wadehra, Journal of Physics B: Atomic, Molecular and Optical Physics **29**, L127 (1996).

[293] R. McEachran, A. Ryman, A. Stauffer, and D. Morgan, Journal of Physics B: Atomic and Molecular Physics **10**, 663 (1977).

[294] S. Chen, R. McEachran, and A. Stauffer, Journal of Physics B: Atomic, Molecular and Optical Physics **41**, 025201 (2008).

[295] D. Assafrão, H. R. J. Walters, F. Arretche, A. Dutra, and J. R. Mohallem, Physical Review A **84**, 022713 (2011).

[296] A. Zecca, L. Chiari, G. García, F. Blanco, E. Trainotti, and M. Brunger, Journal of Physics B: Atomic, Molecular and Optical Physics **43**, 215204 (2010).

[297] A. Zecca, L. Chiari, G. García, F. Blanco, E. Trainotti, and M. Brunger, New Journal of Physics **13**, 063019 (2011).

[298] A. S. Barbosa, F. Blanco, G. García, and M. H. Bettega, Physical Review A **100**, 042705 (2019).

[299] J. S. Germano and M. A. Lima, Physical Review A **47**, 3976 (1993).

[300] F. Frighetto, A. S. Barbosa, and S. d. Sanchez, Physical Review A **108**, 012818 (2023).

[301] J. Lino, J. Germano, and M. Lima, Journal of Physics B: Atomic, Molecular and Optical Physics **27**, 1881 (1994).

[302] F. Arretche, R. da Costa, S. d. Sanchez, A. Hisi, E. De Oliveira, M. d. N. Varella, and M. Lima, Nuclear Instruments and Methods in Physics Research Section B: Beam Interactions with Materials and Atoms **247**, 13 (2006).

[303] J. L. Lino and B. Christ, Chinese Journal of Physics **50**, 398 (2012).

[304] J. L. Lino, Revista mexicana de Física **60**, 156 (2014).

[305] E. P. da Silva, J. S. Germano, and M. A. Lima, Physical Review A **49**, R1527 (1994).

[306] M. T. d. N. Varella, C. R. de Carvalho, and M. A. Lima, Nuclear Instruments and Methods in Physics Research Section B: Beam Interactions with Materials and Atoms **192**, 225 (2002).

[307] M. V. Barp, W. Tenfen, and F. Arretche, Atoms **11**, 8 (2023).

[308] G. Gribakin and J. Ludlow, Physical Review A **70**, 032720 (2004).

[309] D. Green and G. Gribakin, Physical Review A **88**, 032708 (2013).

[310] V. Dzuba, V. Flambaum, G. Gribakin, and W. King, Journal of Physics B: Atomic, Molecular and Optical Physics **29**, 3151 (1996).

[311] C. M. Surko, G. Gribakin, and S. J. Buckman, Journal of Physics B: Atomic and Molecular Physics **38**, R57 (2005).

[312] J. Hofierka, B. Cunningham, C. M. Rawlins, C. H. Patterson, and D. G. Green, Nature **606**, 688 (2022).

[313] G. Gribakin, J. A. Young, and C. Surko, Reviews of Modern Physics **82**, 2557 (2010).

[314] V. Stancalie, Journal of Physics B: Atomic and Molecular Physics **576**, 012010 (2015).

[315] S. A. Abdel-Naby, C. P. Ballance, T. G. Lee, S. D. Loch, and M. S. Pindzola, Physical Review A **87**, 022708 (2013).

[316] K. Joshipura and P. Patel, Zeitschrift für Physik D Atoms,Molecules and Clusters **29**, 269 (1994).

[317] R. J. W. Henry, P. G. Burke, and A.-L. Sinfailam, Physical Review **178**, 218 (1969).

[318] P. M. Stone and Y. S. Kim, Surface and Interface Analysis **37**, 966 (2005).

[319] M. S. Pindzola, J. Colgan, F. Robicheaux, and D. C. Griffin, Physical Review A **62**, 042705 (2000).

[320] F. B. Malik, Zeitschrift für Naturforschung A **16**, 500 (1961).

[321] ICRU, *Stopping Powers for Electrons and Positrons*, Tech. Rep. (1984).

[322] T. Majeed and D. J. Strickland, Journal of Physical and Chemical Reference Data **26**, 335 (1997).

[323] L. Sharma, R. Srivastava, and A. Stauffer, Journal of Physics B: Atomic and Molecular Physics **40**, 3025 (2007).

[324] P. Johnson, J. McConkey, S. Tayal, and I. Kanik, Canadian Journal of Physics **83**, 589 (2005).

[325] Y. Itikawa and A. Ichimura, Journal of Physical and Chemical Reference Data **19**, 637 (1990).

[326] J. Williams and L. Allen, Journal of Physics B: Atomic, Molecular and Optical Physics **22**, 3529 (1989).

[327] G. Sunshine, B. B. Aubrey, and B. Bederson, Physical Review **154**, 1 (1967).

[328] R. Neynaber, L. L. Marino, W. Rothe, and S. Trujillo, Physical Review **123**, 148 (1961).

[329] E. W. Rothe, L. L. Marino, R. Neynaber, and S. Trujillo, Physical Review **125**, 582 (1962).

[330] R. R. Laher and F. R. Gilmore, Journal of Physical and Chemical Reference Data **19**, 277 (1990).

[331] P. Barklem, Astronomy & Astrophysics **462**, 781 (2007).

[332] K. Joshipura, B. Vaishnav, and C. Limbachiya, Pramana **66**, 403 (2006).

[333] A. Hleli, R. Riahi, P. Teulet, Y. Cressault, and H. Ghalila, in *Journal of Physics: Conference Series*, Vol. 1243 (IOP Publishing, 2019) p. 012014.

[334] A. Zecca, L. Chiari, E. Trainotti, D. Fursa, I. Bray, and M. Brunger, The European Physical Journal D **64**, 317 (2011).

[335] C. Makochekanwa, J. Machacek, A. Jones, P. Caradonna, D. Slaughter, R. McEachran, J. Sullivan, S. J. Buckman, S. Bellm, B. Lohmann, *et al.*, Physical Review A **83**, 032721 (2011).

[336] S. Fayer, A. Loreti, S. Andersen, Á. Kövér, and G. Laricchia, Journal of Physics B: Atomic and Molecular Physics **49**, 075202 (2016).

[337] A. Zecca, L. Chiari, E. Trainotti, and M. J. Brunger, Journal of Physics B: Atomic and Molecular Physics **45**, 085203 (2012).

[338] M. Charlton, Reports on Progress in Physics **48**, 737 (1985).

[339] L. Chiari and A. Zecca, The European Physical Journal D **68**, 1 (2014).

[340] C. Ballance, D. Griffin, M. Pindzola, and S. Loch, Journal of Physics B: Atomic and Molecular Physics **40**, F27 (2007).

[341] P. J. Marchalant and K. Bartschat, Journal of Physics B: Atomic and Molecular Physics **30**, 4373 (1997).

[342] S. Nakazaki and K. Berrington, Journal of Physics B: Atomic and Molecular Physics **24**, 4263 (1991).

[343] J. Berengut, S. Loch, M. Pindzola, C. Ballance, and D. Griffin, Physical Review A **76**, 042704 (2007).

[344] E. Robinson and S. Geltman, Physical Review **153**, 4 (1967).

[345] S. Ormonde, Physical Review Letters **38**, 690 (1977).

[346] W. D. Robb and R. J. W. Henry, Physical Review A **16**, 2941 (1977).

[347] T. Rescigno, A. Hazi, and N. Winter, Physical Review A **16**, 2488 (1977).

[348] K. S. Baliyan and A. K. Bhatia, Physical Review A **50**, 2981 (1994).

[349] C. Makochekanwa, O. Sueoka, and M. Kimura, Nuclear Instruments and Methods in Physics Research Section B: Beam Interactions with Materials and Atoms **247**, 79 (2006).

[350] O. Sueoka, S. Mori, and Y. Katayama, Journal of Physics B: Atomic and Molecular Physics **20**, 3237 (1987).

[351] H. Bluhme, N. Frandsen, F. Jacobsen, H. Knudsen, J. Merrison, R. Mitchell, K. Paludan, and M. Poulsen, Journal of Physics B: Atomic, Molecular and Optical Physics **32**, 5825 (1999).

[352] C. Makochekanwa, O. Sueoka, and M. Kimura, in *Journal of Physics: Conference Series*, Vol. 80 (IOP Publishing, 2007) p. 012012.

[353] C. R. de Carvalho, M. T. do N Varella, M. A. Lima, E. P. da Silva, and J. S. Germano, Nuclear Instruments and Methods in Physics Research Section B: Beam Interactions with Materials and Atoms **171**, 33 (2000).

[354] A. S. Barbosa, The Journal of Physical Chemistry A **126**, 7924 (2022).

[355] S. d. Sanchez, F. Arretche, and M. Lima, Physical Review A **77**, 054703 (2008).

[356] B. H. Bransden, *Atomic Collision Theory* (WA Benjamin, Inc., New York, 1970).

[357] C. Froese-Fischer, *Computational Atomic Structure: An MCHF Approach* (Taylor & Francis, Boca Ranton, 1979).

[358] O. Zatsarinny, K. Bartschat, J. Mitroy, and J.-Y. Zhang, The Journal of Chemical Physics **130**, 124310 (2009).

[359] I. Bray and A. Stelbovics, Advances In Atomic, Molecular, and Optical Physics **35**, 209 (1995).

[360] I. Bray and A. T. Stelbovics, Physical Review A **46**, 6995 (1992).

[361] T. F. O'Malley, Physical Review **130**, 1020 (1963).

[362] D. D. Reid and J. M. Wadehra, Journal of Physics B: Atomic and Molecular Physics **47**, 225211 (2014).

[363] P. G. Burke, *Potential Scattering in Atomic Physics* (Plenum press, 1977).

[364] F. Salvat, Physical Review A **68**, 012708 (2003).

[365] G. Staszewska, D. W. Schwenke, and D. G. Truhlar, Chemical Physics **81**, 335 (1984).

[366] I. Bray and A. T. Stelbovics, Computer Physics Communications **85**, 1 (1995).

[367] F. Blanco and G. García, Physics Letters A **317**, 458 (2003).

[368] R. D. J. III, "Nist computational chemistry comparison and benchmark database," NIST Standard Reference Database Number 101 (2022).

[369] K. Haris and A. Kramida, Astrophysical Journal Supplement Series **233**, 16 (2017).

[370] A. Das and A. J. Thakkar, Journal of Physics B: Atomic and Molecular Physics **31**, 2215 (1998).

[371] P. Schwerdtfeger and J. K. Nagle, Molecular Physics **117**, 1200 (2019).

[372] E.-A. Reinsch and W. Meyer, Physical Review A **18**, 1793 (1978).

[373] G. F. Gribakin and W. A. King, Journal of Physics B: Atomic and Molecular Physics **27**, 2639 (1994).

[374] V. Jonauskas, Astronomy & Astrophysics **620**, A188 (2018).

[375] G. Karwasz, The European Physical Journal D **35**, 267 (2005).

[376] M. Asai, M. A. Cortés-Giraldo, V. Giménez-Alventosa, V. Giménez Gómez, and F. Salvat, Frontiers in Physics , 660 (2021).

[377] R. A. Alpher and D. R. White, Physics of Fluids **2**, 153 (1959).

[378] D. Thwaites, Journal of Radiation Research **95**, 495 (1983).

[379] O. Zatsarinny, K. Bartschat, J.-Y. Zhang, and J. Mitroy, Molecular Physics **107**, 2387 (2009).

[380] A. Nicklass, M. Dolg, H. Stoll, and H. Preuss, The Journal of Chemical Physics **102**, 8942 (1995).

[381] J. Mitroy and J.-Y. Zhang, Physical Review A **76**, 032706 (2007).

[382] A. A. Radzig and B. M. Smirnov, *Reference data on atoms, molecules, and ions* (Springer, 1985).

[383] J. Carlsson, P. Jönsson, L. Sturesson, and C. F. Fischer, Physical Review A **49**, 3426 (1994).

[384] P. Jönsson, C. F. Fischer, and M. Godefroid, Journal of Physics B: Atomic, Molecular and Optical Physics **29**, 2393 (1996).

[385] C. F. Fischer and G. Tachiev, Atomic Data and Nuclear Data Tables **87**, 1 (2004).

[386] A. D. Pradhan, H. Partridge, and C. W. Bauschlicher Jr, The Journal of Chemical Physics **101**, 3857 (1994).

[387] J. Lino, Revista Mexicana de Física **63**, 303 (2017).

[388] S. Anderson, J. Morton, and K. Mauersberger, The Journal of Chemical Physics **93**, 3826 (1990).

[389] U. Kaldor, The Journal of Chemical Physics **87**, 467 (1987).

[390] W. J. Brigg, J. Tennyson, and M. Plummer, Journal of Physics B: Atomic, Molecular and Optical Physics **47**, 185203 (2014).

[391] N. Watanabe, D. Suzuki, and M. Takahashi, The Journal of Chemical Physics **134**, 064307 (2011).

[392] N. Padial and D. Norcross, Physical Review A **29**, 1742 (1984).

[393] A. Jain, Journal of Physics B: Atomic, Molecular and Optical Physics **23**, 863 (1990).

[394] K. Baluja, R. Zhang, J. Franz, and J. Tennyson, Journal of Physics B: Atomic, Molecular and Optical Physics **40**, 3515 (2007).

[395] A. Zecca, G. P. Karwasz, and R. S. Brusa, La Rivista del Nuovo Cimento **19**, 1 (1996).

Every reasonable effort has been made to acknowledge the owners of copyright material. I would be pleased to hear from any copyright owner who has been omitted or incorrectly acknowledged.